THE UNIVERSITY *of* EDINBURGH

Evaluating Wind Load Simulation Methods in Wave Basin Testing of Floating Offshore Wind Turbines While Balancing Complexity and Test Objectives

Anita Leite

Doctor of Philosophy

The University of Strathclyde

2025

Dedicated to my parents, the most selfless people I know,

Avelino Leite and Maria das Dores Leite

Abstract

The development of floating offshore wind turbines (FOWTs) has accelerated in recent years, drawing heavily on experience from the oil & gas and naval architecture sectors. Numerical modelling tools originally developed for these industries are now being adapted for floating wind applications. However, to ensure their reliability, these tools require experimental validation, typically through wave basin testing.

Basin testing of FOWTs presents unique challenges due to the scaling incompatibility between aerodynamics experienced by the rotor and hydrodynamics experienced by the floater, making the accurate representation of both loads particularly difficult. In basin testing, various methods for simulating the wind loads have been proposed, ranging from simplistic to highly complex. Yet, no consensus exists on which method is most appropriate for different testing objectives or technology readiness levels (TRLs).

This thesis investigates how the complexity of wind actuation systems influences test outcomes and whether simpler alternatives to Software-in-the-Loop (SIL) methods may suffice depending on test goals. A dedicated methodology was developed to compare three actuation approaches: static weight, constant thrust, and SIL, using the same FOWT model, the UMaine VolturnUS-S platform with a 15 MW IEA wind turbine, tested at the FloWave basin. The three campaigns differed only in their wind actuation approach, enabling a direct comparison of their influence on system response. Additional considerations included metocean condition selection and the adaptation of the mooring system for physical testing.

Results show that while SIL enables full coupling between aerodynamic and hydrodynamic responses, its effectiveness depends on the responsiveness and fidelity of the control implementation. Insufficient tuning can introduce negative damping effects or overly amplified motions. The proportional–integral (PI) control method yielded the best agreement with the numerical model across most degrees of freedom, particularly pitch and surge, while the Static Weight approach introduced the largest discrepancies, especially in dynamic scenarios, though it offered reasonable agreement in mooring tension predictions. Directional wave–wind misalignment tests further demonstrated the importance of reproducing asymmetries in yaw and sway, where differences in applied thrust orientation (e.g., via winch angle shifting during large yaw excursions) can introduce additional discrepancies.

Based on these findings, preliminary guidance is proposed for selecting wind actuation strategies according to the Technology Readiness Level (TRL) of the system under test. For early-stage development (TRL 2–3), the Static Weight method may be sufficient for basic hydrodynamic characterisation and capturing mooring line tensions. At intermediate stages (TRL 3–4), the

PI method offers greater fidelity and improved agreement with numerical models, particularly when the primary focus of the test remains on hydrodynamic behaviour. For high-fidelity testing and validation at advanced TRL (5 and above), the SIL method is recommended, provided the actuation system is responsive enough to avoid introducing amplifications. Moreover, for testing and validating control methodologies, SIL is the only approach capable of capturing the dynamic interaction between the controller and the platform.

Lay Summary

Complexity is tempting: more knobs to turn, more data to collect, and the sense that *more* must mean *better*. Yet complexity costs time and money, so the smart move is to choose the least complex setup that still answers the question. That idea sits at the heart of this work. Floating offshore wind pushes turbines into deeper waters with steadier winds, but putting a 15 MW machine on a moving platform is hard. We de-risk with scale-model tests in a wave basin and cross-check against simulations. I put the same floating offshore wind turbine (FOWT), the UMaine VolturnUS-S with the IEA 15 MW wind turbine, through three wind-actuation strategies that span the spectrum of complexity: static weight, constant-thrust control (PI), and Software-in-the-Loop (SIL). I ran calm, regular, irregular, and extreme seas, with wind both aligned with and misaligned with the waves, and I measured platform motions (for example pitch and surge) and mooring-line tensions while comparing to a numerical model.

The story that emerges is pragmatic. SIL gives the fullest aero-hydro coupling but only pays off when the control is tuned and responsive, otherwise it can amplify motions. PI often strikes the best balance between fidelity and deployment effort. Static weight is surprisingly serviceable for early hydrodynamics and tension characterisation. From these results I offer clear thresholds that map actuation choice to Technology Readiness Level. For TRL 2 to 3 use static weight. For TRL 3 to 4 prefer PI. For TRL 5 and above choose SIL if the actuation is responsive enough to avoid amplifications. In the end progress is not about maximising complexity, it is about right-sizing it. This work was supported by EPSRC & NERC through the Industrial CDT in Offshore Renewable Energy (EP/S023933/1). Experiments were conducted at, and supported by, the FloWave Ocean Energy Research Facility in Edinburgh between 1 September 2021 and 28 August 2025. This study involves laboratory experiments only and poses no risk to the public.

Acknowledgements

I would like to express my deepest gratitude to my supervisors, Dr. Thomas Davey, Dr. Ajit C. Pillai, Dr. David Dai, and Professor Tom Bruce, for their invaluable guidance, constructive feedback, and continuous encouragement throughout this research. Their expertise, understanding, and support were fundamental to the completion of this thesis.

I also wish to thank my colleagues at the FloWave Ocean Energy Facility as a whole, and especially Callum Guy and Martyn Lennon, for their patience in teaching me how to handle the tools, for sharing their knowledge, and above all for their friendship and companionship during the hard times.

This work was supported by EPSRC and NERC through the Industrial CDT in Offshore Renewable Energy (EP/S023933/1) and sponsored by the FloWave Ocean Energy Research Facility, whose financial and technical assistance I gratefully acknowledge.

Finally, I am profoundly grateful to my partner, family and friends for their constant encouragement, patience, and belief in me. To my parents, I owe a special thanks for all their hard work and the sacrifices that have helped me reach this objective.

Contents

Abstract iii

Lay Summary v

Acknowledgements vi

Figures and Tables x

1 Introduction 1

1.1 Aims and Objectives . . . 2

1.2 Thesis Structure . . . 3

2 Background and Literature Review 4

2.1 Overview of the floating offshore wind sector . . . 5

2.2 Technology Readiness Level . . . 6

2.3 Physical testing of floating wind turbines: TRL 1 - TRL 4 . . . 10

2.3.1 Physical Testing Challenges . . . 11

2.4 Methods of applying aerodynamic loads in wave basins . . . 12

2.4.1 Preliminary methods . . . 15

2.4.2 Full-Approach . . . 16

2.4.3 Hybrid Approach . . . 20

2.5 Numerical tools . . . 24

2.5.1 Comparison between existent software . . . 26

2.6 Current recommendations . . . 31

2.6.1 Standards and Guidance Documents . . . 31

2.7 Staged Development Approach . . . 33

2.7.1 Identified Knowledge Gaps . . . 39

3 Experimental and Numerical Methodology 40

3.1 Model Inputs . . . 42

3.1.1 FOWT Reference Model . . . 42

3.1.2 Site Characterisation . . . 42

3.2 Numerical Modelling Tools . . . 45

3.2.1 Determination of Moments of Inertia, Mass, and Center of Gravity of the Model . . . 46

3.2.2 Only thrust simulation . . . 49

3.3 Physical Testing . . . 50

3.3.1 Description of the wave basin: FloWave . . . 51
3.3.2 Selection of model scale . . . 52
3.3.3 Coordinate system . . . 55
3.3.4 Design and construction of the FOWT model . . . 56
3.3.5 Simulation Length . . . 60
3.3.6 Wind field . . . 60
3.3.7 Waves . . . 61
3.3.8 Application of aerodynamic loads in the wave basin . . . 61
3.3.9 Mooring System Design . . . 74
3.4 Tank test plan . . . 82
3.4.1 Frequencies of interest . . . 83
3.4.2 Test plan . . . 84
3.4.3 Data processing . . . 92
3.5 Chapter summary and outlook . . . 94

4 Results: Numerical–Experimental Evaluation 95
4.1 Metocean Data Analysis Results . . . 97
4.1.1 Application of the Inverse–First Order Reliability Method (I-FORM) . . . 98
4.2 Numerical Sensitivity Analysis: Constant Force vs. Aerodynamic Model . . . 103
4.2.1 Still Water Case: Static vs. Dynamic Loading . . . 103
4.2.2 Regular waves: Response comparison . . . 107
4.2.3 Irregular waves: Response comparison . . . 110
4.3 Model Characterisation: Experimental vs. Numerical Representation . . . 112
4.3.1 Wave calibration and diffraction analysis . . . 112
4.3.2 Irregular wave calibration . . . 113
4.3.3 Diffraction analysis and hydrodynamic coefficients . . . 114
4.3.4 Mooring pre-tensions . . . 116
4.3.5 Natural frequencies and damping . . . 117
4.3.6 No Wind Load: RAO and Extreme Wave Validation of Mooring System Representations . . . 121
4.4 Effect of Wind Actuation Method on Platform Response . . . 135
4.4.1 Response Amplitude Operators . . . 136
4.4.2 Irregular waves . . . 145
4.4.3 Wind–wave misalignment ($\Delta = -30^{\circ}$) . . . 156

5 Discussion: Balancing Test Objectives and Actuation Complexity 171
5.1 Limitations and Simplifications . . . 172
5.1.1 Inherent Differences Between Numerical and Experimental Hydrodynamic Models . . . 173
5.1.2 Mooring-system simplification and its implications . . . 174

5.1.3 Actuation System Constraints and Control Fidelity 175
5.1.4 Synthesis of PI and SIL Control Performance 184
5.1.5 Wind–wave misalignment and directional fidelity 185
5.2 Does Complexity Improve Accuracy? 186
5.3 Is Complexity Justified? 188
5.3.1 Cost and Effort vs. Performance 190
5.4 Staged Development Approach: Recommended Application Strategy 191

6 Conclusions and Recommendations 194
6.1 Summary of Findings 194
6.2 Limitations 196
6.3 Recommendations for Future Work 197
6.4 Closing Statement 197

Appendices

A Model Build 198

B Winch System Set-up 200
B.1 Overview 200
B.2 Component Specifications 200
B.3 General scheme of the DAQ and actuator connection 201

C Submitted manuscript: Implementation of wave basin spring–rope mooring system for floating offshore wind turbines 202

Figures and Tables

Figures

2.1 Visual representation of the offshore wind projects in Europe. It includes online, partially online and under construction projects. The size of the circles is related to the installed capacity in MW. Note: Adapted from WindEurope. 5
2.2 Timeline of floating offshore wind turbine deployments, including prototypes, demonstrators, and farms. Adapted from Edwards et al. (2023). 7
2.3 Detailed explanation of each one of the nine TRL levels. Note: Adapted from OffshoreWindInnovationHub (2024). 8
2.4 Wind turbine shaft coordinate system. Note: Adapted from Jonkman and Buhl Jr. (2006). 13
2.5 WindFloat model testing using a drag disk Cermelli et al. (2009). 16
2.6 General principle of the hybrid approach. 21
2.7 Numerical model basic mode of operation. 27
2.8 Staged Development Approach on the Wave energy Sector (BSI, 2024). 34

3.1 High-level schematic of the different phases of the tank test campaign, with increasing complexity in aerodynamic load representation. 41
3.2 Overall simplification of the methodology sections, representing the process flow of the study. 41
3.3 Location of Haugesund in the map. 43
3.4 Occurrence probabilities of sea states (H_s vs. T_p) at 59.5° N, 5° E (1990–2019). Colours range from green (0%) to red (higher percentages). Yellow and blue borders indicate the FloWave regular- and irregular-wave envelopes; additional overlays show candidate sweep selections used for planning. 44
3.5 The FloWave Ocean Energy Research Facility. 51
3.6 FloWave dimensions (adapted from: Sutherland et al. (2017)) 52
3.7 Different systems of applying constant rotor thrust in FloWave basin during AXIS EP Ltd. experiments. 53
3.8 General arrangement of the VolturnUS-S platform. Adapted from Allen et al. (2020). 54
3.9 Global coordinates of the VolturnUS-S model. Adapted from Allen et al. (2020). . 56
3.10 Models of the VolturnUS-S in 1:50 scale. 58
3.11 Schematic of the tank test set-up at FloWave. 59
3.12 Visualisation of the location of the centre of gravity of the scaled model. 60
3.13 Power and thrust curve for the IEA 15 MW WT. Adapted from Bortolotti et al. (2020). 63

3.14 Static weight rig used in Phase I to impose an equivalent constant rotor thrust. A dead-weight is suspended and routed over a low-friction sheave to the model at hub height, producing a steady horizontal line load with tension $\approx F_T$ (Eq. 3.23). 65
3.15 Hardware components of the winch system at FloWave. 68
3.16 Open-loop (feedforward) actuation used for current–force calibration: a pre-set current produces a nominal force based on prior calibration; no feedback is applied. 69
3.17 Experimental setup for PI tuning of the motor drive. 69
3.18 PID tuning results in tank scale (1:50). 71
3.19 SIL closed-loop force-control scheme. A real-time BEM model supplies the time-varying thrust set-point $F_T(t)$ (in N). A PI controller with gains K_p and K_i (running at $10\,\mathrm{Hz}$ tank scale) computes the motor current command $I_{\mathrm{cmd}}(t)$ (in A), which is converted to PWM to drive the winch. The winch/spindle apply the line force at hub height; the in-line load cell measures $F_{\mathrm{meas}}(t)$ and feeds it back to close the loop. 72
3.20 Step-by-step procedure for the mooring system stiffness matrix calculation. (Reproduced from Amaral et al. (2022) with permission from Elsevier). 77
3.21 Methodology applied to convert a catenary mooring system into a spring-rope configuration for the testing of ORE devices in wave basins. 79
3.22 Illustration of the essential parameters required for the calculation of mooring line local stiffness. Where: $P^{(i)}$ and $A^{(i)}$ are the fairlead and anchor positions, k is the line local stiffness, and α is the line declination angle. 80
3.23 Iterative process used for the choice of the R_f. 81

4.1 Structure of the results chapter showing the comparisons made with increasing level of complexity. 96
4.2 Scatter plots of metocean parameters at 59.5° N, 5° E (1990–2019). 98
4.3 Three-parameter Weibull fit to H_s (1990–2019): histogram and Q–Q diagnostics. 99
4.4 Lognormal fits of $T_p \mid H_s$ across 1 m H_s bins. 99
4.5 Fitted parameter trends $\mu(h)$ and $\sigma(h)$ for $T_p \mid H_s$. 100
4.6 Q–Q plot comparing T_p with a Lognormal model. 100
4.7 I-FORM environmental contours (1- and 50-year) in H_s–T_p space. 101
4.8 I-FORM contours in H_s–U space. 102
4.9 Coordinate systems used for the sensitivity study: (a) shaft and (b) nacelle/yaw. . 104
4.10 Comparison of time series for Rotor Thrust and YawBrFxn under still water sensitivity analysis. 105
4.11 Comparison of still water results for different variables. For each case, statistical values are extracted from the time series, including the mean (average value), standard deviation (variability of the signal), maximum (peak value), and minimum (lowest value). 106

4.12 Comparison of regular wave results for different variables. For each case, statistical values are extracted from the time series, including the mean (average value), standard deviation (variability of the signal), maximum (peak value), and minimum (lowest value). 109
4.13 Comparison of irregular wave results for different variables. For each case, statistical values are extracted from the time series, including the mean (average value), standard deviation (variability of the signal), maximum (peak value), and minimum (lowest value). 111
4.14 Irregular wave calibration example at 0° wave incidence showing the free surface elevation time series, FFT amplitude, and comparison between measured PSD and theoretical JONSWAP spectrum ($H_s = 5$ m, $T_p = 11.5$ s). 115
4.15 Irregular wave calibration example at 30° wave incidence showing the free surface elevation time series, FFT amplitude, and comparison between measured PSD and theoretical JONSWAP spectrum ($H_s = 5$ m, $T_p = 11.5$ s). 115
4.16 Comparison of RAOs for Surge at 1 m and 4 m wave heights, comparing experimental results with both numerical mooring configurations. 124
4.17 Comparison of RAOs for Pitch at 1 m and 4 m wave heights, comparing experimental results with both numerical mooring configurations. 124
4.18 Comparison of RAOs for Heave at 1 m and 4 m wave heights, comparing experimental results with both numerical mooring configurations. 125
4.19 Ratio of RAOs for Surge at 1 m and 4 m wave heights, comparing experimental results with the two numerical models (OpenFAST catenary and OpenFAST adapted). 126
4.20 Ratio of RAOs for Pitch at 1 m and 4 m wave heights, comparing experimental results with the two numerical models (OpenFAST catenary and OpenFAST adapted). 126
4.21 Ratio of RAOs for Heave at 1 m and 4 m wave heights, comparing experimental results with the two numerical models (OpenFAST catenary and OpenFAST adapted). 127
4.22 Comparison of pitch, surge, and heave displacements under 3 extreme sea states. 131
4.23 Comparison of mean fairlead mooring line tensions for the Fore (F), Port (P), and Starboard (S) lines under the three extreme wave conditions. Error bars show ± 1 standard deviation. 133
4.24 Stiffness coefficient values in surge, heave, pitch and yaw, obtained when changing the line length input value in MAP++ input file. Grey area represents the values for the chosen line length. The horizontal lines labelled with the respective DOF represent to the target value from the linear stiffness matrix (Table 4.8). . . 134
4.25 RAOs for Surge at different wave heights under rated wind conditions. 137
4.26 RAOs for Pitch at different wave heights under rated wind conditions. 138

4.27 RAOs for Heave at different wave heights under rated wind conditions. 139
4.28 RAOs for Surge at different wave heights under below-rated wind conditions. . . 141
4.29 RAOs for Pitch at different wave heights under below-rated wind conditions. . . . 142
4.30 RAOs for Heave at different wave heights under below-rated wind conditions. . . 144
4.31 Comparison of mean pitch displacement and standard deviation for irregular waves across different wind speeds and actuation methods. 147
4.32 Comparison of mean surge displacement and standard deviation for irregular waves across different wind speeds and actuation methods. 150
4.33 Comparison of mean heave displacement and standard deviation for irregular waves across different wind speeds and actuation methods. 152
4.34 Comparison of mean fore mooring tension and standard deviation for irregular waves across different wind speeds and actuation methods. 155
4.35 Grouped mean and standard deviation for surge displacement across all wind speeds. 158
4.36 Grouped mean and standard deviation for sway displacement across all wind speeds. 160
4.37 Grouped mean and standard deviation for heave displacement across all wind speeds. 161
4.38 Grouped mean and standard deviation for roll motion across all wind speeds. . . 163
4.39 Grouped mean and standard deviation for pitch motion across all wind speeds. . 164
4.40 Grouped mean and standard deviation for yaw motion across all wind speeds. . . 166
4.41 Grouped mean and standard deviation for fore mooring line tension across all wind speeds. 167
4.42 Grouped mean and standard deviation for port mooring line tension across all wind speeds. 168
4.43 Grouped mean and standard deviation for starboard mooring line tension across all wind speeds. 169

5.1 Normalised and low-pass-filtered control signals over 11.5 seconds period waves. The black trace is the physical wave elevation, the blue trace the commanded set-point, the red trace the low-pass filtered load-cell force, the magenta trace the low-pass filtered motor current, and the green trace the platform pitch. 177
5.2 Normalised RMSE (% of F_{cmd}) as a function of wave peak period for the three load levels. 180
5.3 Overlay of normalised wave elevation, SIL set-point, and measured pitch for a regular wave of $H = 6\,\mathrm{m}$ and $T = 13.5\,\mathrm{s}$. 181
5.4 Time series of the measured wind load-cell signal (blue) versus the commanded force set-point (orange) for each free-stream wind speed. Within each subplot, the three traces correspond to wave periods $T_p = 1.63, 1.98, 2.55\,\mathrm{s}$ from top to bottom. 183

A.1 Constituent parts of the 50th scaled VolturnUS-S model built at FloWave. 199

B.1 Overview of the DAQ and actuator system for the SIL application. 201

Tables

2.1 Comparison of fan and winch systems for aerodynamic load actuation. 22
2.2 Summary of previous studies implementing aerodynamic load application methods for floating offshore wind turbine model testing. The table lists the applied method, associated WT rating, model scale, and other relevant setup details. . . 23
2.3 Aero-hydro-servo-elasto numerical models used for coupled analysis of FOWTs. 30
2.4 List of tank testing deployments with the corresponding technique used to simulate aerodynamic loads, the TRL value at the time of the testing, and the TRL value at the present time.* 37
2.5 Theoretical proposed set-ups for stages 1 and 2 for a Staged Developemnt Approach for FOWT. 38

3.1 Extreme sea states adopted for physical testing (derived via I-FORM). 45
3.2 Table summarising the parameters for each one of the cases used for comparison between the 'Only thrust' and 'Normal' scenarios. 50
3.3 Scaling factors for various physical quantities according to the Froude number. . 53
3.4 Model properties 55
3.5 Comparison between the target values and measured values of the scaled model properties. 58
3.6 Simulation lengths for regular and irregular waves at 1:50 Scale and Full-Scale. . 62
3.7 Wind speeds and correspondent rotor thrust values acquired from OpenFast simulations at full-scale and at 1:50 scale. 64
3.8 Target thrust and corresponding weights for the various wind conditions in tank scale. 66
3.9 Summary of PI gain values and test types. 70
3.10 Operating points used for BEM–AeroDyn comparison and SIL setup. 73
3.11 BEM vs. `AeroDyn` outputs for matched operating points. 74
3.12 Per-step runtime (single time-step evaluation). 74
3.13 Rigid-Body natural frequencies given in full-scale. 83
3.14 Model characterisation tests (no environmental forcing). 85
3.15 Summary of performed tests for Regular Waves. 87
3.16 Summary of performed tests for Irregular Waves, including extremes. 89

3.17 Summary of performed tests for Wind/Wave Misalignment for both Regular and Irregular Waves. 91

4.1 Relative difference between Only Thrust and Normal configurations using mean values, with Normal as reference. 108
4.2 Regular-wave calibration results from wave-gauge records (Gauge 4). Target values are defined by the run naming convention. Full-scale quantities are obtained using Froude scaling (1:50). 113
4.3 Irregular wave calibration summary (full scale). 114
4.4 Mooring line pre-tensions as measured in the physical experiment, converted to full-scale values. Refer to Figure 3.11 for line labels. 117
4.5 Comparison of theoretical and experimental natural periods at full-scale. 117
4.6 Comparison of experimental and MoorDyn adapted mooring natural periods at full-scale. 119
4.7 Comparison of damping ratios obtained from experimental and numerical decay tests. 120
4.8 Scaled mooring linear stiffness matrix, **m** (N/m, N/rad, N, and Nm/rad). 134
4.9 Baseline mooring pretensions for SIL, PI, and Adapted numerical model. 169

5.1 Absolute performance metrics for each test condition. 179
5.2 Normalised error metrics (percent of F_{cmd}). 179
5.3 Summary of SIL absolute performance metrics for each free-stream wind speed U_∞ and peak wave period T_p after correction of the load-cell calibration. 182
5.4 Qualitative comparison of implementation effort and expected fidelity for the three wind actuation methods investigated in this study. 191

B.1 List of components of the winch system. 200

Chapter 1

Introduction

Floating offshore wind (FOW) expands access to stronger and more persistent wind resources by enabling deployment in deep waters beyond the reach of fixed-bottom foundations. As the sector scales, developers and researchers face a familiar tension: designs must be de-risked early and cost-effectively, yet the coupled aero–hydro–servo–elastic physics that govern floating wind turbine (FOWT) response are complex and interdependent. Across Technology Readiness Levels (TRL) 1–5, physical model testing and numerical simulation are the principal tools for building confidence in new concepts, validating models and informing design choices.

Within this pre-commercial space, a persistent practical question remains unresolved: how complex does the wind-load actuation need to be in a wave basin to produce results that are accurate enough for the test objectives at hand? Facilities and research groups employ a spectrum of approaches, from simple constant-thrust methods, through performance-scaled to full Software-in-the-Loop (SIL) control that reproduces rotor–nacelle–assembly (RNA) dynamics and control loops. More fidelity generally implies greater setup time, equipment cost, failure modes and operational constraints. In contrast, too little fidelity risks biased motion statistics, incorrect load paths, and misleading design inferences.

Despite growing experience, the community lacks evidence-based guidance that links actuation choice to test objective, sea state, and platform characteristics, and that quantifies when the added complexity of advanced actuation materially improves decision relevant metrics. This gap complicates planning, inflates campaign costs and makes it harder to compare results across facilities and studies.

This thesis addresses that gap by systematically evaluating the accuracy–complexity trade-off of wind-load actuation for FOWT model tests. It combines controlled basin experiments with a numerical model to (i) compare actuation methods across regular and irregular seas (ii) quantify sensitivity of platform responses and mooring loads to actuation fidelity, including wind–wave misalignment, and (iii) propose a staged, TRL-aligned application strategy that helps practitioners select the simplest actuation capable of meeting specified accuracy targets.

Contributions of this work include: (a) quantitative thresholds indicating when simpler actuation suffices, and when SIL/closed-loop methods become necessary; (b) a planning framework that maps test objectives to recommended actuation fidelity; and (c) reproducible datasets and workflows to support cross-study comparison.

1.1 Aims and Objectives

Aim: To determine the level of wind-load actuation complexity required in wave-basin testing to achieve decision-relevant accuracy for floating wind turbine response metrics.

Research questions (RQs):

RQ1. Under which sea states, wind conditions, and response metrics do simple actuation schemes (for example, constant thrust) reproduce platform motions and mooring loads within acceptable error relative to higher-fidelity approaches?

RQ2. When is full or hybrid closed-loop actuation (for example, SIL/PI control) indispensable, and which aspects of the response (for example, pitch near the natural-frequency region, low-frequency surge, line tensions) are most sensitive to actuation fidelity?

RQ3. How do wind–wave misalignment and mooring representation influence the perceived benefits of added actuation complexity?

RQ4. How can a staged development approach be formalised to balance accuracy, cost, schedule, and risk across TRL 1–5?

Objectives:

1. Establish metocean design space. Compile and analyse site-representative environmental conditions, including directional extremes, using reliability-based methods to select test cases that span operational and extreme seas.
2. Develop numerical baselines by isolating the effects of thrust-only versus aerodynamic models in still water, regular, and irregular waves.
3. Design and execute basin campaigns. Construct a scaled FOWT model, mooring system, and actuation hardware; define coordinate systems, scaling, and simulation lengths and implement multiple actuation methods (Static weight, PI controlled winch, and hybrid setup).
4. Quantify responses. Measure and compare Response Amplitude Operators (RAOs), time-domain statistics, natural frequencies and damping, and extreme responses, with and without wind and under wind misalignment.
5. Assess mooring representation. Evaluate how catenary versus spring-rope mooring models affect the dynamic response of the system.
6. Derive guidance. Synthesise results into accuracy thresholds and a staged application strategy that links test objectives to recommended actuation methods, with documented limitations and uncertainty bounds.

1.2 Thesis Structure

- Chapter 2 – Background and Literature Review. Provides sector context and explanation of the TRL levels; reviews physical testing practices for FOWTs and their challenges; surveys methods for applying aerodynamic loads in basins (preliminary, full, and hybrid); summarises numerical tools and software comparisons; outlines current standards and guidance; presents a staged development approach and identifies knowledge gaps that motivate this thesis.
- Chapter 3 – Experimental and Numerical Methodology. Details model inputs, reference turbine selection, and site characterisation. Describes numerical tools and the determination of mass properties. Defines the numerical thrust-only sensitivity study and the physical testing programme: facility description (FloWave), model scale selection, coordinate system, model build, simulation lengths, wind and wave definitions, actuation implementations, and mooring system design. Presents the tank-test plan (including frequencies of interest and data processing) and closes with a summary and outlook.
- Chapter 4 – Results: Numerical–Experimental Evaluation. Reports metocean analyses (including I-FORM). Compares numerical sensitivity between constant force and aerodynamic models in still water, regular, and irregular waves. Presents experimental–numerical characterization (mooring pre-tensions; natural frequencies and damping; RAOs and extreme waves without wind). Evaluates the effect of wind-actuation method on platform response (RAOs, irregular waves, and wind–wave misalignment).
- Chapter 5 – Discussion: Balancing Test Objectives and Actuation Complexity. Examines limitations and simplifications, including differences between numerical and experimental hydrodynamics, mooring-system simplifications, and control fidelity constraints. Synthesises the performance of PI and SIL control and addresses the central questions: does complexity improve accuracy?; Is complexity justified? It then proposes a staged development strategy that balances accuracy, cost, and effort.
- Chapter 6 – Conclusions and Recommendations. Summarises key findings with their limitations and outlines future work.
- Appendices. Provide model-build details; winch system set-up and data-acquisition/control schematics; and a submitted manuscript on a spring–rope wave-basin mooring implementation.

Chapter 2

Background and Literature Review

This chapter frames the research undertaken in this thesis by offering background on the offshore wind sector, with a specific emphasis on scale testing. It sets the foundation for achieving the thesis's aim and objectives by examining current challenges in testing Floating Offshore Wind Turbines (FOWTs), pinpointing gaps in current procedures, and proposing potential enhancements for current practices.

It begins with an overview of the current state and future trends of the offshore wind industry, highlighting the challenges, targets, and opportunities, with a particular focus on the floating wind sector. Following this, the relevance of tank testing for the development of the sector is discussed, along with the specific challenges associated with it.

FOWTs are subjected to a variety of environmental loads, including aerodynamic, hydrodynamic and mooring induced forces, and understanding the coupled effects of these loads on platform dynamics is essential for their effective design and operation. This information helps determine the maximum and cyclical loads and displacements under operational conditions and extreme events, which in turn informs energy production efficiency and structural design. This chapter outlines various methods used to achieve this understanding using scale testing, with an emphasis on the techniques for applying aerodynamic loads in wave basins. The advantages and disadvantages of each method are presented, providing a comprehensive and critical evaluation of their limitations and benefits.

Finally, the current guidance and standards for tank testing are reviewed. The importance of developers having a clear understanding of the objectives and limitations of the methods used in tank tests is emphasised, highlighting the critical role these standards play in advancing the floating wind sector. Lessons can be learned from the Staged Development Approach applied in the wave energy sector, which could inform the development of a structured protocol for the wind energy sector in relation to the technology readiness level of the model being tested.

2.1 Overview of the floating offshore wind sector

The European Green Deal (Commission, 2019) sets the framework for tackling climate change and its environmental-related challenges. Renewable energy, specifically offshore wind, is at the forefront of decarbonising the energy sector to reach net-zero emission targets with significant efforts being made to increase Europe's offshore wind capacity.

Currently, Europe has approximately 34.2 GW of installed offshore wind power capacity, according to WindEurope, with 270 MW attributed to floating wind technology. Figure 2.1 shows the distribution of offshore wind projects that are currently online, partially online, or under construction. According to the European Union (EU) strategy on offshore renewable energy, this capacity needs to reach at least 60 GW by 2030 and 300 GW by 2050 (European Commission). Significant progress has been made in installing fixed offshore wind turbines, particularly in the North Sea and Baltic Sea, where shallow waters and consistent wind conditions prevail. However, achieving these goals requires expanding into less favourable areas with water depths exceeding 200 meters. This presents opportunities for the growth of the floating wind sector. Within the 270.9 MW of floating wind installed in Europe, 80 MW are located off the northeast coast of the United Kingdom, comprising the Kincardine Pilot and Hywind Scotland projects. Norway is also at the forefront of the floating offshore sector with the recent installation and commissioning of the Hywind Tampen wind farm.

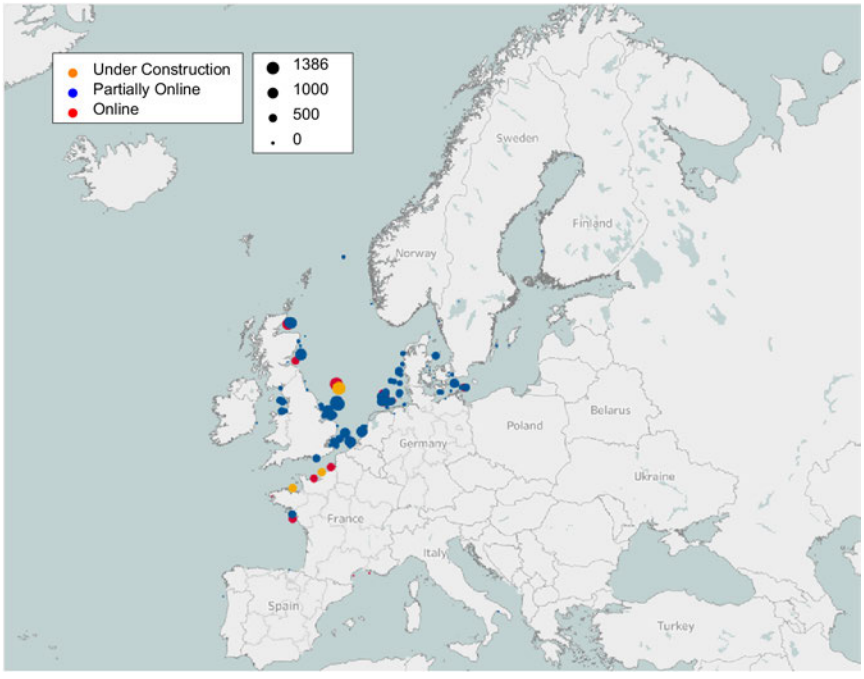

Figure 2.1: Visual representation of the offshore wind projects in Europe. It includes online, partially online and under construction projects. The size of the circles is related to the installed capacity in MW. Note: Adapted from WindEurope.

Figure 2.2 shows the timeline of floating offshore wind turbine deployments, including prototypes, demonstrators, and commercial farms. The installed capacity has been increasing over the past seven years, with demonstration projects accelerating the technological development of various floating platforms that are now being deployed in multi-MW wind farms. Although there has been a convergence towards four main types of floating structures based on their design and restoring forces mechanisms, various hybrid model designs have emerged to address the significant factor of cost reduction (Edwards et al., 2023).

The installation of wind turbines offshore, benefits from steeper wind shear, higher wind speeds, and less competition for space compared to onshore sites. However, these installations must be economically viable and capable of competing with alternative energy technologies in the market (Breeze, 2016). Other challenges include the port infrastructure that must accommodate larger and deeper draft floating structures, as well as increasingly large wind turbine blades. Additionally, vessels used for transportation and lifting must also adapt to these increased sizes (Dedecca et al., 2016). Overall, the development of the floating wind sector impacts various other sectors, creating challenges but also opportunities for social and economic growth.

Newer concepts in the early stages of Technology Readiness Level (TRL) are being developed to target these challenges, in line with the European Union's objectives for a sustainable, secure and competitive energy supply, as outlined in the REPowerEU Plan (European Commission, 2022). Many of these concepts remain at TRL 1–4 and require rigorous experimental validation before commercial deployment becomes feasible. This underlines the continuing need for physical testing in controlled environments, particularly scale-model testing in wave basins, to investigate the coupled responses of floating wind platforms to wind, wave and current conditions. Such testing not only supports the safe and cost-effective advancement of individual designs but also contributes to industry-wide knowledge on design optimisation, performance prediction and risk reduction. Continuous innovation, coupled with systematic low-TRL testing, will be critical to overcoming current obstacles and achieving economic viability in the floating offshore wind sector.

2.2 Technology Readiness Level

The concept of discrete TRL classification was first used by NASA in 1970 as a benchmarking tool on the development of spacecraft technologies (NASA, 2020) and since been adopted by many other programs and sectors, including the European Horizon Program (WindEurope, 2017). The TRL concept, in which technologies are placed on a scale of 1-9 depending on maturity, has also been adopted for the development of offshore renewable technologies. An example for the offshore wind sector is provided by Offshore Wind innovation Hub, illustrated in Figure 2.3.

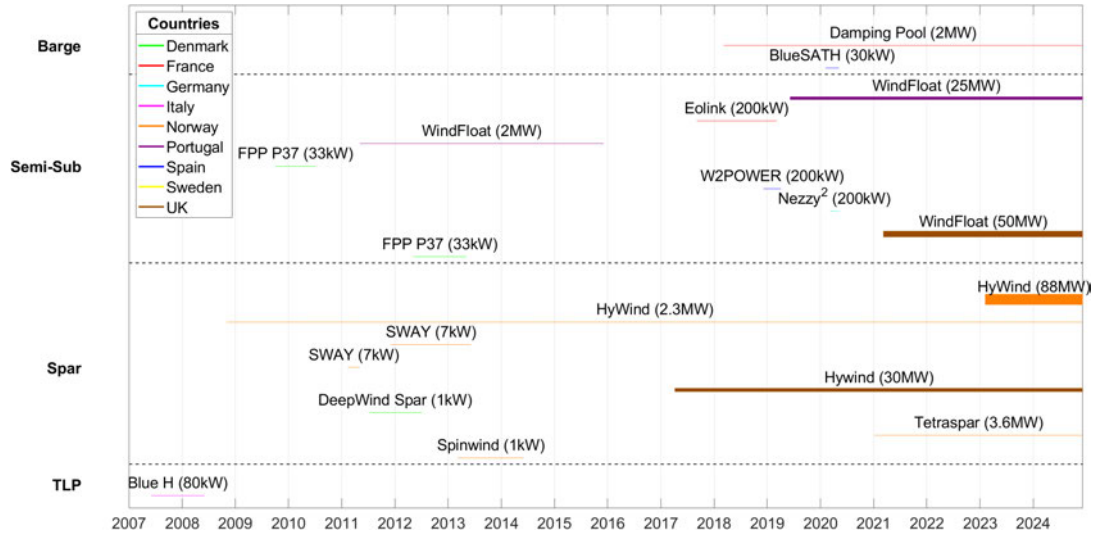

Figure 2.2: Timeline of floating offshore wind turbine deployments, including prototypes, demonstrators, and farms. Adapted from Edwards et al. (2023).

At early stages, specifically from TRL 1 to TRL 4, an iterative procedure is employed that combines laboratory tests and numerical simulations to assess technical feasibility. The objectives of these tests include validating numerical models, understanding the dynamics of the model under both uncoupled and coupled external loads, and analysing mean displacement offsets and mooring line tensions under survivability and operational conditions. By the time the project reaches TRL 4, a detailed design is expected.

From TRL 5 to TRL 7, smaller scale or full-scale prototypes are tested in relevant environments. To achieve TRL 8, the full-scale prototype must be operational for three years, after which it can reach its final design stage, TRL 9 (De Rose et al., 2017). Although this process is often presented linearly, it is intended to be iterative, with various areas of development overlapping. Design development continues beyond TRL 4, and commercialisation efforts begin well before TRL 8. (Catapult, 2020).

The floating wind sector is still in its developmental phase, particularly in the design and commercialisation of floater concepts. There is no "one-size-fits-all" solution, as the sector faces numerous demanding challenges (Watson et al., 2019). These challenges necessitate the creation of modular, adaptive, and cost-effective concepts to drive the industry forward.

Currently, there are two floater concepts that have achieved TRL 8 and TRL 9, the HyWind concept by Equinor and the WindFloat concept by Principle Power. The first publication of the HyWind concept was made 18 years ago, describing the numerical model used to predict the dynamic behaviour of the system as well as its tank testing at the Ocean Basin Laboratory at Marintek in Trondheim (Nielsen et al., 2006). Currently, the HyWind floater is used in HyWind Tampen installation which has an installed capacity of 88 MW to power offshore oil and gas installations.

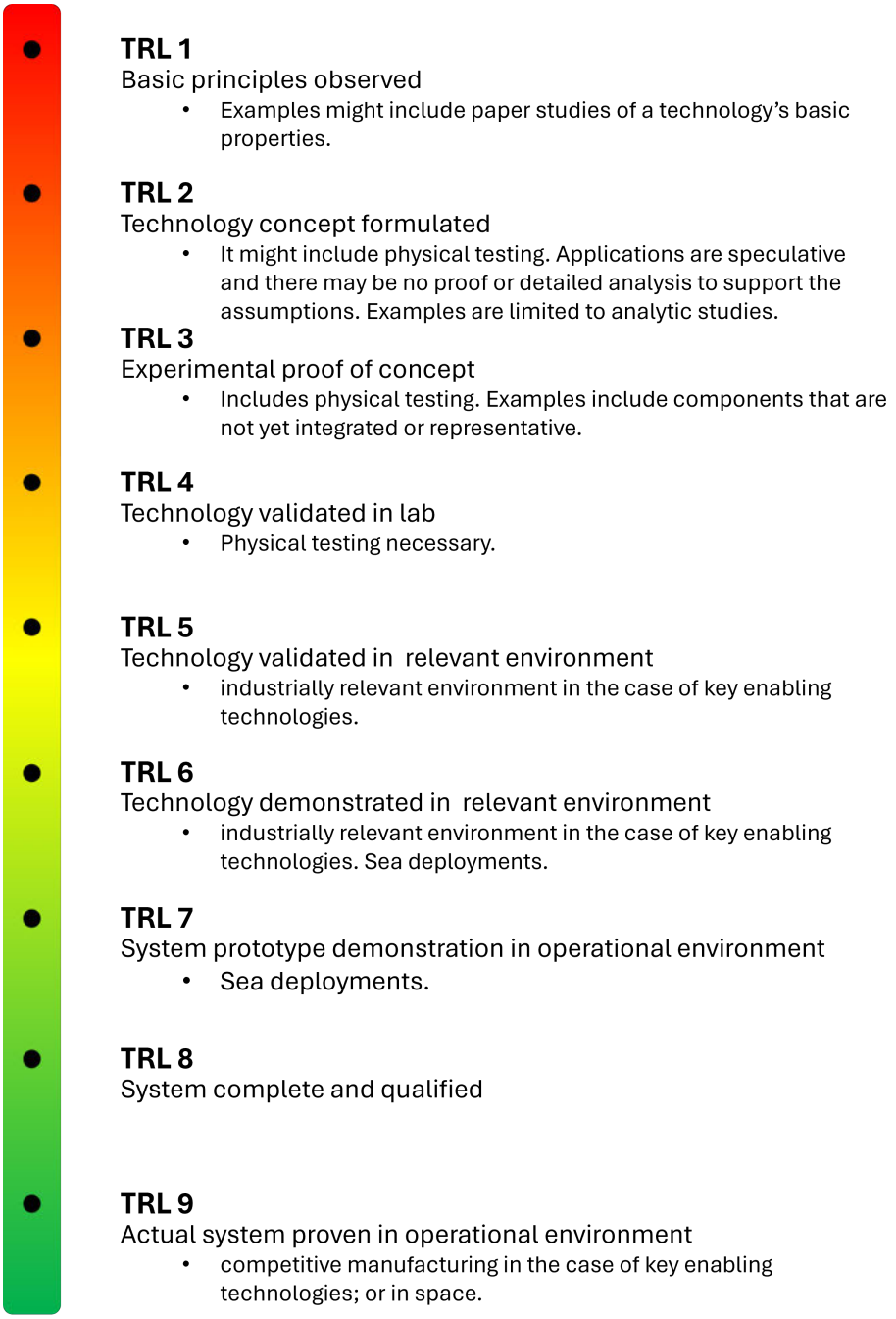

Figure 2.3: Detailed explanation of each one of the nine TRL levels. Note: Adapted from OffshoreWindInnovationHub (2024).

The WindFloat concept was first published 15 years ago (Roddier et al., 2009), with extensive technical qualification of the hull performed during the five years previously by Marine Innovation Technology (Cermelli and Roddier, 2005). WindFloat is a semi-submersible floating platform concept designed to provide hydrostatic stability and favourable dynamic response, allowing offshore deployment in deep water sites where bottom-fixed foundations are not feasible. Following staged validation and progressive design qualification, the technology has reached full-scale deployment. In Portugal, the WindFloat Atlantic project installed three floating wind turbines off Viana do Castelo, totalling 25 MW. In addition, WindFloat technology has been deployed at larger scale through the Kincardine floating wind project in Scotland, demonstrating further commercial credibility.

Both of these technologies went through the TRL stages systematically to reach credibility and design maturity for commercialisation. It can be a lengthy process, taking several years, even decades to deploy a full-scale prototype. Key issues surrounding this delay include the platform's stability and dynamic response under extreme loads, fatigue under operational conditions, and the cost of these structures. Only by tackling each of these, will the technologies progress through to commercialisation, TRL 9.

Importantly, categorising technologies according to TRL not only provides a common framework for tracking maturity, but also enables the selection of testing approaches that are appropriate to the development stage. In the context of floating offshore wind turbine scale testing, the method used to apply aerodynamic loads in a wave basin can be correlated with the TRL of the technology under investigation.

Early-stage concepts (TRL 1–4) may benefit from simplified, lower-cost methods that enable rapid iteration and early validation of fundamental design principles. As the technology advances to higher TRLs, more complex and high-fidelity methods become necessary to capture the full coupled dynamics of the system and to provide the robust evidence base required for commercial readiness. Establishing clear guidance on matching aerodynamic load application methods to TRL levels could therefore help optimise resource use, reduce unnecessary costs, and accelerate the progression of floating wind technologies through the development pipeline.

2.3 Physical testing of floating wind turbines: TRL 1 - TRL 4

In the development of a floater that will support a turbine to produce energy, physical testing is a crucial step. As previously mentioned, to progress to higher TRL levels, the technology must be validated under controlled conditions in a laboratory or test facility. This is not undertaken merely for the sake of laboratory experimentation, but because it provides a cost-effective means of evaluating concepts in a highly controllable environment, allowing detailed investigation of system responses and de-risking the design before committing to more expensive and challenging sea trials.

Physical model testing in wave basins is a well-established practice, with extensive guidance provided by the International Towing Tank Conference (ITTC) on experimental procedures, scaling laws and uncertainty analysis (ITTC (2017b). However, floating offshore wind (FOW) presents a unique case, as it spans multiple physical domains, combining the hydrodynamics of the floating platform, the aerodynamics of the wind turbine, and the dynamics of the mooring system. This multi-physics nature requires more careful consideration than is typically needed for traditional tank testing of ships or offshore structures, or for wind tunnel testing of fixed or onshore wind turbines, where the aerodynamic loads are studied in isolation.

In FOW, replicating the interactions between the system and external loading is not straightforward. For example, the coupled effects between the turbine and the floater can influence turbine performance (Cermelli et al., 2009); aerodynamic loads can contribute to the damping of the system; mean aerodynamic thrust can affect mooring loads; and rotor torque can generate heeling moments (Cermelli et al., 2009). Additionally, gyroscopic moments in some types of floating structures may be significant, potentially exciting unwanted motions such as yaw (Cermelli et al., 2009).

According to the IEC 61400-3-1:2019, Part 3-1: Design requirements for fixed offshore wind turbines design standards (IEC), an integrated load analysis is needed before the certification of the wind turbine (WT) in order to develop a cost-effective and safe FOWT (Oguz et al., 2018). Tank testing is typically combined with numerical modelling to achieve this, as physical experiments provide essential validation for model predictions. However, numerical models may not capture all complex phenomena, including extreme wave loads, viscous loads (such as roll and yaw damping of ship-shaped floaters), and wave–current interaction effects on floating moored structures that are not fully understood or included in current models (Sauder et al., 2016). For these reasons, physical testing remains a critical approach for validating offshore wind modelling tools. Compared to full-scale deployment at sea, it is often a simpler and more cost-effective way to assess a design. It also allows the motion response of the structure to be studied under uncoupled and controllable external loads, which is not possible in sea deployment (Martin et al., 2012).

2.3.1 Physical Testing Challenges

To evaluate the combined effects of aerodynamic and hydrodynamic loads on a floating wind turbine (FWT), physical tests are typically conducted in wave basins. When testing a scaled model, it is crucial to scale the mass and inertia properties, the structure's elasticity, the external loads, and the associated characteristic frequencies (Urbán and Guanche, 2019). In practice, however, it is not possible to satisfy all similarity requirements simultaneously for a single small model. As the geometric scale decreases, departures from full-scale conditions introduce scale effects such as increased apparent viscous damping, altered boundary-layer behaviour, and the influence of surface tension. These effects should be minimised and, where possible, quantified.

Mechanical similarity is essential to obtain representative and scalable results, requiring geometric, kinematic, and dynamic similarity (Heller, 2012). While geometric and kinematic similarity are relatively straightforward, dynamic similarity is enforced by keeping key dimensionless numbers constant, as they represent ratios of specific force terms:

- **Froude number** = $\left(\frac{\text{inertial force}}{\text{gravity force}}\right)^{1/2}$
- **Reynolds number** = $\frac{\text{inertial force}}{\text{viscous force}} = \frac{LV}{\nu}$
- **Weber number** = $\frac{\text{inertial force}}{\text{surface tension force}} = \frac{\rho V^2 L}{\sigma}$
- **Cauchy number** = $\frac{\text{inertial force}}{\text{elastic force}} = \frac{\rho V^2}{E}$
- **Euler number** = $\frac{\text{pressure force}}{\text{inertial force}} = \frac{p}{\rho V^2}$

The parameters involved are characteristic velocity (V), characteristic length (L), gravitational acceleration (g), kinematic viscosity (ν), fluid density (ρ), surface tension (σ), Young's modulus (E), and pressure (p).

In FWT testing, scaling is further complicated by the presence of two fluids, air and water, with very different properties. The requirements for matching different dimensionless numbers often conflict for example, matching the Froude number to preserve gravity–inertia scaling typically requires a different characteristic velocity than matching the Reynolds number, which governs viscous effects. This incompatibility means that exact similarity for all forces cannot be achieved simultaneously, so it is necessary to prioritise the dimensionless numbers most critical for the phenomena under investigation.

In wave dynamics and fluid–structure interactions, inertial and gravitational forces dominate, which is why the Froude number is typically maintained constant between model and full scale in experiments focusing on hydrodynamic loads (Urbán and Guanche, 2019). Conversely, viscous forces are critical for characterising airflow, influencing aerodynamic performance, vortex formation, turbulence, and flow separation from blade surfaces. The Reynolds number is the relevant dimensionless parameter for these effects.

Achieving similarity in both Froude and Reynolds numbers simultaneously is only possible if the model scale is 1:1. In wave basin testing, maintaining Reynolds similarity is impractical because the wind velocity required would be far higher than full-scale values, and the resulting forces would not scale proportionally to hydrodynamic and hydrostatic loads (Martin et al., 2012). One alternative approach is to change the working fluid for aerodynamic testing, using a denser medium than air can help achieve Reynolds similarity without unrealistic velocities. For this reason, aerodynamic testing is often conducted in wind tunnels or specialised facilities, separate from hydrodynamic tank tests.

Another challenge is that correctly matching the mass and inertia of the system can make certain scaled components too small to manufacture easily. As noted by Martin et al. (2012), a model blade of $1\ m$ length might require a mass of only $0.14\ kg$, and matching elasticity would require Cauchy scaling, which may be difficult to achieve with available materials. To simplify manufacturing, model blades are often treated as rigid bodies, while the tower may be built with rigid intermediate sections and hinges if full flexibility is not required (Chakrabarti, 1998).

Finally, physical testing in wave basins is primarily concentrated on wave loading. For FWTs, depending on the design phase, this may not be sufficient, and methods for including aerodynamic loads in the test programme must be considered. However, it should be noted that the availability of aerodynamic data may be limited either by the Original Equipment Manufacturer (OEM) turbine manufacturer's reluctance to disclose such information, or because an OEM has not yet been selected at this stage of the design process.

2.4 Methods of applying aerodynamic loads in wave basins

Accurately simulating aerodynamic loads in a wave basin is crucial for several reasons. Floating wind turbines experience both aerodynamic forces from the wind and hydrodynamic forces from the waves, and a realistic evaluation of their performance and structural integrity requires accurate representation of these combined loads (ma and Sun (2023). Aerodynamic loads significantly impact the structural response, including deflections, tower fatigue (Meng et al. (2025)), vibrations, and stresses, and influence the stability and control of the turbine. Additionally, these loads affect the turbine's yaw, pitch, and overall stability, necessitating precise simulation to design effective control systems (Didier et al. (2026)). Accurate aerodynamic load simulation is also essential for evaluating power output and efficiency, optimising design for improved performance and reduced costs, and ensuring safety and reliability by identifying and mitigating potential fatigue-related risks.

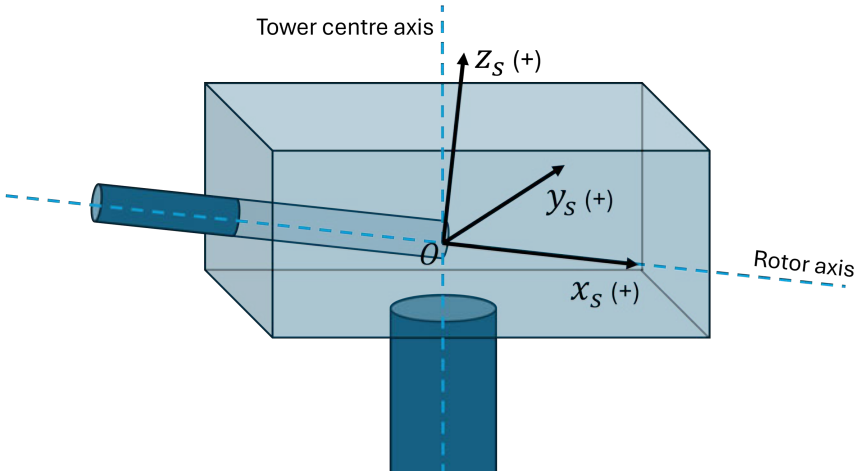

Figure 2.4: Wind turbine shaft coordinate system. Note: Adapted from Jonkman and Buhl Jr. (2006).

To accurately simulate aerodynamic loads in a wave basin, understanding the components involved is essential. At the wind turbine rotor, the wind vector is a position-dependent three-component vector (x, y, z), reflecting variations in wind direction and speed across the rotor plane. According to Blade Element Momentum (BEM) theory, each two-dimensional profile of the blade (airfoil section) experiences lift and drag forces as it moves through the air. Lift acts perpendicular to the relative wind direction, while drag acts parallel to it. These distributed forces along the blade span are integrated to determine the total lift and drag on the blade. The cumulative effect of these forces contributes to the rotor's torque and thrust, affecting both power generation and structural loading (Burton et al. (2011)).

However, lift and drag are not the only contributors to the rotor load vector. Additional forces and moments arise from gravitational loads, inertial effects due to rotational motion, aerodynamic moments, and potential unsteady aerodynamic phenomena such as dynamic stall (Söker (2013)). Considering these factors is crucial for fully understanding the complex loading and performance of wind turbine rotors.

Defining aerodynamic loads on a floating wind turbine is most conveniently done in a local reference frame fixed to the rotor axis. This allows the aerodynamic loads to be described independently from the global motions of the floater and the tower. Floating wind turbines have several degrees of freedom: the six rigid body motions of the floater, nacelle yaw about the tower, and rotor rotation about the shaft. Because of these motions, the aerodynamic load vector acting on the rotor has components in the lateral (y) and vertical (z) directions in addition to the axial (x) component, and the resulting moments include pitch and yaw moments as well as torque. These components are defined with respect to the shaft coordinate system shown in Figure 2.4.

In this frame of reference, the origin aligns with the intersection of the y_n-/z_n- plane and the rotor axis. The x_s axis is oriented along the shaft, possibly with a tilt, in the nominal downwind direction. The z_s points upward, perpendicular to the rotor axis, while the y_s axis is directed to the left of the $x_n-/zn-$ plane, following the right-hand rule for alignment. The shaft coordinate system does not rotate with the rotor, but it does translate and rotate with the tower and it yaws with the nacelle and furls with the rotor.

The rotor load vector comprises three force components along the x_s, y_s, and z_s axes, as well as three moments denoted as M_x, M_y, and M_z. Among these, the force acting along the x_s axis represents the rotor thrust, denoted as F_x. Existing literature, as perceptible by Table 2.2, highlights F_x as a pivotal component of rotor load due to its propensity for its substantial contribution to the overturning moment in FWTs, exceeding that of the aerodynamic rotor torque, M_x, commonly referred to as Q_g (Martin et al., 2012).

Bachynski et al. (2015) conducted a study on the sensitivity of limited aerodynamic actuation in a semi-submersible structure using the aero-hydro-servo-elastic simulation tool SIMO-RIFLEX-AeroDyn. The study found that the exclusion of aerodynamic yaw moment (M_z) has minimal impact on yaw motions under aligned wind and wave conditions. However, the effects become more noticeable under misaligned conditions. Additionally, removing the local aerodynamic pitch moment (M_y) can lead to an increase in low-frequency (< 0.05 Hz) platform pitch, which in turn can elevate mooring line tension.

Despite these variations, the overall motions changed by less than 1% in surge, sway, and roll, and by under 0.1° in yaw amplitude, except for pitch where the low-frequency component (below 0.05 Hz) increased by approximately 10%. While these findings underscore the complexity of FWT dynamics, the methodology's scope was limited to specific operational conditions and to one type of semi-submersible platform.

An important outcome of the study is the heightened awareness of the simplifications made during tank testing in respect to aerodynamic load actuation. Simplifying aerodynamic loads to a single main component, for example, may result in non-comparable outcomes to real-world scenarios. While the effects of these simplifications can be somewhat accounted for numerically, this approach also carries the inherent limitations relating to the numerical models used.

Performing a sensitivity analysis prior to tank testing may be particularly important for novel or hybrid floating concepts, where limited prior knowledge of the coupled dynamics exists. In addition, structuring the experimental campaign in progressive stages can improve clarity of interpretation. For example, initial tests may be conducted under single-environment conditions (e.g. waves only, wind only), followed by combined wave–current cases, and ultimately fully coupled wind–wave–current scenarios. By incrementally increasing environmental com-

plexity while maintaining comparable baseline conditions, the individual and combined effects of each loading component can be isolated. This staged approach enables clearer comparison with numerical simulations and provides a more transparent assessment of how simplified aerodynamic actuation influences the global system response.

Lastly, the study emphasises the importance of advanced modelling techniques that incorporate all relevant physical phenomena to accurately predict the behaviour of floating wind turbines and optimise their design for real-world conditions.

2.4.1 Preliminary methods

The main characteristics of these preliminary approaches, along with examples from past studies, are summarised in Table 2.2. This review highlights how such methods, while often limited in capturing dynamic aero-hydro-servo interactions, have played an important role in early FOWT testing, particularly for concept validation, extreme load assessment, and when facility or project constraints limit the feasibility of more advanced methods.

One of the first approaches used to simulate aerodynamic loads on models consisted of a static weight attached to a line connected to the nacelle (Chujo et al., 2011). This is a very rudimentary way of applying static wind load as it omits the motion response of the structure, and consequently the coupling between floater motion and thrust. Moreover, the thrust generated by a mass-driven load will not remain perfectly steady; the mass has inertia, so nacelle accelerations will induce additional transient force components. The wind variability and gyroscopic effects are also not accounted for. This method should therefore only be considered for rough estimation of maximum mooring offset (ITTC, 2017b).

While these limitations are valid, it might not be entirely fair to dismiss this method. Depending on the objectives of the tank test, this approach can still be useful for understanding the maximum displacements and mooring tensions the model will experience under extreme load cases where the turbine is idling. This method may be particularly suitable for developers in the early stages of TRL, where only accounting for steady thrust force might be enough.

Another method initially adopted was the use of a drag disk to simulate the mean static thrust on the rotor of a wind turbine. For the WindFloat project, this method was combined with a motor placed at the top of the tower behind the drag disk, spinning at Froude-scaled speed to reproduce gyroscopic effects. The model was then exposed to a wind field generated by a group of fans in the tank (Cermelli et al., 2009), as shown in Figure 2.5.

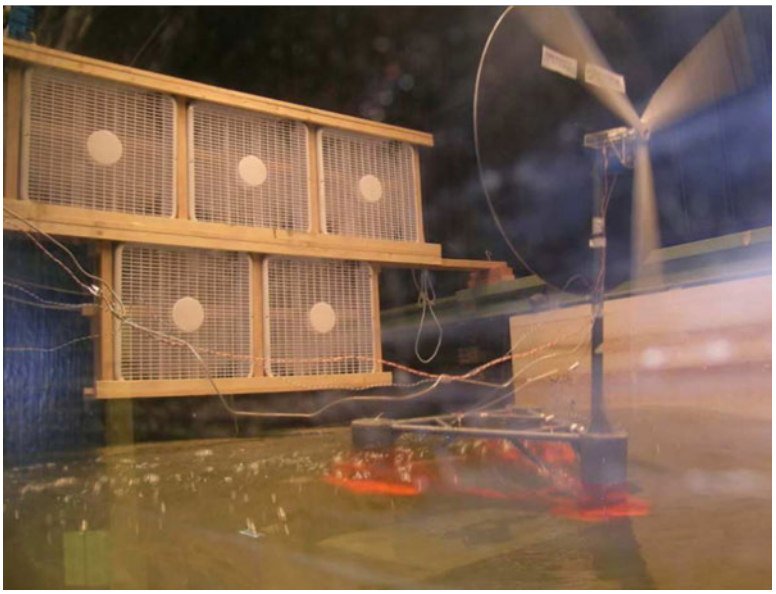

Figure 2.5: WindFloat model testing using a drag disk Cermelli et al. (2009).

Although straightforward to design and deploy, realistic testing requires the facility to generate a steady wind with low turbulence intensity (Gueydon et al., 2020). Achieving this typically demands a wind generation system of considerable size to ensure uniform flow, which can be particularly challenging for smaller wave basins (McElman et al., 2016). Moreover, vortex shedding behind the disk can occur, and control systems cannot be simulated (Urbán and Guanche, 2019). These factors may introduce additional uncertainties into the experiment, making it more difficult to calibrate the numerical model to match test results accurately.

To mitigate some of the disadvantages of these methods, new strategies are recently being adopted. These strategies aim to include more components of the aerodynamic load vector and improve ways of actuating the loads, thereby better resembling reality. However, the increased complexity makes the process of actuating the wind loads more challenging. Gueydon et al. (2020) categorises these strategies as either "full-approach" or "hybrid-method."

2.4.2 Full-Approach

The full-approach comprises the use of a scaled wind turbine model exposed to a generated wind field with the objective to correctly match the aerodynamic forces acting on the rotor. This means that the lift and drag coefficients for different values of tip-speed ratio (TSR) should match the full scale FOWT. The two methods included in this approach are *Geometrically Scaled* and *Performance Scaled*.

The geometrically scaled wind turbine, originally termed by Wen et al. (2020) as Froude-scaled Rotors (FSRs), maintains the scaled mass and inertia properties of the full-scale prototype using Froude scaling. As previously mentioned, Froude scaling is traditionally used in wave dynamics and fluid-structure interaction problems due to the dominance of inertial and gravitational forces. However, achieving dynamic similarity in aerodynamic loads requires maintaining the Reynolds number.

In full-scale applications, wind turbines operate at higher Reynolds numbers. When the rotor is geometrically scaled, these turbines operate at lower Reynolds numbers, which does not maintain dynamic similarity. While Froude scaling was believed to achieve dynamic similarity by scaling the blades and rotor, this approach fails to account for the aerodynamic discrepancies caused by the change in Reynolds number.

One of the main projects developed using this type of turbine was by the DeepCwind consortium in 2011 at the Maritime Research Institute Netherlands (MARIN). It included the testing of three main floating structures, semi-submersible, spar and tension leg platform (TLP) with a geometrically Froude scaled version of the National Renewable Energy Laboratory (NREL) 5 MW reference wind turbine. The motions of the different platforms and performance of the turbine were studied for a range of different wind and wave conditions (Goupee et al., 2014).

However, the low Reynolds number associated with Froude scaling for the model testing altered the lift and drag coefficients of the wind turbine significantly. This means that the turbine under-performed greatly and in order to match the thrust, considered the most significant aerodynamic load, higher values of Froude scaled wind speeds needed to be used (Fowler et al., 2013). Although the model geometrically represented the real wind turbine and could generate gyroscopic effects - which are crucial due to their significant impact on the dynamic behavior and tower torsion loads of FOWTs (Høeg and Zhang, 2021) — the thrust could only be matched by increasing wind speed. Other aerodynamic loads, such as torque, were still not accurately matched.

Although the simulation of gyroscopic effects is seen as an advantage, it is important to consider its varying importance across different types of platforms. Gyroscopic effects are most pronounced in spar-type FOWTs, though TLPs can also be similarly sensitive. For both idling and operational FOWTs, aerodynamic loads dominate, but gyroscopic effects remain important, especially in operational conditions where neglecting them can lead to significant overestimation of tower torsion. In contrast, the semi-submersible platform is least sensitive to gyroscopic effects (Høeg and Zhang, 2021). Examples of studies adopting this method include the DeepCwind campaign (Goupee et al., 2014) and others summarised in Table 2.2.

In order to overcome the challenges associated to not matching the aerodynamic loads, including thrust, when using geometrically scaled blades, an alternative method was created within the full-approach strategy. It consists of a model of a WT that is able to better match the performance of the full scale prototype. Referred to as performance scaled WT, this approach involves designing the blades to match specific performance characteristics of the full-scale prototype. This is achieved by modifying the airfoil chord length and blade twist, while maintaining the original blade length, gross blade mass, and rotor operational speeds (Fowler et al., 2013).

Although the blades will not replicate the exact surface geometry of the prototype, they are designed to yield the appropriate thrust when subjected to Froude-scaled wind conditions (Martin et al., 2012). The key properties to be matched include aerodynamic performance, specifically power and thrust coefficients for different TSR values, as well as 1P (rotor rotational speed) and 3P (blade passing frequency) loads. These factors ensure that the scaled model accurately simulates the operational conditions of the full-scale wind turbine. Studies employing performance-scaled designs are listed in Table 2.2, including MARIN's MSWT (de Ridder et al., 2014) and similar approaches by Le Boulluec et al. (2013) and Huijs et al. (2014).

MARIN, following the tests using a geometrically scaled wind turbine in 2011, developed a model-scale stock wind turbine (MSWT) (de Ridder et al., 2014) that achieved comparable thrust performance to the full-scale NREL 5 MW prototype for a TSR of 7. Other projects have also implemented performance-scaled wind turbines (Le Boulluec et al., 2013; Huijs et al., 2014).

For the MARIN MSWT, it was found that the power coefficient was lower than that of the full-scale prototype, and that the thrust coefficient matched the prototype only at one or two specific operating points, characterised by particular TSR values. Similar trends have been reported in other performance-scaled rotor designs, indicating that matching thrust across the entire operating range remains a challenge (Wen et al., 2020). This limitation can complicate the testing of control systems and unsteady aerodynamic behaviour in FOWTs.

When comparing both full-approach methods, Kimball et al. (2014) concluded that the geometrically scaled wind turbine and the performance scaled wind turbine configurations showed similar results on the platform pitch response when the wind turbine was tested under operational conditions. Therefore, in case studies where active pitch control is not used and only the relative motion of the model exposed to thrust is important, the use of a geometrically scaled wind turbine is advised.

This recommendation stems from the observation that, despite differences in mass properties and natural frequencies (0.037 Hz for the geometrically scaled turbine and 0.031 Hz for the performance scaled turbine), both configurations produced similar reductions in resonant platform pitch response when the turbine was operating. This indicates that for tests focusing solely on thrust force sensitivities due to platform motion, a performance scaled wind turbine is not critical.

On the other hand, for tests requiring more realistic wind environment conditions, the use of a performance scaled WT is crucial. For instance, when subjected to dynamic winds, the geometrically similar configuration exhibited a significantly larger platform pitch response compared to the performance scaled. This discrepancy arises because the realistic wind speed needed to produce the correct thrust for the geometrically similar model has much larger wind speed standard deviations, leading to excessive platform pitch response. Conversely, the performance scaled WT allows for the use of lower speed dynamic wind closer to the full-scale target, yielding improved mean and dynamic responses. Therefore, for accurate testing of dynamic responses using pitch control systems, a performance-matched wind turbine is essential.

Despite these advantages in replicating aerodynamic loads, performance scaled rotors are generally more challenging to design and fabricate than geometrically scaled rotors. Achieving the desired aerodynamic characteristics often requires iterative aerodynamic modelling, custom blade geometries, and specialised manufacturing to meet the modified chord and twist distributions. This increases design complexity, cost, and lead time. Additionally, their performance sensitivity to small deviations in manufacturing or setup means that more rigorous calibration and verification are needed before testing, which can be particularly constraining in early-stage development or when testing resources are limited.

Overall, while the geometrically scaled wind turbine accurately maintains inertial loads, it presents challenges in simulating aerodynamic loads, necessitating adjustments to Froude scaled wind speeds to match wind thrust. The performance scaled wind turbine addresses this gap, although it does not maintain geometric similarity of the turbine rotor. Even when rotor thrust is replicated, achieving accurate representation for different TSR values is challenging. Other methods may provide mean displacements and mooring tensions more easily under various environmental conditions, emphasising the need to understand the test objectives and the complexities of each method for applying aerodynamic loads beforehand.

2.4.3 Hybrid Approach

A more recently developed method, known as the *hybrid approach*, aims to simplify the process of applying aerodynamic loads in a wave basin compared to the full approach. This method avoids geometric scaling of the rotor, eliminating the need to reproduce exact wind speeds, depending on the application and the challenging task of designing custom scaled blades. Instead, it enables replication of various environmental conditions with a single setup, improving both efficiency and flexibility in tank testing.

The hybrid approach incorporates either *Software-in-the-Loop* (SIL) or *Hardware-in-the-Loop* (HIL) methods, first developed by Azcona et al. (2014). In both cases, the experimental setup involves real-time coupling between a physical basin model and an external system through sensors and actuators (Sauder et al., 2016), as shown schematically in Figure 2.6.

In practice, both SIL and HIL rely on physical actuators to apply loads in the basin. The distinction lies in where the aerodynamic behaviour is resolved. In SIL, aerodynamic forces are computed numerically in real time and transmitted to the model via hardware actuators, which function purely as load application devices. In contrast, HIL incorporates physical hardware that directly represents part of the aerodynamic or control subsystem. The difference is therefore conceptual rather than mechanical: SIL resolves the aerodynamic response numerically, whereas HIL retains part of the subsystem in physical form.

The physical model may be a performance-scaled wind turbine exposed to aerodynamic loads in a wind tunnel (Bayati et al., 2018), or a floating structure exposed to hydrodynamic loads in a wave basin (Sauder et al., 2016; Oguz et al., 2016; Azcona et al., 2014; Fontanella et al., 2020; Antonutti et al., 2020; Carmo et al., 2024). In the former, loads from the numerical model are applied to the physical model using a six degree-of-freedom parallel kinematic machine (PKM). In the latter, load actuation can range from a simple ducted fan (Oguz et al., 2016; Azcona et al., 2014) to a multi-fan array (Urbán and Guanche, 2019; Fontanella et al., 2020) or a more complex winch system (Sauder et al., 2016; Antonutti et al., 2020).

In all cases, the numerical model runs at full scale, avoiding the scaling conflicts of the full approach. Dynamic similarity is preserved, and only the rotor loads are Froude scaled before being applied to the physical model through the actuators. The hybrid approach has been applied in several experimental campaigns at different scales and WT ratings (see Table 2.2), including the studies by Azcona et al. (2014), Sauder et al. (2016), and Fontanella et al. (2020).

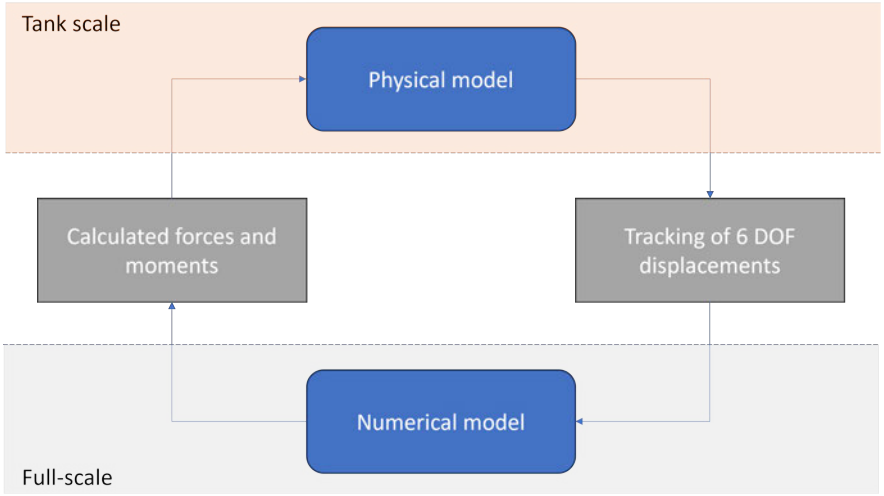

Figure 2.6: General principle of the hybrid approach.

Fan vs. Winch Systems

The main actuator types used in hybrid approaches are fans and winch systems. Their differences lie in how loads are generated and the range of rotor load components they can replicate. A simple ducted fan or single degree-of-freedom winch can only apply rotor thrust, whereas multi fan systems or square frame winches can additionally generate torque, tangential aerodynamic forces, and aerodynamic moments (Sauder et al., 2016; Fontanella et al., 2020; Vittori et al., 2022).

The work of Arnal (2020) is expanded in Table 2.1 and compares the two systems qualitatively under *Force Application* and *Force Control*. The (+) and (–) symbols follow Arnal (2020): (+) indicates an advantage over the other system, while (–) indicates either no clear advantage or a disadvantage.

In summary, fans are easier to install, less affected by platform motion when wind is misaligned, and less sensitive to disturbance rejection issues, but require direct cabling and more complex thrust measurement. Winches, on the other hand, provide more deterministic force measurement, simpler calibration, and avoid adding cables to the model, but are harder to install, sensitive to misalignment errors, and more affected by platform motion.

For the present work, the winch system was chosen based on prior deployment experience at FloWave and the availability of necessary equipment. Future studies at FloWave could explore fan based systems to enable a direct quantitative comparison.

---

0. Here, “misaligned wind” refers to the relative angle between wind and wave alignment, not the nacelle yaw angle. The yaw control system is generally aligned with the wind direction, but may not respond effectively to very high frequency or small angle platform motions.

Table 2.1: Comparison of fan and winch systems for aerodynamic load actuation.

Category	Subcategory	Fan	Winch
Force Application	Reproduced load components	(–) Able to apply different load components	(–) Able to apply different load components
	Installation	(+) Easy to deploy; directly installed on the structure	(–) Requires earth fixed installation
	Connecting cables	(–) Electrical cables connected directly to structure	(+) All cables earth fixed except winch cable
	Misaligned wind	(+) Maintains thrust angle actuation despite platform motion	(–) Angular error introduced by platform motion
	Highest frequency	(–) Possible vibration issues at different torque levels	(–) Limited by motor inertia–torque characteristics
Force Control	Sensitivity to delay	(+) Sensitive	(–) Very sensitive
	System calibration	(–) Feed forward mechanism	(+) Uses springs
	Determinism	(–) Complex thrust measurement	(+) Thrust easily measured via load cells
	Disturbance rejection from platform motion	(–) Minor influence	(+) Major influence

Deciding which load components from the numerical model should be applied in the physical model depends on both the platform type and the test objectives. Regardless of the actuator type, the system must respond rapidly to the forces computed by the numerical model and receive input motions in real time (Sauder et al., 2016).

The hybrid approach offers several advantages: no need for a wind generation system in the basin, the ability to capture high frequency aerodynamic responses, and the capability to model turbine control systems and blade elasticity. However, disadvantages include high complexity, long setup times, and the fact that no current actuator can replicate the entire rotor load vector. Accuracy also depends heavily on the numerical model's fidelity, which in turn requires validation through ongoing physical testing.

The main characteristics and applications of all these approaches, along with examples from previous studies, are summarised in Table 2.2, which has been reframed as a review of past work rather than a purely methodological summary.

Method	Description	Control Methodology	Applied load component	WT rating	Model scale	Advantages	Limitations	References
Static Weight	Attachment of a weight to the nacelle corresponding to the scaled wind thrust to be applied. Weight must be able to move freely with model's movements.	NA	F_x	5 MW	1:100	• Easy deployment; • Provides rough estimation of the maximum mooring offset and model displacements.	• It neglects the aerodynamic damping imparted by the rotor on the system as well as the gyroscopic effects and the steady torque; • The total mass and moments of inertia of the system will inevitably be incorrect; • No means for incorporating the impact of wind turbine controls.	Chujo et al. (2011)
Drag Disk	Use of a porous disc sized to generate a drag load in the incoming generated wind field, corresponding to the predicted mean thrust on the turbine. A separate rotating arm can be placed downwind of the disc to capture the coupled response of the structure.	NA	F_x; Gyroscopic effects.	5 MW	1:105	• Easy deployment of the disk and spinning arm; • Correct rotor inertial loads; • Suitable for applying the gross wind turbine loads;	• It neglects other rotor loads; • Flow generation in a wave basin carries its own challenges; • Unsteadiness of the flow around the disc when pitching in waves not accounted for; • No means for incorporating the impact of wind turbine controls.	Cermelli et al. (2009)
Geometrically scaled	Use Froude scale to geometrically scale the turbine blades and it might use a motor to spin the rotor blades in accordance to rotor rpm requirements or the wind generated will spin the blades.	Blade pitch control	F_x; Q_g; Gyroscopic effects.	5 MW	1:47	• Easy process in regards to the scaling of the turbine blades; • Able to capture the rotor load vector including excitation from 1P and consequent blade excitation loads; • Impact of wind turbine controls can be applied.	• Flow generation in a wave basin carries its own challenges; • Poor rotor aerodynamic performance since the scaled generate a lower thrust and power coefficient with a Froude-scaled wind velocity.	Nielsen et al. (2006)
		NA		5 MW	1:100			Nihei2010
				5 MW	1:50			Koo et al. (2014); Robertson et al. (2013); Martin et al. (2014)
				5 MW	1:50			Li et al. (2018)
			F_x; Gyroscopic effects.	5 MW	1:50			Philippe et al. (2013)
Performance scaled	Blades are purposely designed in order to match the full-scale blades' performance in regards to power and thrust coefficient curves. The geometry of the full-scale and scaled model blades by Froude-scale will not be maintained.	Blade pitch control; Generator torque control.	F_x; Q_g; Gyroscopic effects.	5 MW	1:50	• Able to capture the rotor load vector including excitation from 1P and consequently other blade excitation loads; • Impact of wind turbine controls can be applied.	• Flow generation in a wave basin carries its own challenges; • The blades' geometry has to be redesigned for each different wind turbine type and scale; • Rotor thrust and torque hard to reproduce.	de Ridder et al. (2014); Huijs et al. (2014)
		NA		1 MW	1:25			Le Boulluec et al. (2013)
		Blade pitch control		12 MW	1:50			Doisenbant et al. (2018)
Hybrid-Approach	Connection between numerical model and physical model. The numerical model calculates the aerodynamic loads in real-time which are then applied by the action of an actuator, on the physical model. Motion tracking systems will provide the numerical model with displacements in all DOF which together with the hub velocities, will be used as input to the numerical model. If instead of a numerical model a surrogate model is used, the aerodynamic loads applied correspond to the loads present at the look-up table.	Control mechanisms included on the numerical tool.	Fan: F_x	6 MW	1:40	• Able to adapt quickly to the specifications of the tank test in regards to wind turbine rating; • The scale of the tests is dictated only by the hydrodynamics of the floater; • The impact of the turbine control system and blade elasticity on the applied loads may be modelled in the tests; • No need for a wind generation system in the test tank.	• It has to operate in real-time in order to not induce negative damping; • Application of other components of the rotor load vector might not be straightforward; • The testing of misalignment wind-wave conditions might introduce angular errors; • The applied load is only as good as the numerical model used in the hybrid testing.	Azcona et al. (2014)
				5 MW	1:45			Azcona et al. (2019)
				5 MW	1:36.67			Oguz et al. (2016, 2018)
				10 MW	1:60			Gueydon et al. (2021)
			Multi-fan: F_x; M_y; M_z	10 MW	1:49			Vittori et al. (2022)
			Winch:F_x; F_y;Q_g; M_y; M_z	5 MW	1:30			Bachynski et al. (2015); Sauder et al. (2016); Bachynski et al. (2016); Luan et al. (2018)
			Winch: Rotor Thrust, Fx; My and Mz	6 MW	1:35			Antonutti et al. (2020)
			Multi-fan: F_x; M_y; M_z	5 MW	1:50			Fontanella et al. (2020)
			Fan: F_x	15 MW	1:70			Ransley et al. (2023)

Table 2.2: Summary of previous studies implementing aerodynamic load application methods for floating offshore wind turbine model testing. The table lists the applied method, associated WT rating, model scale, and other relevant setup details.

2.5 Numerical tools

In the floating wind sector, computer models of varying degrees of fidelity, from simplified engineering tools to fully resolved fluid–structure interaction solvers, play a crucial role in the design, analysis, and optimisation of FOWTs. These models are essential for capturing the complex interactions between wind, waves, and the floating structure, enhancing performance, reliability, and safety.

Various types of models are used, each differing in complexity and application. Advanced methodologies include Computational Fluid Dynamics (CFD) models, such as Large Eddy Simulation (LES) and Direct Numerical Simulation (DNS), which numerically solve the Navier-Stokes equations to capture detailed turbulent flow interactions around turbine blades. Smoothed Particle Hydrodynamics (SPH) models are used for complex wave–structure interactions, and high-fidelity control system models replicate the dynamic response of the turbine and platform. In addition, machine learning and data-driven approaches, such as digital twins and surrogate models, provide rapid and accurate predictions based on real-world data.

Among these, aero–hydro–servo–elastic models are the most commonly used, especially in the lower TRLs. These are engineering-type simulation tools that integrate aerodynamic, hydrodynamic, structural dynamic, and control system models within a single framework. Examples include NREL's *OpenFAST* and Orcina's *OrcaFlex*, which are widely used for time-domain analysis of FOWT behaviour. Such tools typically solve the coupled equations of motion for the platform and rotor–nacelle assembly, and can incorporate modal analysis modules to investigate natural frequencies and mode shapes of the structure. They are advantageous in that they require less computational power and less extensive prior data compared to high-fidelity CFD or SPH approaches, while still capturing the key coupled responses. As a result, they offer a balanced trade-off between accuracy and computational efficiency, making them particularly well suited for early-stage design, parametric studies, and control system assessment.

The structure of typical aero-hydro-servo-elastic models, as depicted in Figure 2.7, provides a framework for solving the second-order differential equation of motion (EOM) in the time domain considering all static, dynamic, and external loads acting on the system. The general EOM can be formulated as:

$$\mathbf{M}\ddot{\mathbf{x}} + \mathbf{C}\dot{\mathbf{x}} + \mathbf{K}\mathbf{x} = \mathbf{F}_{\text{aero}} + \mathbf{F}_{\text{hydro}} + \mathbf{F}_{\text{mooring}} \tag{2.1}$$

where:

- $\mathbf{M}$ is the mass matrix, incorporating both the structural mass and the added mass from hydrodynamic effects;
- $\ddot{\mathbf{x}}$ is the acceleration vector;
- $\mathbf{C}$ is the damping matrix, which includes contributions from structural, hydrodynamic, and aerodynamic damping;
- $\dot{\mathbf{x}}$ is the velocity vector;
- $\mathbf{K}$ is the stiffness matrix, representing the structural and mooring system stiffness;
- $\mathbf{x}$ is the displacement vector;
- $\mathbf{F}_{\text{aero}}$ is the aerodynamic force vector;
- $\mathbf{F}_{\text{hydro}}$ is the hydrodynamic force vector;
- $\mathbf{F}_{\text{mooring}}$ is the mooring force vector.

Each numerical model has its own intricacies, however, in general, they all integrate the effects of aerodynamics, hydrodynamics, structural dynamics, and control systems. Each of these components is typically handled by separate modules that compute the respective forces acting on the system. These computed forces serve as inputs for the structural module, which then calculates the kinematics (positions, velocities, and accelerations) of the structure. These kinematic outputs are subsequently used as inputs for the hydrodynamic, aerodynamic, and mooring dynamics modules in the following iteration. The control module, designed to manage the wind turbine operations, also makes use of the position data, more specifically of the tower and blades positions, power output, rotor speed and wind speed to adjust the control parameters according to specific control strategies.

Prior to performing the coupled time-domain analysis, each module might require specific inputs:

- **Hydrodynamic Module**: Requires output files from hydrodynamic pre-processor software or a boundary element method solver. These tools perform radiation/diffraction analysis, providing hydrodynamic coefficients of added mass, radiation damping, and linear and second-order wave excitation forces. In regards to wave generation, it is usually generated within the hydrodynamic module;

- **Aerodynamic Module**: Depending on the modelling approach, this module may require input files defining the geometry and aerodynamic characteristics of the rotor. For BEM type models or when performing modal analysis with blade discretisation, these inputs typically include the coordinates of blade nodes and lookup tables for lift and drag coefficients as a function of angle of attack. In other cases, the aerodynamic model may

only require global rotor parameters. Wind generator software is often used to create the wind field with specific parameters such as turbulence, whereas simpler steady wind fields can often be generated directly within the aerodynamic module;

- **Control Module**: External control algorithms can be used in the format of dynamic link libraries (DLLs) as it is the case of ROSCO used in OpenFast. Some softwares may have embedded control algorithms as well;

At the outset of a numerical simulation, an initialisation phase is conducted by the driver code where all necessary input variables are defined and allocated. During this phase, the simulation achieves a steady-state solution, i.e., a condition in which all state variables remain constant in time because forces and moments are balanced, assuming steady environmental and operational inputs. In practice, convergence to a steady state may not always occur, for example if the initial conditions are unstable or if the model is run under unsteady conditions.

As the simulation progresses, during each iteration, modules representing different physical domains (such as structural dynamics, fluid dynamics, and control systems) exchange input and output variables. This modular interaction ensures that the influence of one aspect of the system is reflected across all others, maintaining the inter dependencies inherent in the real-world behavior of the system.

Throughout each computational step, state variables are updated based on the latest inputs and the results from the previous iteration. This iterative approach allows the simulation to incrementally solve the EOM, continuously refining the accuracy of the predicted system behavior.

The results of each step are compiled into an output file, capturing a comprehensive range of data as specified by the user. Typical outputs include forces, moments, velocities, positions in various degrees of freedom and time series data for environmental conditions, including wind speed and wave elevation.

2.5.1 Comparison between existent software

Faraggiana et al. (2022) emphasises the critical importance of these models in optimising floating support structures during the preliminary design phase. The study includes a comparison table, which has been adapted to form Table 2.3 in this present study. Such tables are invaluable for understanding the variety of models employed in coupled dynamic analysis simulations, also provided in DNV-RP-0286 (DNV, 2021) and in Vorpahl2014 (Vorpahl et al., 2014). For consistency and clarity, the same abbreviations have been retained.

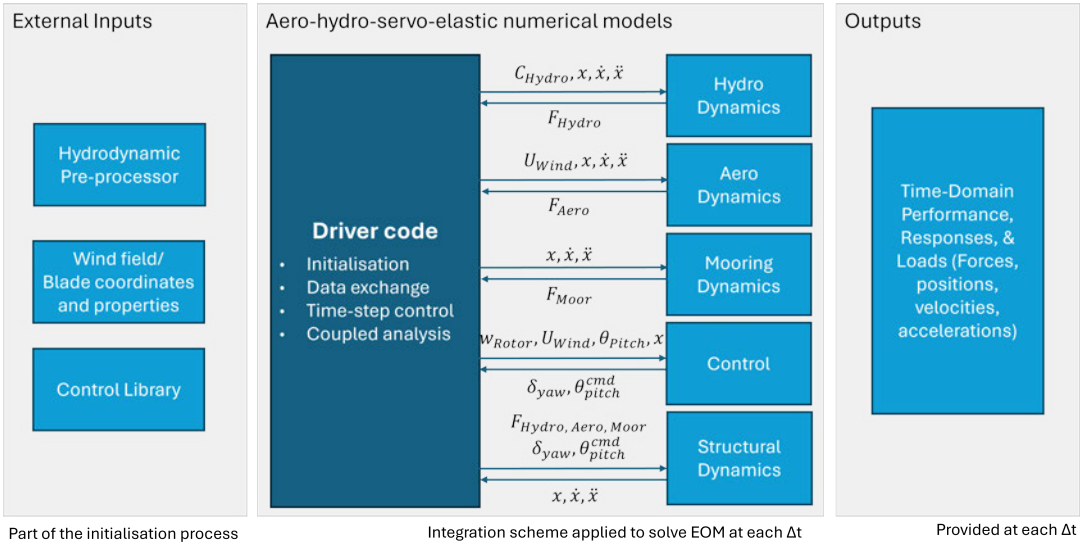

Figure 2.7: Numerical model basic mode of operation.

In this study, only a select number of numerical tools were chosen based on their relevance and ability to perform coupled analyses without the need for additional external software, focusing specifically on all-in-one solutions for the dynamic analysis of FOWTs equipped with horizontal-axis wind turbines.

According to Table 2.3, three main theories are considered for the calculation of aerodynamic loads, each increasing in complexity, fidelity, and computational requirements:

Blade Element Momentum Theory (BEMT): This fundamental theory calculates aerodynamic loads on the blades, combining the actuator disk model and momentum conservation theory.
General Dynamic Wake (GDW): This theory accounts for unsteady aerodynamic effects and dynamic inflow.
Free Vortex Wake (FVW): This method provides a more accurate simulation of the wake by explicitly modeling vorticity, crucial for understanding wake interactions and complex inflow conditions.

As seen in Table 2.3, most software can apply the first two methods, BEMT and GDW. BEMT can be used with Dynamic Stall (DS) and Dynamic Inflow (DI) models to increase fidelity without significantly increasing computational power. These models can also include losses, such as tip and hub losses, skewed wakes, and the capability of accounting for the deflected shape of the blades and their elasticity, including tower effects.

Regarding hydrodynamics, most numerical models perform the linearisation of wave loads and interactions between waves and floating structures to manage computational power, increasing fidelity by adding second-order terms. Typically, a BEM pre-processor applies potential flow theory to solve for radiation/diffraction and first- and second-order wave forces. These forces are used as inputs for the EOM, usually the Cummins Equation (CE).

However, this approach has its limitations, as potential flow theory assumes the fluid is incompressible, non-viscous, and irrotational. This assumption holds if the platform's diameter is large compared to the wavelength, especially for lower wave amplitudes (Chakrabarti, 2005). Applying second-order loads, mean-drift (MD), Newman's Approximation (NA) and Quadratic Transfer Functions (QTFs), enhances model fidelity by accounting for the impact of sum and difference wave frequencies on the low-frequency response of the floater and including non-linear boundary conditions. For slender structures, viscous forces, including friction and pressure drag, become more important and are often applied using Morison's equation (ME) (Chakrabarti, 2005).

For structural dynamic analysis, despite not being the main focus of this study, it is helpful to understand the main methods and their application in the software used. Table 2.3 categorises these methods by increasing fidelity and computational power: rigid-body (RB), modal analysis (MOD), multi-body (MB), and finite-element analysis (FE). Most numerical models can perform multi-body and modal analyses of the structure, while higher-fidelity models can use FE analysis.

In terms of mooring dynamics, software that offers FE analysis provides higher fidelity compared to lumped mass (LM) or quasi-static (QS) approaches, making them more suitable for studies where mooring dynamics play a critical role.

From Table 2.3, it is clear that the selected models generally offer similar features and performance, indicating notable uniformity in their capabilities. While the theoretical frameworks across the software are broadly consistent, there are subtle differences. For example, some models, like OrcaFlex, perform time-domain simulations in stages, incorporating a ramp-up stage to provide a gentle start to the simulation and reduce transients as the system transitions from a static position to full dynamic motion. In contrast, OpenFAST lacks this feature, but users can extend the simulation time to achieve system stability.

Additionally, the models vary in aspects such as integration schemes and user interfaces. Some models include a graphical user interface (GUI) for ease of use, while others require execution through a command window, reflecting different levels of user accessibility and interaction.

Among the tools compared, OpenFAST is the only open-source code. While it supports system linearisation about a steady state, it does not provide built-in frequency-domain analysis. For studies focused on coupled effects and non-linearities, however, time-domain simulation is paramount. From FAST v8 to OpenFAST v1.0 and through to v3.1, the code gained numerous enhancements, including offshore linearisation capability (HydroDyn), improved aerodynamic modelling in AeroDyn (unsteady airfoil aerodynamics and multi-rotor support), and advances in HydroDyn for simulating large-amplitude platform rotations and flexible floating platforms.

Table 2.3: Aero-hydro-servo-elasto numerical models used for coupled analysis of FOWTs.

	AeroDynamics	HydroDynamics	Structural Dynamics	Mooring Dynamics	Control	Dyn. Analysis	License
OpenFAST (NREL (2024))	BEMT + DI + DS, GDW	ME, CE + QTF	MOD, MB, FE	SM, QS, LM	BPC, VSTC, YC, UD	TD	OS
OrcaFlex (Orcina (2024))	BEMT + DI + DS	ME, CE + QTF + NA	MB + beam/line (FE-type)	LM/FE†, QS	BPC, VSTC, YC, UD	TD, FD	CO
Bladed (DNV (2024))	BEMT + DI + DS	Potential flow (radiation/diffraction) + Morison	MOD, MB	External coupling	BPC, VSTC, YC	TD, FD	CO
DeepLines Wind (Principia (2024))	BEMT + DI + DS	ME, CE + MD + QTF + NA	FE	FE	BPC, VSTC, YC, UD	TD, FD	CO
SIMA (SIMO/RIFLEX) (SINTEF (2024))	BEMT + DI + DS	ME, CE + MD + NA	MB, FE	SM, QS, FE	BPC, VSTC, UD	TD, FD	CO
Aerodynamics:							
BEMT = Blade Element Momentum Theory; DI = Dynamic Inflow; DS = Dynamic Stall; GDW = Generalised Dynamic Wake; FVW = Free Vortex Wake							
Hydrodynamics:							
ME = Morison Equation; CE = Cummins Equation; QTF = Quadratic Transfer Function; MD = Mean Drift; NA = Newman's Approximation							
Structural Dynamics:							
MOD = Modal formulation; MB = Multi-body formulation; FE = Finite Element formulation							
Mooring Dynamics:							
QS = Quasi-static; LM = Lumped Mass; FE = Finite Element; SM = Stiffness Matrix approach							
Dynamic Analysis Approach:							
TD = Time-domain; FD = Frequency-domain							
License:							
OS = Open-source; CO = Commercial							

† OrcaFlex represents lines using a discretised nonlinear beam formulation with nodal masses and elastic segments. While often described as a lumped-mass (LM) method, the formulation is also characterised by Orcina as a finite-element (FE) line model. The notation LM/FE reflects this dual terminology.

2.6 Current recommendations

Tank testing is crucial for advancing through the Technology Readiness Level (TRL) scale since it allows the validation of numerical tools and to assess the structure's response in certain load conditions deemed critical for its safe deployment and operation. Given the complexities and uncertainties associated with building a representative scaled model and testing it in wave basins, it is essential to consider recommendations from current guidelines and standards.

2.6.1 Standards and Guidance Documents

Multiple standards and guidance documents exist for the design of FOWTs. Each organisation brings its expertise, resulting in a range of documents tailored to different needs:

International Electrotechnical Commission (IEC)

The IEC provides internationally recognised standards for design, testing, and certification, making them widely accepted in the industry. The IEC 61400 series addresses wind energy generation systems, with IEC TS 61400-3-2:2019 specifically focusing on floating offshore wind turbines (IEC, 2025). This document outlines the required steps for ensuring the engineering integrity of FOWTs. It includes design load cases (DLCs) for operational, extreme, and failure conditions, covering scenarios such as turbine shutdown, flooding, wave multi-directionality, wind-wave misalignment and many others.

Det Norske Veritas (DNV)

DNV provides rigorous design and certification guidelines, emphasizing safety and reliability. Analogously to the IEC standards, the DNV-ST-0119 standard specifies design requirements for the safe deployment of FOWTs, serving as a contractual reference document between suppliers and purchasers (DNV, 2018). The DNV-RP-0286 recommended practice focuses specifically on model testing of FOWT substructures, offering guidance for modeling, load analysis, and model testing based on the state-of-the-art methodologies from the joint industry project (JIP) 'Coupled analysis of floating wind turbines' (DNV, 2021).

In addition to these, other DNV standards provide guidance on the definition of environmental conditions for load cases, mooring system design, structural integrity assessment, and other aspects relevant to FOWT design and certification.

International Towing Tank Conference (ITTC)

The ITTC offers detailed procedures for hydrodynamic and wave basin tests, including scaling, wave generation, and data analysis. Although ITTC guidelines are not laws in themselves, their use can be mandated by regulators or contractual requirements. They are nonetheless highly regarded due to their comprehensive nature and the expertise of committee members from industry and academia. The ITTC guidelines cover subjects such as model construction (ITTC, 2021), model testing (ITTC, 2017b), and analysis (ITTC, 2017a).

These guidelines do not establish a direct correlation between the methods of applying aerodynamic loads and the TRL of the model being tested. However, they do differentiate between preliminary and more advanced design stages of floater concepts, providing advice on considerations for each stage.

In the preliminary stages of testing a FOWT model, a decoupled analysis focusing solely on hydrodynamic loads may suffice. As the model progresses to more advanced stages, it becomes typical to include both aerodynamic and hydrodynamic loads in the analysis. Initially, this can be achieved with a simple system that applies constant thrust to simulate aerodynamic loads, accounting for the maximum tilt angle and surge displacement. However, this approach does not account for the coupling between the structure's displacements and the applied aerodynamic loads. Therefore, hybrid or comprehensive methods should be considered for further design development.

The guidelines recommend understanding the limitations of each method of applying aerodynamic loads and advise on which methods are best suited for different development phases of a floater's design. These recommendations extend to the type of tank testing conditions, the necessary capabilities of the numerical model, and considerations regarding model construction. They also highlight the importance of accounting for uncertainties associated with simplifications and physical constraints of model building, such as achieving correct mass distribution. For example, at smaller scales, the RNA mass decreases to values that might require the use of very light materials to replicate the mass distribution accurately.

Another consideration is the elastic behaviour of the tower and blades, which can be challenging to reproduce at smaller scales. Often, the model is considered rigid as a simplification. In these cases, it is advised to use a 'model the model' procedure, where the numerical model closely approximates the tested model in the wave basin. The sensitivity of the full-scale model to these simplifications should be considered when validating the numerical model.

Despite this comprehensive exploration, no official, internationally accepted protocol for physical testing of floating offshore wind turbines currently exists and there is no active work item on this topic within IEC TC88. This lack of a standardised protocol can potentially cause confusion for developers and tank testing facilities. However, due to the multidisciplinary and complex nature of tank testing, and the variety of models being tested, developing a general and standardised approach might be challenging.

2.7 Staged Development Approach

In contrast, the wave energy industry has adopted a staged development approach under the IEC TS 62600-103 (BSI, 2024) to de-risk the design and development of Wave Energy Converters (WEC). This process, which categorises development from concept to multi-device commercial deployment into five stages (Figure 2.8), offers a clear pathway. The first two stages (covering TRL 1-4) are particularly informative for laboratory-scale testing, while stages 3-5 describe the transition to sea-based testing through sub-system models, solo device demonstrations, and multi-device deployments. This structured approach provides a useful model that the wind energy sector currently lacks, highlighting the need for an official protocol for the tank testing of floating wind turbines to guide developers and testing facilities effectively.

The floating offshore wind sector, building on the experiences of the onshore wind sector and the oil & gas industry, has not required a structured staged development approach as critically as wave energy development. This is because the wind sector benefits from existing knowledge and higher revenue potential. However, adopting such an approach is still valuable as it provides a common framework for floater developers, helping to standardise processes, reduce risks, and enhance the overall development and deployment of FOWT technologies.

When looking for transferable approaches to FOWT testing the key lesson may be the distinction between concept model testing in Stage 1 (TRL 1-3) and Design Model testing in Stage 2 (TRL 4). In the wave energy sector one of the key distinguishing features between these stages is the move to more representative power take-off and control, and more realistic simulated seaways. This is similar conceptually to the difference in complexity between the more rudimentary wind loading and drivetrain implementations for FOWT models, and the more complex hybrid approaches adopted by Azcona et al. (2014), Oguz et al. (2016) and Bachynski et al. (2016).

Wave energy testing is complicated by the fact that there is no archetypal wave energy device. Arguably the wind industry has seen convergence, perhaps in part due to the greater maturity of the technology. However, this maturity perhaps makes it more surprising that there is no standardised approach to exploring combined aerodynamic and hydrodynamic loading in the

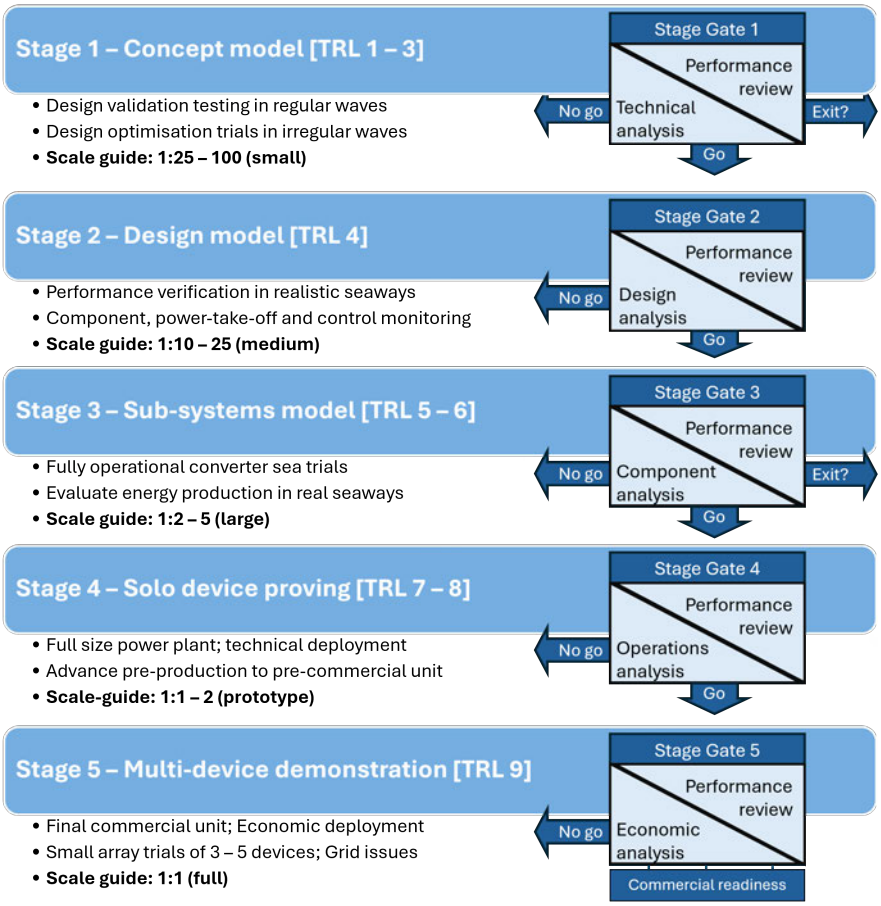

Figure 2.8: Staged Development Approach on the Wave energy Sector (BSI, 2024).

laboratory. A lesson that can be taken from the wave testing sector is that these standards need not be overly prescriptive, and can still provide adaption on emerging technologies. The IEC 62600-103 guidance (BSI, 2024) requires the production of a Design Statement, setting out the key objectives of the test programme and aiding in the process of setting priorities and resolving compromises in test design. A similar approach may allow for resolution when exploring differing requirements between the various FOWT platform concepts.

These basic requirements serve as guidance and a common ground for testing of WEC, giving the developer the freedom to make their own programme. First stage will require more iterations serving as an experimental stage to tune the design. Stage two may require up to two iterations while stage 3 should be done in a single implementation. The scale of the model and complexity of the model and trials increase to reduce the uncertainty in the prototype extrapolation.

Table 2.4 summarises publicly documented projects that performed tank testing of FOWT concepts in wave basins as part of their development pathway. These projects span a range of floater typologies, including spar-buoy, semi-submersible, tension-leg platform (TLP), and novel geometries (e.g., inverted conical cylinder), and were undertaken by a mix of academic, industrial, and public–private consortia. The primary objectives varied, some focused on validating coupled numerical models against physical test results (e.g., WindFloat, Dutch Tri-Floater, WINFLO), others investigated motion characteristics under specific mooring configurations (e.g., SPAR type OWT, TLP type OWT), while a few targeted optimisation of aerodynamic load simulation methods or platform stability (e.g., Iberdrola TLP, MERMAID Project, Eolink).

Although different methods were employed to represent aerodynamic loads, ranging from geometrically scaled rotors and performance scaling to drag disks and hybrid approaches, no clear correlation emerges between the chosen method and the technology readiness level (TRL) at the time of testing. Instead, the selection of the load application technique appears to be primarily dictated by the available capabilities of the test facility, the scale of the model, and the specific objectives of the campaign.

It is therefore proposed that the design of a tank test program should be driven by the maturity of the design, expressed in terms of Stage 1 (TRL 1-3) and Stage 2 (TRL 4) as shown in table 2.5. This design can vary in terms of complexity, depending on the way that the aerodynamic loads are applied especially within the Hybrid approach. It is expected that for Stage 1, concept model, a simpler setup, for example the use of a winch system to apply a constant thrust force in 1 degree of freedom will suffice. This provides information regarding the maximum trim angle and mooring offsets which is theoretically ideal for initial development stages. Testing of control systems it is not proposed at this stage.

Progressing to more complex systems, for Stage 2 it is proposed the application of a dynamic thrust based on a look-up-table or by the full deployment of SIL in real-time. By using this approach, it is possible to perform a fully coupled analysis introducing controlled aerodynamic loading and testing of control systems can be included. Antonutti et al. (2020) concluded that, for the objective of validating global coupled aero-hydrodynamic behaviour and turbine control effects, a hybrid SIL approach combined with a winch actuation system represented the most appropriate compromise. Compared to fan-based thrust application, the winch system enabled multi-degree-of-freedom load allocation and more accurate reproduction of time-varying aerodynamic forces and moments, while maintaining real-time coupling with a numerical turbine model. However, this conclusion is context-dependent. Simpler actuation systems, such as ducted fans applying axial thrust only, may be sufficient where the objective is limited to mean load representation or preliminary response assessment. The winch-based SIL architecture becomes particularly advantageous when two-way coupling, controller dynamics, and multi-component aerodynamic loading are required.

At this stage, the inclusion of other forces from the wind load vector in more than one DOF could be investigated. For example, the representation of the gyroscopic effects to allow a more accurate representation of the aerodynamic coupling between the rotor and the support structure ITTC (2017b). These considerations may be influenced by the type of model being tested, as observed by Høeg and Zhang (2021), the gyroscopic effects are more significant for a spar-type FOWT than for a semi-submersible or TLP.

As shown by Gueydon et al. (2020), within the software-in-the-loop, several actuators can be used to simulate different forces from the wind load vector. However, there's no comparison of what each application may bring to the results and how can it influence the platform responses. As stated by the author, comparisons between different testing techniques are needed to continuously improve tank testing results.

Table 2.4: List of tank testing deployments with the corresponding technique used to simulate aerodynamic loads, the TRL value at the time of the testing, and the TRL value at the present time.*

Design	Concept Model (Stage 1)			Design Model (Stage 2)	Method(s)	Test Aim	Present TRL	References
	TRL 1	TRL 2	TRL 3	TRL 4				
HYWIND	X	X	X	X	Geometrically scaled	Validate motions characteristics under coupled wind and waves	TRL 8	Cermelli et al. (2009)
WindFloat	X	X	X		Drag Disk	Validation of numerical tools	TRL 8	Roddier et al. (2010)
TLP type OWT	X	X	X		Geometrically scaled	Clarify the motion characteristics of the platform	TRL 3	Nihei and Fujioka (2010)
SPAR type OWT	X	X	X		Static weight/ Geometrically scaled	Resultant motions with variation of moorings' attaching points	TRL 3	Chujo et al. (2011)
Dutch Tri-Floater	X	X	X		Geometrically scaled	Validation of numerical tools	TRL 4	Philippe et al. (2013)
WINFLO Floater	X	X	X		Performance scaled	Validation of numerical tools	TRL 5	Le Boulluec et al. (2013)
Inverted conical cylinder	X	X	X		Geometrically scaled	Motions characterisation	TRL 3	Shin et al. (2014)
GustoMSC Tri-Floater	X	X	X		Performance scaled	Validation of numerical tools	TRL 4	Huijs et al. (2014)
MERMAID Project	X	X	X		Performance scaled	Validation of numerical tools	TRL 3	Armesto et al. (2016)
Iberdrola TLP	X	X	X		Hybrid	Validation of numerical tools	TRL 3	Oguz et al. (2018)
Eolink OWT	X	X	X		Performance scaled	Validation of numerical tools	TRL 5	Doisenbant et al. (2018)

*This TRL classification is based on the articles referenced and on the author's best judgment.

Table 2.5: Theoretical proposed set-ups for stages 1 and 2 for a Staged Developemnt Approach for FOWT.

Test Feature	Concept Model (Stage 1)	Design Model (Stage 2)
Wind Loading Application	Constant thrust winch system	Performance scaled/ Hybrid approach
Control	No controller	Control methodologies can be applied
Degrees of Freedom	1	≥ 1
Environmental Parameters	Long-crested waves and/or uniform wind; regular waves with/without regular wind; irregular waves with/without turbulent wind	Misalignment of wind and wave directions/ short-crested irregular waves
Test objectives	Acquire maximum platform's displacements and mooring tensions; Obtain hydrodynamic coefficients and natural frequencies; Verification of static and dynamic stability parameters; Validation of numerical tools	Understanding of the coupled effects in the structure's response; Validation of numerical tools; Test of more realistic conditions; Sensitivity to limited wind actuation

The objectives of experimental tests differ between the two stages of development. In the initial stages, overall parameters such as the stability and frequency response of the structure are prioritised. In later stages, coupled analyses of wind and waves become necessary, along with consideration of the effects of limited wind actuation. In both stages, the validation of the numerical tools is essential and the main objective since this would allow the development of the design numerically.

The environmental parameters for each stage are selected based on current guidelines (ITTC, 2017b; DNV, 2021). In the early stages, characterising the linear response is the minimum requirement. In contrast, later stages demand accurate performance estimation in the time domain, where non-linearities are included.

This proposal aims to encourage the development of a more structured protocol to minimise ambiguities associated with tank testing. At all stages, limitations and error sources should be considered and, whenever possible, quantified.

2.7.1 Identified Knowledge Gaps

Despite the range of concept- and design-stage model tests summarised in Table 2.4, several gaps remain in the publicly available knowledge base. Firstly, there is a lack of standardised protocols for physical testing of FOWTs, particularly regarding scaling strategies for aerodynamic loading, mooring system representation, and the selection of environmental conditions. The choice of load-application method is often dictated by facility limitations rather than by standardised best practice, leading to difficulties in comparing results across different studies.

Furthermore, limited information is available on the testing of novel control strategies, wind-wave-current interaction effects, and extreme sea state performance, especially for higher-TRL designs approaching full-scale deployment. Much of the recent and ongoing work remains proprietary, restricting dissemination of lessons learned. Addressing these gaps would support greater consistency, comparability, and confidence in the experimental validation of FOWT designs.

Chapter 3

Experimental and Numerical Methodology

This chapter outlines the methodology employed to address the research questions. As stated in the previous chapter, there is no standardised process for scaled testing of floating offshore wind turbines (FOWTs), in wave basins, considering how best to include aerodynamic loads as a function of the Technology Readiness Level (TRL) of the model and the objectives of the test plan. Current guidelines (e.g. IEC (2025)) only offer general guidance on the advantages and disadvantages of each method of aerodynamic actuation to be used in wave tank tests.

The main objective of this work is to provide more prescriptive guidance and to explore the value and limitations of increasing the complexity of aerodynamic actuation. To this end, three phases of testing were carried out, each introducing aerodynamic loads with progressively greater fidelity (see Figure 3.1). The experimental results are analysed both comparatively across test phases and against a numerical model.

Phase I employed a static weight, representing the simplest way of applying a constant uncoupled rotor thrust force. Phase II introduced a constant force applied by a PI-controlled motor via a winch system, providing more accurate and controllable thrust representation. Lastly, Phase III used a Software-in-the-Loop (SIL) approach, the most complex method, where the same winch system was coupled with a simplified Blade Element Momentum (BEM) code. In this setup, rotor thrust was dynamically calculated at each time step based solely on the measured platform pitch acceleration, thus coupling aerodynamic and hydrodynamic effects.

To conduct the present study, several key steps were undertaken, as summarised in the process flow of Figure 3.2. Section 3.1 presents the model inputs, including the selection of a reference floating wind turbine used consistently across all phases of the tank testing campaign (Section 3.1.1), as well as the definition of the metocean conditions to be reproduced in the basin (Section 3.1.2). This is followed by Section 3.2, which describes the numerical modelling tools employed in the study. Section 3.3 details the physical testing methodology,

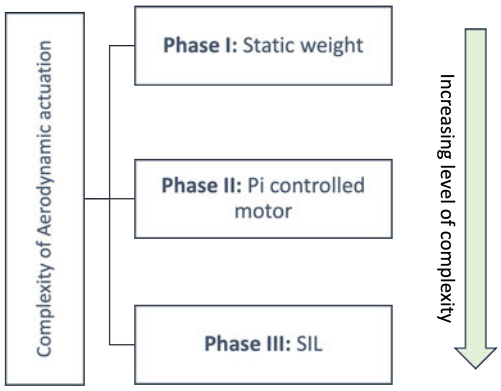

Figure 3.1: High-level schematic of the different phases of the tank test campaign, with increasing complexity in aerodynamic load representation.

including the tank facility and model scaling approach (Section 3.3.1), mooring system design (Section 3.3.2), and implementation of aerodynamic actuation (Section 3.3.3). Finally, Section 3.4 outlines the tank testing plan, covering the selection of frequencies of interest (Section 3.4.1) and the overall testing procedure (Section 3.4.2).

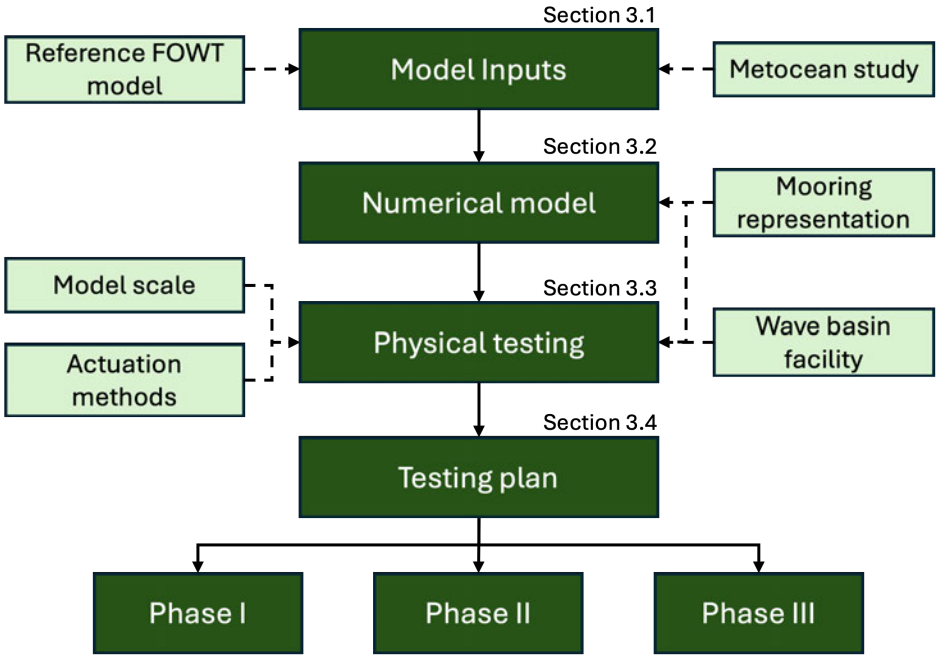

Figure 3.2: Overall simplification of the methodology sections, representing the process flow of the study.

Each of these steps presented its own challenges and limitations, which will be explained in detail in this chapter. This will provide with an understanding of the various compromises made to successfully achieve the objectives of this research.

3.1 Model Inputs

In line with the study's objectives, as the present work compares the relative impact of different aerodynamic actuation systems, the selection of platform to conduct this comparison is not of utmost importance. The key requirement is that the model remains the same with known characteristics, as designing the FOWT model is not a primary focus of this study.

3.1.1 FOWT Reference Model

For this study, the semi-submersible VolturnUS-S platform, developed by the University of Maine to support the IEA 15 MW reference wind turbine, was selected as the reference floating offshore wind turbine (FOWT) model. This choice was guided by three key considerations: (1) its alignment with industry trends toward higher-capacity turbines, (2) the maturity and documentation of the concept compared to other publicly available floating platforms, and (3) the open accessibility of its design data, which facilitates reproducibility and comparison with numerical modelling.

At the time of this study, the VolturnUS-S represented one of the most advanced and well-documented floating platform concepts available, making it a suitable and forward-looking choice for the tank testing campaign.

3.1.2 Site Characterisation

This study focuses on metocean conditions representative of the Norwegian coast near Haugesund (see Figure 3.3) while excluding sites affected by seasonal ice or tropical cyclones. The ESOX database (LAUTEC/ESOX, 2024), which aggregates ERA5 reanalysis from ECMWF for the Copernicus Climate Change Service (C3S), was used to obtain 30 years of hourly data (1990–2019) on 10 m and 100 m wind speeds, significant wave height H_s, and peak wave period T_p. ERA5 is provided on a $0.25^\circ \times 0.25^\circ$ grid (about 10–30 km) and covers nearshore to offshore regions. The grid point analysed here is centred at 59.5° N, 5° E (Haugesund vicinity).

Wind speed at hub height ($h = 150$ m) was estimated from the 100 m wind speed values using the Power Law,

$$V_h = V_r \left(\frac{h}{r} \right)^{\alpha}, \tag{3.1}$$

with V_r the 100 m reference speed, $r = 100$ m, and $\alpha = 0.12$, consistent with typical offshore values and OpenFAST Inflow defaults (Stewart et al., 2015).

Figure 3.3: Location of Haugesund in the map.

To aid test planning, an H_s–T_p probability matrix was constructed from the hourly record. The matrix encodes occurrence probabilities as a colour scale from 0% (green) for least probable states to higher percentages (red) for more probable states. Yellow and blue borders highlight the sea states within the FloWave testing envelope for regular and irregular wave conditions, respectively. Additional overlays indicate candidate rows and columns used for frequency and amplitude sweeps. This plot is used purely as a selection tool where the final sets adopted for testing are listed later in Section 3.4.2.

Extreme sea states were derived with the Inverse First-Order Reliability Method (I-FORM) following Veritas (2025) and implemented in ViroCon v1.2.0 (Haselsteiner et al., 2020). The joint model adopts

$$f(H_s, T_p) = f(H_s)\, f(T_p \mid H_s), \tag{3.2}$$

with $f(H_s)$ a three-parameter (translated) Weibull distribution and $f(T_p \mid H_s)$ Lognormal with parameters that vary with H_s. For $t > 0$,

$$f_{T_p|H_s}(t \mid h) = \frac{1}{t\,\sigma(h)\sqrt{2\pi}} \exp\left[-\frac{\left(\ln t - \mu(h)\right)^2}{2\,\sigma(h)^2}\right], \tag{3.3}$$

where $\mu(h) = a_0 + a_1 h^{a_2}$ and $\sigma(h) = b_0 + b_1 e^{b_2 h}$ are obtained by fitting to T_p conditioned on H_s binned in 1 m intervals (coefficients provided in Section 4.1.1).

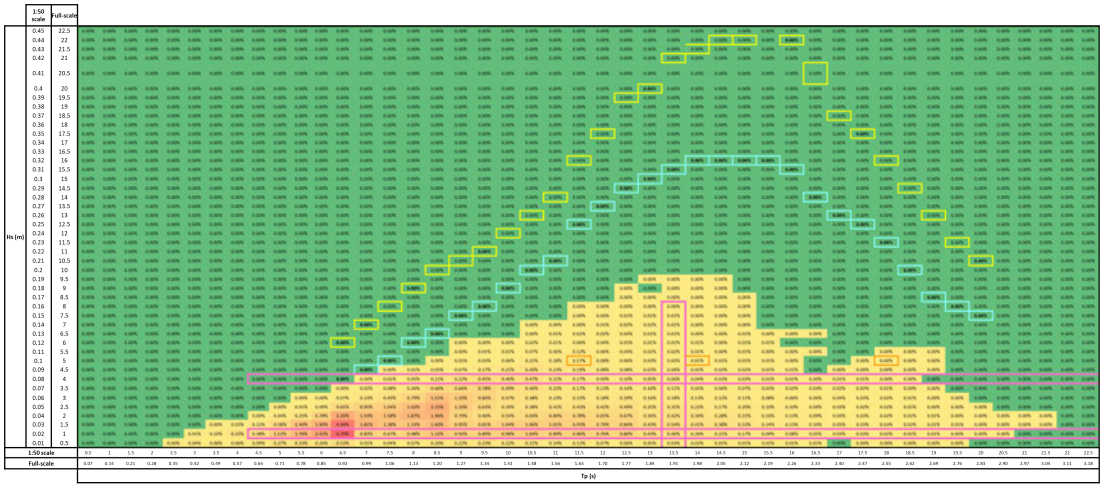

Figure 3.4: Occurrence probabilities of sea states (H_s vs. T_p) at 59.5° N, 5° E (1990–2019). Colours range from green (0%) to red (higher percentages). Yellow and blue borders indicate the FloWave regular- and irregular-wave envelopes; additional overlays show candidate sweep selections used for planning.

The marginal distribution of hourly mean wind speed V is modelled using a two-parameter Weibull distribution, consistent with standard offshore wind resource characterisation practice. The probability density function is

$$f_V(v) = \frac{k(v)}{\lambda(v)} \left(\frac{v}{\lambda(v)} \right)^{k(v)-1} \exp\left[- \left(\frac{v}{\lambda(v)} \right)^{k(v)} \right], \qquad v > 0, \tag{3.4}$$

where $k(v)$ and $\lambda(v)$ denote the shape and scale parameters, respectively. The location parameter is fixed to zero, yielding a standard two-parameter Weibull model.

Within the ViroCon implementation, parameter dependency is defined using the “power3” formulation, such that

$$k(v) = \alpha_0 + \alpha_1 v^{\alpha_2}, \tag{3.5}$$

$$\lambda(v) = \beta_0 + \beta_1 v^{\beta_2}, \tag{3.6}$$

where α_i and β_i are regression coefficients obtained from fitting to the wind data. The fitted parameters are reported in Section 4.1.1.

Let Φ be the standard normal CDF and (u_1, u_2) the Rosenblatt-transformed variables. For hourly observations, the reliability index β for an R-year return period is

$$\beta = \Phi^{-1}\left(1 - \frac{1}{R \times 365.25 \times 24}\right), \tag{3.7}$$

which defines the circle $\sqrt{u_1^2 + u_2^2} = \beta$ in U-space. Mapping this contour back gives the R-year environmental contour in (H_s, T_p).

Fit diagnostics and the resulting 1- and 50-year contours are presented and interpreted in the Results chapter (Section 4.1). This section documents the modelling framework only. The specific sea states selected for tank testing, including sweep definitions and extreme cases, are summarised in the Tank Test Plan (Section 3.4.2). For convenience, the extreme cases used in testing are listed below.

Table 3.1: Extreme sea states adopted for physical testing (derived via I-FORM).

Return Period (years)	H_s (m)	T_p (s)
1	6.9	12.92
50	13	16
50	14	18

Irregular sea states used for numerical simulations and physical testing are represented using the JONSWAP spectrum, appropriate for fetch-limited North Sea conditions. For each selected sea state defined by (H_s, T_p) (Table 3.1), the spectrum is constructed using the specified significant wave height and peak period.

The peak enhancement factor γ is calculated in accordance with DNV-RP-C205 (Veritas, 2025), ensuring consistency with the recommended environmental modelling practice for offshore structures.

This spectral representation is used consistently across numerical simulations and wave basin testing to ensure alignment between environmental characterisation and physical realisation.

3.2 Numerical Modelling Tools

OpenFAST version 3.1 was the numerical tool used in the present work to evaluate the global performance of the VolturnUS-S platform, and the resulting simulations were compared against the outcomes of physical tank testing. In addition to dynamic response prediction, OpenFAST was also employed to extract key physical properties of the model, such as mass,

moments of inertia (MOI), and centre of gravity (COG), via its linearisation tool. Furthermore, it enabled a numerical sensitivity study comparing the effects of a simplified thrust-only excitation applied at nacelle height with those of a fully coupled aerodynamic loading approach. These applications are described in detail in the following subsections.

3.2.1 Determination of Moments of Inertia, Mass, and Center of Gravity of the Model

The properties of the model, such as moments of inertia (MOI), mass, and centre of gravity (COG), can be determined in various ways. The mass of each component is provided in the reference documents and summarised in Table 3.4. The COG is partially specified in the reference document for the floater only. Similarly, the MOI are available, but only for the floater. Given this incomplete information, it was necessary to obtain the complete system properties. For this purpose, the OpenFAST model (NREL) of the VolturnUS-S was used.

The OpenFAST code calculates the model's properties internally. It uses the properties of each component to compute the MOI for the entire system, applying the parallel axis theorem. Instead of performing these calculations manually, the linearisation tool in OpenFAST was employed. The system's dynamics are represented by a state-space formulation where the state variables fully describe the dynamic system and its response for certain inputs.

The linearisation was performed by disabling all modules except ElastoDyn, allowing for the assessment of local stability around a steady-state operating condition. The output of the linearisation is a linear state-space model, consisting of four matrices that describe the relationships between states, inputs, and outputs, which is only valid for small perturbations around that specific operating condition. The ElastoDyn (ED) module, which has continuous-time states, allows for linearisation without restrictions. The linearised form of the equations of motion and output equations is given by:

$$\Delta \dot{x}^{(\mathrm{ED})} = A^{(\mathrm{ED})} \Delta x^{(\mathrm{ED})} + B^{(\mathrm{ED})} \Delta u^{(\mathrm{ED})} \tag{3.8}$$

$$\Delta y^{(\mathrm{ED})} = C^{(\mathrm{ED})} \Delta x^{(\mathrm{ED})} + D^{(\mathrm{ED})} \Delta u^{(\mathrm{ED})} \tag{3.9}$$

In control theory and system dynamics, these equations describe how the state of the system evolves over time and how the outputs are generated from the states and inputs. The first equation is the state equation where $\Delta \dot{x}^{(\mathrm{ED})}$ represents the derivative of the state vector, indicating the rate of change of the system's continuous states. $A^{(\mathrm{ED})}$ is the state matrix,

defining the relationship between the current state and its rate of change. $\Delta x^{(\mathrm{ED})}$ is the state vector, representing the system's states. $B^{(\mathrm{ED})}$ is the input matrix, which defines how the control inputs affect the state changes and $\Delta u^{(\mathrm{ED})}$ is the input vector, representing the control inputs to the system.

The second equation is the output equation where $\Delta y^{(\mathrm{ED})}$ is the output vector, representing the system's outputs. $C^{(\mathrm{ED})}$ is the output matrix, defining the relationship between the states and the outputs. $D^{(\mathrm{ED})}$ is the feed-through (or direct transmission) matrix, defining the direct relationship between the inputs and the outputs.

The OpenFAST user documentation was used to perform this linearisation (NREL, 2024). Important to refer that this linearisation was performed for a rigid body system about the platform reference point, meaning that only the 6 DOF were enabled in ElastoDyn and the requested outputs were the accelerations in the same 6 DOF.

Equations 3.8 and 3.9 can be applied to a spring-damper-mass system upon which an input force, F acts. The second-order differential equation is given by (see X-Engineer, 2024):

$$mx'' + cx' + kx = F \tag{3.10}$$

where:

- m [kg] – mass,
- k [N/m] – spring constant (stiffness),
- c [Ns/m] – damping coefficient,
- F [N] – external force acting on the body,
- x [m] – displacement of the body.

As the order of the differential equation is two, we choose two state variables, x_1 and x_2, defined as:

$$x_1 = x, \quad x_2 = \dot{x} \tag{3.11}$$

Differentiating the state variables, we obtain:

$$\dot{x}_1 = \dot{x}, \quad \dot{x}_2 = \ddot{x} \tag{3.12}$$

Considering the definitions of the state variables, the derivatives can be written as:

$$\dot{x}_1 = x_2, \quad \dot{x}_2 = \ddot{x} \tag{3.13}$$

Using equations 3.10 and 3.13, we express the differential equations as a set of first-order ordinary differential equations:

$$\dot{x}_1 = x_2 \tag{3.14}$$

$$\dot{x}_2 = \frac{1}{m}(F - cx_2 - kx_1) \tag{3.15}$$

Dividing the second equation by m and rearranging gives:

$$\dot{x}_1 = x_2 \tag{3.16}$$

$$\dot{x}_2 = -\frac{c}{m}x_2 - \frac{k}{m}x_1 + \frac{F}{m} \tag{3.17}$$

In matrix format, the set of equations can be represented as:

$$\begin{bmatrix} \dot{x}_1 \\ \dot{x}_2 \end{bmatrix} = \begin{bmatrix} 0 & 1 \\ -\frac{k}{m} & -\frac{c}{m} \end{bmatrix} \begin{bmatrix} x_1 \\ x_2 \end{bmatrix} + \begin{bmatrix} 0 \\ \frac{1}{m} \end{bmatrix} F \tag{3.18}$$

Now, we can identify the state matrix A and the input matrix B:

$$A = \begin{bmatrix} 0 & 1 \\ -\frac{k}{m} & -\frac{c}{m} \end{bmatrix}, \quad B = \begin{bmatrix} 0 \\ \frac{1}{m} \end{bmatrix} \tag{3.19}$$

The 6x6 rigid-body mass matrix (M) of ElastoDyn can be found by taking the matrix inverse of the 6x6 subset of the input matrix (B), associated with the 6 platform load inputs and 6 platform acceleration outputs.

The resultant inverse of matrix B is:

$$B^{-1} = \begin{bmatrix} 2.0255 \times 10^{7} & 8.6373 \times 10^{-7} & -0.4167 & 8.5005 \times 10^{-5} & -2.9943 \times 10^{7} & 1.2241 \times 10^{-4} \\ -2.3262 \times 10^{-11} & 2.0253 \times 10^{7} & 2.1216 \times 10^{-11} & 2.9946 \times 10^{7} & -1.758 \times 10^{-7} & -6.8090 \times 10^{6} \\ 0.7961 & -2.7261 \times 10^{-11} & 2.0252 \times 10^{7} & -1.9402 \times 10^{-4} & 6.8097 \times 10^{6} & -4.0297 \times 10^{-10} \\ 1.8725 \times 10^{-8} & 2.9946 \times 10^{7} & -9.0501 \times 10^{9} & 4.4043 \times 10^{10} & -1.2502 & 9.9996 \times 10^{8} \\ -2.9943 \times 10^{7} & -1.4527 \times 10^{-6} & 6.8114 \times 10^{6} & -1.2504 & 4.3925 \times 10^{10} & -1.8358 \times 10^{-4} \\ 1.8574 \times 10^{-10} & -6.8090 \times 10^{6} & 4.6155 \times 10^{-10} & 9.9996 \times 10^{8} & -2.6277 \times 10^{-6} & 2.3920 \times 10^{10} \end{bmatrix} \tag{3.20}$$

The top left quadrant (i.e., the 3×3) corresponds to the total mass of the system, the top right quadrant and bottom left quadrants corresponds to the COG and the bottom right quadrant correspond to the MOI. This way, the total mass of the system corresponds to 2.0255×10^{7} kg, the COG is $(1.9 \times 10^{-8}, -1.5 \times 10^{-6}, 4.6 \times 10^{-10})$ and the moments of inertia are:

$$I_{xx} = 4.4043 \times 10^{10}\,\mathrm{kg\,m^2}$$

$$I_{yy} = 4.3925 \times 10^{10}\,\mathrm{kg\,m^2}$$

$$I_{zz} = 2.3920 \times 10^{10}\,\mathrm{kg\,m^2}$$

With these properties' values, the scaled model was designed to better represent the full-scale system.

The OpenFAST input files used were the corresponding files available on GitHub for the VolturnUS-S model (Allen et al., 2020). No significant modifications were made to the system's properties; values from the diffraction analysis, as well as the added mass and drag coefficients, remained unchanged. In AeroDyn, the theory used corresponds to the Blade Element Momentum Theory (BEMT) with tower drag not being considered. The time-step chosen for the simulation is 0.025 s, respecting the theoretical value adjusted based on the frequencies that are modelled in the system (typically around a tenth of the fastest frequency). In this case, the heave natural frequency is the highest frequency, 0.046 Hz which means that a minimum time-step of 2 seconds is needed. In this case, the simulation is stable at a time-step of 0.025s. The simulation duration is 3600 s.

To numerically assess the implications of limited wind actuation, a sensitivity study was conducted comparing two scenarios: (1) applying a constant force at hub height and (2) including the full aerodynamic load vector. The first scenario represents the limited actuation case, replicated in physical testing by applying a constant thrust force.

3.2.2 Only thrust simulation

To replicate the "only thrust" scenario in OpenFAST, one possible approach would be to modify the aerodynamic source code such that only the rotor thrust contribution is retained while all other aerodynamic loads are suppressed. However, an equivalent and more transparent implementation is achieved by directly applying the thrust force as a user-defined load at hub height (150 m).

In this study, the thrust load is prescribed through the Structural Control (StC) submodel within ServoDyn, while the AeroDyn and InflowWind modules are disabled. This approach isolates the axial thrust contribution explicitly, ensuring that no additional aerodynamic moments or distributed blade loads are introduced.

The StC submodel is usually used to simulate tuned mass dampers and tuned liquid column dampers although, it also provides an option for applying a force time series load at the location of the Structural Control node. The simulation of only thrust force was performed by using a force time series load file with the same time-step (0.025s) and a simulation duration of 3600 s.

The selected cases for this sensitivity study include one regular wave and one irregular wave case from the tank testing plan presented in Section 3.4.2. Additionally, a still water case was run to verify that the forces applied at hub height were accurate, validating the method. Table 3.2 summarises the parameters for these cases, each featuring a different rotor thrust value. This variation occurs because rotor thrust is sensitive to the dynamics of the floating system.

As shown in Table 3.2, the rotor mean thrust value slightly decreases in the presence of waves. The values for the "Normal" scenario correspond to the mean rotor thrust under steady wind conditions of 11 m/s, while for the "Only thrust" scenario, these forces are applied as a constant load. In both cases, the structure is modeled as a rigid body with six degrees of freedom (6DOF), meaning that elastic deformations of the tower and blades are not accounted for.

	Normal	**Only thrust**
Still water		
Wind speed (m/s)	11	-
Rotor thrust (kN)	2716	2716
Regular wave		
Wind speed (m/s)	11	-
Rotor thrust (kN)	2668	2668
$H(m)$	6	6
$T(s)$	13.5	13.5
Irregular wave		
Wind speed (m/s)	11	-
Rotor thrust (kN)	2684	2684
$H_s(m)$	5	5
$T_p(s)$	14	14

Table 3.2: Table summarising the parameters for each one of the cases used for comparison between the 'Only thrust' and 'Normal' scenarios.

The results of this sensitivity analysis are presented in Section 4.2.

3.3 Physical Testing

This section outlines the experimental campaign undertaken to validate and complement the numerical simulations described earlier. Physical testing was conducted using a scaled model of the VolturnUS-S floating wind platform at the FloWave Ocean Energy Research Facility. The goal of the experimental work is to investigate the dynamic response of the system under various wind and wave conditions and to evaluate different methods for applying aerodynamic loads in a controlled tank environment. The subsections below present the

characteristics of the wave basin, the rationale behind the selected model scale, the design and construction of the scaled FOWT model, and the procedures followed during testing, including wave generation, wind representation, mooring system design, and aerodynamic thrust application.

3.3.1 Description of the wave basin: FloWave

This study was carried out in collaboration with the FloWave Ocean Energy Research Facility, located at the University of Edinburgh, UK (see Figure 3.5). All experimental work, including the three tank tests, were conducted at this facility. FloWave features a 25-meter diameter circular tank capable of generating both waves and currents. This is achieved through 168 active-absorbing force-feedback wavemakers and a recirculating flow system powered by 28 impeller units mounted in a plenum chamber beneath the tank floor (see Figure 3.6).

Figure 3.5: The FloWave Ocean Energy Research Facility.

The FloWave basin was originally designed to support the wave and tidal energy sectors, with an optimum scale range of 1:20 to 1:40, enabling the simulation of complex wave, current, and combined wave–current scenarios. While not initially developed with floating offshore wind turbines (FOWTs) in mind, the facility is increasingly being used for FOWT applications, demonstrating its adaptability and value to the sector. Past FOWT experiments at FloWave include tests by AXIS Energy Projects Ltd. on a 1:55 scale tension spar buoy with a 10 MW rated wind turbine (in Global Business, 2024), where rotor thrust was applied using both a constant-thrust winch system (Figure 3.7a) and an experimental water jet setup (Figure 3.7b). The W2Power concept has also been tested at FloWave. This study builds on that growing body of work by further exploring the tank's capability to support experimental FOWT testing.

This study contributes to the ongoing discussion around how facilities like FloWave can best support the floating offshore wind sector, particularly in terms of accurately representing aerodynamic effects in physical model tests.

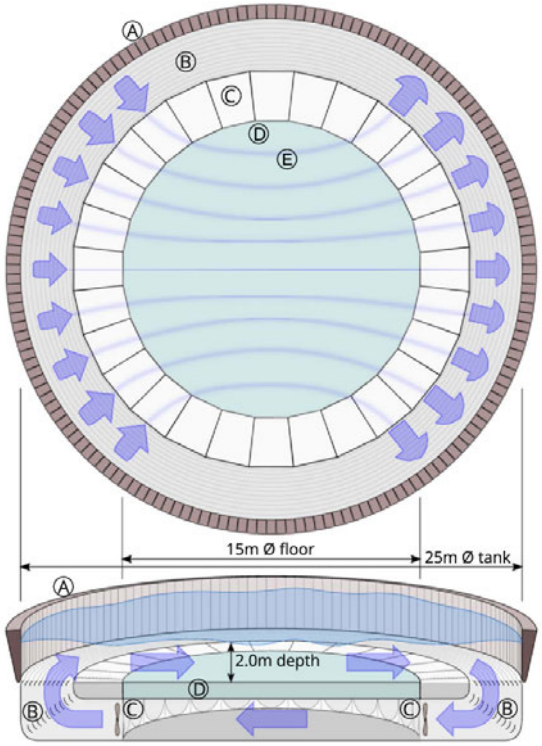

Figure 3.6: FloWave dimensions (adapted from: Sutherland et al. (2017))

3.3.2 Selection of model scale

Complete similitude between scaled and full-scale models cannot be achieved unless at a one-to-one scale, making it difficult to ensure geometric, kinematic, and dynamic similarity (see Chakrabarti, 1994). In practice, it is not feasible to maintain all scaling laws simultaneously, so prioritisation is necessary regarding which force ratios to preserve. In fluid flow problems involving a free surface, the Froude number is typically used. By maintaining the ratio of inertial to gravitational forces between the model and the real-life scenario, the Froude number ensures dynamic similarity. This is crucial for accurately replicating the behaviour of waves and their interactions with structures.

In this study, the model's geometry, masses, inertia, and forces were scaled according to the Froude number, as detailed in Table 3.3. The scaled length is determined by dividing the full-scale length by the scaling factor, λ. The choice of the scaling factor is critical for selecting an appropriate floating model suitable for the wave basin dimensions and its simulation capability of the environment. For instance, the OC3-Hywind concept (Jonkman and Musial (2010)) has a draft of 120 meters. With a scaling factor between 50 and 100, this length scales down to between 2.4 m and 1.2 m, respectively. Therefore, the wave basin must be sufficiently deep to accommodate this scaled length. Consequently, given the depth of the tank used in this work, the Spar-buoy configuration was not selected.

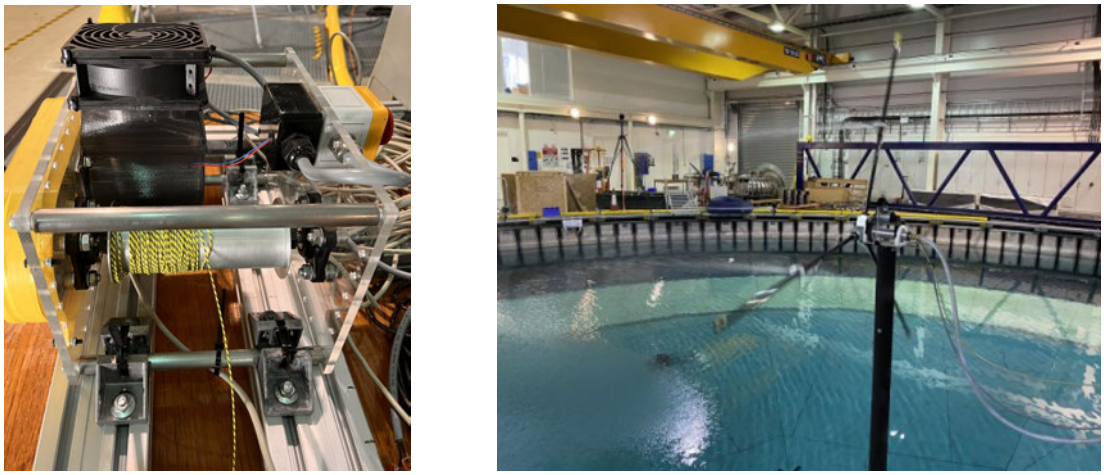

(a) Winch system.

(b) Novel jet system.

Figure 3.7: Different systems of applying constant rotor thrust in FloWave basin during AXIS EP Ltd. experiments.

Designation	Unit	Scale Factor
Acceleration	m/s^2	λ^0
Area	m^2	λ^2
Density	kg/m^3	λ^0
Force	N	λ^3
Frequency	s^{-1}	$\lambda^{-0.5}$
Length	m	λ^1
Mass	kg	λ^3
Moment	N-m	λ^4
Pressure	N/m^2	λ^1
Velocity	m/s	$\lambda^{0.5}$
Time	s	$\lambda^{0.5}$

Table 3.3: Scaling factors for various physical quantities according to the Froude number.

Another important consideration is instrumentation. For example, forces scale as λ^3 which means that if the model is too small these loads might be negligible and difficult to measure with the required accuracy.

Regarding the Tension Leg Platform (TLP) configuration, tank testing of such structures presents complexities due to the platform's stability being dependent on high mooring tensions. This introduces additional challenges to the tank testing campaign.

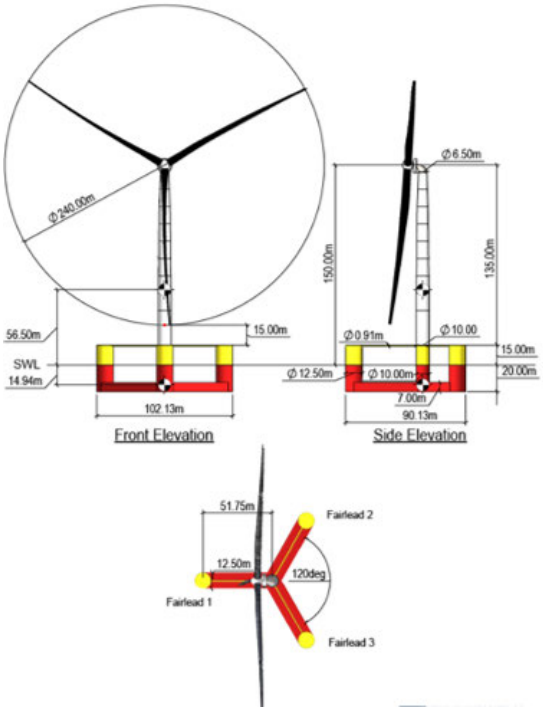

Figure 3.8: General arrangement of the VolturnUS-S platform. Adapted from Allen et al. (2020).

For these reasons, the semi-submersible configuration was chosen for this work, specifically the UMaine VolturnUS-S reference platform developed for the IEA Wind 15 MW Offshore RWT (Allen et al., 2020). This platform represents a large, state-of-the-art turbine size that aligns with current industry trends and development targets. Moreover, the VolturnUS-S is a well-documented and widely studied design for the IEA 15 MW turbine, making it a robust and appropriate choice for both numerical modelling and physical testing at a 1:50 scale in the FloWave basin.

The UMaine VolturnUS-S reference platform is a generic steel adaptation of UMaine's patented concrete floating foundation technology (Viselli et al., 2015), originally developed for smaller turbines in earlier demonstration projects, in collaboration with the U.S. Department of Energy. It corresponds to a semi-submersible type of floater, attached to three chain-catenary moorings, each spread 120 deg apart, with the IEA 15 MW RWT on top (Figure 3.8). For brevity, this platform will hereafter be referred to as the VolturnUS-S platform.

Allen et al. (2020) details the characteristics of the floater while Bortolotti et al. (2020) describes the properties of the 15 MW RWT. Table 3.4 shows the these properties along with the respective scaling factors for 1:50 using Froude number scaling.

Table 3.4: Model properties

	Full-scale	Scale Factor 1:50
RNA mass (kg)	991,000.00	7.93
Tower mass (kg)	1,263,000.00	10.10
Floating Platform mass (kg)	17,839,000.00	142.71
Total mass (kg)	20,711,457.88	165.69
Mooring pre-tension (N)	6,065,000.00	48.52
Centre Column ϕ (m)	10.00	0.20
Edge Columns ϕ (m)	12.50	0.25
Column Height (m)	35.00	0.70
Tower ϕ (m)	8.25	0.17
Tower Height (m)	129.50	2.70
Pontoon Height (m)	7.00	0.14
Pontoon Length (m)	51.75	1.04
Pontoon Width (m)	12.50	0.25
Mooring point above bottom (m)	6.00	0.12
Draft (m)	20.00	0.4

The geometry of the floater needs to closely match the tabulated values because hydrodynamic loads are highly dependent on its shape and mass distribution. In contrast, aerodynamic loads are applied by different systems that do not require exact geometric matching. To ensure the inertia of the systems is accurate, the moments of inertia were meticulously matched and the structure was considered as rigid body, where the elasticity of the tower was not scaled. According to DNV recommended practices DNV (2021), rigid models are usually sufficient for validation and global response evaluations.

3.3.3 Coordinate system

The global coordinate system for the VolturnUS-S model has its origin at the model centre of gravity and it is represented in Figure 3.9. The x-axis is positive towards downwind direction, and it corresponds to the surge DOF, the y-axis points positive towards the left when facing downwind direction and it corresponds to sway, and positive z-axis direction is pointing upwards being perpendicular to the xy plane, named heave. The rotational DOF, Roll, Pitch and Yaw are positive clockwise. The local rotor coordinate system was explained in Chapter 2.

In this work, all references to the 6 degrees of freedom (DOF) motions of the rigid body pertain to the global coordinate system. When discussing aerodynamic forces, they are applied within the local rotor coordinate system.

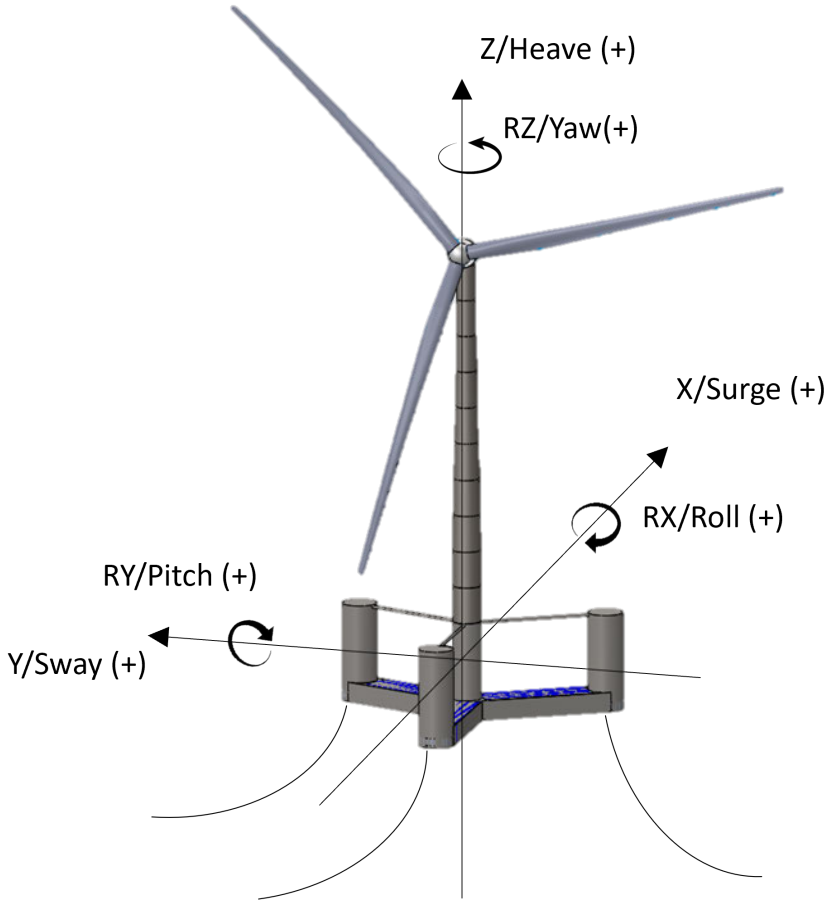

Figure 3.9: Global coordinates of the VolturnUS-S model. Adapted from Allen et al. (2020).

3.3.4 Design and construction of the FOWT model

The objective in designing and constructing the VolturnUS-S model was to ensure it would be modular, adaptable to various types and sizes of wind turbines (WT), and primarily composed of materials that could be readily purchased off the shelf. The design was carried out in SolidWorks, allowing for verification of key properties, such as total mass, COG and moments of inertia, prior to construction.

The design and construction of the model was carried out in close collaboration with FloWave's team, including Dr Thomas Davey, Dr Callum Guy, and Martyn Lennon.

Beyond meeting the requirements of this specific study, the model was also intended to serve as a general purpose experimental platform for future FOWT research at FloWave. By designing a scalable, modular structure compatible with a range of thrust input methods, the model offers a flexible foundation for ongoing and future tank testing campaigns in the floating wind sector.

Another important consideration was that the tests were conducted in fresh water. Although the mass correction due to freshwater density differences is relatively small (approximately 2.4%), it can contribute to cumulative errors in physical modeling and was therefore explicitly accounted for during the design process.

Fresh water correction

The seawater density in the VolturnUS-S full-scale model is equal to 1025 kg/m^3, while in the tank test the water density should be that of fresh water, which is 1000 kg/m^3. Thus, the Archimedes' principle (Equation 3.21) was applied to find the corrected mass for fresh water in order to ensure the same total draft and underwater volume.

$$M_1 \cdot g = \rho_{\text{seawater}} \cdot g \cdot V_1 \tag{3.21}$$

M_1 is the VolturnUS-S full-scale platform mass, g is the gravitational acceleration, ρ_{seawater} is the seawater density, and V_1 is the volume of the platform submerged below the seawater line. To maintain the same draft, i.e., the same volume of the platform submerged underwater (V_1), the platform mass (M_2) in fresh water will be:

$$M_2 \cdot g = \rho_{\text{freshwater}} \cdot g \cdot V_1 \tag{3.22}$$

The corrected target values and scaled geometries are presented in Table 3.5 alongside the values measured in the real physical model, referred to as 'Measured value'. Corrections were made to the tower height to keep the moments of inertia as close as possible to the target values. All differences are within 10 $\%$, except for the mooring pre-tension, which will be explained later.

The core part of the floater, had mass less than the total mass requiring ballast mass to make up the difference. This allows for the accommodation of some margin of error. These masses, along with their positions, were carefully designed in a CAD package, SolidWorks. The bottom piece was an assembly of several different aluminium parts connected by bolts and the shape of the pontoons was maintained using foam (Figure 3.10a). The tower was a standard aluminium tube that was cut to match the expected value. The RNA assembly consisted of a solid piece, and the tower ballast was a simple aluminium piece positioned inside the tower. The complete SolidWorks model design is shown in Figure 3.10a, and the fully assembled physical model is shown in Figure 3.10b.

Table 3.5: Comparison between the target values and measured values of the scaled model properties.

	Target value	Measured Value	Difference(%)
RNA mass (kg)	7.73	7.90	2.09
Tower mass (kg)	9.86	10.48	5.94
Floating Platform mass (kg)	139.23	136.92	-1.69
Total mass (kg)	161.65	156.50	-3.29
Centre Column ϕ (m)	0.20	0.20	-
Edge Columns ϕ (m)	0.25	0.25	-
Column Height (m)	0.70	0.70	-
Tower ϕ (m)	0.17	0.17	-
Tower Height (m)	2.70	2.59	-2.67
Pontoon Height (m)	0.14	0.14	-
Pontoon Length (m)	1.06	1.09	2.5
Pontoon Width (m)	0.25	0.25	0.10
Mooring point above bottom (m)	0.12	0.12	-
Draft (m)	0.39	0.38	-0.39
Roll Inertia about Center of Gravity ($kg.m^2$)	137.50	140.99	2.48
Pitch Inertia about Center of Gravity ($kg.m^2$)	137.05	141.08	2.85
Yaw Inertia about Center of Gravity ($kg.m^2$)	74.61	76.07	1.91

(a) SolidWorks model. **(b)** Physical built model.

Figure 3.10: Models of the VolturnUS-S in 1:50 scale.

The layout of the FloWave tank is shown in Figure 3.11. The points labelled A_i where $i \in \{1,2,3\}$ mark the anchor positions, in this case, they are the attachment points to pulleys positioned on the tank floor. The points labelled P_i correspond to the fairlead positions when the system is at equilibrium.

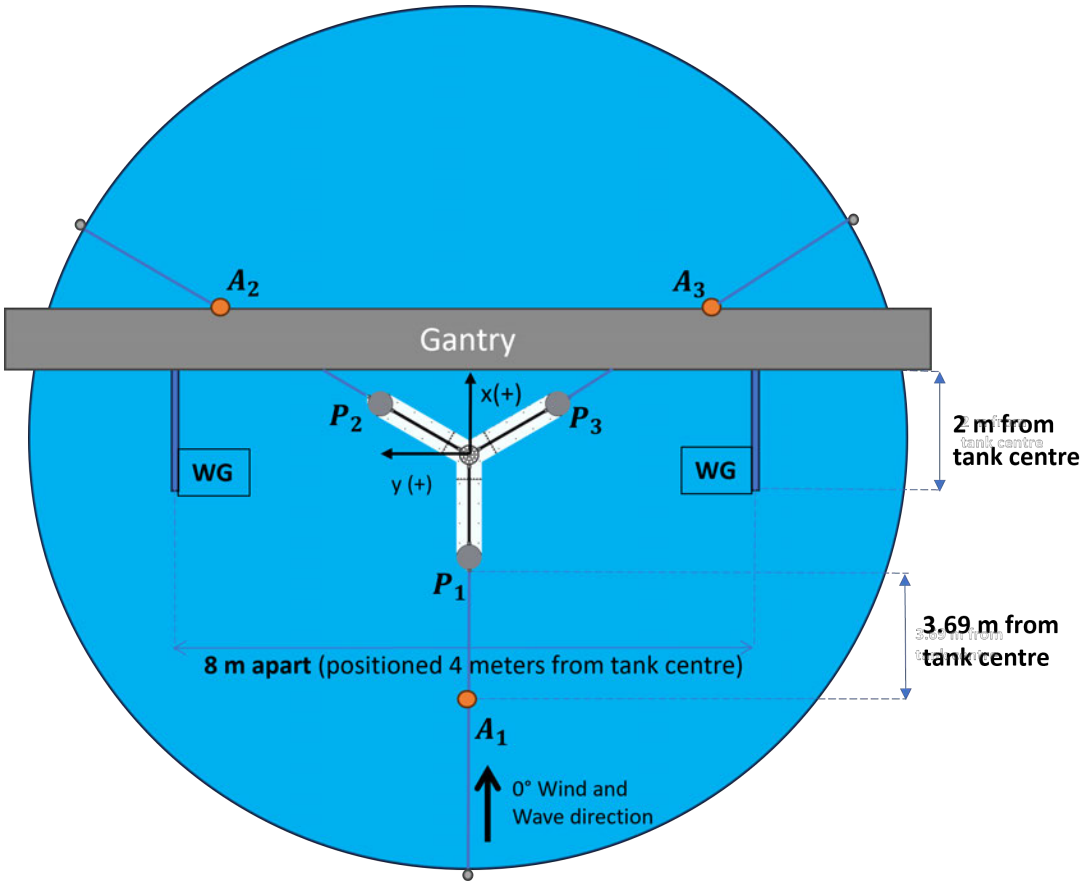

Figure 3.11: Schematic of the tank test set-up at FloWave.

The body's centre of gravity is aligned with the origin of the reference system O_{xy}. In regard to z coordinate, $z = 0$ at the water level which corresponds to, approximately, 0.38 m from the bottom of the floating structure as shown in Figure 3.12. The signal convention used follows the right-hand rule, where x is positive towards the downwind direction, consequently y is positive to the left and z is positive upwards. WG corresponds to the positions of the two wave gauges used.

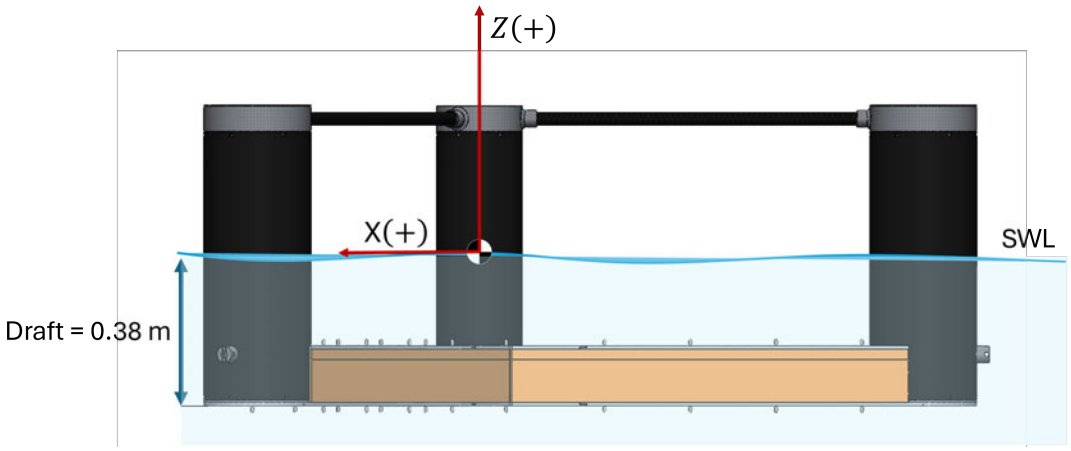

Figure 3.12: Visualisation of the location of the centre of gravity of the scaled model.

3.3.5 Simulation Length

Two types of simulations were conducted: numerical simulations using OpenFAST and physical testing in FloWave. Both types of simulations will have the analysis duration for identical wave conditions. The duration has been carefully selected to effectively capture the dynamics of the structure, including initial transients. In the tank tests, this transient phase corresponds to the system transitioning from a static equilibrium to a dynamic response under wave loading. In OpenFAST, the transients arise from the numerical start-up, where the system begins at rest without environmental loads at $t = 0$, and then transitions to dynamic equilibrium.

3.3.6 Wind field

The wind conditions tested during the three tank tests correspond to steady wind conditions, where the wind speed is maintained relatively constant along the hub height (150 m). These wind conditions are calculated in TurbSim using the Power Law. In the physical testing, the resultant thrust for steady wind conditions is used as the input for the actuation system. The steady wind conditions tested include wind speeds of 8 m/s (under-rated), 11 m/s (rated), and 22 m/s (above-rated), along with their corresponding mean thrust values.

In this project, turbulence in the wind field is not included. The objective of this study is to assess the required level of aerodynamic load complexity in physical model testing, beginning with the most fundamental representation of wind loading. By excluding turbulence, the applied loads remain deterministic and directly comparable across numerical and experimental configurations. This enables clear isolation of the structural and hydrodynamic response to mean thrust alone, without the additional variability introduced by stochastic inflow effects.

Including turbulence would introduce broadband excitation, dynamic load fluctuations, and increased response variability, potentially obscuring the specific influence of thrust-only actuation that this work aims to evaluate. The simplified steady-wind assumption therefore serves as a controlled baseline case.

3.3.7 Waves

According to IEC61400-3-1 (IEC), the recommended simulation length for offshore wind turbine analysis is one hour, with additional time to accommodate transient effects. At a 1:50 model scale, this corresponds to 509 seconds. DNV-RP-C205 (Veritas, 2025) similarly notes that for structures with slower response characteristics, environmental conditions are typically assumed stationary over reference periods of 1 or 3 hours. Applying such durations uniformly to all regular-wave cases would significantly increase the tank test programme without necessarily improving the statistical robustness of deterministic wave tests.

To evaluate the minimum duration required for reliable response estimation, guidance from the EuropeWave programme (EuropeWave, 2024), based on IEC TS 62600-103 (IEC, 2018), was considered. These guidelines recommend including at least 50 wave cycles for regular waves and 250 wave cycles for irregular long-crested waves. Table 3.6 presents the corresponding simulation lengths across the range of tested wave periods.

The purpose of Table 3.6 is to demonstrate how the minimum required duration varies with wave period when applying cycle-based recommendations. While this approach ensures statistical adequacy for each individual case, implementing wave-period-dependent simulation lengths would introduce operational complexity and inefficiencies during physical testing.

For practical implementation, simulation lengths were therefore standardised according to wave type rather than wave period. Regular wave tests were conducted for 15 minutes full-scale (128 seconds at 1:50 scale), while irregular long-crested wave tests were conducted for 60 minutes full-scale (509 seconds at 1:50 scale). These durations satisfy, and in most cases exceed, the minimum cycle-based requirements across the tested wave conditions, while maintaining efficient use of tank time and ensuring statistically meaningful results.

3.3.8 Application of aerodynamic loads in the wave basin

One objective of this study is to compare alternative methods for applying aerodynamic loads during tank testing of FOWTs. For tractability, only the rotor thrust, F_x, is considered, as it is the most influential load on platform dynamics (see Section 2.4). At the outset of the chapter, it is clarified that wind effects are introduced by imposing an equivalent aerodynamic load on the structure rather than physically generating wind in the basin, a standard approach supported by prior studies discussed in Section 2.4.

Table 3.6: Simulation lengths for regular and irregular waves at 1:50 Scale and Full-Scale.

1:50 scale		Full-scale	
Regular Waves (50 wave cycles)			
Wave Period (s)	Length (s)	Wave Period (s)	Length (s)
0.67	34	4.74	237
0.99	49	6.98	349
1.30	65	9.22	461
1.62	81	11.46	573
1.94	97	13.69	685
2.25	113	15.93	797
2.57	128	18.17	909
2.89	144	20.41	1021
3.15	157	22.25	1113
3.41	170	24.10	1205
3.67	183	25.94	1297
3.93	196	27.78	1389
3.96	198	28.00	1400
Irregular Waves (250 wave cycles)			
Wave Period (s)	Length (s)	Wave Period (s)	Length (s)
1.63	408	11.53	2881
1.98	495	14.00	3500
2.55	638	18.03	4508

Geometrical and performance scaling of the rotor blades is not included in either method, as FloWave does not have wind generation capabilities, and aerodynamic thrust is applied directly in the simulations, eliminating the need for full rotor modelling. As a result, blade frequency loads such as the 1P and 3P excitations cannot be reproduced. Flexible modes of the FOWT, such as tower bending, were beyond the scope of this investigation, and the model was treated as a rigid body. The RNA mass was scaled appropriately, and the overall system moments of inertia were preserved as closely as possible.

Across the three tank-test phases, different actuation methods were employed, in increasing order of complexity: (i) a static weight, (ii) a constant-thrust winch, and (iii) a software-in-the-loop (SIL) winch. The three wind conditions simulated in this study correspond to below-rated (8 m/s), rated (11 m/s) and above-rated (22 m/s) wind speeds. When examining the thrust curve presented by the reference document (Bortolotti et al., 2020) and presented in this document in Figure 3.13, the thrust value may be around 1 to 1.5 MN for 8 m/s wind speed and at rated speed and above the thrust remains constant at 2.25 MN.

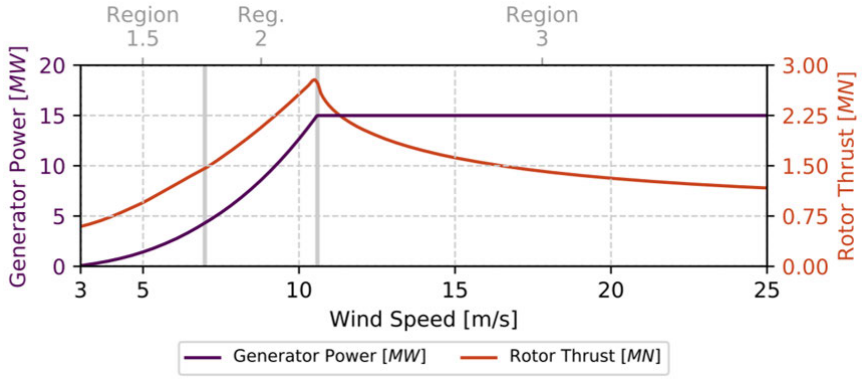

Figure 3.13: Power and thrust curve for the IEA 15 MW WT. Adapted from Bortolotti et al. (2020).

However, the rotor thrust on a wind turbine can vary significantly with the pitch rotation of a floating platform due to changes in the aerodynamic forces experienced by the blades. When the platform pitches forward or backward, it alters the angle at which the wind approaches the rotor blades, known as the angle of attack. These changes affect the lift and drag forces acting on the blades, leading to variations in rotor thrust. Pitching forward decreases this angle, potentially reducing thrust, while pitching backwards increases it, potentially increasing thrust load on the rotor. Additionally, the dynamic inflow effects caused by the pitching motion can introduce transient aerodynamic phenomena that further influence thrust. The uneven distribution of wind across the rotor disk during pitching can also lead to asymmetrical thrust forces, impacting the structural loads and performance of the turbine.

To account for these effects, simulations in OpenFast were conducted for both regular and irregular waves under steady wind conditions, and the mean rotor thrust values were obtained for three different wind speeds. These results are presented in Table 3.7, showing values at a 1:50 scale and at full-scale including the 2.4% fresh water correction. The values were rounded to the nearest integer because targeting the decimal component in various methods of aerodynamic load actuation would not be feasible and could cause additional complexity due to slight variations with changing wave conditions.

In regard to the extreme wind conditions, OpenFast simulations were also conducted for the 1-year and 50-year return period sea states with corresponding steady wind speeds of 25 m/s and 40 m/s. The mean rotor thrust for a 40 m/s wind speed was relatively small at a 1:50 scale, with values ranging between 0.5 and 0.8 N. Consequently, this sea state would not be tested for the coupled analysis and comparison between the load actuation methods. However, the results for this sea state are still useful for comparing displacements and mooring tensions.

With the values of rotor thrust determined, the three different methods of load actuation needed to be designed to match these values.

	Wind Speed (m/s)	Rotor Thrust (N)
	1:50 scale	
Under-rated	1.13	14
Rated	1.56	20
Over-rated	3.11	9
1-yr	3.54	8
50-yr	5.66	0.5 - 0.8
	Full-scale	
Under-rated	8	1,786,000
Rated	11	2,434,000
Over-rated	22	1,198,000
1-yr	25	1,058,000
50-yr	40	83,000

Table 3.7: Wind speeds and correspondent rotor thrust values acquired from OpenFast simulations at full-scale and at 1:50 scale.

The deployment of the wind actuation methods for Phase II and Phase III was carried out in close collaboration with Dr Thomas Davey, while the BEM code implemented in Phase III was developed by Dr Callum Guy.

Phase I: Static weight

In Phase I, an equivalent constant rotor thrust is imposed using a suspended static weight routed over a low-friction sheave and applied to the model at hub height (see Figure 3.14). For a target mean thrust F_T, the required mass is

$$m = \frac{F_T}{g}, \tag{3.23}$$

where the line tension (neglecting small losses) equals the desired thrust.

Figure 3.14: Static weight rig used in Phase I to impose an equivalent constant rotor thrust. A dead-weight is suspended and routed over a low-friction sheave to the model at hub height, producing a steady horizontal line load with tension $\approx F_T$ (Eq. 3.23).

This choice is motivated by simplicity, repeatability, and traceable calibration. A dead-weight provides a low-cost means of imposing the mean aerodynamic thrust without introducing additional mechatronic dynamics or control behaviour, making it suitable for baseline tests and instrumentation checks.

The setup accomplishes the isolation of the platform's response to a constant horizontal load applied at the correct point of action (hub height/shaft line). It enables assessment of mean offsets and low-frequency motions due to thrust alone, independent of rotor, controller, or inflow variability.

The approach intentionally simplifies the problem by removing aeroelastic and control couplings: there is no thrust modulation from turbulence, rotor speed variations, or platform–wind interactions; no torque or gyroscopic effects; and no controller dynamics. Practical considerations include aligning the line to minimise vertical components and accounting for sheave friction.

Equation 3.23 was applied for all the rotor thrust forces, in tank scale, referred to previously and are shown in Table 3.8.

Table 3.8: Target thrust and corresponding weights for the various wind conditions in tank scale.

Wind Condition	Thrust (N)	Weight (kg)
Below-rated	9	1.0
Rated	19	2.0
Above-rated	14	1.5
1-yr	8	0.8

It is important to note that although the hanging mass is intended to represent a constant thrust, the applied line force is not strictly static. When the platform moves, the suspended mass undergoes acceleration, such that the line tension satisfies

$$T = mg - ma,$$

where a is the vertical acceleration of the mass relative to an inertial frame. Consequently, dynamic motion of the platform induces inertial fluctuations in the applied thrust through the term ma. The hanging-mass system therefore introduces an additional dynamic coupling between platform motion and applied load.

In contrast, the closed-loop PI-controlled winch in Phase II actively regulates the measured line tension to maintain the prescribed set-point. The inertia of a suspended mass is therefore absent, and the actuator compensates for motion-induced variations by adjusting motor torque. The PI system thus aims to apply a truly constant force, removing the secondary dynamic effects inherent to the static weight configuration.

Phase II & III: Actuator design

In Phases II and III, a motorised winch acted as the load actuator at hub height. In Phase II it maintained a constant thrust set-point via closed-loop control using an in-line load cell while in Phase III it applied a time-varying thrust $F_T(t)$ generated by the SIL model to capture dynamic effects.

Winch system components

The system was adapted from an existing rig and comprises a motorised winch, an in-line load cell, sheaves/fairleads, and a controller. In Phase II (constant-thrust mode), the controller closes a feedback loop on measured line tension to track a prescribed set-point F_T^*. The error $e(t) = F_T^* - F_{\text{meas}}(t)$ is used to command the winch to pay in or out, compensating for line stretch, rig friction, and slow geometry changes so that $F_{\text{meas}} \approx F_T^*$ is maintained despite platform motion. This delivers a steadier mean thrust than the static weight method while still representing only the steady component of the aerodynamic load. In Phase III (SIL mode), the same hardware applies an unsteady thrust $F_T(t)$ computed in real time by the aerodynamic model, introducing the coupled effects absent in Phase II.

The main constituent parts of the winch system are:

1. Control cabinet (see Figure 3.15a) which includes:
   (a) Electronic motor controller
   (b) Power transformer
   (c) Fan for cooling purposes
2. Load cell (see Figure 3.15b)
3. Data acquisition system (see Figure 3.15c)
4. Electric motor with spindle, rope and encoder (see Figure 3.15d)

The electronic motor controller deployed here was a Maxon Driver Escon 50/5, 4-quadrant pulse width modulation (PWM) servo controller for the control of the brushless EC motor used in the winch. By using the software supported by the driver, Escon Studio, the motor's properties can be set. The power transformer is a critical component in providing the necessary and stable power supply to various parts of the winch system, including the motor. It transforms the supply voltage (which is typically a higher AC voltage, l230 V, into a safe and usable 24 V DC voltage. A fan was also installed in order to keep the motor operating at safe temperatures.

A FUTEK LSB210 load cell with a rated capacity of $10\ \text{lbf}$ ($\approx 44.5\ \text{N}$) was used. This capacity was selected because the expected force did not exceed $44\ \text{N}$, providing headroom while maximising measurement resolution. Data acquisition and control used National Instruments hardware: a cDAQ-9171 USB single-slot chassis for sensor interfacing and a cRIO-9082 real-time controller with an integrated field-programmable gate array (FPGA) for deterministic closed-loop thrust control and logging.

A 160 W Maxon EC brushless motor was selected as the actuator. Sizing was based on the required line–force envelope at the fairlead (9–20 N). With the winch rope on a 30 mm spindle ($r = 0.015\ \text{m}$), the spindle torque is

$$T = F\,r, \tag{3.24}$$

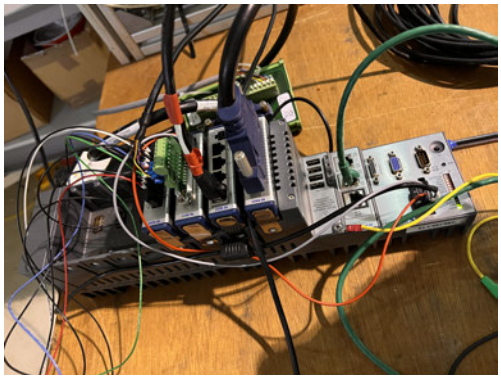

(a) cRIO chassis equipped with C Series I/O modules.

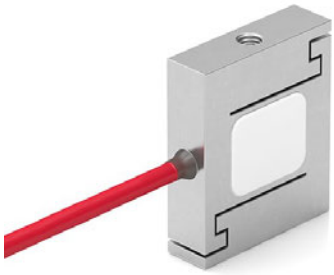

(b) FUTEK LSB210 load cell.

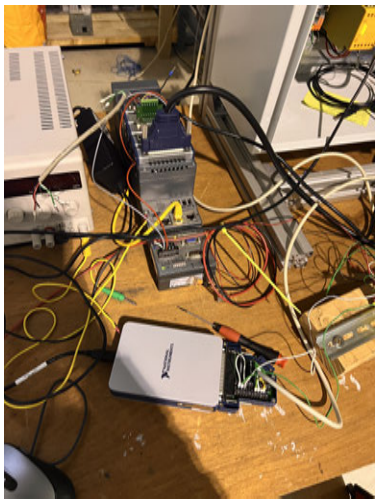

(c) Data acquisition system hardware.

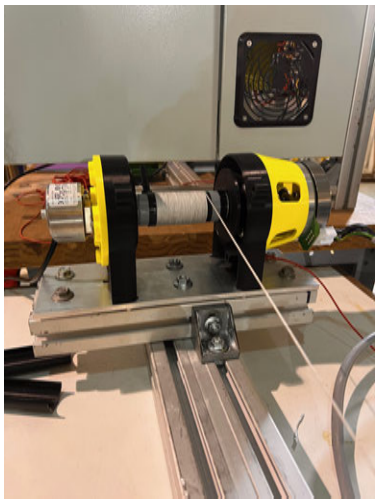

(d) Winch.

Figure 3.15: Hardware components of the winch system at FloWave.

giving $T_{\max} = 20 \times 0.015 = 0.30\,\mathrm{N\,m}$ and $T_{\min} = 9 \times 0.015 = 0.135\,\mathrm{N\,m}$. With the motor torque constant $K_t = 71.2\,\mathrm{mN\,m/A} = 0.0712\,\mathrm{N\,m/A}$,

$$I = \frac{T}{K_t} \;\Rightarrow\; I_{\max} \approx \frac{0.30}{0.0712} = 4.21\ \mathrm{A}, \quad I_{\min} \approx \frac{0.135}{0.0712} = 1.90\ \mathrm{A}. \tag{3.25}$$

The motor's continuous torque rating of $457\,\mathrm{mN\,m}$ ($0.457\,\mathrm{N\,m}$) exceeds $T_{\max}$ with margin, and the available 0–5 A current range covers $I_{\max}$. Allowing for losses and radius growth as layers build on the drum, a conservative design check is

$$T_{\mathrm{cont}} \geq \frac{F_{\max}\, r_{\mathrm{eff}}}{\eta}, \tag{3.26}$$

where r_{eff} is the maximum effective radius and η is the rig efficiency (typically 0.7–0.9).

Phase II: Constant thrust application

Phase II employed two actuator configurations. First, an open-loop (feedforward) approach was used to calibrate the mapping between motor current and applied line force (Fig. 3.16). A prescribed current command was converted to PWM, the motor drove the spindle (rope on a 30 mm drum), and the resulting force was measured with the in-line load cell. This provided an initial current–force relationship, but the applied force was sensitive to friction, line stretch, and effective drum radius.

Figure 3.16: Open-loop (feedforward) actuation used for current–force calibration: a pre-set current produces a nominal force based on prior calibration; no feedback is applied.

To maintain a truly constant thrust, a closed-loop force controller was then implemented. The calibrated in-line load cell (mounted between the winch and the fixed support as depicted in Figure 3.17) served as the process variable. The controller ran on the motor drive as a discrete-time PI loop at $10\,\mathrm{Hz}$ (tank scale, 1:50). Bench tuning was carried out in nine successive tests (Table 3.9) to obtain gains that delivered fast response, minimal overshoot, and negligible steady-state error under both step changes and constant-force holds. Results are reported in tank scale (1:50).

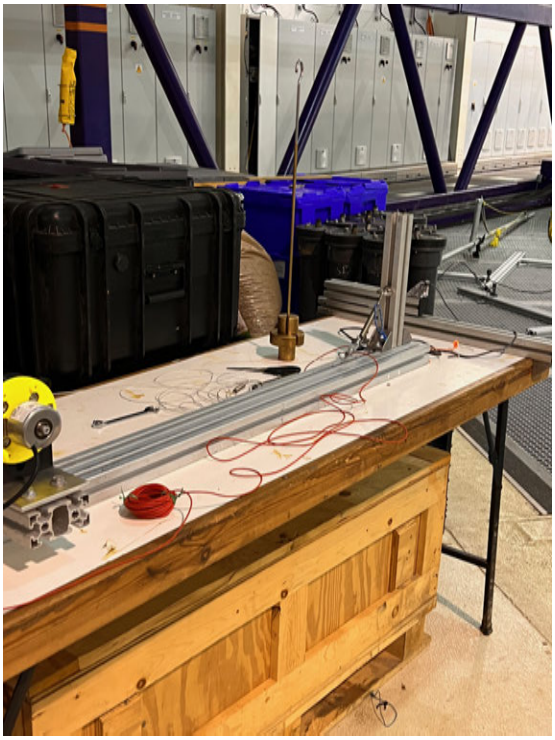

Figure 3.17: Experimental setup for PI tuning of the motor drive.

Each PI-tuning test consisted of two phases:

1. **Changing set-point phase.** Step changes in desired force (“Set point”) from near zero up to $20\,\mathrm{N}$ in $\approx 5\,\mathrm{N}$ increments; the resulting “Measured force” trace was recorded (see Fig. 3.18a).
2. **Constant set-point phase.** A single hold at $10\,\mathrm{N}$ or $20\,\mathrm{N}$ for $60\,\mathrm{s}$ to evaluate steady-state accuracy and low-frequency drift (see Fig. 3.18f).

Table 3.9: Summary of PI gain values and test types.

Test Nr	K_P	K_I	K_D	Changing Set-Point	Constant Set-Point
1	0.10	0	0	✓	–
2	0.20	0	0	✓	–
3	0.12	0	0	✓	–
4	0.14	0	0	✓	–
5	0.15	0	0	✓	–
6	0.075	0.70	0	–	✓
7	0.075	0.70	0	✓	–
8	0.075	0.75	0	–	✓
9	0.075	0.75	0	✓	–

Tests 1–5 (P-only) showed several-newton offsets on long holds and increasing overshoot at higher K_P. With $K_P = 0.075$, $K_I = 0.70$ (test 6), the $20\,\mathrm{N}$ hold offset was nearly eliminated, though step undershoot appeared in test 7. Increasing to $K_I = 0.75$ (tests 8–9) removed steady-state error and yielded crisp, well-damped steps with negligible overshoot.

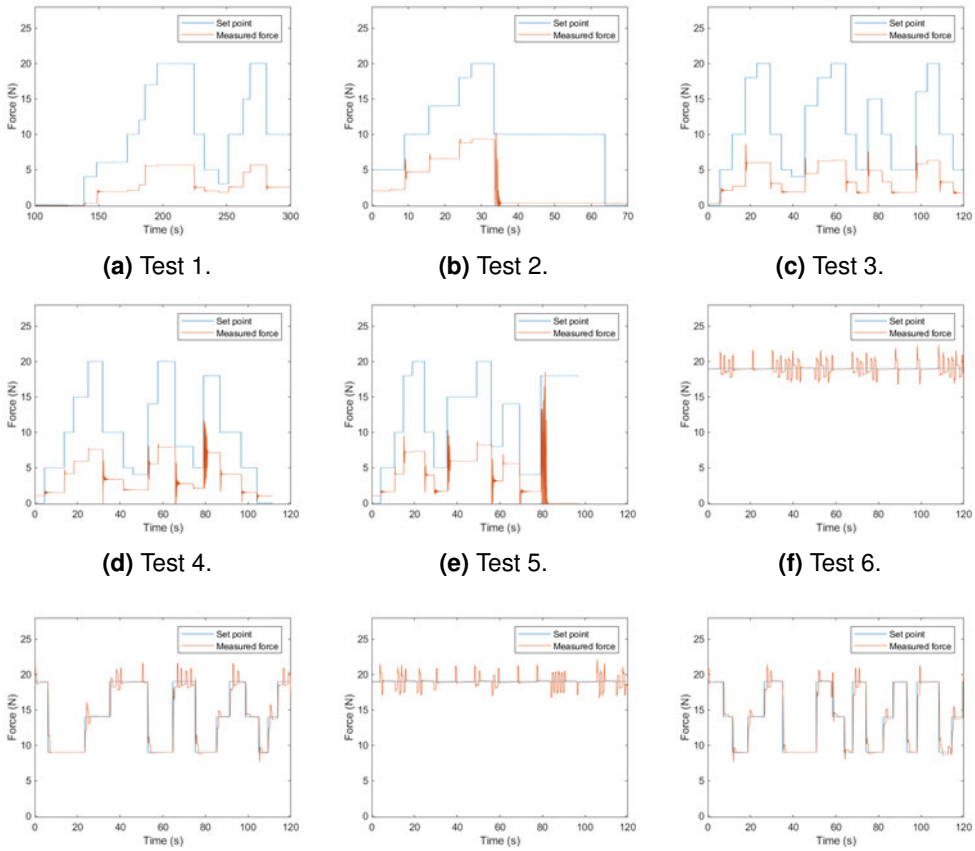

(a) Test 1. **(b)** Test 2. **(c)** Test 3.

(d) Test 4. **(e)** Test 5. **(f)** Test 6.

(g) Test 7. **(h)** Test 8 **(i)** Test 9

Figure 3.18: PID tuning results in tank scale (1:50).

The final tuning used for all subsequent trials was

$$K_P = 0.075, \qquad K_I = 0.75, \qquad K_D = 0,$$

which provided fast, stable tracking of both step and sustained force commands.

Phase III: Software-in-the-loop (SIL) thrust actuation

In Phase III, the commanded thrust is time-varying and generated in real time by an in-house blade-element–momentum (BEM) model. The closed-loop arrangement is shown in Fig. 3.19: the SIL model updates the thrust set-point $F_T(t)$, and a PI force controller tracks this set-point using the load-cell measurement.

The BEM solver (in Python) takes as inputs the hub translational velocities in x, y, z (m/s), the instantaneous collective pitch angle, and the tower tilt. It updates the apparent inflow (including a correction for platform pitch) and returns rotor thrust to be used as the force set-point $F_T(t)$. Tower aerodynamic drag is not modelled in the present implementation.

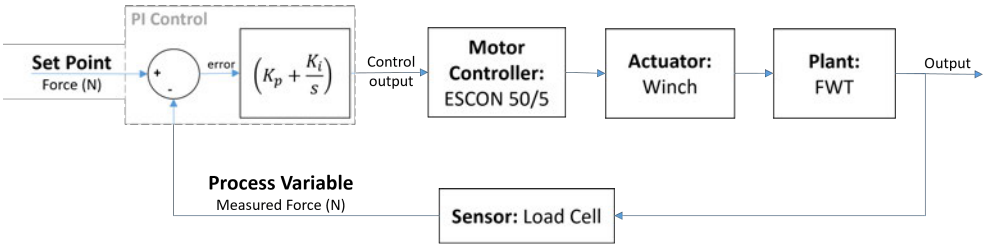

Figure 3.19: SIL closed-loop force-control scheme. A real-time BEM model supplies the time-varying thrust set-point $F_T(t)$ (in N). A PI controller with gains K_p and K_i (running at $10\,\mathrm{Hz}$ tank scale) computes the motor current command $I_{\mathrm{cmd}}(t)$ (in A), which is converted to PWM to drive the winch. The winch/spindle apply the line force at hub height; the in-line load cell measures $F_{\mathrm{meas}}(t)$ and feeds it back to close the loop.

Qualisys motion capture provides the platform kinematics to the host PC where the system's displacements are streamed in real time, hub velocities are computed and scaled to full scale, and these are passed to the BEM code. The resulting full-scale thrust $F_T(t)$ is down-scaled to basin scale (1:50) and supplied as the set-point to the closed-loop force controller on the cRIO/FPGA, which drives the winch motor. The in-line load cell at hub height measures the applied force and feeds it back to the controller, closing the loop. An overall schematic of the DAQ/actuator interconnections is provided in Appendix B.

The controller runs on a National Instruments cRIO-9082 with LabVIEW 2019 (32-bit). Due to this LabVIEW version only supporting Python 3.6 on the RT target, the BEM environment was constrained to Python 3.6. Qualisys LabVIEW Client (QLC) was integrated to stream kinematics with low latency. QLC v22 requires newer LabVIEW versions, consequently the QLC VIs were back-ported using so that they could run under LabVIEW 2019 on the cRIO.

Host–RT communication uses Network-Published Shared Variables (NPSVs). For bench dynamic tests, the variables were configured to use the latest value (buffering disabled); the same mechanism is used during SIL runs to stream $F_T(t)$ to the FPGA force controller. The discrete-time PI controller (gains from Phase II) executes at $10\,\mathrm{Hz}$ (tank scale), commands motor current (converted to PWM), and tracks the load-cell measurement to minimise steady-state error and follow the time-varying thrust.

As with any closed-loop, force-controlled actuation, the SIL configuration introduces a finite time delay between the commanded thrust and the realised line force. This delay arises from a combination of signal acquisition, communication, computation, and actuator dynamics.

In the present system, the dominant contribution is associated with the motor–drive and mechanical response of the winch assembly rather than computational overhead. The effective latency was experimentally characterised and its impact on phase behaviour is quantified in Section 5.1.1. Here it is sufficient to note that this delay introduces a phase lag in the applied thrust, particularly at higher excitation frequencies, and therefore influences the dynamic fidelity of the SIL configuration.

Standalone comparisons of the in-house BEM against AeroDyn module from OpenFast were performed over a set of operating points spanning below-rated to above-rated conditions (see Table 3.10.

Table 3.10: Operating points used for BEM–AeroDyn comparison and SIL setup.

Wind speed (m/s)	Blade pitch (deg)	Rotor speed (RPM)
3	4.50	5.00
5	3.50	5.00
10	0.00	7.00
15	11.50	7.50
20	18.00	7.50
25	22.00	7.50

Across the six matched cases tabulated in Table 3.11, the BEM thrust predictions were within $+2.8\%$ to $+4.4\%$ of AeroDyn (mean absolute percentage error 3.6%). Power-coefficient differences were modest and thrust-coefficient differences were below 2% on average. Per-step runtime measurements (Table 3.12) show microsecond-level evaluation for the BEM versus millisecond-level for `AeroDyn`, corresponding to $\sim 4.6 \times 10^3$–1.9×10^4 speed-ups depending on operating point.

Table 3.11: BEM vs. `AeroDyn` outputs for matched operating points.

	BEM code (outputs)			`AeroDyn` (outputs)		
Wind (m/s)	Rotor thrust (N)	C_P	C_T	Rotor thrust (N)	C_P	C_T
3	181,505	0.073	0.728	174,706.58	0.073	0.723
5	525,571	0.434	0.759	511,348	0.450	0.763
10	2,188,692	0.488	0.790	2,128,360	0.490	0.798
15	1,303,931	0.175	0.209	1,259,641	0.179	0.209
20	945,370	0.071	0.085	905,848	0.072	0.084
25	1,057,130	0.051	0.061	1,015,903	0.052	0.060

Table 3.12: Per-step runtime (single time-step evaluation).

Wind (m/s)	BEM (s)	`AeroDyn` (s)
3	1.20×10^{-6}	6.43×10^{-3}
5	1.10×10^{-6}	9.31×10^{-3}
10	1.40×10^{-6}	6.37×10^{-3}
15	7.00×10^{-7}	7.09×10^{-3}
20	9.00×10^{-7}	1.74×10^{-2}
25	1.00×10^{-6}	8.42×10^{-3}

3.3.9 Mooring System Design

For the purposes of this work, two key scaling challenges must be addressed when designing mooring systems for tank testing. These challenges can be summarised as follows:

1. **Scaling mooring geometry to fit within the tank dimensions:**
   The size, shape, and depth of the wave tank significantly impact the scaling of the mooring system and the allowable platform excursions. This is particularly challenging for catenary moorings, which require much larger footprints and line lengths compared to tensioned moorings. Adjustments, such as truncating the mooring lines, are often necessary to make the geometry fit within the physical limits of the tank (Molins et al., 2015; Qiao and Ou, 2014).
2. **Selecting materials to replicate scaled line properties:**
   A common solution in wave basin testing is the combined use of springs and ropes to achieve the desired axial compliance. In this configuration, the mooring system's restoring force primarily depends on the spring's extension. For catenary systems, materials like lead wires or iron chains are also used to simulate the weight of the mooring lines (Yang et al., 2024). The main difficulty lies in maintaining consistent scaling across all material properties. Prioritisation of certain properties is often required, depending on the objectives of the test and the specific mooring system being modelled (Berthelsen et al., 2016).

Due to these constraints, scaled models in tank testing cannot perfectly replicate all aspects of the full-scale response, and compromises must be made.

For this study, the reference water depth was set to 200 m to represent the site off Haugesund, where depths range from roughly 100 to 200 m. Replicating this at FloWave required special consideration because the tank depth is only 2 m. Under Froude scaling this would imply a model scale of about 1:100 to match the 200 m depth. Even more restrictive, however, is the horizontal footprint of the spread mooring: the scaled anchor radius and inter-line spacing would still exceed the available plan area, and the line touch-down arcs and catenary geometry could not be preserved. Consequently, both depth and spread cannot be reproduced simultaneously within the basin.

To address these limitations, a truncated (surrogate) mooring system was adopted. Anchor locations were brought inboard to the tank perimeter and the line layout was modified, while line properties were adjusted so that, at the fairleads, the surrogate reproduces the full-scale working point (pretensions and angles) and the linearised restoring behaviour in surge, sway, and yaw over the target offset range.

Novel approach

The mooring system is designed to replicate the stiffness matrix of the full-scale catenary system using a tensioned spring-rope configuration. This design ensures that the scaled mooring system accurately captures the essential stiffness characteristics, while remaining practical within the physical constraints of the FloWave wave basin.

The mooring stiffness matrix provides the coefficients that define the reactionary loads of the mooring system in each degree of freedom resulting from applied displacements and rotations. It provides information on the slow drift response of a floating body under second-order waves and it also contributes to the numerical calculation of a body's RAOs (Pessoa et al. (2012)).

The mooring stiffness matrix itself is a linearised numerical representation of the physical mooring system, often taken when the floating body is in static equilibrium. It therefore has its limitations, especially when dealing with dynamic and non-linear behaviours. In reality, the behaviour of mooring systems can exhibit non-linearities, especially under large deformations or extreme loading conditions. Despite these limitations, the mooring stiffness matrix remains a valuable tool for representing the mooring system's influence on a body's hydrodynamic response.

Numerous studies have been published on analytic methods for deriving the mooring stiffness matrix, as summarised in Table 2 of Amaral (2020). These methods vary in the calculation of restoring forces and the DOF for which the stiffness coefficients are defined. The primary advantage of using an analytical method is that it provides developers with a quick and easy way to incorporate mooring dynamics into the design of floating systems.

Analytic formulation

One such analytical method to derive the mooring stiffness matrix that is referred to throughout this section is the work presented by Amaral (2020). This approach develops a 6-DOF closed-form analytical formulation to acquire the mooring system restoring forces. One of the contributions of Amaral (2020) is the development of a general analytical formulation that can be applied not just for the system's equilibrium position but also to a wide range of scenarios with any arbitrary mooring line configuration.

This methodology is defined by four main steps; first the generalised coordinates for the problem are assessed, the system is geometrically defined and the geometric relations of the mooring lines are set. The problem is then focused on the assessment of the restoring force for one mooring line and its decomposition in the vertical and horizontal planes. The formulation considers a conservative system where the friction forces were neglected. This way, the mooring line restoring forces are described as functions of the positions only. Also, the effect of any currents on the mooring line were neglected.

The system is then linearised around a generic position in order to acquire the complete mooring system stiffness matrix. Lastly, individual segments of the mooring line are considered and the tension is calculated for each one of the segments as function of horizontal and vertical distances between anchor and fairlead. It is only at this step, that the specific configuration of the mooring system becomes significant. The procedure for evaluating the mooring stiffness coefficients as laid out by Amaral (2020) is illustrated in 3.20. This particular formulation offers the advantage that only the translational stiffness coefficients require definition, as all the others are functions of these and the system geometry. Further simplifications are introduced when considering a symmetrical mooring.

Amaral (2020) demonstrated this approach using a case study of the OC4-DeepCwind mooring configuration, which features an equidistant three-spread mooring system. Each mooring line in this system is represented as a single-segment mooring chain with a catenary shape. The formulations for non-null stiffness coefficients are presented in Equations 3.27 to 3.34, where l is the radius from the platform vertical central line to the fairleads, $k_{HH} = \left[\frac{\partial F_H}{\partial h_f}\right]_{q_0}$, $k_{VV} = \left[\frac{\partial F_V}{\partial v_f}\right]_{q_0}$ and $k_{HV} = \left[\frac{\partial F_H}{\partial v_f}\right]_{q_0}$ are the horizontal, vertical and coupled local stiffness and $\overline{k}_{HH} = \frac{F_H(h_f^0, v_f^0)}{h_f^0}$ is the so called horizontal "string stiffness", see Amaral et al. (2022).

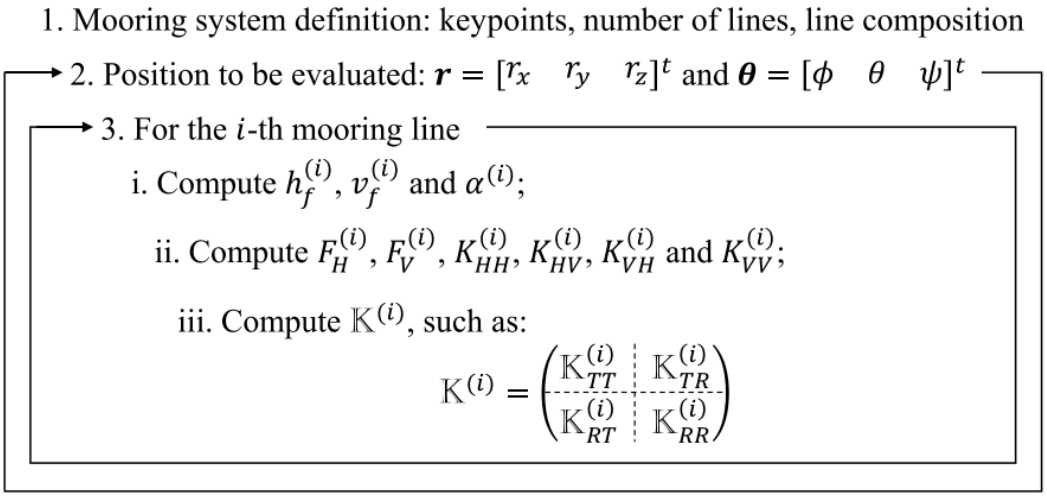

Figure 3.20: Step-by-step procedure for the mooring system stiffness matrix calculation. (Reproduced from Amaral et al. (2022) with permission from Elsevier).

$$K_{11} = \frac{3}{2}(k_{HH} + \bar{k}_{HH}) \tag{3.27}$$

$$K_{15} = K_{51} = \frac{3}{2}(k_{VH}R_f + k_{HHp\zeta} + \bar{k}_{HHp\zeta}) \tag{3.28}$$

$$K_{22} = \frac{3}{2}(k_{HH} + \bar{k}_{HH}) \tag{3.29}$$

$$K_{24} = K_{42} = -\frac{3}{2}(k_{VH}R_f + k_{HHp\zeta} + \bar{k}_{HHp\zeta}) \tag{3.30}$$

$$K_{33} = Nk_{VV} \tag{3.31}$$

$$K_{44} = \frac{3}{2}(p_\zeta^2 k_{HH} + p_\zeta^2 \bar{k}_{HHp\zeta} + 2p_\zeta R_f k_{HV} + R_f^2 k_{VV} + R_f F_H - 2p_\zeta F_V) \tag{3.32}$$

$$K_{55} = \frac{3}{2}(p_\zeta^2 k_{HH} + p_\zeta^2 \bar{k}_{HHp\zeta} + 2p_\zeta R_f k_{HV} + R_f^2 k_{VV} + R_f F_H - 2p_\zeta F_V) \tag{3.33}$$

$$K_{66} = N\bar{k}_{HH}R_f^2(1 + \frac{h}{R_f}) \tag{3.34}$$

In the present document 'local stiffness' refers to the resistance of a specific part or segment of a structure to deformation, and it is particularly relevant when acquiring the linear stiffness coefficients in each DOF. 'Axial stiffness', on the other hand, is a measure of a material's resistance to deformation along its length when subjected to axial forces, such as tension or compression. In the context of mooring system analysis using software packages, e.g.

mooring dynamics modules that are part of the NREL's coupled aero-hydro-servo-elastic simulation tool OpenFAST NREL such as MoorDyn or MAP++, axial stiffness is a critical property of the mooring material, influencing the overall dynamics of the mooring lines under operational and extreme conditions.

Thus, while local stiffness focuses on the behaviour of specific segments in multiple directions, axial stiffness pertains to the longitudinal performance of mooring materials under axial loads. These definitions are crucial for understanding the subsequent application of the analytical formulations in the present work.

Application to the mooring system design

Firstly, the mooring stiffness matrix of the full-scale catenary mooring is found by using a numerical model and the coefficients within this matrix are Froude scaled for application in the wave basin. The coefficients of the scaled mooring stiffness matrix are then interpreted to inform the tank-scale mooring parameters such as the footprint and choice of spring stiffness.

The benefit of this approach is that all geometric contributions to the mooring stiffness are captured within the full-scale mooring stiffness matrix, including water depth. This ensures that the dimensions of the tank do not compromise the tank-scale mooring design. The one limitation of this approach is that any non-linear behaviour of the moorings will not be captured.

The overall four main steps to apply this method are shown in Figure 3.21 and explained in detail below.

Step 1

Acquire the full-scale linear mooring stiffness matrix, **M**, using the analytical formulation described in Section 3.3.9 and presented in Figure 3.20. Then scale **M** using Froude scaling based on the scale for wave tank deployment, designated as matrix **m**. The values located on the diagonal of the scaled linear mooring stiffness matrix, **K**, are the stiffness coefficients required for the next step.

Step 2

Step 2 consists of calculating the required spring-rope setup values: the local stiffness value of each mooring line, k; the horizontal distance from the centre of gravity (CoG) to the fairlead, R_f; and the vertical distance, h, from fairlead, $P^{(i)}$, to tank floor which consequently define the line declination angle, α. These parameters are constrained by the available working area and depth of the wave basin. An iterative approach may be needed to accomplish an acceptable result.

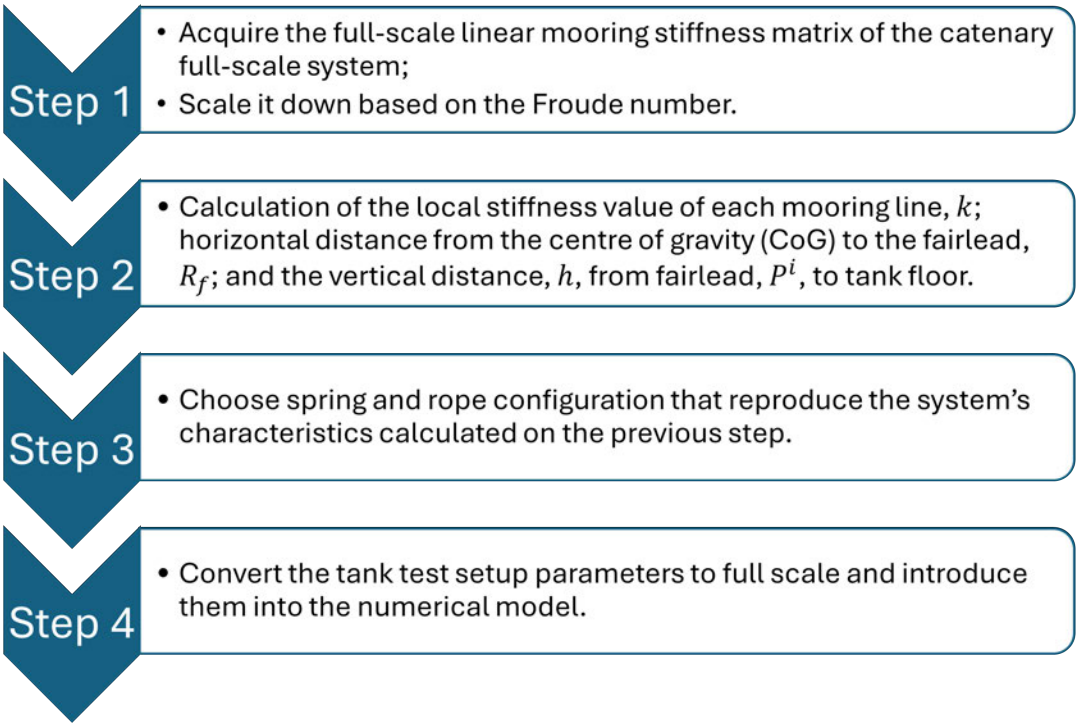

Figure 3.21: Methodology applied to convert a catenary mooring system into a spring-rope configuration for the testing of ORE devices in wave basins.

In accordance with the formulation presented by Amaral (2020), a perfect polar symmetric mooring system can be calculated analytically by the set of equations presented in Section 3.3.9. Of these equations, emphasis will be directed exclusively towards the determination of the mooring stiffness coefficients in surge, K_{11}, heave, K_{33}, and yaw, K_{66}, as these are the DOFs which at a minimum are required for the calculation of the local stiffness value of a singular mooring line.

Following Amaral (2020), the linear mooring stiffness value in heave, K_{33} is given by Equation (3.31). The K_{33} value in the equation is replaced by the value from the scaled mooring stiffness matrix, **M**. N represents the number of mooring lines. The resultant value for K_{vv} represents the 'vertical-vertical local stiffness'.

To find the 'horizontal-horizontal local stiffness value', k_{HH}, the 'horizontal–horizontal string stiffness' value, $\bar{k}_{HH}$ needs to calculated using Equation (3.34).

To determine the value of $\bar{k}_{HH}$, the horizontal distance from the centre of gravity (CoG) to the fairlead, R_f, and the vertical distance, h, from fairlead, $P^{(i)}$, to tank floor, as shown in Figure 3.22, need to be known.

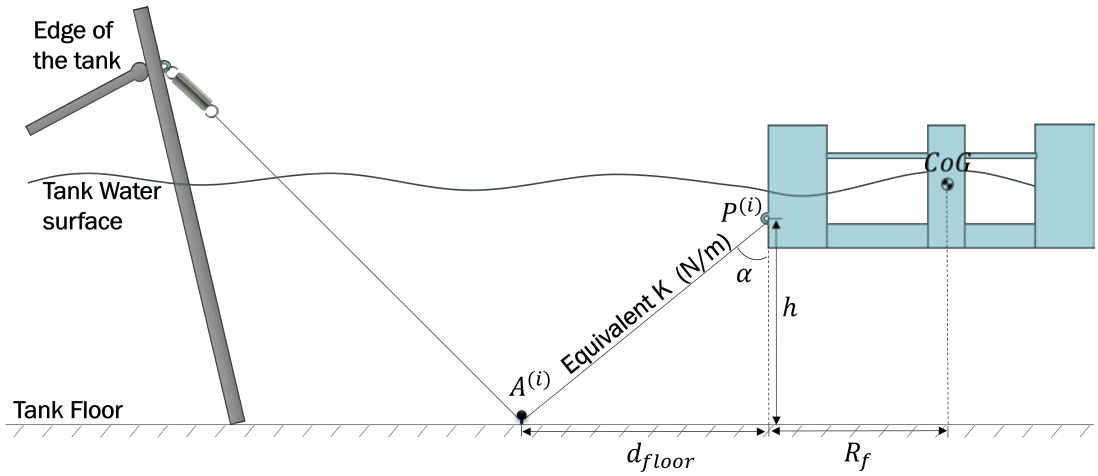

Figure 3.22: Illustration of the essential parameters required for the calculation of mooring line local stiffness. Where: $P^{(i)}$ and $A^{(i)}$ are the fairlead and anchor positions, k is the line local stiffness, and α is the line declination angle.

The choice of the R_f value is dependant on the available space on the tank floor to set up the mooring line. This value has to be scaled to full-scale and its coordinates introduced in the numerical mooring in order to check if the resultant linear stiffness matrix is maintained or is at least relatively close to the original, **M**.

This procedure involves an iterative approach represented in Figure 3.23, alternating between adjusting the declination angle at the fairlead α and assessing the resulting mooring linear stiffness matrix in order to ensure that it matches the stiffness matrix of the original catenary configuration, **M**. This analysis is performed using the specific configuration established in the tank setup, i.e. the values for anchor locations in the numerical model are the full-scale representation of the distances present in the wave basin.

The vertical distance from $P^{(i)}$ to the tank floor is determined by the depth of the tank and the fairlead location. With these two constants known, R_f and h, the $\bar{k}_{HH}$ is calculated using Equation (3.34).

Using Equation (3.27), the value of k_{HH} can then be calculated.

$$K_{11} = \frac{N}{2}(k_{HH} + \bar{k}_{HH}) \tag{3.35}$$

Finally, by applying the Pythagorean theorem with the 'horizontal-horizontal local stiffness' value, k_{HH} and the 'vertical-vertical local stiffness' value, k_{VV}, the value of the local stiffness, k of each mooring line can be calculated.

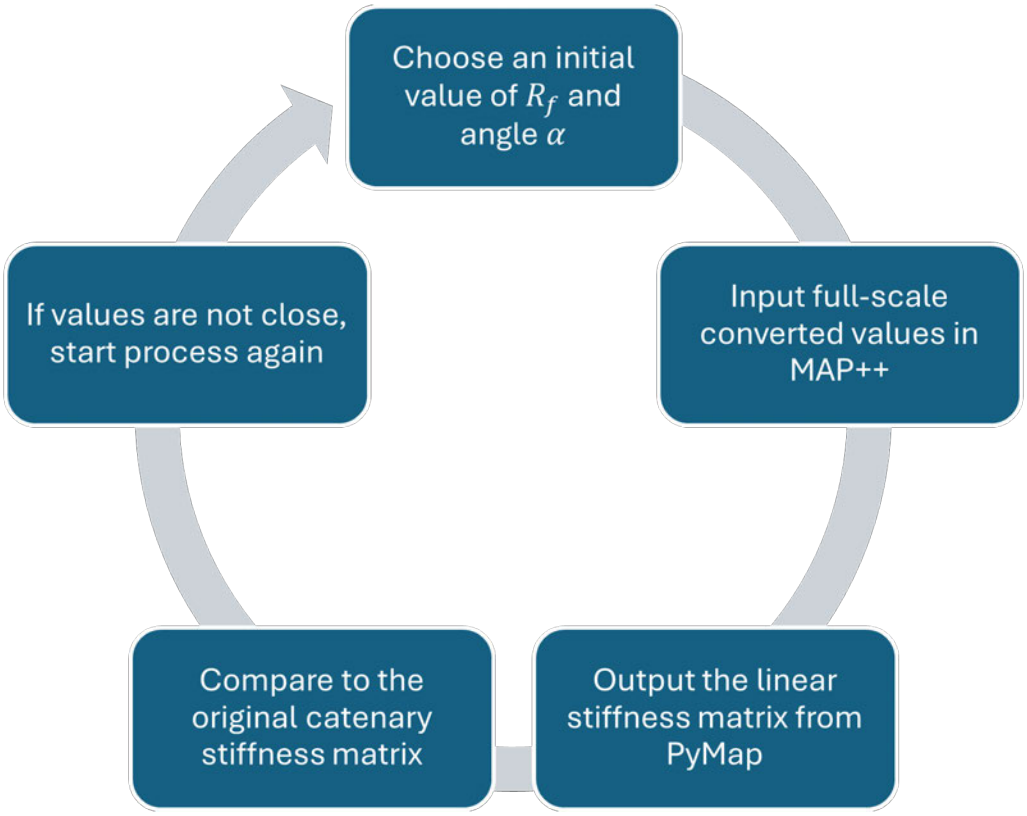

Figure 3.23: Iterative process used for the choice of the R_f.

Step 3

At this stage, with the local stiffness value of each mooring line known, the spring and rope configuration can be chosen in order to obtain that value in the physical experiment.

Step 4

Convert the tank test setup parameters to full scale. These parameters will then be used to tune the numerical model according to the experiment. Lastly, compare the natural frequencies between the tuned numerical model (referred to as the 'adapted system') and the original values with the catenary mooring configuration (referred to as 'catenary') to assess their similarity.

The results obtained using this method, along with an assessment of its quality and effectiveness, will be presented and discussed in the subsequent chapters.

3.4 Tank test plan

To evaluate the required level of wind load actuation complexity across operational, extreme, and misaligned environmental conditions, and to investigate system behaviour under both linear and nonlinear excitation regimes, the set of sea states adopted in the present work comprises:

1. Only waves:
   (a) Regular waves with frequency and amplitude sweep;
   (b) Set of regular and irregular waves with different peak periods;
   (c) Extreme conditions: 1-yr and 50-yr return period;
2. Waves and wind:
   (a) Regular waves with frequency and amplitude sweep:
      i. Under-rated wind speed, 8 m/s;
      ii. Rated wind speed, 11 m/s;
   (b) Set of regular and irregular waves with different peak periods:
      i. Under-rated wind speed, 8 m/s;
      ii. Rated wind speed, 11 m/s;
      iii. Over-rated wind speed, 22 m/s;
   (c) Extreme conditions: 1-yr and 50-yr return period:
      i. Extreme wind speed;
   (d) Misalignment of wind and waves:
      i. Irregular waves with different peak periods:
         A. Wind at 0 deg and wave at 30 deg;
         B. Wind at 30 deg and wave at 0 deg;

Testing the model under hydrodynamic loads alone allows for the acquisition of the uncoupled response of the structure and the validation of the hydrodynamic model, serving as a basis for comparison with scenarios involving wind loads. In the hydrodynamics-only tests, subjecting the model to regular waves enables the analysis of the system's linear response, including its behaviour at various external excitation frequencies. Introducing irregular and extreme waves exposes the model to more realistic conditions where non-linear effects, such as sum- and difference-frequency forces, are present.

When wind is introduced, the same wave scenarios are used in conjunction with three main wind speeds: below rated, at rated, and above rated. Comparing these results to the hydrodynamic-only cases reveals the impact of aerodynamic loads on the structure's dynamics, including its motions and mooring tensions. The three selected wind speeds represent operational conditions, capturing the scenarios where rotor thrust reaches its maximum.

3.4.1 Frequencies of interest

When testing a FOWT, it is crucial to identify the relevant frequencies in the system. These include excitation frequencies such as those from waves, wind, and rotor harmonics like 1P and 3P, as well as the system's natural frequencies in the primary six DOF and coupled modes.

System's natural frequencies

According to the reference document of the VolturnUS-S (Allen et al., 2020), the rigid body natural frequencies in full-scale are presented in table 3.13.

Table 3.13: Rigid-Body natural frequencies given in full-scale.

Rigid-Body Mode	Value	Units
Surge	0.007	Hz
Sway	0.007	Hz
Heave	0.049	Hz
Roll	0.036	Hz
Pitch	0.036	Hz
Yaw	0.011	Hz

Environmental Excitation Frequencies

In this study, the primary external excitation frequencies considered are the waves and wind. The wave excitation frequencies typically range from 0.05 Hz to 0.2 Hz, corresponding to wave periods between 5 and 20 seconds. These frequencies cover both operational and extreme sea states, making them relevant for FOWT dynamic analyses.

Wind excitation frequencies are generally associated with low-frequency variations due to wind gusts and turbulence, typically below 0.05 Hz. These low-frequency wind-induced loads can have a significant impact on the platform's surge and pitch motions.

Understanding the limits of these excitation frequencies is essential for ensuring that they do not coincide with the system's natural frequencies, which could result in resonance and amplify the platform's dynamic response.

Overall range of frequencies

In this study, rotor frequencies were not simulated because a physical rotor with blades was not modelled. Furthermore, flexible structural modes of the FOWT, such as tower bending modes, were not represented, as the tower used in the tank test campaigns was rigid. It is also recognised that using a constant force to simulate rotor thrust does not account for the coupling effects between aerodynamic and hydrodynamic loads. Among the methods investigated, only the SIL approach allows for consideration of these coupling effects. However, even this method is simplified, as it relies solely on Blade Element Momentum (BEM) theory.

3.4.2 Test plan

The tank testing plan outlines a series of experiments designed to evaluate the dynamic behaviour of the FOWT under various conditions. The objectives are to identify natural frequencies and damping, characterise linear responses (RAOs), assess performance in realistic irregular seas (including extremes), and examine wind–wave misalignment effects.

The complete plan is summarised in Tables 3.14, 3.15, 3.16, and 3.17. Values shown are full-scale targets and tank commands were obtained by Froude scaling (1:50). In the tables, H denotes regular-wave height, H_s significant wave height, T and T_p are the associated periods, and U_s is the reference wind speed used to set the aerodynamic load. Direction entries are degrees relative to head seas (0° aligned; 30° port). Unless stated otherwise, all six rigid-body motions and three mooring-line tensions were recorded.

The tests follow the guidance of DNV-RP-0286 (DNV, 2021) and are ordered to build confidence progressively: model characterisation without environmental forcing, regular wave sweeps for RAOs and linearity checks, irregular seas (including extremes), and finally wind–wave misalignment.

- **Model Characterisation:**
  - Includes tests to calculate key variables that characterise the system, such as natural frequencies derived from decay tests.
  - Provides essential data to evaluate how well the physical system represents the theoretical design and previously developed numerical models.
  - Crucial for validating the numerical model.
- **Regular Waves:**
  - Enables the acquisition of response amplitude operators (RAOs), fundamental for tuning numerical models.
  - Provides insights into the platform's dynamic behaviour under linear conditions.
  - Evaluates the platform's sensitivity to wave frequency and amplitude variations and the introduction of wind loads.

- **Irregular Waves, Including Extremes:**
  - Evaluates the system's overall performance in more realistic scenarios.
  - Introduces second-order effects to assess the system's sensitivity to such phenomena.
  - Tests extreme wave conditions, which are difficult to simulate accurately in numerical models.
- **Wind-Wave Misalignment:**
  - Poses unique challenges in the physical testing of FOWTs, especially with winch system setups.
  - Critical for understanding the platform's performance under misaligned conditions.
  - Part of the Design Load Cases (DLCs) specified in standards such as *DNV-ST-0437*.

The tests included are part of a normal tank test campaign of a FOWT model as advised by DNV-RP-0286 (DNV, 2021).Table 3.14 lists the characterisation tests. These contain no environmental forcing and provide the baseline properties used later to compare the physical and numerical models: natural periods and damping from decays, and horizontal mooring stiffness from static pull-outs.

Table 3.14: Model characterisation tests (no environmental forcing).

Test	With moorings	Without moorings	Objective
Decay	6 DOF	Roll, pitch, heave	Identify natural periods and damping ratios.
Static pull-out	Surge, sway	—	Determine mooring restoring in surge and sway.

Table 3.15 presents the regular-wave programme. The first six rows are frequency sweeps for RAOs at two wave heights (1 m and 4 m) and with/without mean wind loading (represented by constant-thrust cases corresponding to $U_s = 8$ and 11 m/s). Periods span $T = 2.5$–28 s in ≈ 2.24 s increments, covering the platform and mooring resonance ranges. The final three rows probe linearity by varying wave height from 1 to 8 m at a fixed $T = 13.5$ s, again with/without wind.

Table 3.16 covers irregular seas. The "Global performance" cases use $H_s = 5$ m with $T_p = 11.5$, 14, and 18 s, each repeated with wind set-points $U_s = 0$, 8, 11, and 22 m/s to study coupled aero–hydro effects. The "Extremes" block comprises design sea states representative of 1-year and 50-year return periods ($H_s = 6.9$ m, $T_p = 12.92$ s; $H_s = 13$ m, $T_p = 16$ s; $H_s = 14$ m, $T_p = 18$ s).

Table 3.17 examines misalignment. Two series were run: (i) waves at 30° with wind aligned (0°), and (ii) wind at 30° with waves aligned. Each series was repeated for regular and irregular seas, and for wind set-points $U_s = 8$, 11, and 22 m/s. These cases quantify sway–yaw coupling and directional sensitivity that are not observable under aligned conditions.

Group	Test name	DOF	Objective	Environmental Loads			Direction	
				$H/H_s(m)$	$T/T_p(s)$	$U_s(m/s)$	Waves	Wind
Regular Waves	RAOs	All 6 DOF motions were acquired including mooring tensions	Acquire RAOs for each DOF	1	2.5 - 28 (increments of 2.24 sec)	-	0	-
	RAOs	All 6 DOF motions were acquired including mooring tensions	Acquire RAOs for each DOF	1	2.5 - 28 (increments of 2.24 sec)	8	0	0
	RAOs	All 6 DOF motions were acquired including mooring tensions	Acquire RAOs for each DOF	1	2.5 - 28 (increments of 2.24 sec)	11	0	0
	RAOs	All 6 DOF motions were acquired including mooring tensions	Acquire RAOs for each DOF	4	2.5 - 28 (increments of 2.24 sec)	-	0	-
	RAOs	All 6 DOF motions were acquired including mooring tensions	Acquire RAOs for each DOF	4	2.5 - 28 (increments of 2.24 sec)	8	0	0
	RAOs	All 6 DOF motions were acquired including mooring tensions	Acquire RAOs for each DOF	4	2.5 - 28 (increments of 2.24 sec)	11	0	0
	Sensitivity to wave amplitude	All 6 DOF motions were acquired including mooring tensions	Check system's response sensitivity to wave amplitude	1 - 8 (increments of 1 m)	13.5	-	0	-
	Sensitivity to wave amplitude	All 6 DOF motions were acquired including mooring tensions	Check system's response sensitivity to wave amplitude	1 - 8 (increments of 1 m)	13.5	8	0	0
	Sensitivity to wave amplitude	All 6 DOF motions were acquired including mooring tensions	Check system's response sensitivity to wave amplitude	1 - 8 (increments of 1 m)	13.5	11	0	0

Table 3.15: Summary of performed tests for Regular Waves.

Group	Test name	DOF	Objective	Environmental Loads			Direction	
				$H/H_s(m)$	$T/T_p(s)$	$U_s(m/s)$	Waves	Wind
Irregular Waves	Global performance	All 6 DOF motions were acquired including mooring tensions	Check system's global performance in conditions closer to reality	5	11.5	-	0	-
	Global performance	All 6 DOF motions were acquired including mooring tensions	Check system's global performance in conditions closer to reality	5	11.5	8	0	0
	Global performance	All 6 DOF motions were acquired including mooring tensions	Check system's global performance in conditions closer to reality	5	11.5	11	0	0
	Global performance	All 6 DOF motions were acquired including mooring tensions	Check system's global performance in conditions closer to reality	5	11.5	22	0	0
	Global performance	All 6 DOF motions were acquired including mooring tensions	Check system's global performance in conditions closer to reality	5	14	-	0	-
	Global performance	All 6 DOF motions were acquired including mooring tensions	Check system's global performance in conditions closer to reality	5	14	8	0	0
	Global performance	All 6 DOF motions were acquired including mooring tensions	Check system's global performance in conditions closer to reality	5	14	11	0	0
	Global performance	All 6 DOF motions were acquired including mooring tensions	Check system's global performance in conditions closer to reality	5	14	22	0	0
	Global performance	All 6 DOF motions were acquired including mooring tensions	Check system's global performance in conditions closer to reality	5	18	-	0	-
	Global performance	All 6 DOF motions were acquired including mooring tensions	Check system's global performance in conditions closer to reality	5	18	8	0	0

Group	Test name	DOF	Objective	Environmental Loads			Direction	
				$H/H_s(m)$	$T/T_p(s)$	$U_s(m/s)$	Waves	Wind
	Global performance	All 6 DOF motions were acquired including mooring tensions	Check system's global performance in conditions closer to reality	5	18	11	0	0
	Global performance	All 6 DOF motions were acquired including mooring tensions	Check system's global performance in conditions closer to reality	5	18	22	0	0
Irregular Waves: Extremes	Global performance in extreme conditions	All 6 DOF motions were acquired including mooring tensions	Check system's global performance in extreme conditions, 1-yr and 50-yr return period sea states	6.9	12.92	-	0	-
	Global performance in extreme conditions	All 6 DOF motions were acquired including mooring tensions	Check system's global performance in extreme conditions, 1-yr and 50-yr return period sea states	6.9	12.92	25.5	0	0
	Global performance in extreme conditions	All 6 DOF motions were acquired including mooring tensions	Check system's global performance in extreme conditions, 1-yr and 50-yr return period sea states	13	16	-	0	-
	Global performance in extreme conditions	All 6 DOF motions were acquired including mooring tensions	Check system's global performance in extreme conditions, 1-yr and 50-yr return period sea states	14	18	-	0	-

Table 3.16: Summary of performed tests for Irregular Waves, including extremes.

Group	Test name	DOF	Objective	Environmental Loads			Direction	
				$H/H_s(m)$	$T/T_p(s)$	$U_s(m/s)$	Waves	Wind
Wind/Wave Misalignment	Misaligned cases: regular and irregular waves	All 6 DOF motions were acquired including mooring tensions	Check system's global performance and impact of misaligned conditions	5	11.5	8	30	0
	Misaligned cases: regular and irregular waves	All 6 DOF motions were acquired including mooring tensions	Check system's global performance and impact of misaligned conditions	5	11.5	11	30	0
	Misaligned cases: regular and irregular waves	All 6 DOF motions were acquired including mooring tensions	Check system's global performance and impact of misaligned conditions	5	11.5	22	30	0
	Misaligned cases: regular and irregular waves	All 6 DOF motions were acquired including mooring tensions	Check system's global performance and impact of misaligned conditions	5	14	8	30	0
	Misaligned cases: regular and irregular waves	All 6 DOF motions were acquired including mooring tensions	Check system's global performance and impact of misaligned conditions	5	14	11	30	0
	Misaligned cases: regular and irregular waves	All 6 DOF motions were acquired including mooring tensions	Check system's global performance and impact of misaligned conditions	5	14	22	30	0
	Misaligned cases: regular and irregular waves	All 6 DOF motions were acquired including mooring tensions	Check system's global performance and impact of misaligned conditions	5	18	8	30	0
	Misaligned cases: regular and irregular waves	All 6 DOF motions were acquired including mooring tensions	Check system's global performance and impact of misaligned conditions	5	18	11	30	0
	Misaligned cases: regular and irregular waves	All 6 DOF motions were acquired including mooring tensions	Check system's global performance and impact of misaligned conditions	5	18	22	30	0
	Misaligned cases: regular and irregular waves	All 6 DOF motions were acquired including mooring tensions	Check system's global performance and impact of misaligned conditions	5	11.5	8	0	30

Group	Test name	DOF	Objective	Environmental Loads			Direction	
				$H/H_s(m)$	$T/T_p(s)$	$U_s(m/s)$	Waves	Wind
Wind/Wave Misalignment	Misaligned cases: regular and irregular waves	All 6 DOF motions were acquired including mooring tensions	Check system's global performance and impact of misaligned conditions	5	11.5	11	0	30
	Misaligned cases: regular and irregular waves	All 6 DOF motions were acquired including mooring tensions	Check system's global performance and impact of misaligned conditions	5	11.5	22	0	30
	Misaligned cases: regular and irregular waves	All 6 DOF motions were acquired including mooring tensions	Check system's global performance and impact of misaligned conditions	5	14	8	0	30
	Misaligned cases: regular and irregular waves	All 6 DOF motions were acquired including mooring tensions	Check system's global performance and impact of misaligned conditions	5	14	11	0	30
	Misaligned cases: regular and irregular waves	All 6 DOF motions were acquired including mooring tensions	Check system's global performance and impact of misaligned conditions	5	14	22	0	30
	Misaligned cases: regular and irregular waves	All 6 DOF motions were acquired including mooring tensions	Check system's global performance and impact of misaligned conditions	5	18	8	0	30
	Misaligned cases: regular and irregular waves	All 6 DOF motions were acquired including mooring tensions	Check system's global performance and impact of misaligned conditions	5	18	11	0	30
	Misaligned cases: regular and irregular waves	All 6 DOF motions were acquired including mooring tensions	Check system's global performance and impact of misaligned conditions	5	18	22	0	30

Table 3.17: Summary of performed tests for Wind/Wave Misalignment for both Regular and Irregular Waves.

3.4.3 Data processing

This section documents the data processing workflow applied to all tank data prior to analysis. The pipeline is identical across phases, with Phase III additionally using the time-varying thrust set-point from the SIL model.

Inputs

The following time series are imported for each run: platform 6 DOF from motion capture system, in-line thrust (load cell), individual mooring-line tensions, wave-gauge elevation(s), winch/motor signals (commanded current/PWM and measured current), and, when applicable, the SIL thrust set-point $F_T(t)$.

Pre-processing

(1) Import, time base, and synchronisation. All channels are read with their native timestamps, a common time origin is set, and streams are synchronised.

(2) Units, sign conventions, and scaling. Signals are converted to SI units and mapped to the global right-handed tank axes used throughout this work. When reported in full scale, Froude scaling (1:50) is applied consistently to time, translations, kinematics and loads.

(3) Quality control and filtering. Obvious dropouts and spikes are removed; a low-pass Butterworth filter is used to suppress sensor noise while preserving the wave band and low-frequency (LF) content.

(4) Windowing and de-trending. Start-up transients are cut. For regular waves, exactly five wave cycles are removed. For irregular waves, a fixed analysis window is used (tank-scale duration defined in the test plan).

RAO estimation from regular waves: general procedure

The RAOs are obtained from single–frequency regular wave tests as follows.

1. Pre-process each time series (wave elevation $\eta(t)$ and response $q(t)$): the steady portion is selected.
2. Compute one-sided spectra: obtain the complex Fourier coefficients $a_\eta(f), a_q(f)$ and the one-sided PSDs $S_{\eta\eta}(f), S_{qq}(f)$.
3. Identify the target excitation frequency $f_0 = 1/T$ and take a narrow averaging band around it (e.g. $f \in [f_0 \pm \Delta f]$).

4. RAO magnitude:

$$|H_q(f_0)| = \sqrt{\frac{S_{qq}(f_0)}{S_{\eta\eta}(f_0)}}.$$

Units follow the DOF (e.g. m/m for surge, deg/m for pitch).

Natural frequency and linear/quadratic damping from free decays

Natural frequency and damping were identified from free–decay tests by fitting an under-damped oscillator model directly to the measured motion response. After selecting a steady decay window, the time series of the degree-of-freedom response $X(t)$ (in m for surge/sway/heave, in degrees for roll/pitch/yaw) was fitted using the analytical expression

$$X(t) = -A\,e^{-\zeta\omega_n t}\cos(\omega_d t - \phi) + X_0$$

where A is the oscillation amplitude, ζ is the damping ratio, ω_n is the undamped natural circular frequency, ϕ is the phase angle, and X_0 is a constant offset accounting for any signal bias. The damped circular frequency ω_d is defined as

$$\omega_d = \omega_n\sqrt{1-\zeta^2}.$$

The model parameters were identified by minimising the sum of squared differences between the measured response and the analytical model using nonlinear optimisation. The fitted parameter vector is defined as

$$\theta = [A, \zeta, \omega_n, \phi, X_0].$$

The fitted value of ζ was taken directly as the damping ratio for the considered degree of freedom, while ω_n was used to compute the natural period and natural frequency as

$$T_n = \frac{2\pi}{\omega_n}, \qquad f_n = \frac{1}{T_n}.$$

The natural period obtained at model scale was converted to full scale using Froude scaling as

$$T_{n,\text{full}} = T_{n,\text{model}}\sqrt{\lambda},$$

where λ is the geometric scale factor of the model. For the present experiments, $\lambda = 50$.

3.5 Chapter summary and outlook

This chapter set out a structured methodology to evaluate how increasing the fidelity of aerodynamic actuation influences the measured response of a semi-submersible FOWT. A single, well-documented reference system (VolturnUS-S with the IEA-15 MW turbine) and a representative North Sea site were adopted; geometry, mass and inertia were scaled by Froude similitude, and a truncated mooring surrogate was designed to reproduce full-scale fairlead pretensions and linear restoring behaviour within the constraints of the basin. OpenFAST provided a consistent numerical baseline (including linearised properties) and a sensitivity path for “only-thrust” versus fully coupled aerodynamics.

Three test phases implemented rotor thrust with increasing realism: static weight, PI-controlled constant thrust, and a SIL winch driven by a simplified BEM model. A test plan spanning regular and irregular seas, extremes, and wind–wave misalignment was defined to extract RAOs, identify natural periods and damping, and assess global performance. A common data pipeline was specified for synchronisation, scaling, quality control, windowing, RAO estimation from regular waves, and damping identification from free decays.

The approach is deliberately pragmatic. It prioritises platform-scale dynamics over rotor harmonics and elastic modes, applies thrust as the dominant aerodynamic load, and uses a stiffness-matched surrogate mooring. These choices bound the scope and clarify interpretation of the results to be presented in the following chapter.

Chapter 4

Results: Numerical–Experimental Evaluation

This chapter presents a detailed comparison between numerical simulations and experimental results to evaluate different wind actuation methods applied in a wave basin. The work progresses from a sensitivity analysis using OpenFAST, comparing limited actuation, where a constant load is applied at nacelle height, with a fully coupled aero- and hydrodynamic model, to physical testing with various wind actuation strategies under different loading conditions. The overarching aim is to assess the fidelity and limitations of these actuation methods and to determine if added complexity results in meaningful gains in representativeness.

An overall schematic of how the results are organised is shown in Figure 4.1. We first characterise the Haugesund metocean conditions (Section 3.1.2) by deriving joint H_s–T_p–U statistics and the 1- and 50-year I-FORM environmental contours. These define the envelope used to select the regular, irregular, and extreme test cases compared in this chapter.

Thereafter, the effect of simplified aerodynamic loading is isolated through a numerical comparison between two approaches: (i) a constant rotor thrust force applied at nacelle height and (ii) a fully coupled aero-hydrodynamic simulation with OpenFAST. The constant-thrust implementation is described in Section 3.2.2, and the motivation and limitations are summarised in the literature review (Section 2.4). These simulations are performed for still water, regular waves, and irregular waves, providing a basis to evaluate the impact of representing the aerodynamic loading solely through constant thrust while neglecting other aerodynamic force components.

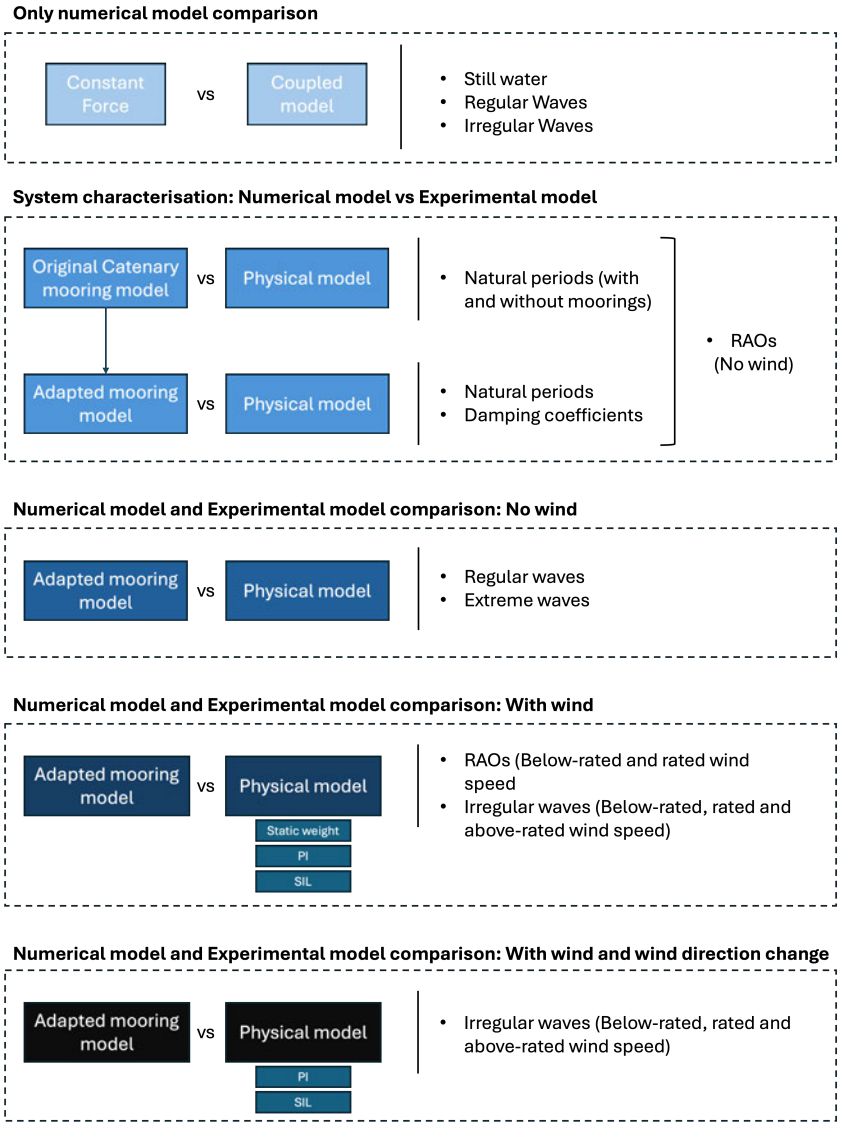

Figure 4.1: Structure of the results chapter showing the comparisons made with increasing level of complexity.

Following this numerical sensitivity, the chapter presents a comparison between experimental and numerical characterisation of the system, focusing on natural frequencies and damping coefficients. This step establishes a common baseline and assesses how representative the physical model is of its numerical counterpart. It is particularly important to note that no further tuning of the numerical model is performed beyond the adaptation of the mooring system, ensuring that the comparison reflects the inherent characteristics of both models rather than adjustments made post-validation.

Subsequently, the system's response in regular wave conditions without wind is analysed, with particular attention given to the performance of the spring-rope mooring system specifically designed for the tank. Due to the size and dimensions of the tank, the original catenary mooring configuration could not be replicated, and a custom-designed spring-rope system was implemented instead. This section evaluates the extent to which the physical mooring system reflects the behaviour of the original catenary model, using both regular and extreme wave results. The mooring design and its experimental validation are documented in a companion manuscript submitted to the *Journal of Ocean Engineering and Marine Energy* and currently under peer review. The submitted version is reproduced in Appendix C.

The chapter then concludes with the core objective of this thesis: evaluating the system response under wind loading. Results from regular and irregular wave conditions, as well as from wind–wave directional misalignment cases, are presented for three actuation strategies, ranging from simplified constant-force methods to software-in-the-loop (SIL). These comparisons aim to assess how well each method reproduces coupled aero-hydrodynamic responses in the physical testing environment and to provide guidance on the suitability of each strategy depending on the test objectives and desired level of fidelity.

While this chapter focuses on a structured and factual presentation of results, with local interpretations where relevant, a broader discussion and overall interpretation of the findings will follow in the subsequent Discussion chapter.

4.1 Metocean Data Analysis Results

Building on the methodology described in Section 3.1.2, which defined the Haugesund site and the selection workflow, the following results summarise the relationships that informed the conditions to be tested. Figure 4.2a shows the relationship between peak period T_p and significant wave height H_s where most occurrences are concentrated at lower wave heights and shorter periods, with variability increasing toward longer T_p. Figure 4.2b shows the expected co-variation between wind speed at 150 m (U) and H_s. A minority of events with large H_s at relatively low U suggests additional forcing such as swell or current effects. These characterisations were used directly to select the sea states executed in the physical testing campaigns (see Section 3.4.2).

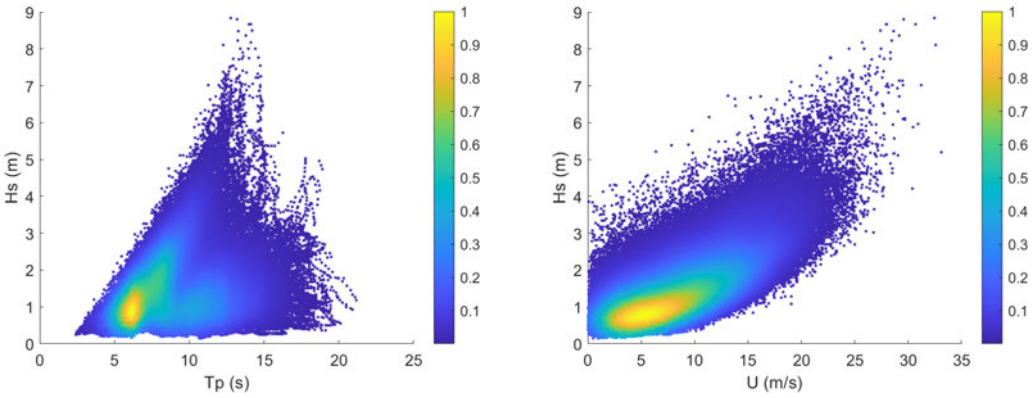

(a) H_s vs. T_p.

(b) H_s vs. U at 150 m.

Figure 4.2: Scatter plots of metocean parameters at 59.5° N, 5° E (1990–2019).

4.1.1 Application of the Inverse–First Order Reliability Method (I-FORM)

Applying the I-FORM method described in the Methodology section 3.1.2, a three-parameter (translated) Weibull distribution is fitted to the significant wave height H_s data. The results are presented in Figure 4.3, with a histogram of the observations (left) and a Q–Q plot (right), which together evaluate the model's goodness-of-fit across the distribution and its quantiles.

The histogram of significant wave heights shows that the three-parameter Weibull distribution generally approximates the central tendency of the data well. However, there are discrepancies in the tails where the model slightly underestimates the probability density at the mode and overestimates it in the tail regions. This suggests that while the Weibull model is reasonable, it does not perfectly capture the behaviour of the extreme values in the dataset. The fitted shape parameter, $\beta = 1.71$, suggests a moderately heavy-tailed distribution, while the scale parameter, $\eta = 1.61$, provides a measure of spread. The threshold value of 0.19 represents the lower bound above which the Weibull distribution is applied. Together, these parameters define the statistical characteristics of the fitted model, and while they are reasonable, the limitations in capturing extreme behaviour should be considered when applying the model in a design context.

The Q-Q plot indicates a good alignment between the theoretical and observed quantiles, especially in the middle range. Nonetheless, deviations in the upper tail reveal that the observed values exceed the fit parameters, highlighting a potential underestimation of extreme wave heights by the model.

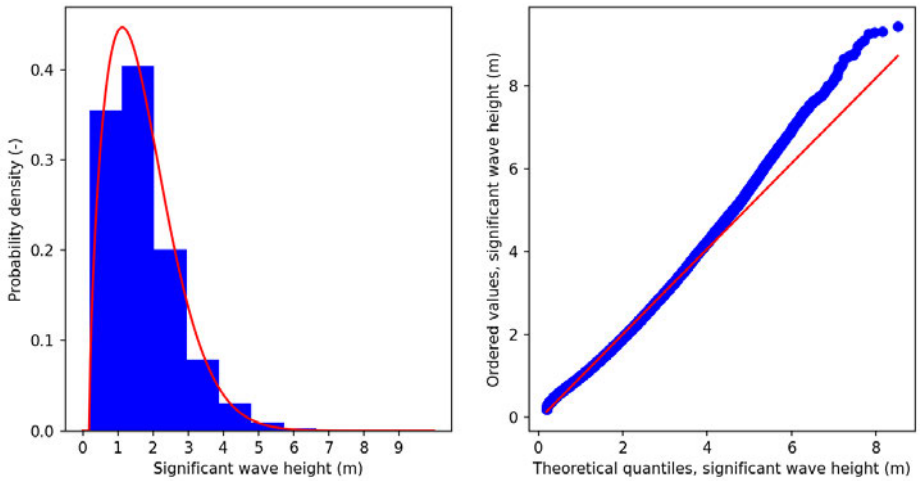

Figure 4.3: Three-parameter Weibull fit to H_s (1990–2019): histogram and Q–Q diagnostics.

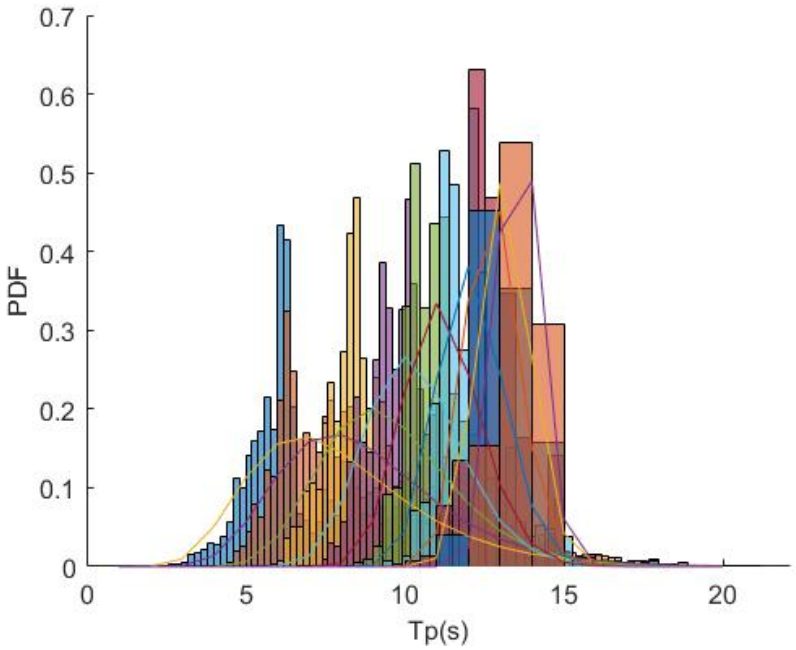

Figure 4.4: Lognormal fits of $T_p \mid H_s$ across 1 m H_s bins.

For $T_p \mid H_s$, a Lognormal model was fitted within 1 m H_s bins, and the parameters $\mu(h)$ and $\sigma(h)$ were then expressed as smooth functions of h_s (Figures 4.4 and 4.5). Performance is acceptable across most conditions however, the global Q–Q comparison for T_p shows systematic departures at longer periods, indicating that tail behaviour is not fully captured (Figure 4.6).

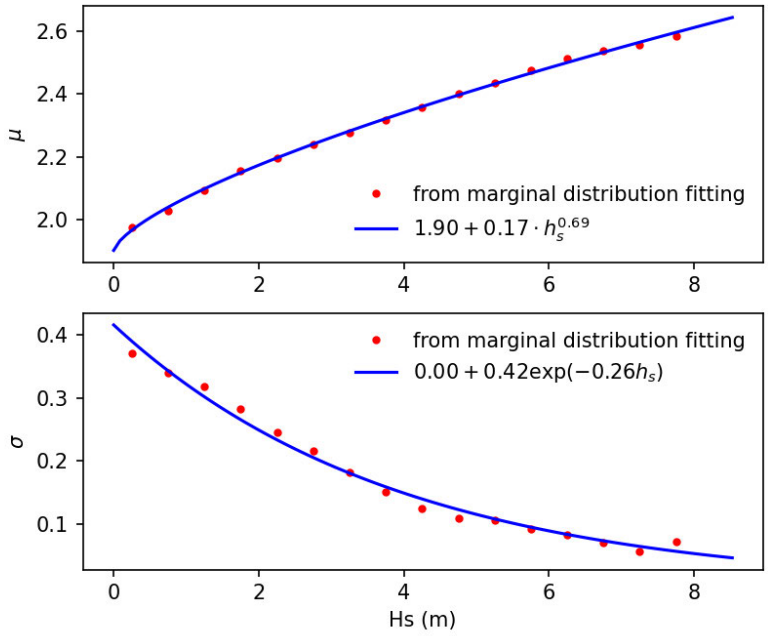

Figure 4.5: Fitted parameter trends $\mu(h)$ and $\sigma(h)$ for $T_p \mid H_s$.

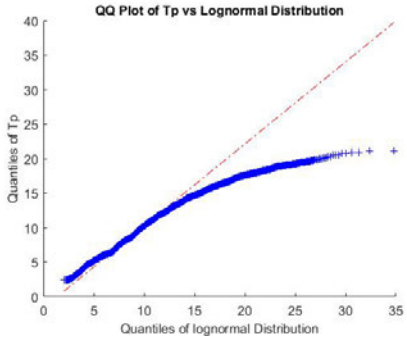

Figure 4.6: Q–Q plot comparing T_p with a Lognormal model.

I-FORM contours for 1- and 50-year return periods are shown in Figure 4.7. Firstly, the Weibull distribution's failure to accurately model the upper tail of the H_s dataset likely leads to an underestimation of extreme wave heights, as evidenced by the 53 data points (red diamonds) located outside the 50-year contour. These points signify wave conditions more severe than those anticipated within a typical 50-year period, indicating that the contour does not sufficiently encompass these higher, more extreme events.

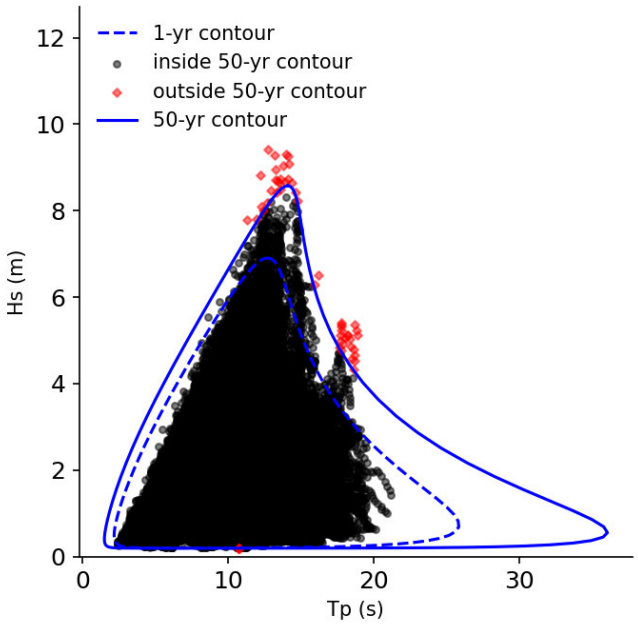

Figure 4.7: I-FORM environmental contours (1- and 50-year) in H_s–T_p space.

Additionally, the distribution's location parameter, which suggests a minimum non-zero wave height, does not align with real-world observations where a significant wave height of zero, indicative of calm sea states, is both physically meaningful and essential for comprehensive environmental modelling (Ochi and Wahlen, 1980).

Moreover, employing a global modelling approach, while advantageous in utilising all available data without the need for pre-processing and allowing the application of common parametric distributions, carries inherent limitations and potential errors. This is due primarily to the characteristics of the data and the chosen modelling techniques. Significant wave height time series often display strong auto correlation, implying that individual data points are not independent and identically distributed (Mackay et al., 2021). This auto correlation undermines the effectiveness of standard fitting methods like maximum likelihood estimation (MLE) and least squares estimation, which treat all data points equally.

The left part of the contour lines, where T_p is shorter, might indirectly indicate areas with relatively short fetch, thus limiting the generation of long-period waves. The steep rise in H_s at these shorter periods could suggest rapid energy accumulation over a brief fetch. However, despite the proximity of both contour lines to the data points, they fail to accurately capture the correct shape.

Furthermore, the data used in the analysis spans 30 years, implying that the extreme conditions depicted by the data points outside the 50-year contour occur more frequently than previously predicted, at least once every 30 years. This observation highlights significant flaws in the current environmental contour modelling, as it does not adequately represent the range and likelihood of extreme sea states vital for the design and safety of marine and coastal structures.

These insights emphasise the necessity for caution when interpreting results from this global modelling approach. The identified limitations suggest that improvements in model selection, data treatment, and fitting methodologies are crucial to enhance the accuracy and applicability of environmental contour models in marine design and analysis.

The primary aim of this analysis was to determine the 1-year return period sea state, complementing the 50-year return period data previously provided by an external partner. The 1-year sea state was selected based on the upper boundary of the environmental contour, specifically focusing on the limiting value of significant wave height. This choice reflects a conservative interpretation of the contour edge, intended to represent the maximum expected wave height associated with a relatively frequent return period. The extreme sea states adopted for the tank test are detailed in the Methodology section 3.1.2.

An analogous contour in H_s–U space (Figure 4.8) relates the 1-year H_s to a concurrent wind speed where for $H_s = 7$ m, the corresponding U is 25 m/s.

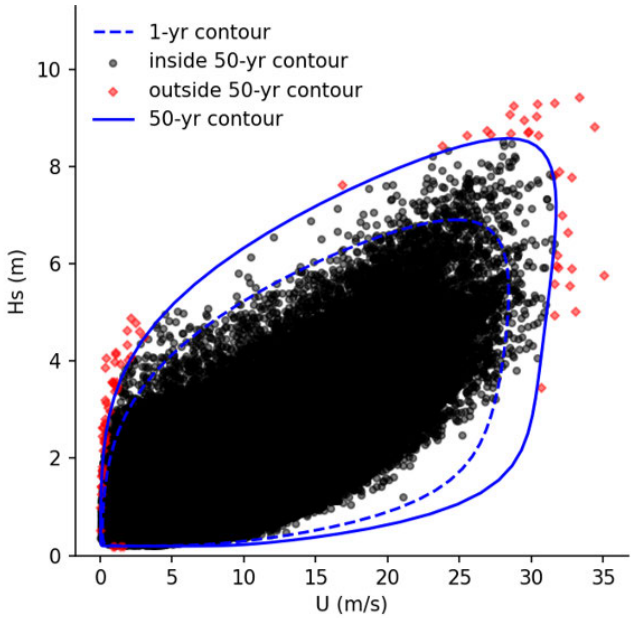

Figure 4.8: I-FORM contours in H_s–U space.

4.2 Numerical Sensitivity Analysis: Constant Force vs. Aerodynamic Model

To begin understanding the sensitivity of floating offshore wind turbines to wind load actuation, an initial numerical comparison was conducted in OpenFAST between two rigid-body models: one subjected to a constant thrust force (hereafter referred to as *Only Thrust*) and another using a full aerodynamic model (hereafter referred to as *Normal*). In the former, a constant force was applied at nacelle height to represent rotor thrust, while the latter computed aerodynamic loads based on rotor characteristics and inflow conditions. This comparison helps assess the influence of additional components of the wind load vector and provides insight into their dynamic coupling. The analysis follows the methodology described in Section 3.2.2.

4.2.1 Still Water Case: Static vs. Dynamic Loading

The constant force simulation was performed under still water conditions using a time series load file with a time step of 0.025 s and a total simulation duration of 2000 s. A constant thrust of 2716 kN was applied at nacelle height (148.7 m). This value corresponds to the mean aerodynamic rotor thrust when the wind turbine is operating at its rated wind speed, as shown in the thrust curve in Figure 3.13. It was chosen because it represents a maximum loading condition under normal operating conditions.

To verify that the constant-force implementation delivers the intended thrust while retaining physical consistency with the fully coupled aero-hydrodynamic model, two OpenFAST output channels were examined: *RotThrust*, which corresponds to the axial load in the shaft coordinate system (x_s, Figure 4.9a), and *YawBrFxn*, which corresponds to the axial load transmitted through the nacelle–yaw interface (x_n, Figure 4.9b).

RotThrust primarily captures the load path between the hub and the main-shaft bearings. As the constant-force case applies the thrust directly to the nacelle rather than to the shaft, the *RotThrust* signal reflects only secondary effects (e.g., tower and platform tilt, the rotor weight component along x_s) and is therefore not a reliable indicator of the imposed load. By contrast, *YawBrFxn* measures the force delivered to the yaw bearing, i.e. the point of application of the constant thrust and for that reason is the appropriate channel for validating the actuation.

Figure 4.10 illustrates these points where panel (a) confirms that *RotThrust* in the *Only Thrust* scenario (blue) settles to a value an order of magnitude lower than in the *Normal* aero-coupled run (orange); the shaft sees only the residual projection of the thrust. Panel (b) shows that *YawBrFxn* carries the full constant load in the *Only Thrust* case, while the aero-coupled case settles to a lower steady value. This difference arises because, in the aero-coupled simulation, the rotor thrust is generated through blade aerodynamics and regulated by the pitch controller.

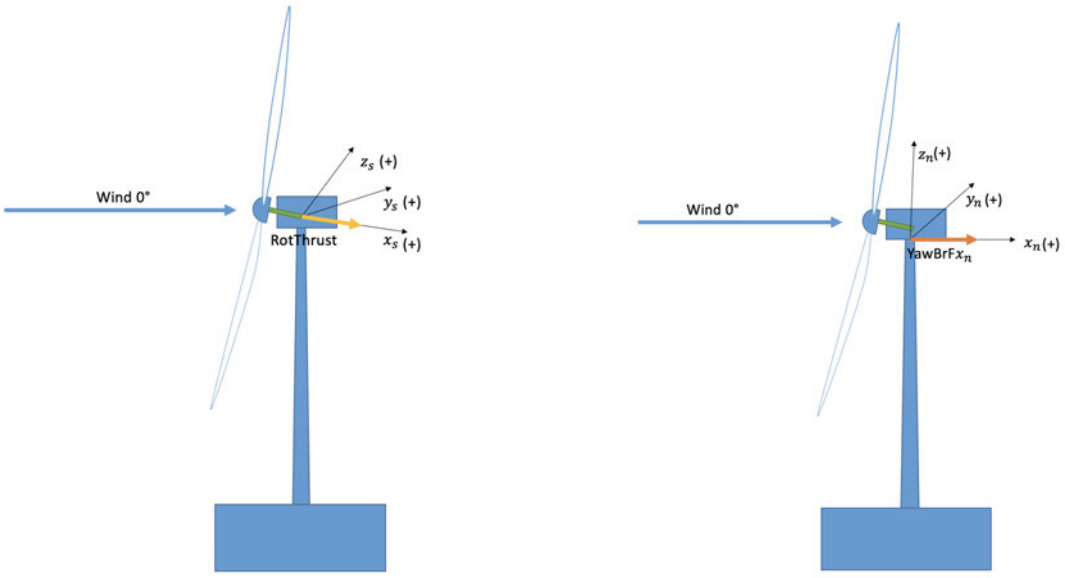

(a) Shaft coordinate system

(b) Nacelle/yaw coordinate system

Figure 4.9: Coordinate systems used for the sensitivity study: (a) shaft and (b) nacelle/yaw.

At rated wind speed, the controller adjusts the blade pitch to maintain constant rotor speed, which results in a slightly lower steady thrust compared to the prescribed constant-force case. This difference in pitch angle modifies the aerodynamic loading and introduces additional aerodynamic damping through blade–flow interaction, thereby altering the equilibrium force transmitted through the yaw bearing.

Furthermore, although the wind speed is constant, the aero-coupled case exhibits smaller oscillations than the constant-force case. This is because the aerodynamic model includes inherent damping mechanisms arising from blade aerodynamics and pitch control feedback. When the platform moves, the relative wind speed and angle of attack change, and the controller responds by adjusting blade pitch, which moderates thrust variations and dissipates energy. In contrast, the *Only Thrust* implementation applies a prescribed force independent of platform motion and does not include aerodynamic feedback or pitch control. As a result, no aerodynamic damping is present, and the platform–tower system behaves as a lightly damped mechanical oscillator, leading to larger and more persistent oscillations following the initial load step.

The constant-force implementation reproduces the mean nacelle thrust with acceptable accuracy but eliminates the higher-frequency aerodynamic load variations that are present in the fully coupled model. Subsequent sections will show how this simplification propagates into platform motions and mooring loads.

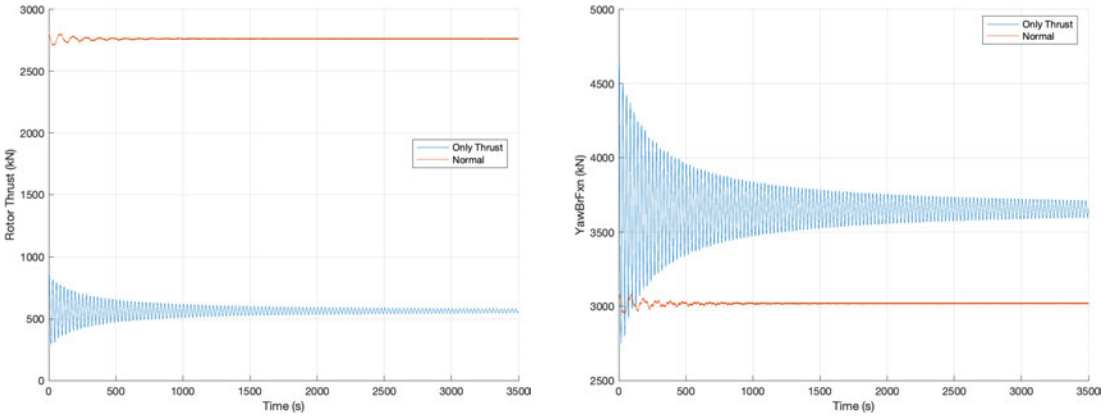

(a) Rotor Thrust time series comparison **(b)** YawBrFxn time series comparison

Figure 4.10: Comparison of time series for Rotor Thrust and YawBrFxn under still water sensitivity analysis.

Figure 4.11 summarises the still water OpenFAST sensitivity run carried out with (i) a constant nacelle thrust (*Only Thrust*) and (ii) the full aerodynamic module (*Normal*). Panel (a) confirms the previous assumption that *YawBrFxn* is the correct channel for monitoring the applied load. The constant-force case delivers a mean of 3656 kN, whereas the aero-coupled model settles at 3020 kN, corresponding to a 17% difference. Due to the prescribed thrust being independent of platform motion and lacking aerodynamic feedback, the *Only Thrust* case exhibits larger transient oscillations following the initial load step. These oscillations reflect the natural structural dynamics of the platform–tower system without the stabilising effect of aerodynamic damping. In contrast, the aero-coupled case benefits from aerodynamic and controller-induced damping, which reduces oscillation amplitude and results in a lower variability of the transmitted load. This difference in load bandwidth represents the missing unsteady component anticipated in simplified actuation.

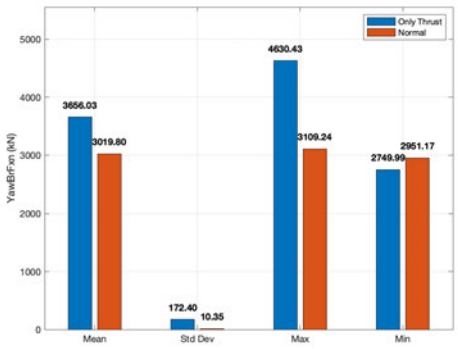

(a) Yaw bearing force along x_n axis

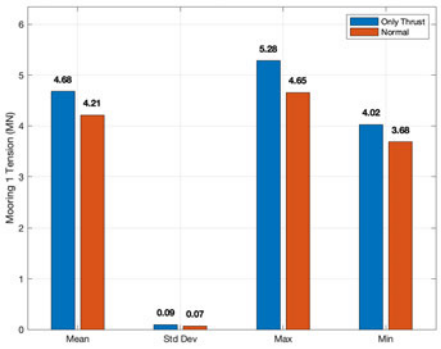

(b) Fore mooring tension

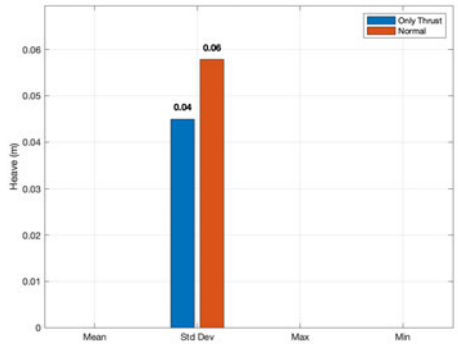

(c) Heave

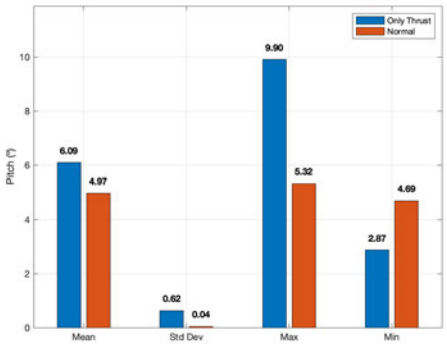

(d) Pitch

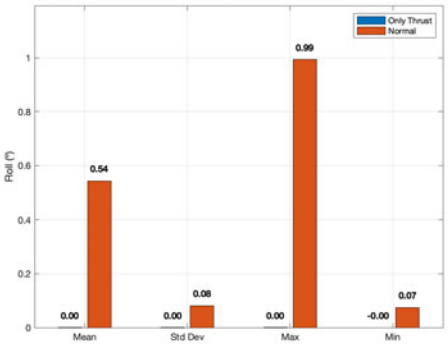

(e) Roll

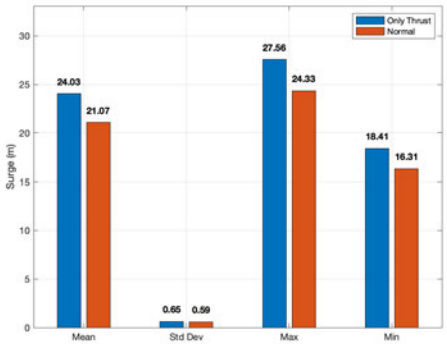

(f) Surge

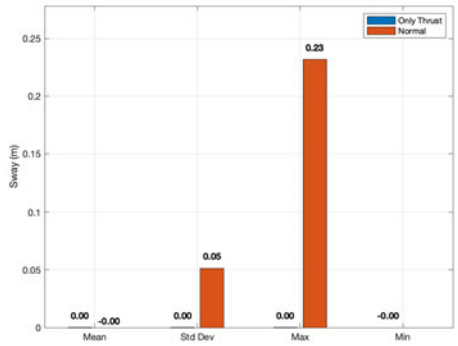

(g) Sway

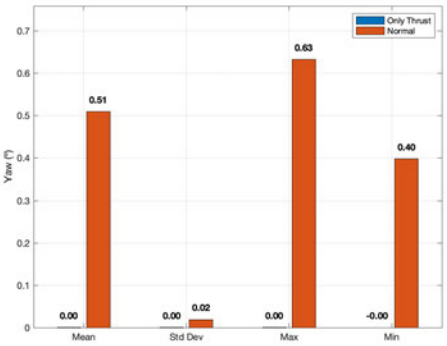

(h) Yaw

Figure 4.11: Comparison of still water results for different variables. For each case, statistical values are extracted from the time series, including the mean (average value), standard deviation (variability of the signal), maximum (peak value), and minimum (lowest value).

The statistical values for fore mooring tension, pitch and surge are higher in the constant thrust case (see Figures 4.11b, 4.11d, and 4.11f). This is due to the consistent unidirectional loading along the x-axis. Conversely, the motions in sway, roll, and yaw degrees of freedom are negligible in this scenario, as no loads are applied along or around those axes. This behaviour is consistent with what is expected, given the simplified nature of the loading.

4.2.2 Regular waves: Response comparison

The regular wave test case (H = 6 m, T = 13.5 s) does not coincide with the natural periods of any of the six degrees of freedom of the system. As a result, the response does not exhibit any resonance effects. This enables a clearer evaluation of the differences introduced solely by the type of thrust loading, constant force versus coupled aerodynamic forcing.

The comparison of results across the different response variables (Figure 4.12) highlights key differences between the constant thrust and aerodynamic models under regular wave excitation. The constant-force implementation continues to over-estimate the mean yaw bearing thrust by approximately 20% (Figure 4.12a), as also quantified in Table 4.1. This bias propagates into noticeably higher mooring loads and slightly larger surge and pitch motions once waves are introduced. Meanwhile, the absence of aerodynamic load fluctuations removes a source of natural damping, so the platform's force and motion envelopes are wider than in the aero-coupled simulation.

For pitch (Figure 4.12d), the response is higher in the constant thrust case, with a mean difference of approximately 21%, as summarised in Table 4.1. This can be attributed to the continuous and steady application of force at nacelle height, which induces a persistent overturning moment. In contrast, the aerodynamic case includes time-varying thrust and aerodynamic damping, which moderates the platform's pitch motion.

Similarly, surge (Figure 4.12f) is higher in the constant thrust scenario, with a mean difference of approximately 15%, as shown in Table 4.1. This is consistent with the absence of aerodynamic damping and rotor dynamics that would otherwise resist or modify the surge motion. The aerodynamic model introduces unsteady forces that act both with and against the platform motion, leading to a slightly reduced mean and standard deviation.

In terms of Heave (Figure 4.12c), the results for the mean values are closer which is expected as heave is less influenced by nacelle-level thrust and more directly by wave excitation. However, the standard deviations are slightly different where the constant-force run settles into a narrower oscillation band (lower standard deviation) and the larger standard deviation in the *Normal* case comes from additional vertical forcing components that the simplified model omits (tower-aerodynamic loads, rotor vertical load share, and gyroscopic coupling).

For the Yaw, Roll, and Sway motions (Figures 4.12h, 4.12e and 4.12g, respectively), the responses are negligible or close to zero in the constant thrust case, as expected, since the applied force is unidirectional along the x-axis and does not excite these rotational or lateral modes. However, the aerodynamic case shows small but non-zero responses due to the asymmetric, time-varying nature of aerodynamic forces, including possible wind shear or azimuthal variations in blade loading.

Mooring line tension (Figure 4.12b) is higher in the constant thrust model, with a mean increase of approximately 12% compared to the aerodynamic case (Table 4.1). This is a direct consequence of the higher surge and pitch responses, which stretch the mooring lines more than in the damped aerodynamic case. The steady load leads to more pronounced platform offsets and larger quasi-static mooring tension. However, minimum tension values are matched.

To quantify these differences systematically, the relative error between the Only Thrust and Normal configurations was calculated using the Normal case as reference, as presented in Table 4.1.

Table 4.1: Relative difference between Only Thrust and Normal configurations using mean values, with Normal as reference.

Variable	Error (%) Still Water	Error (%) Regular Waves
Yaw bearing force	21.4	20.5
Fore mooring tension	11.2	11.9
Heave	0.0	9.3
Pitch	22.5	21.5
Roll	100.0	100.0
Surge	14.0	15.2
Sway	0.0	100.0
Yaw	100.0	100.0

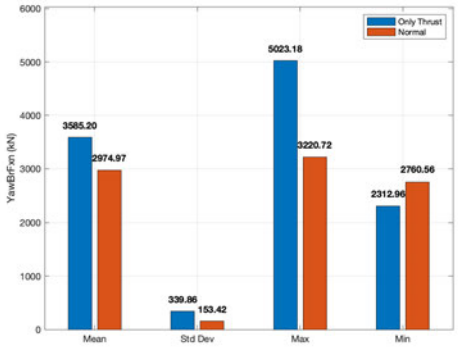

(a) YawBrFxn

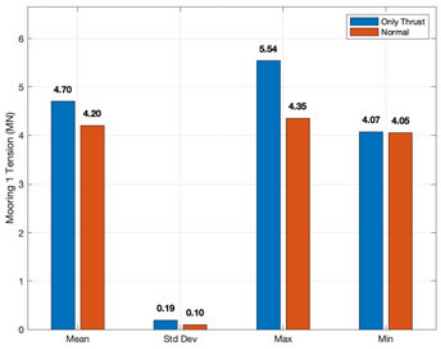

(b) Fore Mooring Tension

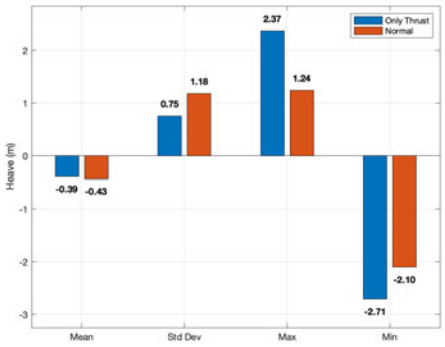

(c) Heave

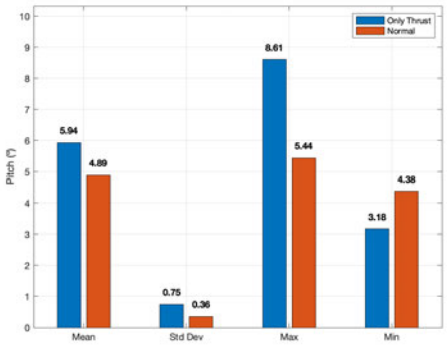

(d) Pitch

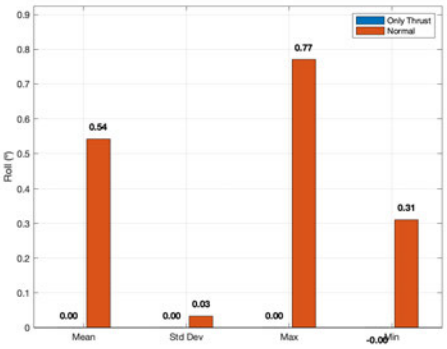

(e) Roll

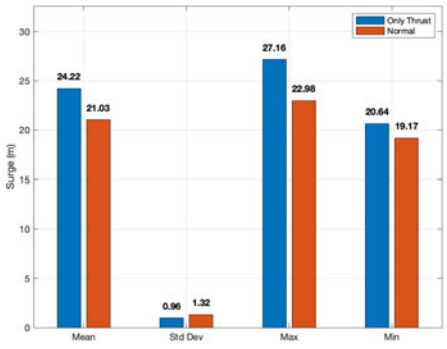

(f) Surge

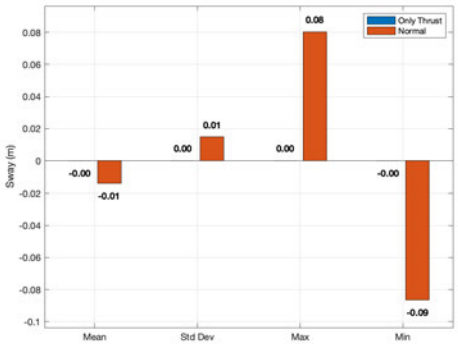

(g) Sway

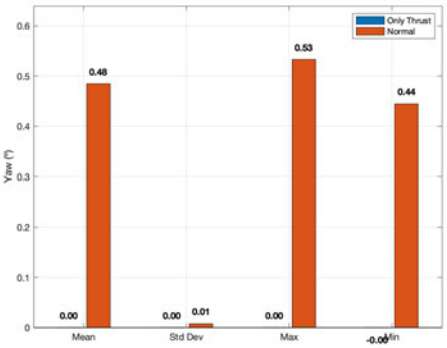

(h) Yaw

Figure 4.12: Comparison of regular wave results for different variables. For each case, statistical values are extracted from the time series, including the mean (average value), standard deviation (variability of the signal), maximum (peak value), and minimum (lowest value).

4.2.3 Irregular waves: Response comparison

The results under irregular wave excitation ($H_s = 5$ m, $T_p = 14$ s), shown in Figure 4.13, follow a similar trend to those observed in the regular wave cases. As in the previous scenarios, the peak period of the wave spectrum does not coincide with the natural periods of the platform's six degrees of freedom, and thus resonance effects remain negligible.

The constant-force implementation continues to overpredict the mean nacelle thrust, and consequently the fore-line pre-tension, surge offset, and nose-down pitch, by roughly the same amounts observed under still water and regular wave conditions.

However, once irregular seas are introduced, wave-frequency loads obscure the absence of unsteady aerodynamic forcing. As a result, standard deviations and extreme values now converge for nearly all response variables.

Summary of Findings

The constant-force implementation reproduces the intended location and steady magnitude of the nacelle thrust, but it overestimates that magnitude by approximately 17% relative to the fully coupled aerodynamic model. In still water, this bias shifts the quasi-static equilibrium forward ($+0.35$ m surge) and down-pitches the platform ($+0.15^\circ$), leading to a 12–15% increase in mean and peak fore-line tension. The absence of unsteady aerodynamic loads also removes a natural damping source, so the constant-force case displays larger first-cycle overshoots and a wider load envelope in calm-water transients.

When regular waves are introduced ($H = 6$ m, $T = 13.5$ s), the thrust bias persists, continuing to elevate line tension and surge/pitch statistics. In the irregular-sea case ($H_s = 5$ m, $T_p = 14$ s), wave drift loads overshadow the missing aerodynamic fluctuations and standard deviations and extremes for all rigid-body modes converge, leaving only the steady thrust offset as a systematic difference.

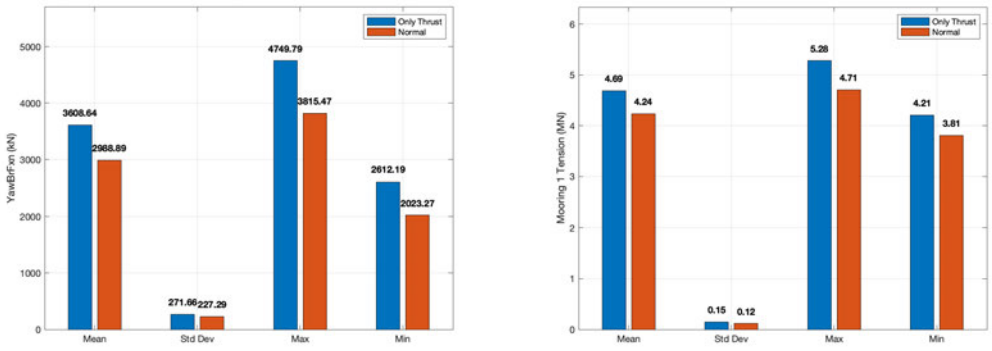

(a) YawBrFxn

(b) Fore Mooring Tension

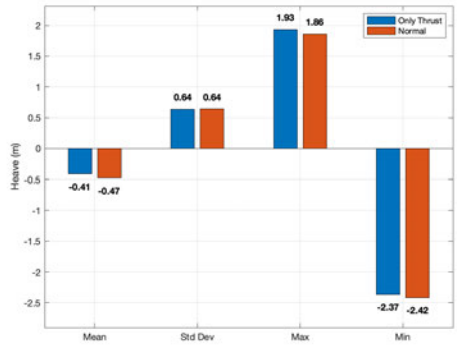

(c) Heave

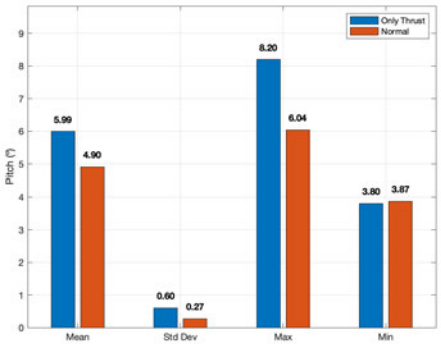

(d) Pitch

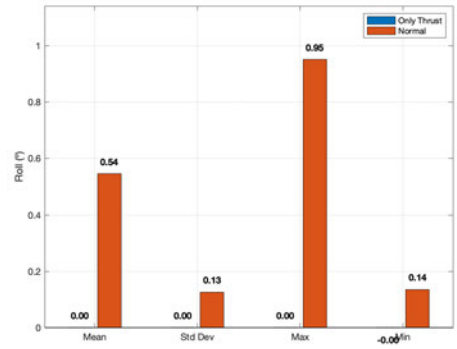

(e) Roll

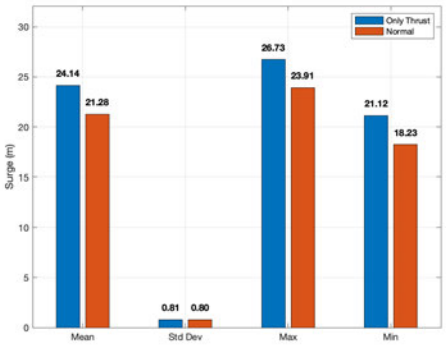

(f) Surge

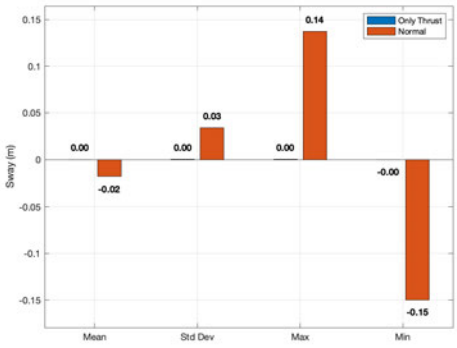

(g) Sway

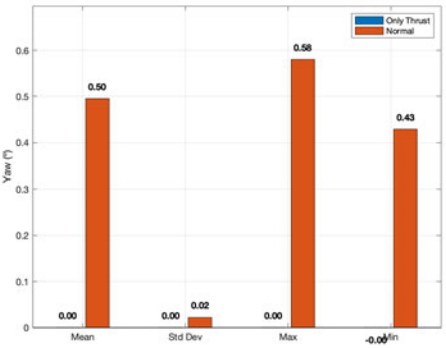

(h) Yaw

Figure 4.13: Comparison of irregular wave results for different variables. For each case, statistical values are extracted from the time series, including the mean (average value), standard deviation (variability of the signal), maximum (peak value), and minimum (lowest value).

4.3 Model Characterisation: Experimental vs. Numerical Representation

This section presents a comparison between the experimental and numerical representations of the floating wind system, focusing on two key characteristics: natural frequencies and damping coefficients. These comparisons help evaluate the agreement between the theoretical and experimentally observed behaviour in terms of natural response properties derived from free-decay motion.

Importantly, the purpose of this comparison is not to calibrate or tune the numerical model to match the experimental data. In typical industrial workflows, numerical models are adjusted based on tank test results to improve correlation. However, in the present study, no such tuning is performed. Instead, the goal is to highlight the inherent differences between the numerical and physical representation of the same system.

The physical results for natural frequencies are compared with two numerical model variants: one using the original catenary mooring configuration, and the other adapted to replicate the spring-rope mooring system used in the experimental tests. This allows for a direct evaluation of how mooring system changes affect the dynamic response and influence the agreement between numerical and experimental models.

4.3.1 Wave calibration and diffraction analysis

Wave calibration was performed to confirm that the wavemaker reproduced the prescribed regular-wave conditions used for the RAO tests. For each case, the free-surface elevation was measured using the FloWave wave-gauge array and processed using Gauge 4. The initial transient interval was removed and the remaining record was analysed in the steady-state portion. The realised wave period was estimated from peak-to-peak timing, and the realised wave height was obtained from the mean peak-to-trough amplitude over multiple cycles. Target values were defined by the run naming convention (e.g., `Reg_0_08m_1_62s` corresponds to $H = 0.08$ m and $T = 1.62$ s at tank scale). Full-scale values were obtained using Froude scaling (1:50), with $H_{\mathrm{FS}} = 50\,H_{\mathrm{tank}}$ and $T_{\mathrm{FS}} = \sqrt{50}\,T_{\mathrm{tank}}$.

Table 4.2 summarises the calibration results for the regular-wave cases used in the RAO programme. In general, the realised periods agree closely with the targets (typically within a few percent). Larger deviations are observed for some wave heights, particularly for the smallest-amplitude cases, where measurement noise, residual reflections, and finite wavemaker resolution can have a greater influence on the extracted peak-to-trough height. One case was excluded from the calibration table due to insufficient valid samples after cleaning of the wave-gauge record.

Table 4.2: Regular-wave calibration results from wave-gauge records (Gauge 4). Target values are defined by the run naming convention. Full-scale quantities are obtained using Froude scaling (1:50).

Run	H_{tar} (m)	T_{tar} (s)	H_{meas} (m)	T_{meas} (s)	ΔH (%)	ΔT (%)
Reg_0_08m_0_67s	4.00	4.74	2.60	4.71	-34.91	-0.54
Reg_0_08m_0_99s	4.00	7.00	3.87	6.95	-3.28	-0.73
Reg_0_08m_1_30s	4.00	9.19	3.78	9.25	-5.49	+0.60
Reg_0_08m_1_62s	4.00	11.46	3.74	11.46	-6.54	+0.04
Reg_0_08m_1_937s	4.00	13.70	4.14	13.76	+3.42	+0.43
Reg_0_08m_2_253s	4.00	15.93	4.12	15.88	+3.09	-0.32
Reg_0_08m_2_57s	4.00	18.17	3.87	18.11	-3.23	-0.35
Reg_0_08m_2_89s	4.00	20.44	4.14	20.60	+3.51	+0.79
Reg_0_08m_3_15s	4.00	22.27	3.92	22.07	-1.95	-0.92
Reg_0_08m_3_41s	4.00	24.11	3.44	23.76	-13.90	-1.47
Reg_0_08m_3_93s	4.00	27.79	3.31	26.04	-17.19	-6.31
Reg_0_08m_3_96s	4.00	28.00	3.29	28.09	-17.85	+0.32
Reg_0_02m_0_67s	1.00	4.74	0.34	4.77	-66.29	+0.63
Reg_0_02m_0_99s	1.00	7.00	0.74	7.02	-25.68	+0.30
Reg_0_02m_1_30s	1.00	9.19	0.91	9.24	-9.48	+0.57
Reg_0_02m_1_62s	1.00	11.46	0.82	11.47	-17.72	+0.14
Reg_0_02m_1_94s	1.00	13.72	1.10	13.71	+10.04	-0.07
Reg_0_02m_2_253s	1.00	15.93	1.11	15.88	+11.01	-0.34
Reg_0_02m_2_57s	1.00	18.17	1.00	18.11	+0.43	-0.34
Reg_0_02m_2_89s	1.00	20.44	1.13	20.31	+12.86	-0.61
Reg_0_02m_3_15s	1.00	22.27	0.91	22.12	-8.78	-0.69
Reg_0_02m_3_41s	1.00	24.11	0.88	23.83	-12.10	-1.16
Reg_0_02m_3_67s	1.00	25.95	0.82	25.88	-17.60	-0.29
Reg_0_02m_3_93s	1.00	27.79	0.87	27.34	-12.55	-1.63
Reg_0_02m_3_96s	1.00	28.00	0.98	28.16	-1.72	+0.56

Note: One case (Reg_0_08m_3_67s; RCAL_20240408T110624) was excluded because the wave-gauge record contained insufficient valid samples after cleaning. Errors are computed relative to the target values.

4.3.2 Irregular wave calibration

Irregular wave calibration was performed to verify that the generated wave conditions in the basin accurately reproduced the target full-scale sea states defined by the JONSWAP spectrum. The free surface elevation was measured using calibrated wave gauges and converted to full scale using Froude scaling. The measured time series were analysed in the frequency domain using the Welch power spectral density (PSD) method, and compared with the theoretical JONSWAP spectrum corresponding to the target significant wave height H_s, peak period T_p, and peak enhancement factor γ.

Table 4.3 summarises the calibration results for all irregular wave cases. The measured significant wave height was obtained from the zeroth spectral moment, while the peak period was determined from the frequency corresponding to the maximum PSD value. The percentage error in H_s relative to the target value is also reported.

Overall, the calibration demonstrates good agreement between the measured and target wave conditions. The measured significant wave height is consistently within approximately 5–8% of the target value, which is considered acceptable for basin testing of floating offshore wind turbines. The peak period is also well reproduced, with deviations generally below 10%. These discrepancies are attributed to physical limitations of the wavemaker, spectral discretisation, and basin effects such as wave reflection and viscous dissipation.

Figures 4.14 and 4.15 present representative examples of the calibration results for an operational sea state with $H_s = 5$ m and $T_p = 11.5$ s at 0° and 30° wave incidence, respectively. The measured PSD shows good agreement with the theoretical JONSWAP spectrum, particularly around the peak frequency, confirming that the spectral shape and energy distribution were accurately reproduced. Slight underestimation of spectral energy is observed at higher frequencies, which is consistent with expected viscous and wavemaker limitations.

These results confirm that the basin-generated irregular waves provide an accurate representation of the intended full-scale metocean conditions and are suitable for subsequent hydrodynamic and aero-hydro-servo-elastic testing of the floating offshore wind turbine model.

Table 4.3: Irregular wave calibration summary (full scale).

Case	H_s target (m)	H_s meas (m)	Err (%)	T_p target (s)	T_p meas (s)	γ
Irreg_0_10m_1_63s	5.00	4.61	-7.8	11.50	12.87	1.00
Irreg_0_10m_1_98s	5.00	4.67	-6.6	14.00	13.63	1.00
Irreg_0_10m_2_55s	5.00	4.59	-8.1	18.00	16.55	1.00
Irreg_50yr_0_26m_2_26s	13.00	12.10	-6.9	16.00	16.55	1.91
Irreg_50yr_0_28m_2_55s	14.00	13.09	-6.5	18.00	17.82	1.24
Irreg_1yr_0_14m_1_83s	6.90	6.32	-8.4	12.92	12.87	1.10
Irreg_0_10m_1_63s_30_deg	5.00	4.65	-6.9	11.50	12.87	1.00
Irreg_0_10m_1_98s_30_deg	5.00	4.73	-5.3	14.00	13.63	1.00
Irreg_0_10m_2_55s_30_deg	5.00	4.63	-7.3	18.00	16.55	1.00

4.3.3 Diffraction analysis and hydrodynamic coefficients

The hydrodynamic diffraction characteristics of the floating platform were not recomputed in the present work but instead adopted from the reference model of the VolturnUS-S platform developed for the IEA 15-MW offshore reference wind turbine (Allen et al., 2020). In that reference definition, the hydrodynamic coefficients were obtained using the boundary-element method solver WAMIT, which is commonly used for frequency-domain analysis of floating structures.

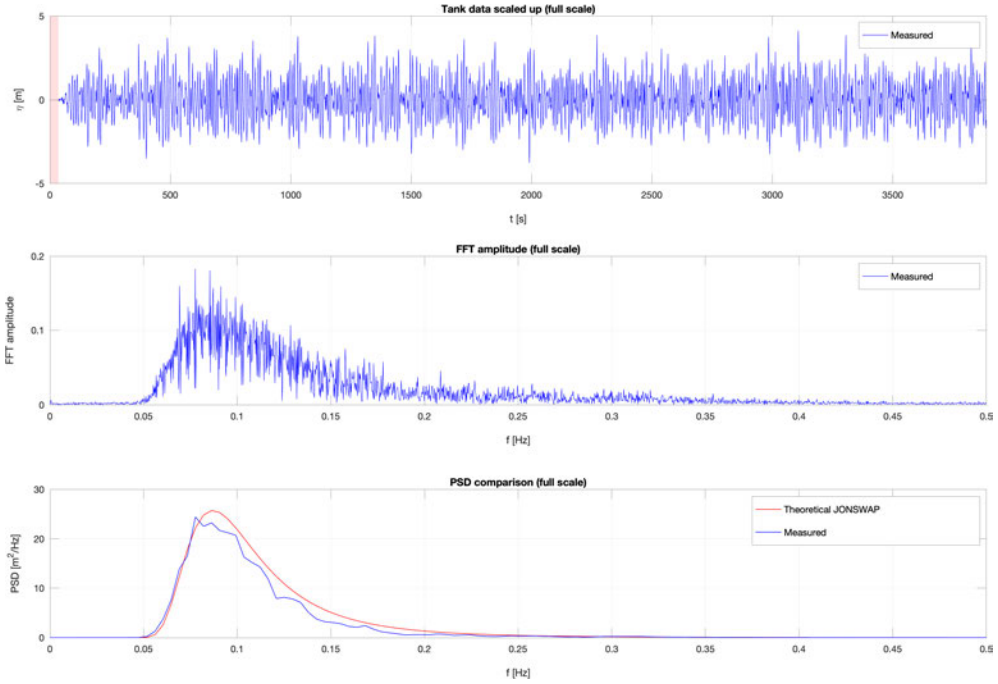

Figure 4.14: Irregular wave calibration example at 0° wave incidence showing the free surface elevation time series, FFT amplitude, and comparison between measured PSD and theoretical JONSWAP spectrum ($H_s = 5$ m, $T_p = 11.5$ s).

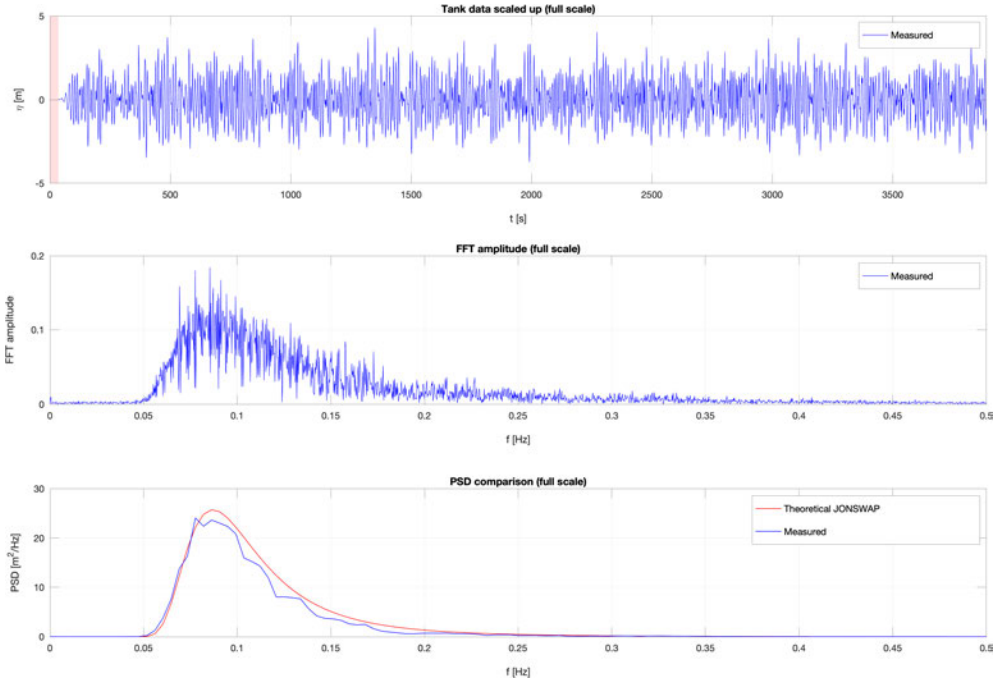

Figure 4.15: Irregular wave calibration example at 30° wave incidence showing the free surface elevation time series, FFT amplitude, and comparison between measured PSD and theoretical JONSWAP spectrum ($H_s = 5$ m, $T_p = 11.5$ s).

The WAMIT analysis provides the frequency-dependent hydrodynamic quantities required for time-domain simulations of floating offshore wind turbines, including added mass, radiation damping, and first-order wave excitation forces. These coefficients are computed by solving the linear potential-flow diffraction and radiation problem for the platform geometry under harmonic wave excitation. The resulting hydrodynamic data are supplied as hydrodynamic databases and can be directly implemented in aero-hydro-servo-elastic simulation tools such as OpenFAST.

For the VolturnUS-S reference platform, the WAMIT calculations were carried out for a range of wave frequencies and headings, producing the hydrodynamic transfer functions required to describe the platform response. The results include frequency-dependent added mass and radiation damping matrices as well as first-order wave excitation forces, which represent the primary hydrodynamic loading acting on the structure in linear wave theory (Allen et al., 2020). These coefficients form the basis of the diffraction model used in the numerical simulations presented in this work.

4.3.4 Mooring pre-tensions

The comparison begins with the mooring pre-tension between the physical model and the numerical configurations. In the adapted numerical model, the spring–rope mooring system was represented using equivalent linear stiffness properties, which produced a defined level of pre-tension at the fairleads. During the tank test setup, the physical spring–rope mooring system was adjusted to reproduce this target pre-tension as closely as possible. This approach ensured that the restoring characteristics of the experimental system were consistent with those assumed in the adapted numerical configuration.

In contrast, the original catenary mooring configuration generates pre-tension primarily through the submerged weight and geometric configuration of the mooring lines rather than through elastic stiffness. Consequently, the initial tension levels in the catenary model differ from those of the adapted configuration, reflecting the fundamentally different mechanisms by which pre-tension is produced in the two mooring systems.

The mooring pre-tension from the *OpenFAST adapted* system in static water is equal to 9.3 N at tank scale, which corresponds to 1162.8 kN at full scale. This value served as the target during the experimental setup. The final measured pre-tensions for the physical model are presented in Table 4.4. Notably, the experimental values show slight asymmetries between the lines, which do not occur in the idealised numerical model.

Table 4.4: Mooring line pre-tensions as measured in the physical experiment, converted to full-scale values. Refer to Figure 3.11 for line labels.

Scale	Fore (P_1A_1)	Starboard (P_2A_2)	Port (P_3A_3)
Tank	$9.67\ N$	$9.08\ N$	$9.97\ N$
Full	$1.21 \times 10^6\ N$	$1.14 \times 10^6\ N$	$1.25 \times 10^6\ N$

4.3.5 Natural frequencies and damping

Table 4.5 presents a comparison between the natural periods obtained from the physical model tests and those predicted by the numerical model in OpenFAST, considering both unmoored and moored conditions.

In the unmoored case, only three degrees of freedom are compared, since these are the only modes whose restoring force or moment does not depend primarily on the mooring system. For these modes, the agreement is generally good. In heave, the difference is only 0.5%, indicating that hydrostatics, vertical added mass, and scale density are well represented. This close agreement suggests that the vertical restoring behaviour of the platform is captured reliably without the influence of the mooring system.

In pitch and roll, the deviation is more pronounced (-11.4%), pointing to a mismatch in rotational inertia, hydrostatic water-plane properties, or added inertia effects. As discussed previously, the added-mass contribution around the pontoon caps is difficult to represent accurately using the potential-flow-based numerical model and may therefore be underestimated.

Table 4.5: Comparison of theoretical and experimental natural periods at full-scale.

Rigid-Body Model	Theoretical Natural Period (s)	Experimental Natural Period (s)	Difference (%)
No moorings attached			
Heave	20.4*	20.50	0.5%
Pitch	29.9*	33.3	-11.4%
Roll	29.9*	33.3	-11.4%
With moorings attached			
Surge	142.9	131.5	8.0%
Sway	142.9	164.7	-15.0%
Heave	20.4	19.45	4.7%
Roll	27.8	32.71	-17.7%
Pitch	27.8	32.18	-15.8%
Yaw	90.9	91.78	-1.0%

* Values estimated using the numerical model without mooring lines attached.

For the moored case, larger discrepancies are observed, particularly in the pitch and roll rotational modes. The most accurately represented mode remains yaw, with only a 1% difference. Surge and sway differ by $+8\%$ and -15%, respectively, while pitch and roll differ by approximately 16% to 18%. Although part of this mismatch may stem from modelling limitations or uncertainty in the hydrodynamic coefficients, a major contributor is the difference in mooring system representation.

In the tank, the original catenary mooring system was approximated using a spring–rope configuration, as explained in Section 3.3.9. The spring–rope system provides higher horizontal stiffness than an ideal catenary, resulting in a shorter experimental period in surge. Additionally, the vertical component of pretension in the spring–rope system introduces additional restoring stiffness in heave, reducing the experimental heave natural period from $20.50\,\mathrm{s}$ in the unmoored case to $19.45\,\mathrm{s}$ when moored. In contrast, the catenary representation in the numerical model has only a limited influence on heave because its vertical restoring contribution is small.

A more detailed examination of pitch and roll helps clarify the observed differences. In the catenary numerical model, the mooring system reduces the natural periods of these modes relative to the unmoored case, indicating an increase in rotational restoring stiffness. By contrast, the spring–rope configuration used in the experiment has a weaker influence on these rotational degrees of freedom. Consequently, the remaining discrepancy in pitch and roll is attributed both to the same sources identified in the unmoored case, namely uncertainties in inertia and added-mass representation, and to the different mooring restoring mechanisms.

To evaluate the impact of the mooring system simplification, further comparisons were made between the experimental results and a modified numerical model, referred to hereafter as the *Adapted* configuration. In this adapted version, the numerical mooring system was modified to better reproduce the spring–rope restoring behaviour used in the tank tests. The comparison is presented in Table 4.6. The adapted mooring system produces natural periods much closer to the experimental values than the original catenary representation. In particular, the surge mode differs by only 0.4%, while pitch and roll also show improved agreement.

In pitch and roll, the adapted mooring system does not impose the same rotational stiffness as the catenary configuration, resulting in higher numerical natural periods and therefore closer agreement with the experimental observations. In heave, however, the adapted model still predicts the same natural period as the unmoored numerical case, indicating that the numerical mooring representation does not reproduce the additional vertical restoring contribution observed experimentally. This is consistent with the experimental reduction in heave period from $20.50\,\mathrm{s}$ to $19.45\,\mathrm{s}$, which demonstrates that the physical mooring system contributes additional effective stiffness in the vertical direction.

Overall, the adapted system provides a clearer improvement over the original catenary model. The yaw mode continues to show near-exact agreement, reflecting its limited sensitivity to the mooring representation, while sway remains the least well matched mode, with a difference of 19.8%.

Rigid-Body Model	Experimental Natural Period (s)	MoorDyn Adapted Mooring Natural Period (s)	Difference (%)
Surge	131.5	132.1	-0.4%
Sway	164.7	132.1	19.8%
Heave	19.45	20.4	-4.9%
Roll	32.71	29.1	11.0%
Pitch	32.18	29.1	9.6%
Yaw	91.78	92.2	-0.4%

Table 4.6: Comparison of experimental and MoorDyn adapted mooring natural periods at full-scale.

This highlights the importance of accurately replicating the mooring stiffness and restoring behaviour when validating numerical models against physical tests. Crucially, the objective here is not to reproduce the full-scale catenary mooring system like-for-like in the basin, but to obtain a faithful representation of its global response within tank limitations, including water depth, footprint, and allowable loads, using a spring–rope surrogate. Accordingly, the adapted model, which reflects this surrogate, more successfully captures the influence of the tank configuration and is therefore the more appropriate baseline for the subsequent comparative analyses.

In addition to the natural periods, the damping behaviour of the system was assessed through decay tests. Damping is reported here in terms of the damping ratio rather than linear and quadratic fitted coefficients, as the damping-ratio comparison provides a more robust and physically interpretable measure of decay behaviour for the present dataset.

Table 4.7 summarises the damping ratios obtained from the experimental tank tests and the OpenFAST decay simulations. In the unmoored case, the experimental damping ratios are consistently higher than the numerical values. Heave shows a damping ratio of 0.036 in the tank compared with 0.0063 in OpenFAST, indicating that the numerical model substantially underestimates the energy dissipation in vertical motion. Pitch and roll show similar trends, with experimental damping ratios of 0.014 and 0.028, respectively, compared with 0.01 in the numerical model.

With moorings attached, the experimental damping ratios increase further, reaching 0.054 in heave, 0.053 in pitch, and 0.068 in roll. These values are substantially larger than the corresponding numerical values of 0.0063, 0.01, and 0.01. This behaviour confirms that the physical system dissipates significantly more energy than the numerical model predicts. The additional damping is attributed to mechanisms not fully represented in the simulation such as viscous drag around the columns and pontoons.

When moorings are present, damping ratios could also be estimated experimentally for the horizontal degrees of freedom. The tank tests yield damping ratios of 0.038 in yaw, 0.38 in sway, and 0.40 in surge. These values are substantially larger than the numerical predictions of 0.045, 0.098, and 0.098, respectively. In particular, the high damping observed in surge and sway reflects the strong energy dissipation introduced by the spring–rope mooring system, which heavily damps horizontal motions in the basin environment.

No additional damping tuning was performed in this study. The aim of the present work is not to produce a fully calibrated hydrodynamic model, but to compare the influence of different wind load actuation approaches under a consistent numerical baseline. Introducing empirical damping corrections would improve agreement with the experimental decay tests, but would also add calibration parameters that are not central to the research question addressed here. The damping discrepancies identified in this section are therefore acknowledged as a modelling limitation and taken into account in the interpretation of the response comparisons presented in the following sections.

Table 4.7: Comparison of damping ratios obtained from experimental and numerical decay tests.

DOF	Tank, no moorings	Tank, with moorings	OpenFAST Adapted, with moorings
Heave	0.036	0.054	0.0063
Pitch	0.014	0.053	0.0100
Roll	0.028	0.068	0.0100
Yaw	–	0.038	0.0450
Sway	–	0.38	0.0980
Surge	–	0.40	0.0980

The overall trend is clear: the experimental model exhibits stronger damping than the numerical model, particularly once the mooring system is present. This implies that the numerical model is likely to decay too slowly and may therefore overestimate the persistence of platform oscillations in some conditions. However, because the primary objective of this work is to compare wind actuation methods rather than to obtain perfect absolute agreement with the decay behaviour, these discrepancies do not invalidate the subsequent comparative analysis. Instead, they define the level of residual model bias that should be kept in mind when interpreting the response differences in the following sections.

With the natural frequencies and damping behaviour established, the following section presents a comparative analysis of the system response under regular wave excitation, considering both numerical mooring configurations and the experimental results.

4.3.6 No Wind Load: RAO and Extreme Wave Validation of Mooring System Representations

This section presents a comparative analysis of the numerical and experimental results for two wave conditions in the absence of wind loading. The goal is to validate the ability of the numerical models to replicate the hydrodynamic response of the physical system, with a particular focus on the representation of the mooring system.

Response Amplitude Operators (RAOs) are evaluated for both a small wave height (1 m full-scale), where linear behaviour is expected to dominate, and a larger wave height (4 m full-scale), which introduces more pronounced non-linear effects. The numerical models considered include the original catenary mooring configuration and the adapted semi-taut system designed to replicate the experimental spring–rope setup. In addition, the three configurations—experimental, catenary, and adapted—are also compared under selected extreme wave conditions to assess their performance in highly non-linear regimes. These comparisons aim to assess the fidelity of each numerical representation in capturing the motion response of the floating system across a range of sea states.

Response Amplitude Operators

Figures 4.16, 4.17, and 4.18 present the RAO magnitude comparisons for surge, pitch, and heave across both wave heights. In surge, the two numerical curves nearly coincide across the full frequency range, with the adapted mooring model exhibiting slightly larger RAOs than the catenary configuration. This behaviour aligns with the natural period agreement observed earlier: both numerical models have similar horizontal stiffness, but the adapted mooring slightly better reflects the tank behaviour.

Agreement between numerical and experimental results is generally good between approximately 0.05 Hz and 0.20 Hz, with differences typically below 10%. However, at the lowest frequencies (0.03–0.05 Hz), the experimental RAOs exceed the numerical values by approximately 30% to 70%, reaching values above 2.0 m/m compared to 1.2–1.3 m/m numerically. This deviation appears systematic, as it is observed consistently at both $H = 1$ m and $H = 4$ m wave heights.

Since the surge natural period is already matched (with a relative difference of $\Delta T \approx -0.4\%$), the low-frequency underestimation in the numerical results is likely not related to horizontal stiffness mismatches. Instead, it suggests excess effective inertia or damping, or underpredicted excitation in the hydrodynamic model. Contributing factors may include slightly over-

estimated added mass or radiation damping, the absence of second-order excitation effects and mooring–geometry coupling, or small-scale tank effects such as wave reflections or set-down at long periods. The minimal dependence on wave height supports the observation that surge remains largely linear in this range.

In pitch (Figure 4.17), both numerical mooring variants yield similar results and systematically under-predict the experimental RAO at the lowest frequencies. Around $f \approx 0.030$–0.045 Hz, the experimental RAOs reach their highest values, while both numerical models exhibit smaller responses, with the adapted mooring curve lying marginally above the catenary one.

The longer pitch natural period measured in the tank demonstrates that the ratio $(I_{55} + A_{55})/k_{55}$ is larger in the experiment than in the numerical model. The natural period of the pitch mode can be expressed as

$$T_n = 2\pi\sqrt{\frac{I_{55}+A_{55}}{k_{55}}},$$

which shows that an increase in the effective inertia $I_{55} + A_{55}$, a reduction in the restoring stiffness k_{55}, or a combination of both will lead to a longer natural period. This therefore indicates that the experimental platform behaves either as a system with larger rotational inertia, a weaker pitch restoring moment, or both, compared with the numerical model.

For very low wave frequencies $f < 0.05$ Hz (i.e. $\omega \ll \omega_n$), the terms $-\omega^2(I_{55}+A_{55})$ and $i\omega C_{55}$ in the RAO denominator become small relative to the restoring term k_{55}, so the response simplifies approximately to RAO $\approx M_{55}^{\mathrm{ex}}/k_{55}$. Consequently, the smaller k_{55} in the experiment directly produces the larger low-frequency pitch amplitude observed in the RAO results.

Although the tank tests exhibit higher damping ratios than the numerical simulations, the damping term appears in the denominator as $i\omega C_{55}$ and therefore diminishes as $\omega \to 0$, meaning it has only a minor influence in this frequency band. Thus the experimental platform's weaker pitch stiffness and, to a lesser degree, its slightly higher inertia, account simultaneously for its longer natural period and its higher low-frequency RAO.

Both the experiment and the OpenFAST simulation show that the pitch RAO decreases as the incident-wave height rises from $H = 1$ m to $H = 4$ m. In the tank, the drop comes from quadratic viscous drag and second-order hydrostatics. The numerical model reproduces the same trend even though its hydrodynamics are based primarily on WAMIT potential-flow coefficients. Two mechanisms contribute to this behaviour: (i) HydroDyn applies user-specified quadratic viscous damping coefficients whose contribution grows with $|\dot{\theta}|\dot{\theta}$, and (ii) MoorDyn solves the line geometry nonlinearly, so pretension and tangent stiffness increase with platform pitch. As wave height quadruples, these nonlinear mechanisms, quadratic damping and mooring

geometric stiffening, limit the pitch motion, causing the simulated $H_{55}(f)$ to decrease with amplitude similarly to the experiment, even though the absolute RAO level remains slightly lower owing to a somewhat higher baseline pitch stiffness and conservative damping representation in the numerical model.

Above 0.05 Hz, the response is governed primarily by inertia and linear radiation damping, both of which are largely independent of wave height. The nonlinear effects that separate the $H = 1$ m and $H = 4$ m cases at lower frequencies, such as rope stiffening and quadratic drag, become negligible once $\omega \gg \omega_n$. As a result, the RAO curves converge and remain almost identical from 0.05 to 0.20 Hz, where the response is dominated by linear potential-flow hydrodynamics.

In heave (Figure 4.18), the experimental and numerical RAOs exhibit good agreement across most of the frequency range. Excluding a few isolated numerical spikes near the heave resonance ($f \approx 0.05$ Hz), the three curves show consistent trends. The adapted mooring model tracks the experimental response slightly better than the catenary model. For frequencies above 0.07 Hz, the differences are generally within $\lesssim 10\%$ for both wave heights, indicating that the off-resonance heave response is well captured by both numerical configurations.

Around the resonance peak, the experimental RAO is slightly higher than both numerical predictions, with the adapted-mooring curve lying closest and the catenary case slightly lower. This modest residual uplift aligns with the earlier damping characterisation: although the natural period matches well between models, the experimental system displays substantially stronger overall damping, as reflected in the larger decay-test damping ratios. To produce comparable response amplitudes, this suggests either a slightly larger effective excitation force or a smaller effective inertia in the physical system than represented numerically.

This discrepancy is most plausibly attributed to a combination of: (i) under-predicted wave excitation and added-mass/radiation terms in the hydrodynamic database, and (ii) minor tank effects, such as wave set-down or residual reflections that marginally enhance measured motion at long periods. The occasional sharp peaks in the numerical RAOs reinforce this interpretation, pointing to spectral-estimation artefacts (e.g., limited steady-state cycles, windowing, or frequency discretisation).

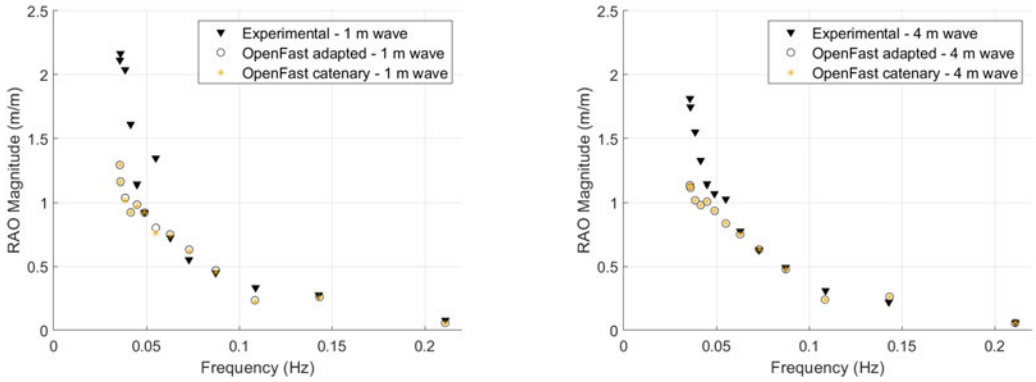

(a) 1 m wave height **(b)** 4 m wave height

Figure 4.16: Comparison of RAOs for Surge at 1 m and 4 m wave heights, comparing experimental results with both numerical mooring configurations.

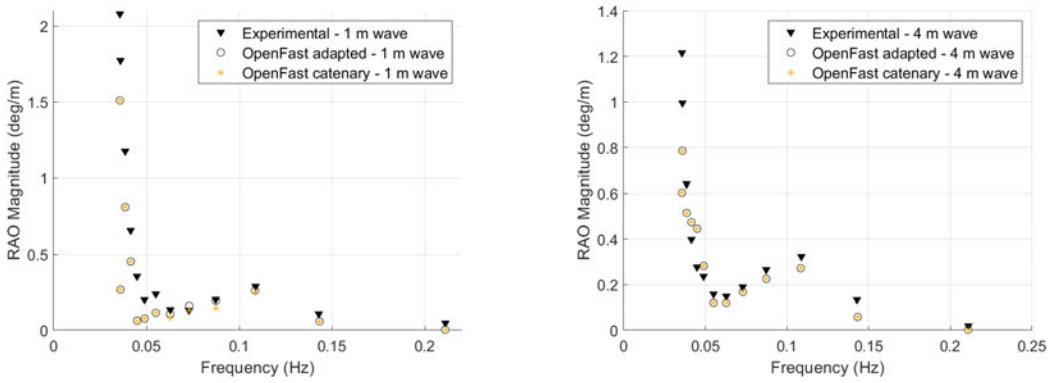

(a) 1 m wave height **(b)** 4 m wave height

Figure 4.17: Comparison of RAOs for Pitch at 1 m and 4 m wave heights, comparing experimental results with both numerical mooring configurations.

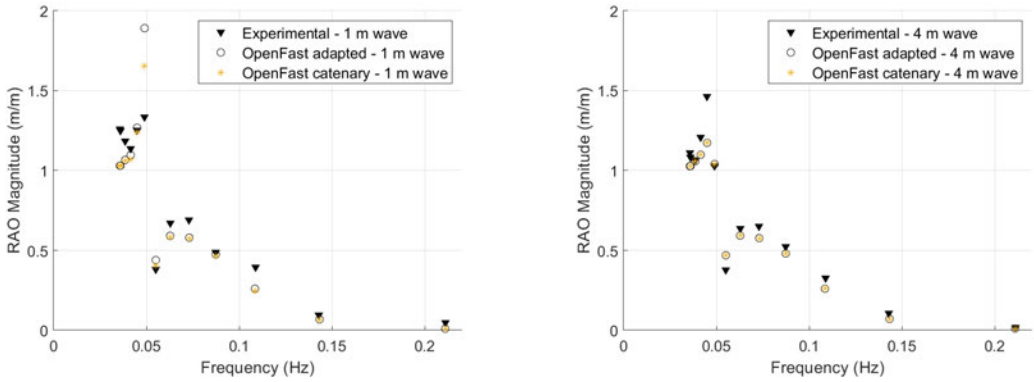

(a) 1 m wave height **(b)** 4 m wave height

Figure 4.18: Comparison of RAOs for Heave at 1 m and 4 m wave heights, comparing experimental results with both numerical mooring configurations.

To further quantify the agreement between experimental and numerical results, RAO magnitude ratios were computed as the ratio between the experimental values and those obtained from the numerical simulations. These are presented in Figures 4.19, 4.20, and 4.21 and quantify the level of agreement between experimental results and the two numerical models: OpenFAST with the original catenary mooring system and OpenFAST with the adapted spring-rope configuration.

In surge (Figure 4.19), experimental-to-numerical RAO ratios exceed unity at low frequencies ($f \lesssim 0.035{-}0.045\,\text{Hz}$), reaching $\sim 1.5{-}2.0$ for $H = 1\,\text{m}$ and $\sim 1.3{-}1.7$ for $H = 4\,\text{m}$. This suggests under-predicted excitation or excess damping in the numerical models, rather than a stiffness mismatch. Above $0.05\,\text{Hz}$, ratios cluster near unity (within approximately $\pm 10\%$), confirming good agreement. The adapted mooring slightly improves alignment, but differences at very low frequency remain linked to hydrodynamic excitation and inertia modelling rather than mooring stiffness.

For pitch (Figure 4.20), the ratio plots confirm the trends observed in the RAO magnitudes: the experimental model shows higher response at low frequencies due to lower pitch stiffness or higher inertia. Agreement improves above resonance, and both numerical models yield similar results, with the adapted mooring slightly closer to the experimental data.

In heave (Figure 4.21), the ratios remain close to unity across the frequency range, reinforcing that the adapted and catenary models perform similarly. Minor deviations near resonance and at high frequencies are consistent with those previously noted in the RAO plots.

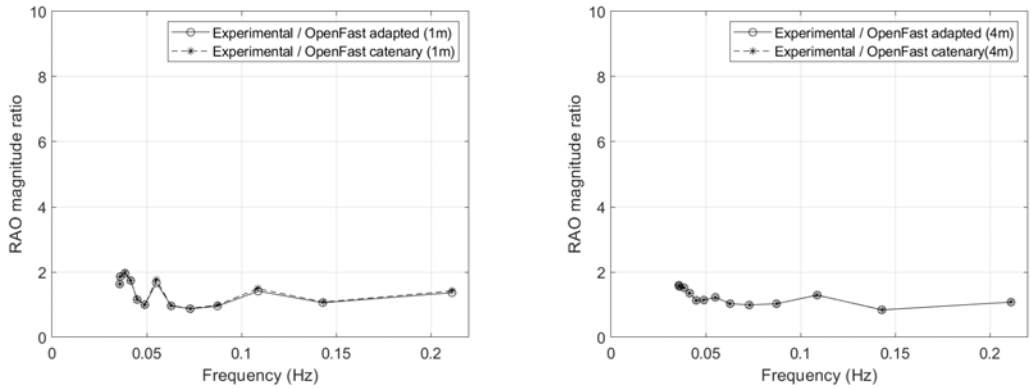

(a) 1 m wave height **(b)** 4 m wave height

Figure 4.19: Ratio of RAOs for Surge at 1 m and 4 m wave heights, comparing experimental results with the two numerical models (OpenFAST catenary and OpenFAST adapted).

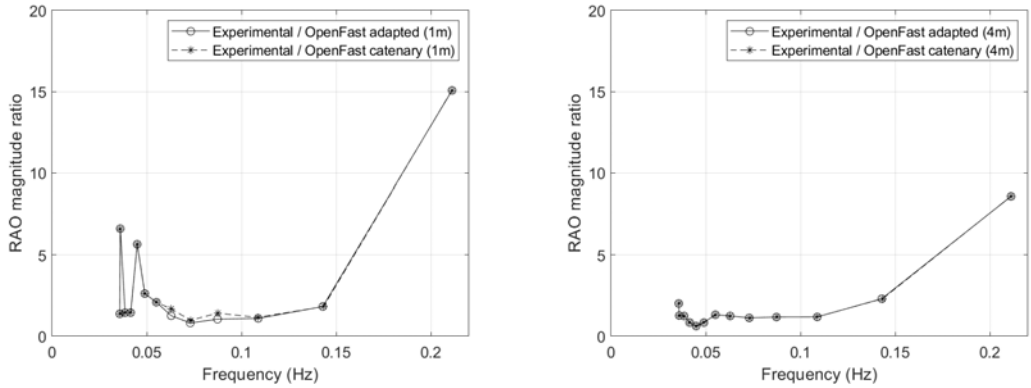

(a) 1 m wave height **(b)** 4 m wave height

Figure 4.20: Ratio of RAOs for Pitch at 1 m and 4 m wave heights, comparing experimental results with the two numerical models (OpenFAST catenary and OpenFAST adapted).

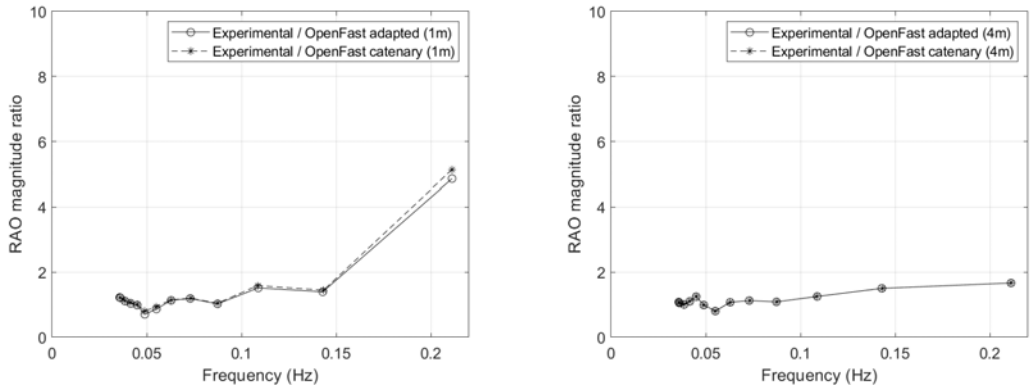

(a) 1 m wave height **(b)** 4 m wave height

Figure 4.21: Ratio of RAOs for Heave at 1 m and 4 m wave heights, comparing experimental results with the two numerical models (OpenFAST catenary and OpenFAST adapted).

Overall, the RAO and ratio comparisons demonstrate good agreement across the primary energy band (approximately 0.05–0.20 Hz), with typical differences under 10–15%. The adapted semi-taut mooring slightly improves the numerical match to the experimental results. Residual discrepancies occur mainly at low frequencies, where the experiments show larger surge and pitch motions. These are attributed to the combined effects of pitch stiffness and inertia imbalance and to limitations in the hydrodynamic excitation and inertia modelling, rather than to mooring stiffness in surge.

In heave, the mismatch remains minor, suggesting that vertical restoring behaviour is accurately captured, and remaining offsets likely stem from added-mass or excitation discrepancies. The ratio plots reinforce these findings: values greater than one at low frequencies, near unity through the mid-frequency band, and artificially elevated ratios in the high-frequency tail due to numerical RAOs tending toward zero. These insights establish a solid reference for interpreting the extreme-wave results, while highlighting that caution is warranted in surge and pitch at very low frequencies, where the experimental platform remains more responsive than either numerical model.

Extreme Waves

The comparison of platform motions and mooring line tensions under three extreme sea states between the numerical models and the experimental results was also conducted (Figures 4.22 and 4.23). For the statistical presentation of the results, mean values with error bars indicating ± 1 standard deviation are used, rather than boxplots.

This choice facilitates direct comparison across categories and wave conditions, particularly when the number of samples per case is limited. It also maintains consistency with earlier RAO-based analyses, which focus on central tendency and overall variability. While boxplots are useful for visualising distribution shape and identifying outliers, the mean $\pm$ standard deviation representation more directly conveys the average response and typical spread, metrics that are more relevant for evaluating agreement between experimental and numerical results in this context.

The observed results reflect the increasing severity of the wave conditions applied. Wave I ($H_s = 6.9$ m, $T_p = 12.92$ s, $\gamma = 1.10$), Wave II ($H_s = 13$ m, $T_p = 16$ s, $\gamma = 1.91$) and Wave III ($H_s = 14$ m, $T_p = 18$ s, $\gamma = 1.24$) were selected to represent 1-year and 50-year return periods as explained in Section 3.1.2. There is little energy in the spectrum at the natural frequencies previously identified in Section 4.3.5.

For pitch, the experimental results show a consistent negative mean across all three extreme seas (approximately –1.3° to –1.5°), with relatively narrow standard deviations ($\sigma \approx 0.6$–0.8°). This stable mean suggests a steady second-order trim caused by low-frequency wave drift moments, bounded by comparatively strong linear damping.

In contrast, the OpenFAST adapted model (semi-taut mooring) exhibits a positive mean in Wave I ($\approx +0.7^\circ$), i.e., opposite in sign, and a less pronounced negative pitch in Waves II–III (around –0.6° to –0.7°). The standard deviations are much larger than experimental values ($\sigma \approx 2$–2.3°), reflecting under-damping in the model. This is consistent with the damping characterisation presented earlier: the experimental model exhibited substantially higher pitch damping ratios than the numerical simulations, leading to faster decay and smaller motion variability in the tank tests. The sign error in Wave I points to a bias in the balance of low-frequency pitch moments, between wave-drift excitation and rotational restoring, which the adapted mooring does not capture at lower sea states.

The OpenFAST catenary model produces mean values closer to the experimental results (around –1.5° for all three seas), though the standard deviations remain elevated relative to the experimental results but lower than in the adapted model. This implies that, although the catenary setup is nominally stiffer in pitch (shorter natural period), the combination of excitation and damping yields a better net trim prediction.

Overall, both numerical models overestimate the variability in pitch response, with the adapted configuration also underestimating the mean pitch. These differences are most pronounced under extreme wave conditions and are consistent with earlier findings that the experimental system features less stiffness in pitch, stronger overall damping, as reflected in the higher experimental damping ratios, and a different excitation balance in pitch than either numerical variant.

For surge, both numerical models predict a larger mean forward offset than measured experimentally, with the adapted mooring configuration producing values consistently closer to the tank data. The mean surge positions rise across the three sea states from approximately 1.0 m (experiment) versus 1.5 m / 2.1 m (adapted / catenary) in Wave I, to 2.4 m (experiment) versus 3.0 m / 3.3 m in Wave II, and 2.0 m (experiment) versus 2.8 m / 3.1 m in Wave III. This suggests that the numerical models predict a stronger net low-frequency drift force, or slightly lower horizontal restoring, resulting in a higher quasi-static surge offset. The adapted semi-taut mooring reduces this discrepancy, consistent with the earlier surge natural-period agreement.

The experimental and adapted models have similar standard deviations, whereas the catenary model's deviations are lower. The catenary mooring, which provides the greatest horizontal restoring force (i.e., it is the stiffest configuration), therefore exhibits more tightly clustered surge excursions. By contrast, the experimental spring–rope system and the adapted semi-taut model are softer in surge, so their responses spread more widely around the (smaller) mean offsets.

For heave, the mean vertical offsets remain small across all cases, indicating that hydrostatic restoring is well represented in both numerical and experimental setups. The experimental means cluster close to zero with a slight downward bias, while the adapted numerical model presents a small positive mean (≈ 0.7–0.8 m) and the catenary model shows a small negative mean (≈ -0.1–-0.2 m). All values lie within $\lesssim 0.8$ m of one another, and there is no systematic increase in mean offset with sea severity. This supports earlier findings that heave stiffness and natural period are well matched, and that vertical second-order set-down effects are limited.

The standard deviations (σ) increase with sea severity, but their relative ordering varies: in Wave I, both numerical models and the experimental results exhibit similar σ values, while in Waves II–III the experimental σ becomes largest, the adapted model remains comparable, and the catenary model is slightly narrower. This behaviour is consistent with the RAO analysis: experimental heave retains more energy near resonance in longer, more energetic seas,

while numerical predictions are sensitive to excitation and added-mass modelling. Overall, agreement in heave is good, with the adapted mooring tracking the experimental behaviour most closely; residual differences are attributable primarily to hydrodynamic forcing representation rather than vertical stiffness mismatches.

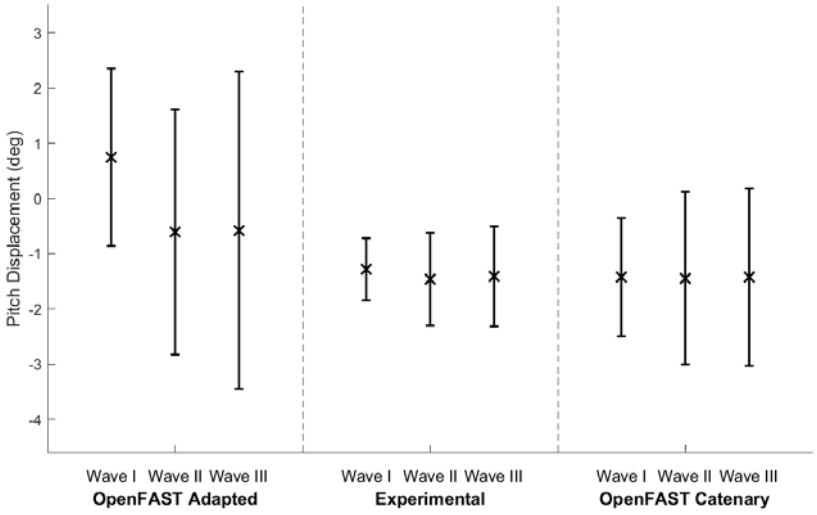

(a) Pitch displacement comparison

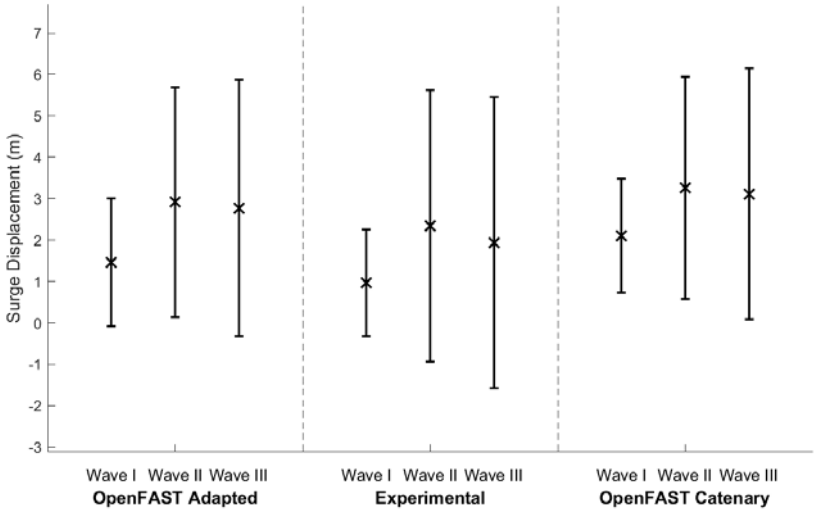

(b) Surge displacement comparison

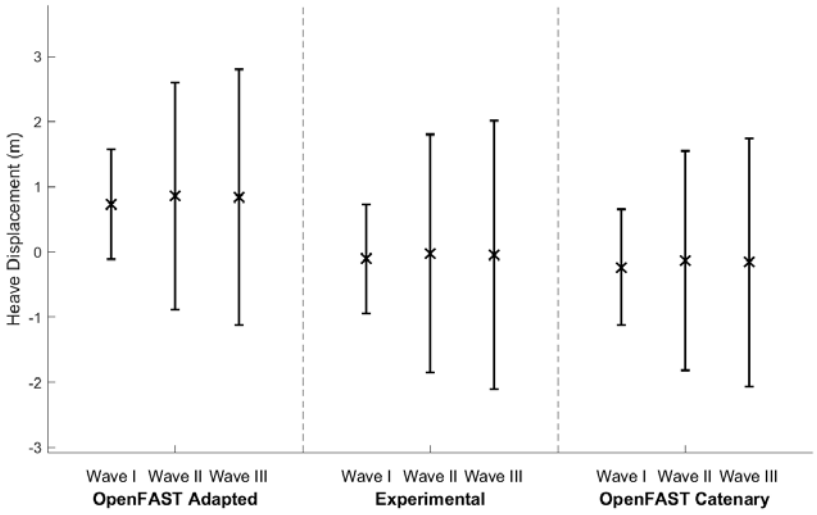

(c) Heave displacement comparison

Figure 4.22: Comparison of pitch, surge, and heave displacements under 3 extreme sea states.

In the interpretation of the mooring line tensions results shown in Figure 4.23, **F** denotes the Fore mooring line, **P** the Port line, and **S** the Starboard line. Across all three extreme sea states, the ordering of line loads aligns with the wave heading: F $>$ S $\approx$ P in terms of mean tension, with the fore line carrying the largest share of the drift-induced load. The adapted semi-taut numerical model captures both this hierarchy and the approximate magnitudes, while the catenary model over-predicts all three line tensions by roughly a factor of two.

For *Wave I* results, the experimental mean tensions are approximately 1.15 MN (F), 0.95 MN (P), and 1.05 MN (S). The adapted model returns about 1.25 MN, 1.10 MN, and 1.10 MN respectively, representing a 5–$15\,\%$ overestimation. In contrast, the catenary model gives values around 2.45–2.55 MN for all three lines, over-predicting by roughly $120\,\%$.

For *Wave II*, the experimental means increase slightly to ≈ 1.25 MN (F), 1.0 MN (P), and 1.05 MN (S). The adapted model remains within 10–$15\,\%$ of these values, while the catenary model again predicts 2.3–2.7 MN, maintaining a similar overestimation.

Lastly, for *Wave III*, the same pattern holds: the adapted model stays within 10–$15\,\%$ of the experimental means, while the catenary predictions remain approximately double the measured values.

The standard deviation bars are small relative to the means in all cases. However, experimental spreads are slightly wider than those of the adapted model, and comparable or larger than the catenary model. This is consistent with earlier findings: numerical simulations under-predict low frequency surge variability, resulting in narrower load excursions about the mean. The persistent over-prediction by the catenary model reflects its higher horizontal restoring and pretension, and the absence of mechanical dissipation mechanisms such as rope hysteresis and sheave friction, which are present in the tank and reduce load amplitudes. The adapted semi-taut mooring system, tuned to the spring-rope quasi-static stiffness of the physical setup, reproduces both the load-sharing across lines and the mean levels to within engineering accuracy. The residual 10–$15\,\%$ positive bias can be attributed to the remaining forward surge offset and the lack of damping in the numerical mooring model.

The gravity-dominated restoring of the catenary model drives uniformly high pretensions and thus over-predicts mean loads in all lines, masking directional load sharing; the EA-dominated semi-taut representation restores the observed asymmetry and brings mean levels close to the measurements.

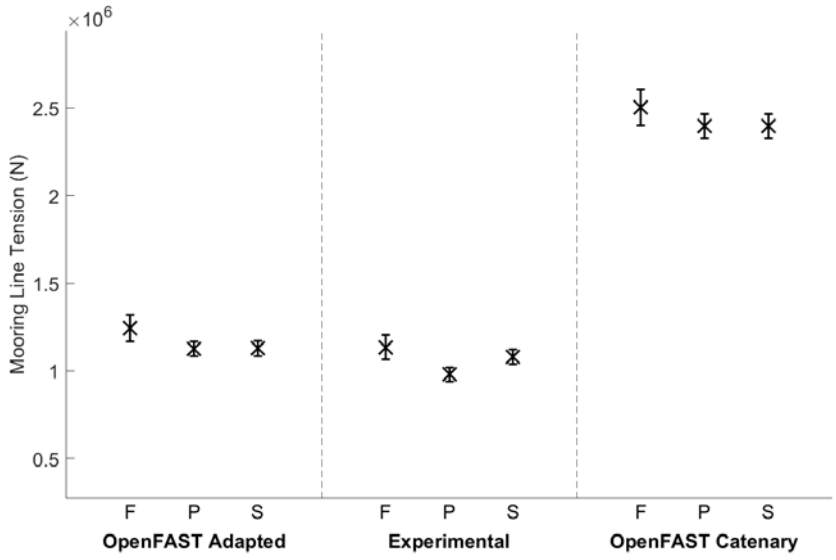

(a) Wave I

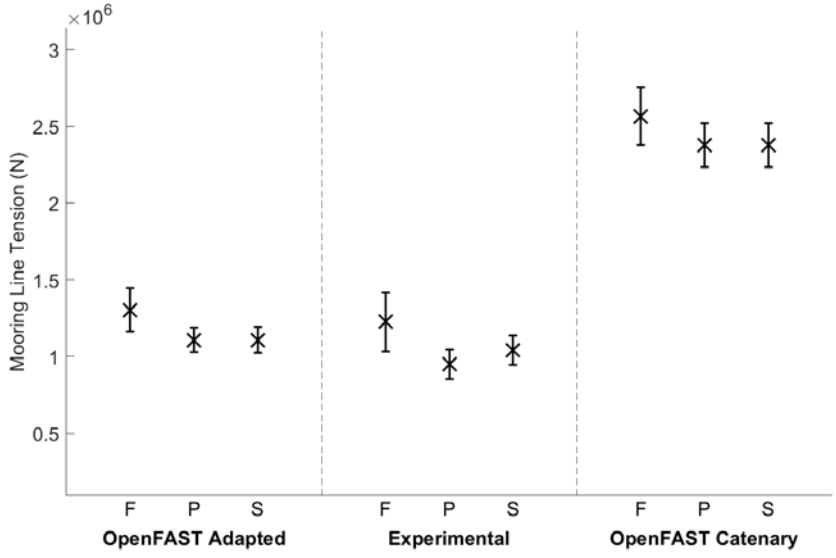

(b) Wave II

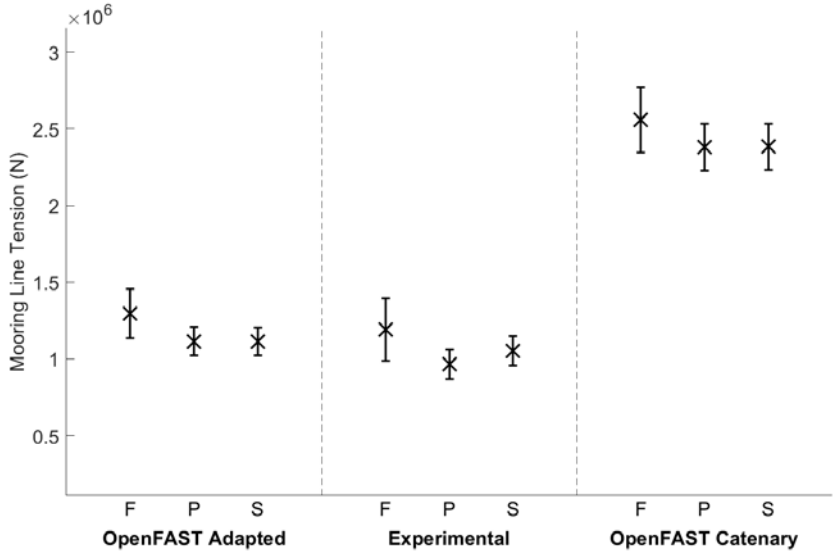

(c) Wave III

Figure 4.23: Comparison of mean fairlead mooring line tensions for the Fore (F), Port (P), and Starboard (S) lines under the three extreme wave conditions. Error bars show ± 1 standard deviation.

These results confirm that the adapted mooring is the appropriate numerical configuration for comparison with the basin data, while the original catenary layout is overly stiff and too highly pretensioned for this experimental setup.

This improved agreement can be attributed to the fact that the adapted model was specifically tailored to replicate the physical tank setup in surge. The scaled mooring stiffness matrix shown in Table 4.8 represents the target values, while the actual values implemented in the adapted mooring system are illustrated in Figure 4.24. The adapted mooring configuration also accounts for the actual tank depth, the anchor positions used during the test campaign, and, crucially, the linear stiffness properties of the spring-rope mooring system implemented in the basin.

Table 4.8: Scaled mooring linear stiffness matrix, **m** (N/m, N/rad, N, and Nm/rad).

	Surge	Sway	Heave	Roll	Pitch	Yaw
Surge	29.26	0	0	0	9.23	0
Sway	0	29.26	0	-9.23	0	0
Heave	0	0	24.44	0	0	0
Roll	0	-9.22	0.01	41.7	0	0
Pitch	9.22	-0.01	0	0	41.7	0
Yaw	0	0	0	0	0	40.88

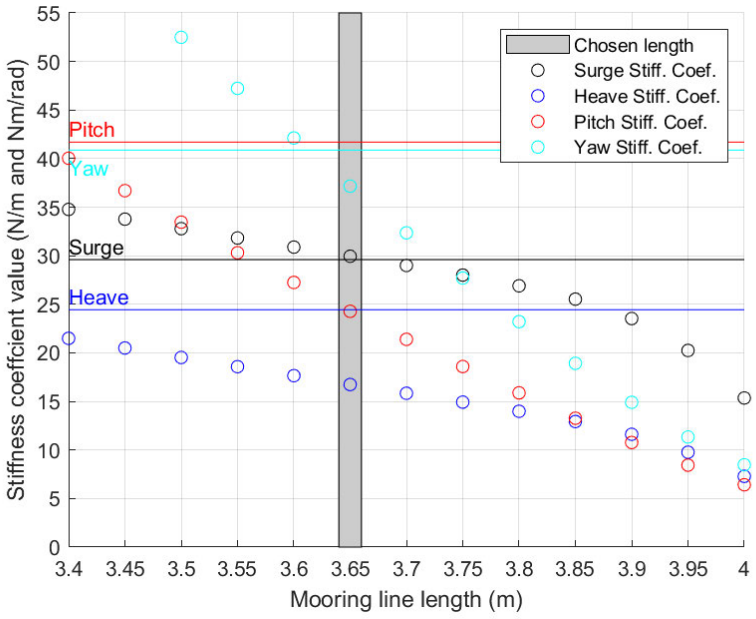

Figure 4.24: Stiffness coefficient values in surge, heave, pitch and yaw, obtained when changing the line length input value in MAP++ input file. Grey area represents the values for the chosen line length. The horizontal lines labelled with the respective DOF represent to the target value from the linear stiffness matrix (Table 4.8).

Based on the collective evidence from natural period matching, RAO behaviour, extreme wave response and mooring line tensions, the adapted semi-taut mooring configuration is adopted as the reference numerical model for subsequent analyses. This configuration reproduces the experimental surge and yaw periods within $\pm 0.5\,\%$, and heave within $\approx 7\,\%$, with improved correspondence in pitch and roll compared to the catenary model.

Across both RAO and extreme-wave comparisons, the adapted model yields closer agreement in response amplitude and variability, particularly capturing the correct load-sharing hierarchy in mooring tensions (Fore $>$ Starboard $\approx$ Port) and reducing the overestimation observed with the catenary layout.

While residual discrepancies remain (most notably an under-prediction of low-frequency surge and under-response in pitch due to damping partitioning), the adapted mooring better reflects the experimental setup. These remaining gaps will be accounted for in subsequent wind-loading comparisons by quoting appropriate uncertainty ranges and acknowledging the conservative limitations of the numerical damping representation.

4.4 Effect of Wind Actuation Method on Platform Response

Having established an adapted numerical model as the comparative basis, the following sections compare the dynamic response of the platform under different wind actuation methods. Three approaches were tested experimentally as described in Section 3.3.8: a static weight system, a constant thrust setup, and a Software-in-the-Loop (SIL) system. These configurations represent increasing levels of complexity and fidelity in simulating aerodynamic loads. All the other tank test conditions were maintained exactly the same, including the model, mooring system and the wave basin used.

Throughout this section, the numerical model is used as a comparative reference rather than as a ground truth. Accordingly, closer agreement with the numerical prediction is interpreted only as consistency with that particular modelling framework, and not as proof of greater physical correctness.

To begin this comparison, RAOs are evaluated for each actuation method under rated and below-rated wind conditions. This step enables a systematic assessment of how the different wind actuation methods influence the measured response, and of the extent to which each method reproduces the dynamic trends observed in the coupled numerical model, without assuming the numerical prediction to be the true response. In this way, the suitability of simpler approaches, such as constant thrust or static weight, can be assessed against the objectives of the test campaign.

This section focuses on surge, heave, and pitch. With wind and waves collinear at 0°, the platform's global motions are primarily in the along-wind plane. Pitch and surge are directly influenced by wind thrust and mooring system dynamics, respectively, while heave plays a key role in vertical wave loading and potential coupling with pitch motion. These DOFs typically exhibit the highest response amplitudes in operational and extreme sea states, when the environmental conditions tested are co-aligned and are the most sensitive to changes in wind actuation. In contrast, sway, roll, and yaw responses are generally smaller in magnitude for symmetric wind and wave loading conditions. Therefore, surge, pitch, and heave offer the most relevant basis for assessing the effectiveness of different aerodynamic load application strategies.

4.4.1 Response Amplitude Operators

The following subsections systematically present RAOs for surge, pitch, and heave across the tested actuation methods and wind speeds, highlighting key differences in amplitude and frequency-dependent behaviour.

RAOs at rated wind speed - Platform Surge

Figure 4.25 shows the RAOs for surge motion under two different wave heights: 1 m (left) and 4 m (right). Each subfigure compares the results from a range of different wind actuation methods and the numerical simulation approach. The label *H* refers to the tank test performed without any wind thrust applied, representing a baseline hydrodynamic-only response. The *Static weight* configuration corresponds to a tank test where an approximately constant mean thrust was applied through a suspended weight. In practice, the transmitted force is not perfectly constant, since small variations arise from the inertia of the moving mass and changes in cable geometry as the platform oscillates. The *PI* case refers to a test where the applied force was actively regulated by a motor controlled via a *PI* controller, simulating rotor thrust using a winch-based system. The *SIL* configuration represents a full Software-in-the-Loop (*SIL*) implementation, where the control logic governs the thrust in real time. Lastly, the *Adapted* results represent the OpenFast numerical model.

In the 1 m wave height case (Figure 4.25a), the tank test without wind actuation (*H*) exhibits the highest surge RAO magnitudes, particularly at low frequencies around 0.03–0.05 Hz. This reflects the absence of aerodynamic damping, allowing a more pronounced low-frequency surge response. Once wind thrust is introduced, either via approximately constant-thrust actuation (*Static weight* and *PI*) or dynamic feedback (*SIL*), the response is suppressed across the full frequency range. All experimental schemes show a similar trend of decaying RAO magnitude with increasing wave frequency, reaching very low values beyond 0.15 Hz.

Among the wind actuation methods, *SIL* consistently yields the smallest RAOs, followed by *PI* and *Static weight*, which are nearly coincident. This ordering is consistent with the amount of aerodynamic damping each method introduces. The *SIL* method includes motion feedback and more closely reproduces unsteady aerodynamic effects, while *Static weight* and *PI* provide primarily mean-thrust actuation, with the PI system actively regulating the applied load and the static-weight system only approximating a constant thrust level. The adapted numerical model with full aerodynamic coupling sits below all experimental curves at most frequencies, especially in the low-frequency range. This continues the trend observed in the no-wind comparisons. The numerical model already under-predicted response at very low frequency, and the inclusion of unsteady aerodynamic damping further suppresses surge motion. These effects are not fully replicated in the tank, particularly for the *Static weight* and *PI* methods, which aim to reproduce the correct mean thrust but do not fully emulate unsteady aerodynamics. Notably, the *SIL* actuation yields results that follow the numerical trend more closely than the other experimental methods.

In the 4 m wave height case (Figure 4.25b), the overall shape of the RAO curves remains consistent, a peak at low frequency followed by a gradual decay. The RAO magnitudes are generally lower than in the 1 m case, which may be attributed to non-linearities at higher amplitudes (already visible in the no-wind assessment) and/or increased mooring line restoring effects. The relative positions of the wind actuation schemes are preserved where the *SIL* produces the lowest responses, *Static weight* and *PI* sit above it, and the numerical model again remains lowest throughout most of the band. This reinforces that wind-induced damping effects are more pronounced under dynamic feedback (SIL), and that the numerical model captures the qualitative trends well.

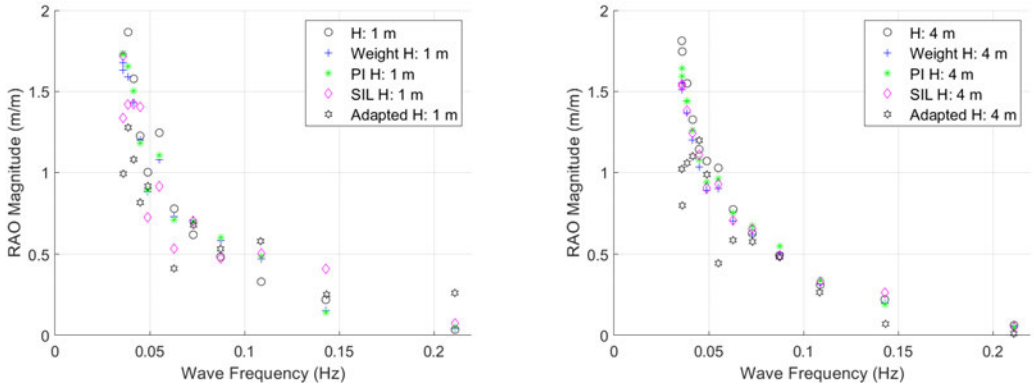

(a) RAOs for Surge at 1 m wave height. **(b)** RAOs for Surge at 4 m wave height.

Figure 4.25: RAOs for Surge at different wave heights under rated wind conditions.

RAOs at rated wind speed - Platform Pitch

The RAO results for pitch motion under rated wind conditions are presented in Figures 4.26a and 4.26b, corresponding to 1 m and 4 m wave heights, respectively. In both cases, the pitch RAO magnitudes follow the expected trend of decreasing with increasing wave frequency. At low frequencies ($f < 0.05$ Hz), the differences among actuation schemes are modest, and the curves remain close.

At 1 m wave height, all experimental wind actuation schemes (*Static weight*, *PI*, and *SIL*) produce significantly lower pitch RAOs than the no-wind baseline (*H*) in the low-frequency range. The responses across the three methods are closely grouped, indicating that even approximate mean-thrust emulation (*Static weight* and PI) introduces sufficient mean aerodynamic restoring to suppress pitch motion. The adapted numerical model under-predicts the RAO across the full frequency range, with the gap being most pronounced at low frequencies, consistent with previous observations that the experimental model is less stiff in pitch and the numerical model includes more linear damping but less quadratic damping than the experiment, and thus damps low-frequency pitch more aggressively. Also important to notice, that in the sensitivity analysis performed at the beginning of this chapter, the inclusion of only thrust could increase the pitch response by almost $17\,\%$.

At 4 m wave height, pitch RAO magnitudes are generally lower than in the 1 m case, though the hierarchy among actuation methods shifts. Interestingly, the *SIL* configuration shows the highest pitch RAOs at low frequencies, slightly above the *PI* and *Static weight* results. This may reflect the onset of non-linear pitch–aerodynamic interactions or saturation of the control-induced damping at higher wave amplitudes. The adapted numerical model continues to predict lower pitch motion at low frequency but again captures the overall shape of the response.

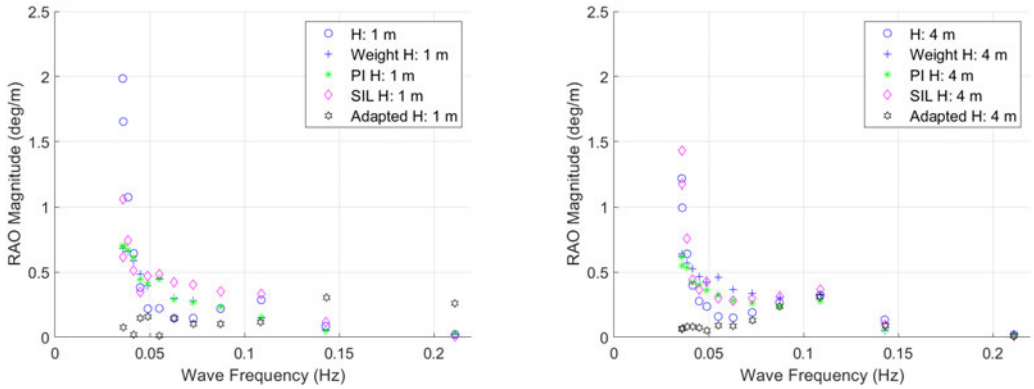

(a) RAOs for Pitch at 1 m wave height.

(b) RAOs for Pitch at 4 m wave height.

Figure 4.26: RAOs for Pitch at different wave heights under rated wind conditions.

RAOs at rated wind speed - Platform Heave

Figures 4.27a and 4.27b show the heave RAO magnitudes for the 1 m and 4 m wave height cases under rated wind conditions. Across both sea states, the overall response follows the expected behaviour: RAO magnitudes peak near the natural frequency and decay as frequency increases. The system's natural period in heave is approximately 20.4 s, corresponding to a frequency of $f \approx 0.049$ Hz, in agreement with both theory and the adapted numerical model.

Wind produces a modest reduction in heave RAOs compared to the no-wind experimental baseline, most visibly around the resonance region ($f \approx 0.05$ Hz). All three actuation methods, *Static weight*, PI, and *SIL* cluster closely together, typically 10–30 % below the no-wind values. Among them, *SIL* and *Static weight* tend to lie slightly below PI, suggesting subtle differences in their effective damping. This reduction is anticipated because while heave is not directly influenced by aerodynamic thrust, the pitch–heave coupling and slight changes in mooring pretension under wind can lead to increased effective damping and reduced excitation.

The adapted numerical model with full aerodynamics remains consistently below all experimental configurations across the frequency range and both wave heights. This continues the trend observed without wind. The numerical model under-predicts the heave RAO near the peak, and the addition of unsteady aerodynamic loads introduces further motion-dependent damping into heave through pitch coupling. This pushes the numerical response even lower. As a result, the gap between model and experiment widens slightly under wind.

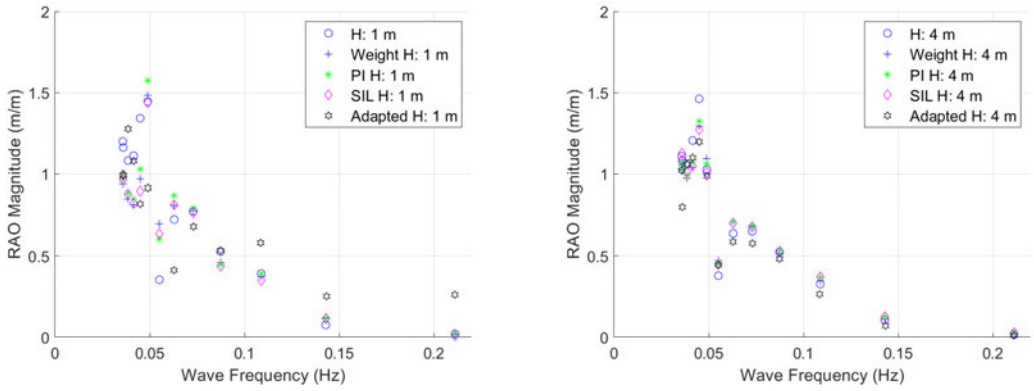

(a) RAOs for Heave at 1 m wave height. **(b)** RAOs for Heave at 4 m wave height.

Figure 4.27: RAOs for Heave at different wave heights under rated wind conditions.

RAOs at below-rated wind speed - Platform Surge

Under below-rated wind conditions, the surge RAOs exhibit similar overall patterns to those observed at rated wind speed (Figure 4.28), with all wind actuation methods reducing the platform response relative to the no-wind baseline. However, the relative behaviour of the actuation schemes changes.

At 1 m wave height, the no-wind displays the highest RAO magnitudes across the frequency range, as expected in the absence of aerodynamic damping. The PI actuation shows a pronounced dip at the lowest frequency band ($\sim$0.04–0.05 Hz), with RAO values dropping to approximately 0.1 m/m, significantly lower than those from the *Static weight* and *SIL* methods, and even below the fully aero-coupled numerical model. Outside this narrow frequency band, *PI* tracks *SIL* and *Static weight* closely, typically returning the lowest RAO values. *SIL* generally sits slightly below *Static weight* between 0.05 and 0.11 Hz, indicating a moderate level of damping that retains sensitivity to motion.

At 4 m wave height, the same pattern strengthens. The three lowest-frequency points correspond to *PI* and again mark the lowest RAO values on the entire plot, reinforcing the strong low-frequency suppression introduced by the *PI* control scheme. Between approximately 0.06 and 0.10 Hz, all methods follow eachother quite well. The numerical model with full aerodynamics remains below all experimental curves except at the very lowest *PI* points, where the RAO minima fall below even the simulated response.

These trends are consistent with the characteristics of each actuation method. The *PI* controller, through integral action based on load cell feedback, can generate a counteracting force that is favourably phased with surge velocity in long waves, resulting in strong low-frequency attenuation. However, this damping behaviour is a control artefact rather than a reflection of true aerodynamic coupling.

SIL, in contrast, introduces motion-dependent thrust and therefore better approximates the physics of aerodynamic feedback. Its RAOs remain between those of *PI* and *Static weight*, avoiding the extreme low-frequency suppression observed in PI. The *Static weight* method applies an approximately constant mean thrust and consistently returns the highest RAO values among the three actuation methods, providing the least damping-like behaviour. Unlike the PI system, however, it does not actively regulate the applied force, and any force variations arise passively from mass inertia and cable kinematics rather than from feedback control.

The fully aero-coupled numerical model continues to deliver the lowest overall RAOs, owing to its inclusion of unsteady aerodynamic damping that cannot be fully replicated by the physical actuation systems. The isolated *PI* minima that fall well below the surrounding experimental and numerical trends should be interpreted as artefacts of control tuning rather than as representative platform behaviour.

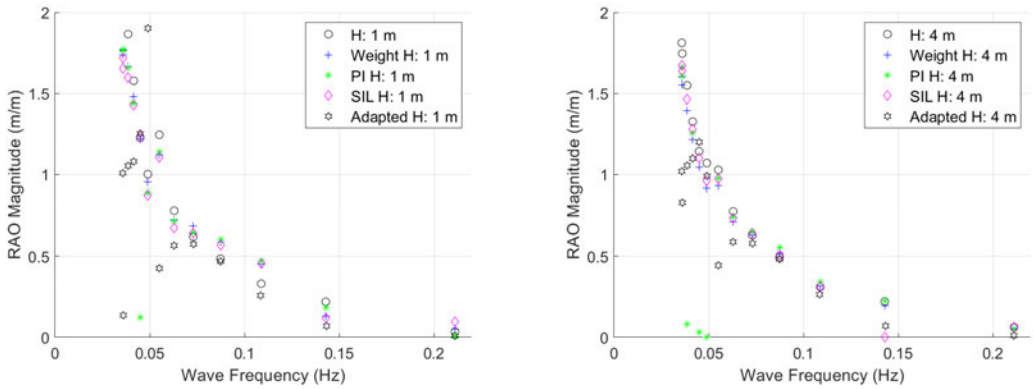

(a) RAOs for Surge at 1 m wave height. **(b)** RAOs for Surge at 4 m wave height.

Figure 4.28: RAOs for Surge at different wave heights under below-rated wind conditions.

RAOs at below-rated wind speed - Platform Pitch

The pitch RAO results at 1 m and 4 m wave heights under below-rated wind conditions (Figure 4.29) reveal broadly similar trends to those observed in surge, though with slightly more spread across the actuation methods. At the 1 m wave height, the adapted numerical model again under-predicts the pitch response near the natural frequency, consistent with previous findings and likely related to incomplete tuning of hydrodynamic coefficients. The largest pitch responses in this frequency region are found in the no-wind case and the *SIL* actuation, while the PI controller produces significantly smaller RAOs, particularly at the lowest frequencies, where it introduces a pronounced dip. This suggests strong controller-induced damping from the PI scheme, which effectively suppresses long period pitch motion, but does so in a way that may exceed the physical damping seen in real aerodynamic coupling.

At 4 m wave height, the same hierarchy is maintained and further accentuated with the *PI* exhibiting the lowest pitch RAOs across all tested frequencies, followed by *SIL* and then *Static weight*. The difference is most evident at low frequencies (below 0.05 Hz), where the PI control again produces very small RAO values, occasionally even lower than the aerodynamic numerical model. While this behaviour demonstrates the *PI* scheme's strong stabilising effect, it also underscores its potential to over-restrict pitch motion when compared with physically representative wind loading.

A small frequency band between approximately 0.05–0.07 Hz shows a modest local uplift in some wind actuated pitch RAOs compared with the no-wind case. This does not contradict the overall trend of aerodynamic damping; instead, it reflects a redistribution of the response energy. At below-rated wind, the effective pitch stiffness is reduced due to the aerodynamic thrust–tilt interaction, which shifts the pitch natural frequency downward. As a result, energy from the suppressed low-frequency region may be displaced into the 0.05–0.07 Hz band. Additionally, actuation dynamics, particularly the phase lag in *PI* and *SIL*controllers, can produce moments slightly out of phase with platform motion, locally amplifying the response. This uplift is absent from the numerical aero model, further suggesting that it arises from actuation dynamics and not a physical resonance.

Overall, pitch response under below-rated wind is highly sensitive to the actuation method. *PI* provides the strongest damping effect, particularly at long periods, but risks over suppressing the motion due to control loop dynamics. *SIL* yields more physically representative behaviour, preserving motion dependent aerodynamic effects, while the *Static weight* configuration shows the lowest damping. The numerical model with full aerodynamics continues to show the lowest overall response, reflecting its inherent damping bias and shorter pitch period. The PI-induced dips should be interpreted as control artefacts rather than as physically representative evidence of enhanced damping.

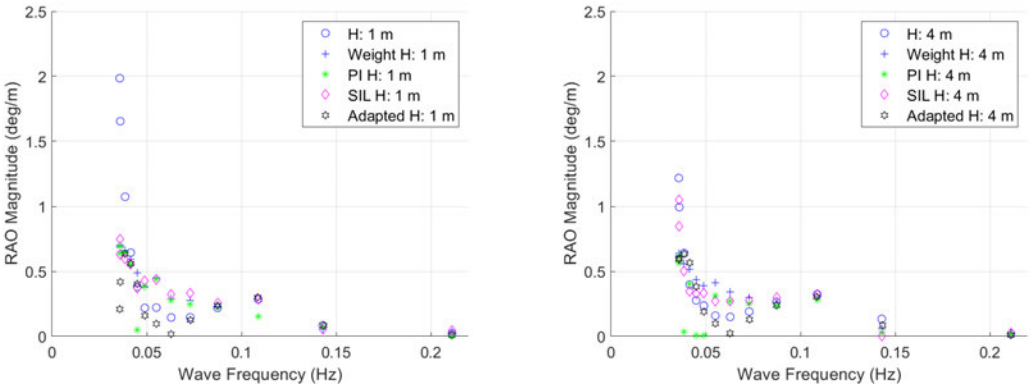

(a) RAOs for Pitch at 1 m wave height.

(b) RAOs for Pitch at 4 m wave height.

Figure 4.29: RAOs for Pitch at different wave heights under below-rated wind conditions.

RAOs at below-rated wind speed - Platform Heave

The heave RAO results under below-rated wind conditions (Figure 4.30) demonstrate consistent trends across wave heights. Compared to the no-wind case, all wind actuation methods lead to a modest reduction in heave response, particularly near the heave natural frequency (around 0.049 Hz). This reduction is attributed to additional aerodynamic damping projected into heave via pitch–heave coupling, along with small changes in mooring pretension introduced by the wind-trimmed equilibrium position.

At 1 m wave height, the *Static weight*, *PI*, and *SIL* configurations cluster between approximately 0.9 and 1.1 m/m near the heave peak. The PI controller introduces a distinct suppression at one frequency (around 0.045 Hz), which likely reflects strong controller-induced damping due to its integral action. Away from the resonance region (i.e., beyond 0.06 Hz), all actuation methods show tight convergence and similar behaviour.

At 4 m wave height, the trends become clearer and more consistent. The *PI* configuration yields the lowest RAOs at low frequencies, in some instances approaching zero, while the *SIL* and *Static weight* setups remain close to one another and slightly above PI. Between 0.06 and 0.10 Hz, all three wind actuation strategies converge, indicating comparable aerodynamic influence and diminishing control-induced differences.

The adapted numerical model sits consistently below the experimental wind actuation methods across most frequencies for both wave heights, extending the no-wind trend where the *Adapted* was already seen to under-predict the heave peak. One outlier is observed at $1\ m$ wave height, where the model shows an anomalously high RAO near 0.04 Hz ($\approx 1.9\ \mathrm{m/m}$), exceeding all measurements. Given its deviation from surrounding points and the absence of similar behaviour at $4\ m$, this is best treated as a numerical extraction artefact rather than a physical response.

The relative behaviour of the actuation methods follows previously established patterns. The PI controller, through load-cell feedback and integral action, introduces a motion opposing force that can be particularly effective at suppressing low-frequency heave via pitch interaction. While this yields deep RAO minima in some cases, these should be interpreted as control artefacts and not physical targets. The *SIL* method, which recovers motion-dependent aerodynamic thrust, offers a more representative response and typically sits just above the numerical model. The *Static weight* case applies an approximately constant mean force and is consistently the least damping of the three. Any departures from constant load arise passively from the suspended-mass inertia and cable geometry, rather than from active control.

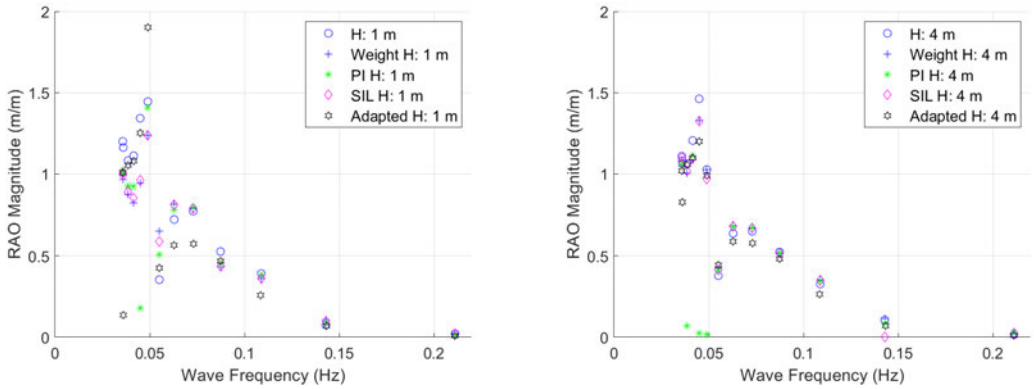

(a) RAOs for Heave at 1 m wave height.

(b) RAOs for Heave at 4 m wave height.

Figure 4.30: RAOs for Heave at different wave heights under below-rated wind conditions.

Across both wave heights, the introduction of wind consistently reduces the surge, pitch, and heave RAOs, with the strongest attenuation observed at the lowest frequencies where the platform is most compliant. At rated wind speed (11 m s^{-1}), the ordering of responses is consistent: the *SIL* method produces the lowest experimental RAOs and lies closest to the aero-coupled numerical model, while the *Static weight* and *PI* configurations are slightly higher and closely aligned. The numerical model remains the lowest overall, continuing its trend from the no-wind case of under-responding at very low frequencies due to added aerodynamic damping.

At below-rated wind speed (8 m s^{-1}), this hierarchy changes slightly: the *PI* method produces the lowest RAOs at the longest periods in all degrees of freedom, sometimes falling below the numerical model, indicating controller-induced over damping. *SIL* remains a close second and more representative of motion dependent aerodynamic behaviour, while the *Static weight* method consistently exhibits the least damping effect. A modest uplift in pitch RAOs around 0.05–0.07 Hz is observed for all wind actuation schemes, particularly *SIL* and *PI*, likely resulting from softening in the linearised stiffness and phase effects in the control loop. At higher frequencies, all methods converge.

4.4.2 Irregular waves

While RAO analysis under regular waves provides valuable insight into the system's frequency response characteristics, it does not fully capture the complexity of real sea states. Therefore, it is essential to evaluate the platform's behaviour under irregular waves to assess its dynamic response in more realistic and broadband conditions. Irregular wave testing allows for the verification of model performance across a continuous frequency spectrum, incorporating the combined effects of multiple wave components and their interactions with aerodynamic and mooring loads. This step is critical for confirming whether the conclusions drawn from regular wave RAOs hold in more representative sea conditions and for validating the suitability of different wind actuation methods in predicting overall system performance.

In this section, results are presented for three wind loading conditions:

- **Below-rated wind:** Corresponding to an 8 m/s inflow, this case produces the second-highest rotor thrust of the three conditions considered.
- **Rated wind:** Corresponding to 11 m/s, this wind speed yields the maximum steady rotor thrust and represents the nominal design operating point.
- **Above-rated wind:** Corresponding to 22 m/s, this regime results in the lowest rotor thrust due to blade pitch regulation limiting aerodynamic loads.

Platform pitch response under irregular waves

Figure 4.31 presents the comparison of mean pitch displacements and corresponding standard deviations for irregular wave conditions. Across all three wind speeds, the application of wind shifts the platform from a small negative trim in the no-wind case (approximately -1 to -1.5°) to a positive equilibrium. Standard deviations remain relatively small and show minimal sensitivity to the peak period T_p, indicating that mean pitch is primarily influenced by the steady wind moment rather than by the wave characteristics.

The ordering of the experimental actuation methods is consistent across wind speeds of $U = 8$, 11, and $22\ \mathrm{m/s}$, with *Static weight* producing the largest mean pitch, followed by *SIL* and then *PI*. At $8\ \mathrm{m/s}$, mean values are approximately $\theta \approx 5.5^\circ$ for *Static weight*, 5.2° for SIL, and 4.4° for *PI*. At $11\ \mathrm{m/s}$, the values rise to around 7.5°, 7.2°, and 6.2°, respectively. At $22\ \mathrm{m/s}$, when rotor thrust is reduced, the means drop to 3.5°, 3.4°, and 2.3°.

The consistent separation among the actuation methods can be explained by their underlying mechanisms: the *Static weight* method imposes the largest effective mean horizontal thrust at the nacelle, although the transmitted load is not perfectly constant because of suspended-mass inertia and cable-motion effects; the *SIL* method applies a motion-dependent thrust

with a slightly lower mean; and the PI controller, constrained by motor friction, backlash, and integral action around a load-cell setpoint, tends to under-deliver the average force. The slightly larger standard deviations observed with *PI* are compatible with this closed-loop control behaviour.

The adapted numerical model closely reproduces the no wind pitch values (clustered near -1 to -1.5° with T_p-dependent spreads), but under wind conditions it predicts smaller positive mean pitch angles than any of the experimental cases. These numerical means are about 3° at $8\ \mathrm{m/s}$, 4.6–4.9° at $11\ \mathrm{m/s}$, and 1.3–1.7° at $22\ \mathrm{m/s}$. This underprediction is attributable to two main factors. First, the numerical system is stiffer in pitch, with a shorter natural period, which leads to a smaller equilibrium angle under the same overturning moment. Second, the aerodynamic model includes additional contributions to the moment balance, such as blade and tower forces, and applies thrust along the shaft axis with a realistic lever arm. In contrast, the tank actuation applies a single horizontal force at the nacelle, leading to a longer effective moment arm and an overestimation of the pitching response. Consequently, all experimental wind cases produce larger mean pitch angles than the numerical model, with *PI* showing the smallest offset from the numerical prediction, followed by *SIL* and then *Static weight*.

These results indicate that the ranking of pitch means across actuation methods is robust across wave periods and wind speeds. The lower means from the numerical model are physically consistent with its stiffer dynamics and more complete aerodynamic moment representation. While the experimental methods introduce a method-dependent bias in the mean pitch, they remain useful for dynamic testing when this bias is acknowledged. For studies in which absolute pitch angle is important, the *Static weight* approach should be used with caution, since applying the load as a suspended mass at the nacelle tends to increase the mean pitch response. The *PI* method can reduce this mean offset, but in the present experiments this appears to be influenced at least partly by under-delivery of thrust and control-loop effects, rather than by improved physical fidelity. For investigations focused on dynamic coupling, *SIL* remains the most representative approach, although its mean trim still tends to exceed that predicted numerically unless further calibration is applied, such as mean thrust tuning or lever-arm adjustment.

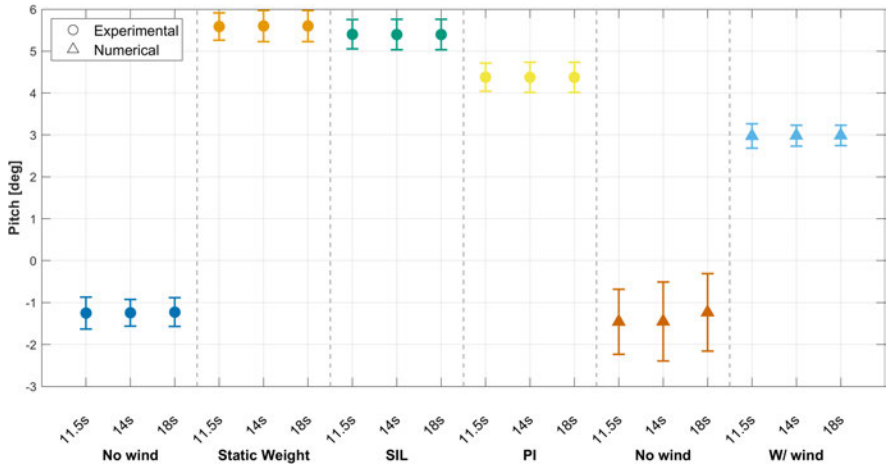

(a) Wind speed 8 m/s

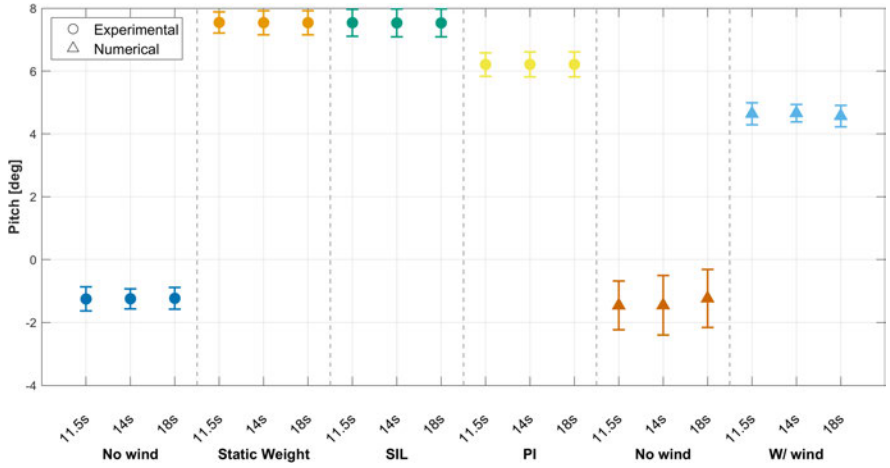

(b) Wind speed 11 m/s

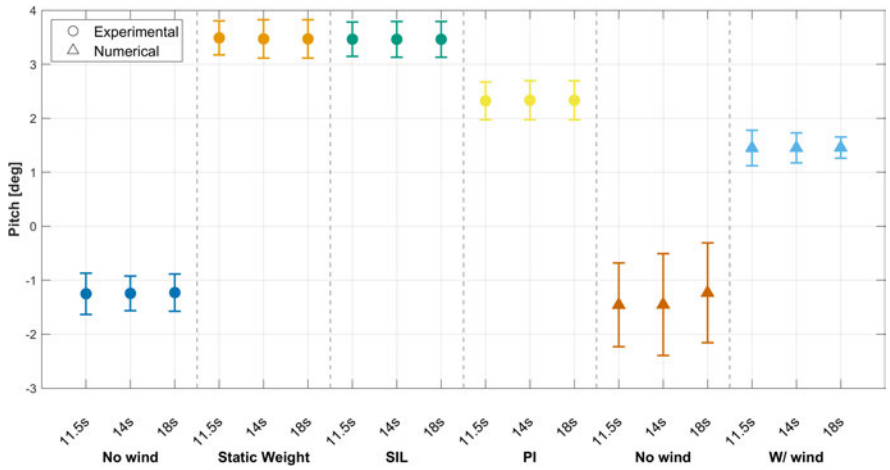

(c) Wind speed 22 m/s

Figure 4.31: Comparison of mean pitch displacement and standard deviation for irregular waves across different wind speeds and actuation methods.

Platform surge response under irregular waves

Figure 4.32 presents the grouped means and standard deviations for surge displacements in irregular waves across all tested wind speeds. Wind introduces a clear forward mean offset, whose magnitude scales with rotor thrust and shows only weak sensitivity to the peak period T_p. Across all three wind cases, the ordering among experimental actuation methods remains consistent, with *Static weight* producing the largest mean offset, followed by *SIL* and then *PI*: *Static weight* $>$ *SIL* $>$ *PI*.

At $8\ \mathrm{m/s}$ wind speed, the mean surge offsets are approximately $32\ \mathrm{m}$ for *Static weight*, $24\ \mathrm{m}$ for SIL, and $21\ \mathrm{m}$ for PI. These values rise with wind speed, reaching roughly $41\ \mathrm{m}$, $33\ \mathrm{m}$, and $29\ \mathrm{m}$, respectively, at $11\ \mathrm{m/s}$. At the above-rated wind speed of $22\ \mathrm{m/s}$, where thrust is reduced, the means fall to around 24–$25\ \mathrm{m}$ (*Static weight*), 16–$17\ \mathrm{m}$ (SIL), and 13–$14\ \mathrm{m}$ (PI). The standard deviations are small, ranging from sub-metre to approximately $1\ \mathrm{m}$. All actuation methods exhibit a mild reduction in mean offset with increasing T_p (from $11.5\ \mathrm{s}$ to $18\ \mathrm{s}$). This trend is consistent with a reduction in slow-drift force, as the wave steepness kA decreases with increasing period at constant significant wave height H_s. It is not governed by the linear RAO, which controls the oscillatory response about the mean.

This hierarchy reflects how each actuation method reproduces the mean horizontal force at the nacelle. The *Static weight* method imposes the target mean thrust directly, without active feedback control, resulting in the largest forward offset. The transmitted load is nevertheless not perfectly constant, since the suspended mass introduce passive force variations as the platform moves. *SIL* applies a motion-dependent thrust that is slightly reduced on average due to actuator friction and bandwidth limitations. *PI* regulates around a load-cell setpoint, but the presence of backlash and integral action tends to suppress the mean thrust delivery, yielding the smallest forward drift among the wind cases.

The adapted numerical model predicts surge means just below the *PI* values for all wind speeds: approximately 20–$21\ \mathrm{m}$ at $8\ \mathrm{m/s}$, 26–$30\ \mathrm{m}$ at $11\ \mathrm{m/s}$, and 11–$13\ \mathrm{m}$ at $22\ \mathrm{m/s}$. This is consistent with previous findings where the numerical system exhibits slightly greater stiffness and damping at low frequencies, and its aerodynamic loading includes distributed forces and moments that reduce net surge drift relative to the experimental single force nacelle actuation. Consequently, when comparing the experimental actuation methods, *PI* produces the smallest mean surge offsets, followed by *SIL*, while *Static weight* produces the largest offsets.

The no wind case also provides a useful reference: the experimental means remain near $0\ \mathrm{m}$, showing slight forward or aft drift within $\pm 1\ \mathrm{m}$, while the numerical model shows a small forward bias of approximately 0.5–$2\ \mathrm{m}$. This difference aligns with known low-frequency discrepancies in second-order drift, hydrodynamic response, and mooring pretension.

These results suggest that if reproducing a lower mean surge offset is critical, such as for evaluating mean mooring tensions, then *PI* provides the smallest offset among the experimental methods, followed by SIL. *Static weight* gives a conservative upper estimate of surge excursion. However, if the primary goal is to reproduce motion-dependent aerodynamic loading more realistically, *SIL* remains preferable. *PI*'s lower mean offsets likely arise at least in part from control limitations rather than from a more physically complete representation of aerodynamic forces. Finally, the consistent decrease in surge offset from $11\ \mathrm{m/s}$ to $22\ \mathrm{m/s}$ reflects the expected reduction in rotor thrust above-rated, confirming the physical consistency of both the experimental actuation and the numerical reference.

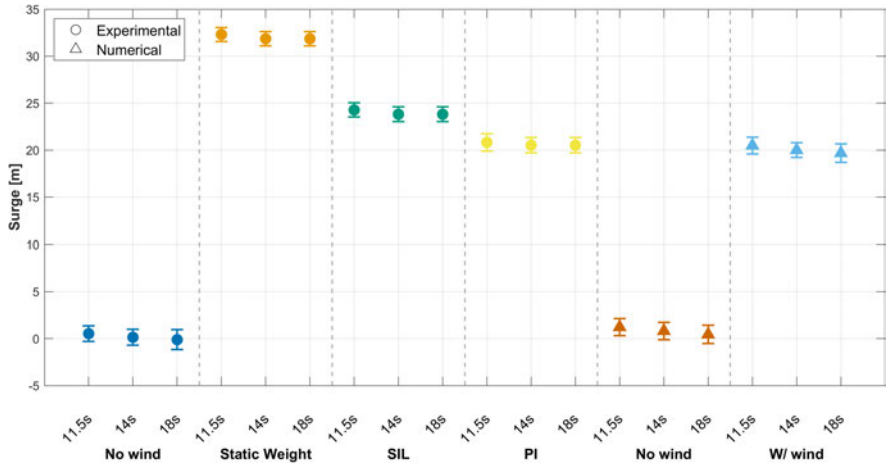

(a) Wind speed 8 m/s

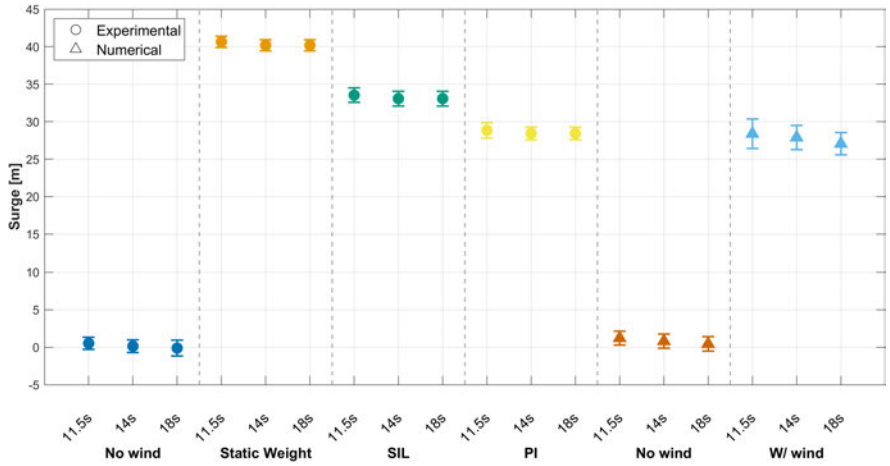

(b) Wind speed 11 m/s

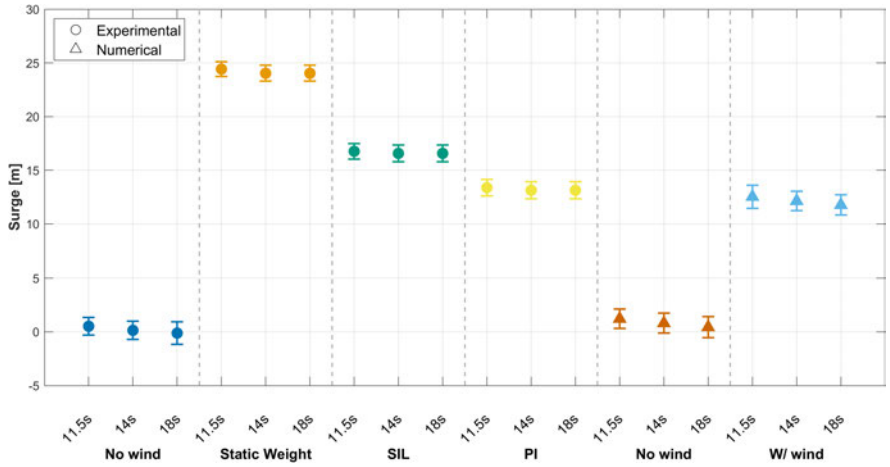

(c) Wind speed 22 m/s

Figure 4.32: Comparison of mean surge displacement and standard deviation for irregular waves across different wind speeds and actuation methods.

Platform heave response under irregular waves

Figure 4.33 presents the mean and standard deviation of the heave response under irregular wave conditions ($H_s = 5$ m). Without wind, the experimental mean is close to zero (slightly negative), as expected. When wind is introduced, a small positive uplift appears in the mean level, arising from pitch–heave coupling caused by the nose-up trim and slight increases in vertical mooring load due to the forward shift in equilibrium.

The mean heave level varies weakly with wind speed. At $8\ \mathrm{m\,s^{-1}}$, the ordering of experimental methods is approximately: *Static weight* $\gtrsim$ *PI* $\gg$ SIL, with mean values around 0.30–0.35 m, 0.25–0.30 m and near zero respectively. At $11\ \mathrm{m\,s^{-1}}$, the uplift increases, with *PI* now giving the largest mean (≈ 0.33–0.35 m), *Static weight* slightly lower (≈ 0.27–0.30 m), and *SIL* still near zero (≈ 0.05–0.10 m). At $22\ \mathrm{m\,s^{-1}}$, corresponding to above-rated conditions and reduced thrust, *PI* drops back to ≈ 0–0.05 m, *SIL* remains near zero, and *Static weight* holds steady around 0.30 m. This behaviour reflects how each method applies the mean horizontal load at the nacelle. The *Static weight* directly imposes the target mean force without feedback regulation, thereby maximising the pitch-induced heave set-up; *PI* uses a closed-loop regulation that can over-deliver the mean moment under rated and below-rated conditions but decreases under above-rated thrust; and *SIL* provides a motion-dependent thrust.

In terms of variability, all experimental cases show one-sigma spreads of about 0.5–0.9 m, with minimal sensitivity to T_p. Differences between actuation methods are modest. Occasionally, *PI* exhibits a slightly wider spread, consistent with its feedback control loop perhaps adding a small amount of low-frequency energy via phase lag.

The adapted numerical model predicts higher positive means ($\sim$0.6–0.7 m) and broader spreads ($\sim$1.0–1.3 m), both with and without wind. This consistent upward bias in mean heave is attributable to the mooring representation. The adapted semi-taut model replicates the horizontal stiffness but lacks the vertical pretension provided by chain-catenary lines in the tank. This omission reduces the fairlead down-pull, allowing the hull to float higher under wind and wave loading. It also limits vertical energy dissipation, contributing to the larger heave variance. Therefore, differences in mooring vertical load are the dominant cause of the heave mismatch between simulation and experiment.

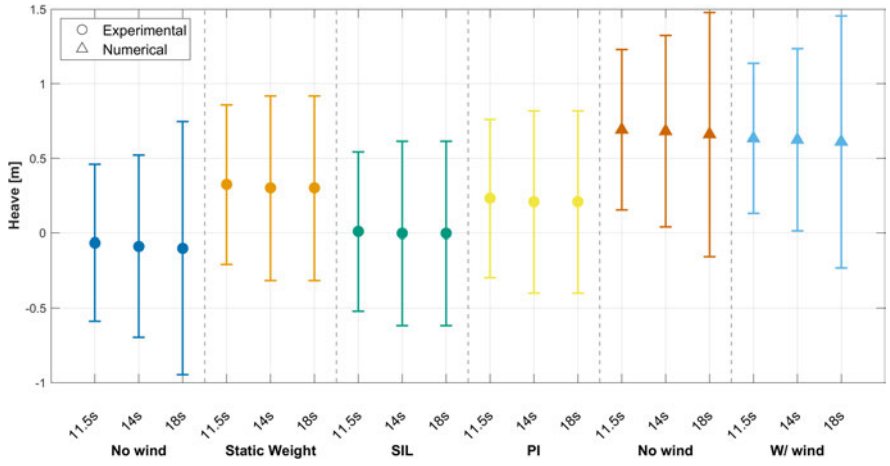

(a) Wind speed 8 m/s

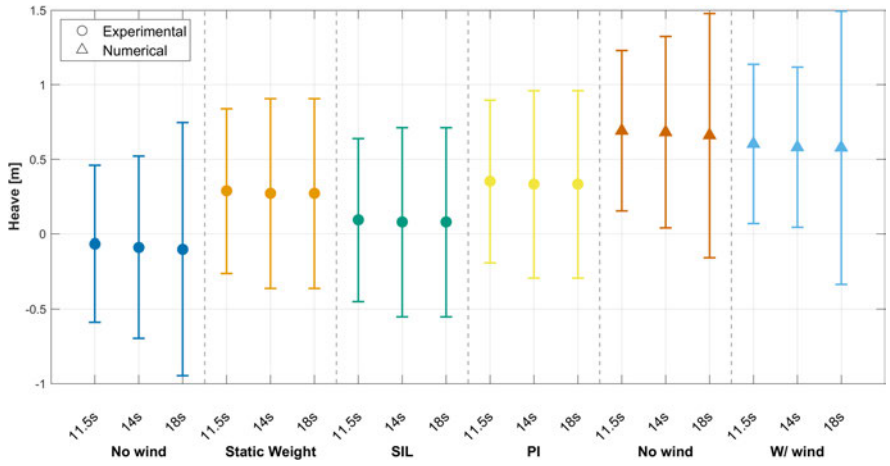

(b) Wind speed 11 m/s

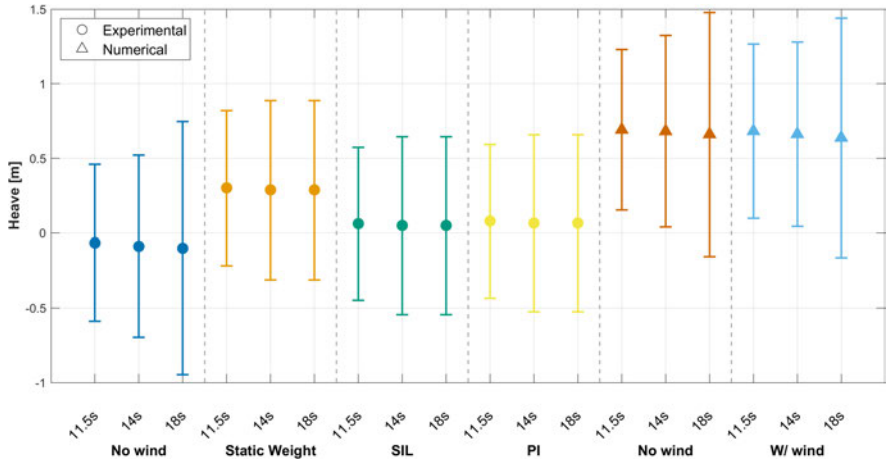

(c) Wind speed 22 m/s

Figure 4.33: Comparison of mean heave displacement and standard deviation for irregular waves across different wind speeds and actuation methods.

Fore mooring line tension under irregular waves

Figure 4.34 presents the mean and standard deviation of fore-line tension across wind speeds. For 8 and $11\ \mathrm{ms}^{-1}$, the *PI* cases produce the highest mean fore-line tensions and the largest spreads. The *Static weight* and *SIL* methods follow, with the *Static weight* slightly above SIL. At $22\ \mathrm{ms}^{-1}$, where rotor thrust is the lowest, all three methods converge, with *PI* only marginally higher than *Static weight* and SIL, which are nearly indistinguishable.

In terms of mean values, the differences between *Static weight* and *SIL* are small. For $8\ \mathrm{ms}^{-1}$, the *Static weight* tensions range from approximately 2.25–2.35 MN, and *SIL* from 2.20–2.30 MN. At $11\ \mathrm{ms}^{-1}$, both methods lie between 2.75–2.90 MN, making their means effectively overlapping. At $22\ \mathrm{ms}^{-1}$, *Static weight* and *SIL* continue to match closely. This ranking reflects how each method reproduces mean nacelle thrust: *PI* tends to deliver a slightly higher effective average force, also adding low-frequency control energy; *Static weight* applies an approximately fixed mean load without active feedback regulation, although passive variations remain due to suspended-mass inertia and cable motion; and *SIL* produces a motion-dependent thrust whose time-averaged value is modestly lower, resulting in the lowest mean fore-line loads.

Despite the similarity in mean tension between *Static weight* and SIL, their dynamic effects differ. At 8 and $11\ \mathrm{ms}^{-1}$, *Static weight* leads to noticeably larger surge offsets and pitch angles compared to SIL. This indicates that the system is operating on a relatively flat portion of the spring–rope stiffness curve, where small increases in line force can cause large displacements. Thus, similar mean tension does not imply similar platform motions.

The standard deviations are also informative. *PI* exhibits the largest variability due to added low-frequency control action. The *Static weight* results show slightly broader spreads than *SIL* at some conditions but lacks the motion-dependent aerodynamic feedback present in *SIL* that helps to damp low-frequency response. Consequently, *Static weight* may match the mean tension, but it cannot replicate the frequency-dependent dynamic behaviour that *SIL* captures, potentially leading to differences in spectral content..

The numerical model shows a distinct pattern. In the no wind condition, it predicts slightly higher pretension than the tank, with means of 1.18–1.25 MN versus 1.08–1.15 MN in the experiments, likely due to a stiffer baseline setting and the absence of vertical line components that reduce fore mooring line load in the tank. When wind is applied, the numerical model underestimates the mean fore line tension relative to all experimental methods by approximately 5–10% at $8\ \mathrm{ms}^{-1}$, 10–15% at $11\ \mathrm{ms}^{-1}$, and around 5% at $22\ \mathrm{ms}^{-1}$. At low wind speed, the numerical predictions are of similar magnitude to the *SIL* values, but at rated wind they fall below all experimental methods. This underestimation arises from two factors: (i) the semi-taut

mooring representation lacks vertical pretension, reducing axial load transfer at the fairleads; and (ii) the numerical model produces a slightly lower effective mean thrust, possibly due to control setpoint, inflow modelling, or blockage effects, resulting in smaller surge offsets and hence reduced horizontal tension.

The numerical model also under-predicts variability, consistent with earlier findings that it filters out low-frequency surge energy. This results in narrower tension distributions compared to experimental methods.

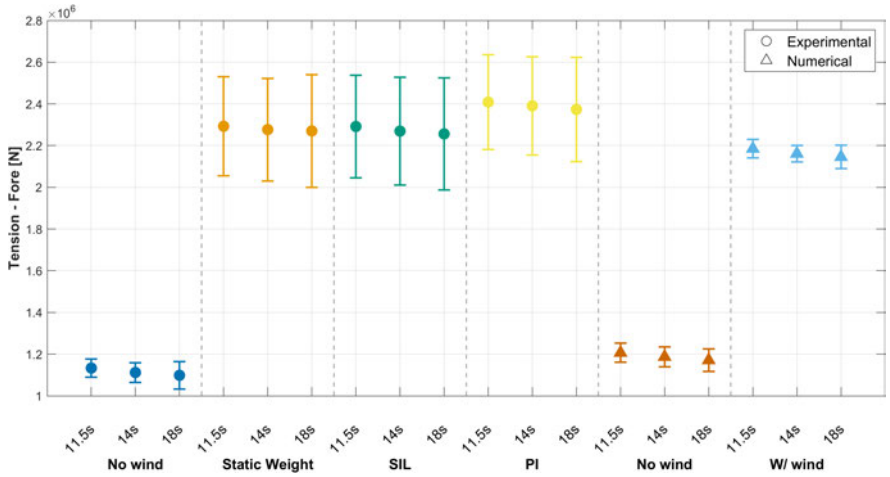

(a) Wind speed 8 m/s

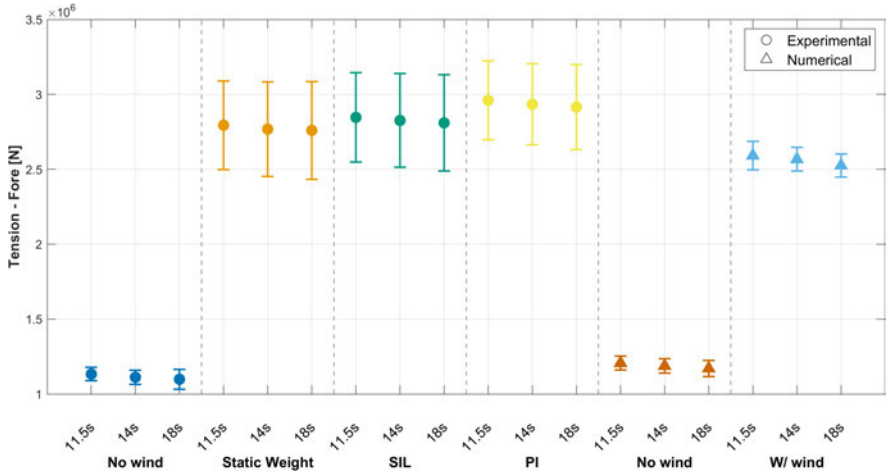

(b) Wind speed 11 m/s

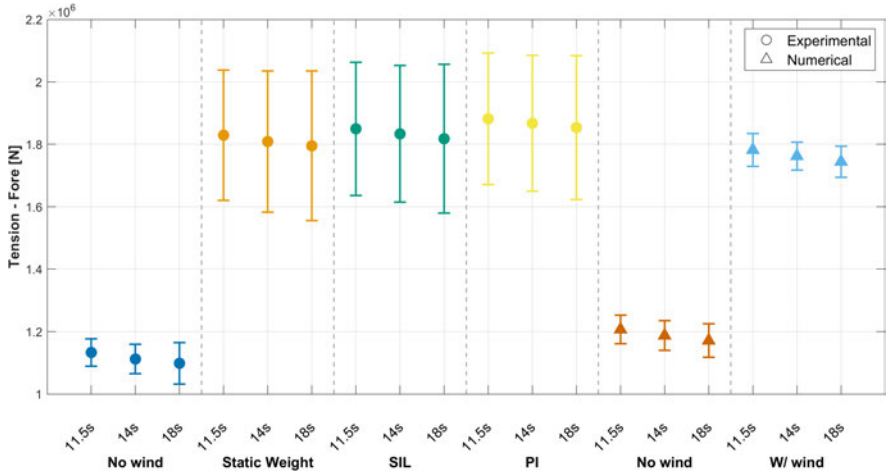

(c) Wind speed 22 m/s

Figure 4.34: Comparison of mean fore mooring tension and standard deviation for irregular waves across different wind speeds and actuation methods.

Under irregular wave conditions with wind, the three actuation methods show consistent trends across wind speeds. *Static weight* produces the largest mean surge and pitch motions, followed by PI, while *SIL* generally yields smaller offsets and narrower spreads than *Static weight*. *PI* introduces the most variability due to control dynamics. Mean heave shifts slightly upward with wind, with minimal differences between methods. In fore-line tensions, *PI* yields the highest and most variable loads, *Static weight* is slightly lower, and *SIL* the lowest; at $22\ \mathrm{m\,s^{-1}}$, all methods converge. *Static weight* approximates *SIL* reasonably well in terms of mean line loads but not in motions or dynamic behaviour. The numerical model captures several of the observed trends, but predicts smaller mean surge and variability and larger mean heave, consistent with its mooring representation.

4.4.3 Wind–wave misalignment ($\Delta = -30^\circ$)

This subsection examines the platform's behaviour under a fixed directional offset between wind and waves. In these tests, waves are incident head-on to the platform (wave heading $\beta_w = 0^\circ$), while the wind approaches from the port side at a fixed heading of $\beta_v = -30^\circ$. This results in a constant misalignment angle of $\Delta = \beta_v - \beta_w = -30^\circ$, which remains steady throughout each run. Two wind speeds are considered: below rated ($U = 8\ \mathrm{m\,s^{-1}}$) and rated ($U = 11\ \mathrm{m\,s^{-1}}$).

The introduction of a fixed wind–wave misalignment breaks the symmetry of the head-sea configuration and activates cross-plane dynamics. As a result, the full set of six rigid-body motions (surge, sway, heave, roll, pitch, yaw) must be considered, along with all three mooring line tensions (fore, port, and starboard). Relative to aligned conditions, this asymmetry is expected to induce non-zero mean values in sway and yaw, increase coupling between roll/sway and pitch/yaw, and generate unequal load sharing between the port and starboard mooring lines.

Only the *PI* and *SIL* wind actuation methods are included in this analysis. The *Static weight* approach is excluded because earlier results showed it either introduced the largest bias when compared to aero-hydrodynamic coupled simulations or collapsed onto trends already bracketed by *PI* and SIL, offering limited diagnostic value for this case.

The above-rated condition ($U = 22\ \mathrm{m\,s^{-1}}$) is also omitted. During those experimental runs, the actuator system exhibited unexpectedly large mean surge offsets, inconsistent with the expected reduction in thrust above rated wind speed. These anomalies suggest a control or saturation issue, and the corresponding data are therefore excluded from interpretation.

Wind–wave misalignment: Results in Surge

With the wind fixed at -30° relative to the wave direction, the experimental *SIL* tests show mean surge offsets of approximately 24–25 m at $U = 8\ \mathrm{m\,s^{-1}}$ and 35–36 m at $U = 11\ \mathrm{m\,s^{-1}}$ (Figure 4.35). The *PI* implementation consistently yields slightly lower means, around 20–21 m at $8\ \mathrm{m\,s^{-1}}$ and 29–30 m at $11\ \mathrm{m\,s^{-1}}$. In both cases, the standard deviations are modest and vary little with T_p, indicating that the misalignment primarily shifts the mean drift equilibrium rather than significantly altering wave-by-wave variability.

By contrast, the adapted OpenFAST model predicts much smaller mean surge offsets, around 7–8 m at $8\ \mathrm{m\,s^{-1}}$ and 9–10 m at $11\ \mathrm{m\,s^{-1}}$, again with small spreads. This means the experimental surge means exceed the numerical predictions by a factor of roughly 3–4, although the internal ordering (SIL $>$ PI) is consistent with the head-sea results.

In an ideal $\Delta = -30^\circ$ case, the effective forward thrust component should be reduced by $\cos 30^\circ$, and part of the aerodynamic load should be resolved into sway and yaw, leading to a smaller surge mean compared to the aligned configuration. The numerical model reflects this where the surge offsets drop relative to the head-sea simulations, as the applied thrust vector remains at -30°, and the sway–yaw coupling absorbs part of the load. The experimental data, however, show surge means comparable to the aligned case, suggesting that a large portion of the applied thrust continued to act in the surge direction.

This discrepancy is explained by the experimental setup. The winch cable and nacelle connection were initially positioned at -30° in static conditions, but once the platform moved in waves, the cable orientation shifted toward the bow and its vertical angle changed. As a result, the experimental thrust vector deviated from the intended -30° direction, maintaining a large forward (surge aligned) component. The effect is stronger for *SIL*, which tracks a higher instantaneous thrust and therefore delivers a larger forward load whenever the cable deviates from its nominal direction.

Two additional factors likely contributed to the difference in the experimental results: (i) the numerical model's semi-taut mooring provides greater lateral stiffness and facilitates yaw/sway load sharing, which suppresses surge drift under misalignment; and (ii) the experimental thrust application introduces low-frequency damping via winch control and line friction, which limits fluctuations but does not correct the mean offset when the force direction is biased. These aspects help explain why the surge means diverge while the standard deviations remain similar and relatively insensitive to T_p.

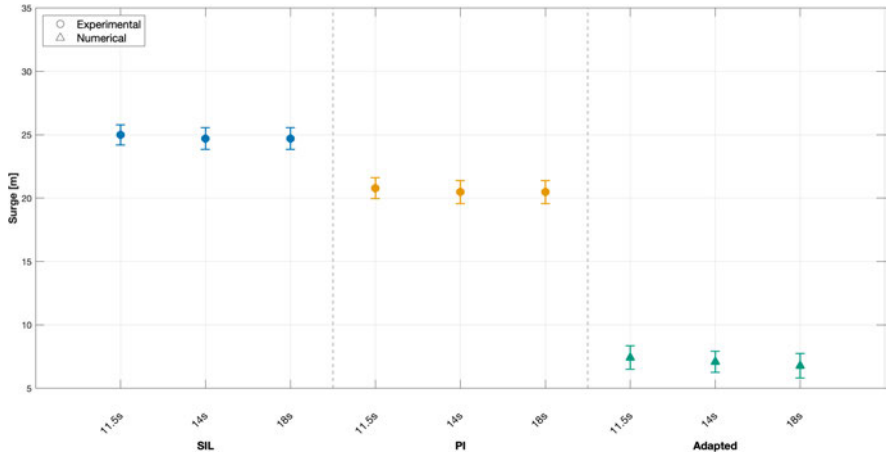

(a) 8 m/s wind speed

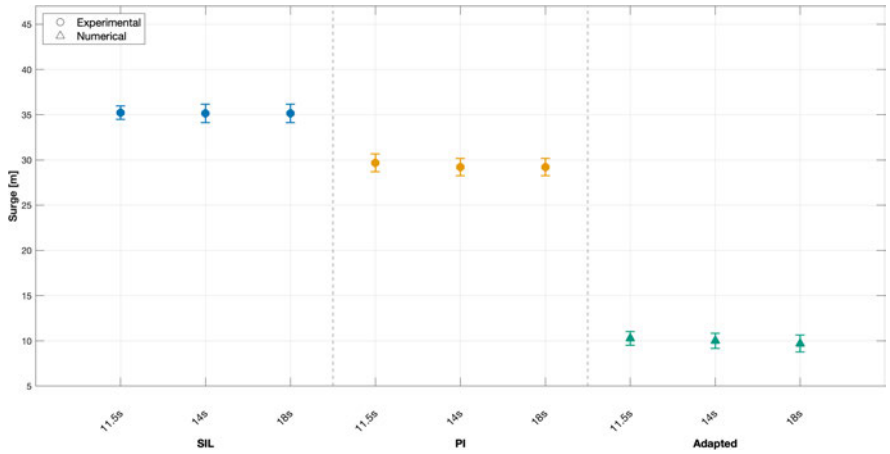

(b) 11 m/s wind speed

Figure 4.35: Grouped mean and standard deviation for surge displacement across all wind speeds.

Wind–wave misalignment: Results in Sway

Figure 4.36a and Figure 4.36b present the grouped mean and standard deviation values for sway displacement under below-rated ($U = 8\ \mathrm{m\,s^{-1}}$) and rated ($U = 11\ \mathrm{m\,s^{-1}}$) wind speed conditions. At the below-rated wind speed, the experimental *SIL* tests show mean sway displacements of approximately 11.3–11.6 m, while *PI* gives significantly smaller values of about 3.9–4.1 m. The adapted numerical model predicts a similar range of 4.0–4.3 m. This indicates that the *PI* results are of similar magnitude to the simulation (within roughly 5–10%), while the *SIL* response is larger by a factor of approximately 2.7–3. This similarity should be interpreted only as consistency with the numerical prediction, not as proof that the *PI* response is more physically correct.

Standard deviations are small for all cases and vary only weakly with T_p, suggesting that sway is primarily governed by the quasi-static lateral thrust component balanced by mooring restoring, rather than by wave-frequency excitation.

At rated wind speed, the same ordering persists, but the differences grow with increased thrust. *SIL* sway means rise to about 18.6–19.4 m, *PI* to 7.4–7.8 m, and the numerical model gives 6.3–6.6 m. Again, *PI* remains closer in magnitude to the simulation (10–20% higher), while *SIL* gives a substantially larger sway response than the numerical prediction, by a factor of around 3. As with the lower wind case, standard deviations remain modest and insensitive to T_p.

This behaviour stems from how thrust is applied. In the numerical model, the thrust vector is fixed at a -30° azimuth, so the lateral force component is $T \sin 30^\circ$, and part of the load is absorbed by yaw and resisted by the semi-taut mooring, which provides significant transverse stiffness. In the basin, however, the winch cable does not maintain a constant heading once the platform moves. For *SIL* in particular, where thrust magnitude varies continuously, the winch line tends to reorient, so a substantial portion of the thrust vector resolves laterally, producing larger steady sway offsets than the model predicts. Any relative reduction in transverse restoring from the spring-rope mooring (compared to the numerical representation) further amplifies this bias.

By contrast, the *PI* method applies a lower and more constant thrust, making it less sensitive to changes in the cable's instantaneous azimuth. As a result, the effective lateral load and resulting sway equilibrium are more stable and yield values of similar magnitude to the numerical prediction. The similarity in magnitude between *PI* and the simulation at $8\ \mathrm{m\,s^{-1}}$ supports this interpretation and highlights directional fidelity as a likely factor behind the larger *SIL* sway response relative to the numerical prediction.

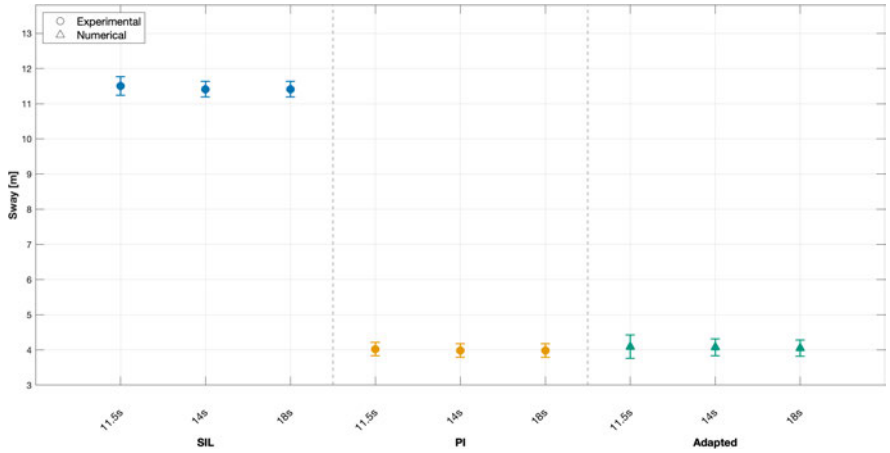

(a) 8 m/s wind speed

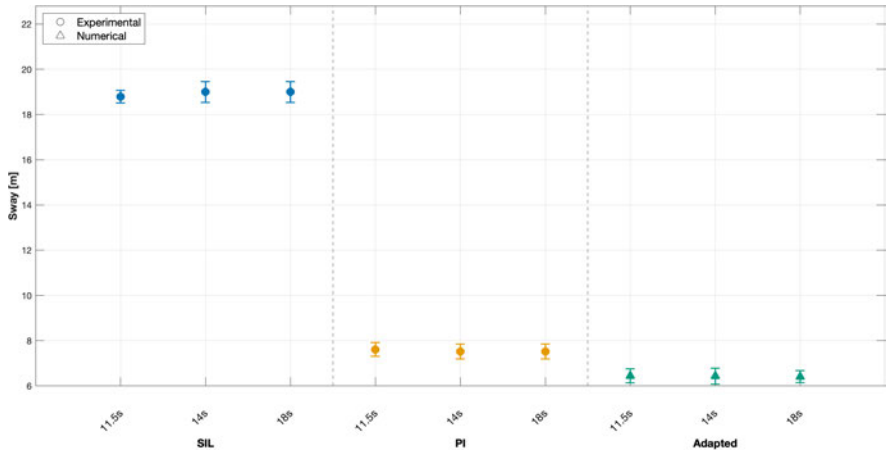

(b) 11 m/s wind speed

Figure 4.36: Grouped mean and standard deviation for sway displacement across all wind speeds.

Wind–wave misalignment: Results in Heave

Figure 4.37a and Figure 4.37b present the grouped mean and standard deviation values for heave displacement under below-rated ($8\ \mathrm{m\,s^{-1}}$) and rated ($11\ \mathrm{m\,s^{-1}}$) wind speed conditions. Under $8\ \mathrm{m\,s^{-1}}$ conditions, the experimental *SIL* and *PI* methods exhibit mean values slightly above zero, with standard deviations in the range of -0.5–0.9 m. The adapted numerical model predicts lower mean heave displacements, consistently below 0.2 m, compared to the experimental cases, with slightly reduced standard deviations for the smallest period, increasing until the highest period.

At $11\ \mathrm{m\,s^{-1}}$ wind speed, the same trend persists: experimental methods present higher mean values compared to the numerical model, with the *PI* method showing marginally larger means than *SIL*. Standard deviation values across both actuation methods and the numerical model remain similar to those observed at $8\ \mathrm{m\,s^{-1}}$, and the variability across wave periods is small.

This systematic offset can be traced to a cross-coupling pathway: the off-axis thrust introduces additional surge and pitch, which alters line tension distribution and generates a net upward vertical force. This is most noticeable in the *PI* due to the applied force not taking into account the platform's motion.

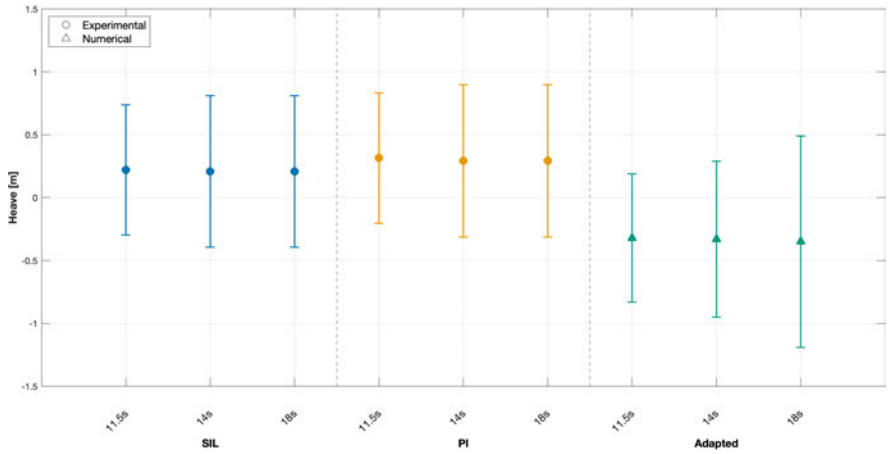

(a) 8 m/s wind speed

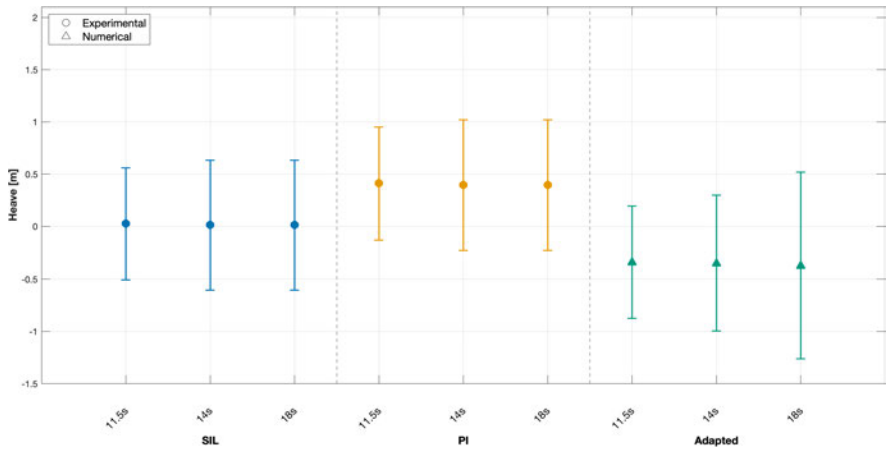

(b) 11 m/s wind speed

Figure 4.37: Grouped mean and standard deviation for heave displacement across all wind speeds.

Wind–wave misalignment: Results in Roll

Figure 4.38 presents the mean and standard deviation of roll under wind–wave misalignment ($\Delta = -30°$) for both below-rated ($8\ \mathrm{m\,s^{-1}}$) and rated ($11\ \mathrm{m\,s^{-1}}$) wind speeds. In all cases, the experimental *SIL* and *PI* methods produce negative mean roll, while the adapted numerical model remains close to zero.

At $8\ \mathrm{ms}^{-1}$, *SIL* yields the largest negative mean roll of about -3°, followed by *PI* at approximately -1.5°. The numerical model predicts a small positive roll near 0.5° with minimal variability across wave periods. At $11\ \mathrm{ms}^{-1}$, *SIL* mean rolls deepen to around -4.5°, with *PI* again intermediate and the numerical model near zero. The mean roll difference between *SIL* and the numerical model is roughly 91% at $8\ \mathrm{ms}^{-1}$, while the *SIL–PI* gap is about 44%. At $11\ \mathrm{ms}^{-1}$, the *SIL–PI* difference grows to about 53%.

Standard deviations remain small for all methods, indicating limited roll variability. The largest spread difference, 61%, occurs between *SIL* and the numerical model at the shortest peak period ($T_p = 11.5$ s). In contrast, *PI* shows the smallest spread difference relative to the adapted model at that same period (around 6%).

Two factors likely contribute to the larger experimental roll magnitudes. First, the winch cable and fairlead were set statically at -30°, but as the platform moves under wave loading and the actuator responds, the actual thrust vector rotates away from the intended heading. This inadvertent change in the force direction increases cross-coupling into roll. Second, the control strategy amplifies this effect: the *PI* method maintains a nearly constant thrust based on load-cell feedback, whereas *SIL* actively tracks platform motions and updates the thrust vector in real time. When the line direction deviates, *SIL* more faithfully transmits the misaligned load, leading to larger roll offsets than *PI*. A more detailed examination of these control-induced differences will be presented in Chapter 5.

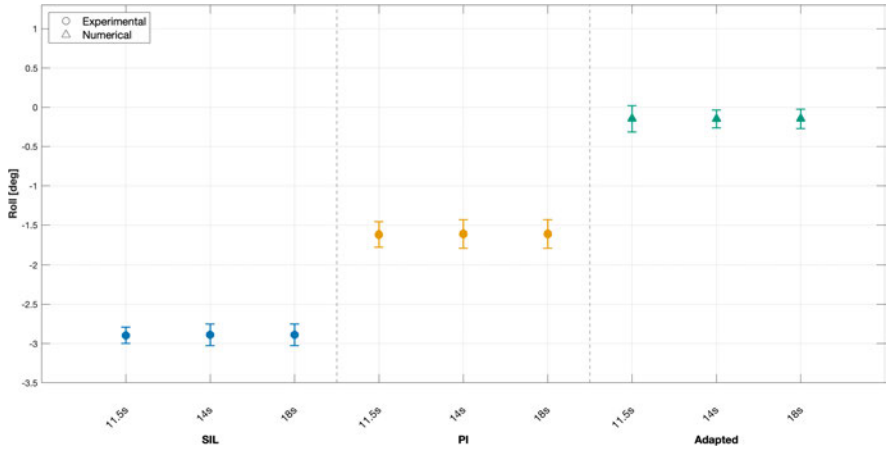

(a) 8 m/s wind speed

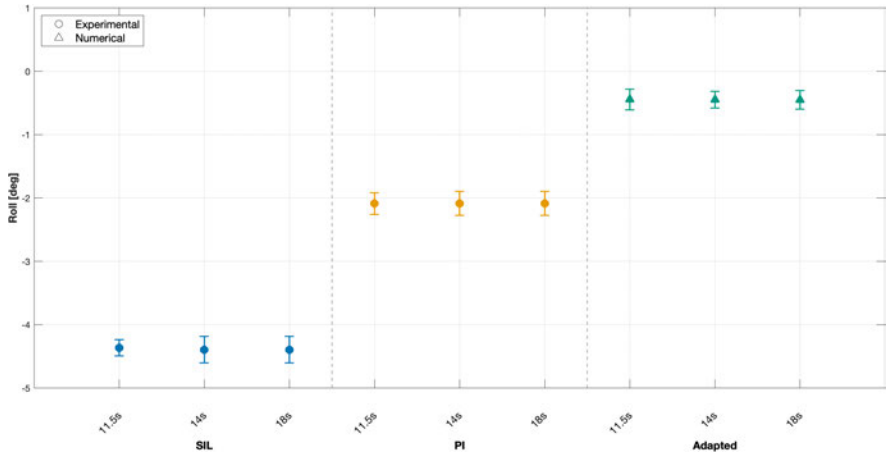

(b) 11 m/s wind speed

Figure 4.38: Grouped mean and standard deviation for roll motion across all wind speeds.

Wind–wave misalignment: Results in Pitch

Figure 4.39 shows that, under a fixed misalignment of $\Delta = -30^\circ$, the mean pitch angles from both experimental actuation methods far exceed those of the adapted numerical model. At $U = 8\ \mathrm{m\,s^{-1}}$, *SIL* produces a mean pitch of approximately 5.0° and *PI* about 4.5°, whereas the numerical model remains near 0° for all T_p. At $U = 11\ \mathrm{m\,s^{-1}}$, *SIL* rises to $\sim 7.0^\circ$, *PI* to $\sim 6.0^\circ$, while the numerical prediction sits around 1.0°. In both cases the experimental means exceed the numerical by roughly 87%, and *SIL* lies about 12% above *PI*.

The standard deviations from the experiments also increase with T_p, reflecting enhanced slow-drift coupling, whereas the numerical spreads remain uniformly small. The minimal pitch excursion in the numerical model arises because it applies a perfectly fixed thrust vector at -30°. There are no unintended cable reorientations or controller-induced phase lags to inject additional moment into the pitch DOF.

By contrast, the tank tests exhibit the same cable-vector errors and control dynamics that produced large roll offsets: the winch line, initially set to -30°, swings toward the bow under wave motion and actuator feedback, so a substantial component of the thrust continues to act in the pitch axis. *SIL*, which continuously updates thrust based on instantaneous platform kinematics, faithfully transmits this misaligned component, driving higher mean pitch than *PI*, whose integral control around a fixed load-cell setpoint partially filters out rapid vector shifts. Thus, both the magnitude of the pitch bias and the relative ordering

$$SIL > PI > \text{Adapted}$$

mirror the roll behaviour already discussed and highlight the critical importance of maintaining directional fidelity in force application.

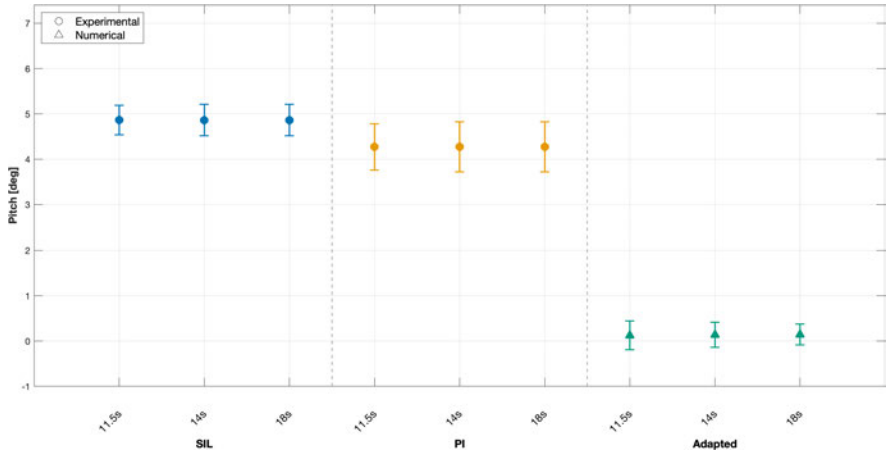

(a) 8 m/s wind speed

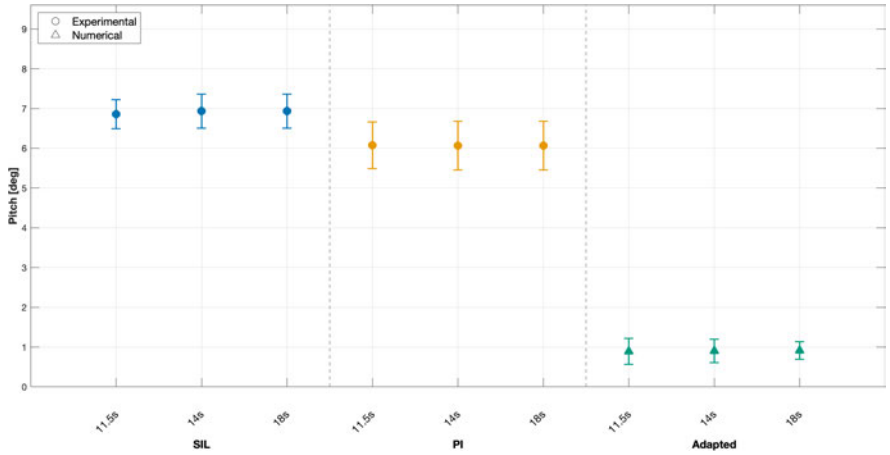

(b) 11 m/s wind speed

Figure 4.39: Grouped mean and standard deviation for pitch motion across all wind speeds.

Wind–wave misalignment: Results in Yaw

Figure 4.40 shows that, under a fixed misalignment of $\Delta = -30^\circ$, the mean yaw angles from both experimental actuation methods exceed those of the adapted numerical model. At $U = 8\ \mathrm{m\,s^{-1}}$, *SIL* yields a mean yaw of approximately -0.3° and *PI* about -0.9°, whereas the numerical model remains near -1.6° for all T_p. At $U = 11\ \mathrm{m\,s^{-1}}$, *SIL* produces mean yaw around -0.2°, *PI* around -0.8°, and the numerical prediction stays close to -1.7°. In both wind regimes, the experimental means are roughly 40–60% less negative (i.e. closer to zero) than the numerical values, with *SIL* always lying about 50%–60% above *PI* in magnitude.

Standard deviations are small and vary little with wave period, indicating that yaw variability is dominated by the steady misaligned thrust rather than by wave-frequency fluctuations. The numerical model's consistent yaw (-1.6°) reflects its application of a perfectly fixed thrust vector at -30° combined a semi-taut mooring that provides strong rotational resistance. No cable reorientation or control-phase effects alter its applied moment.

In contrast, the tank tests exhibit reduced mean yaw magnitudes because the actual tank thrust vector shifts as the cable and winch react to platform motion. This dynamic reorientation reduces the net yawing moment compared to the ideal -30° case. Moreover, *SIL* actively updates thrust based on instantaneous platform kinematics, so any vector deviation is faithfully transmitted, resulting in slightly less negative mean yaw than *PI*, whose integral-control loop around a static setpoint filters out some of the instantaneous misalignment.

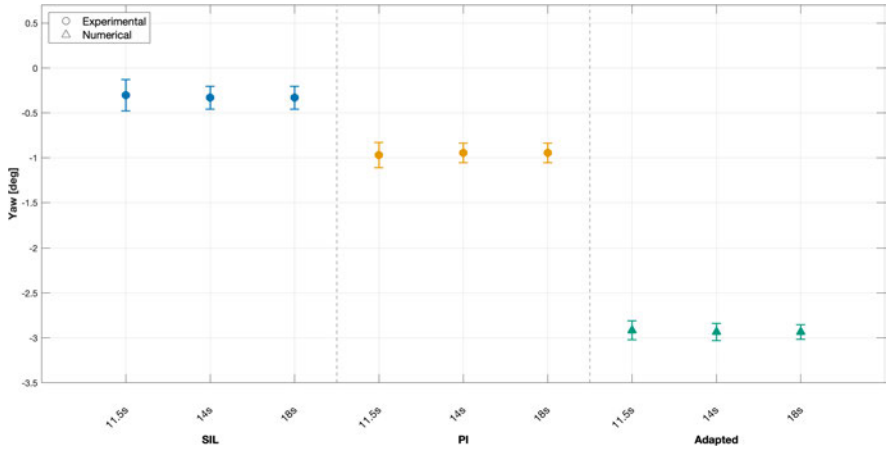

(a) 8 m/s wind speed

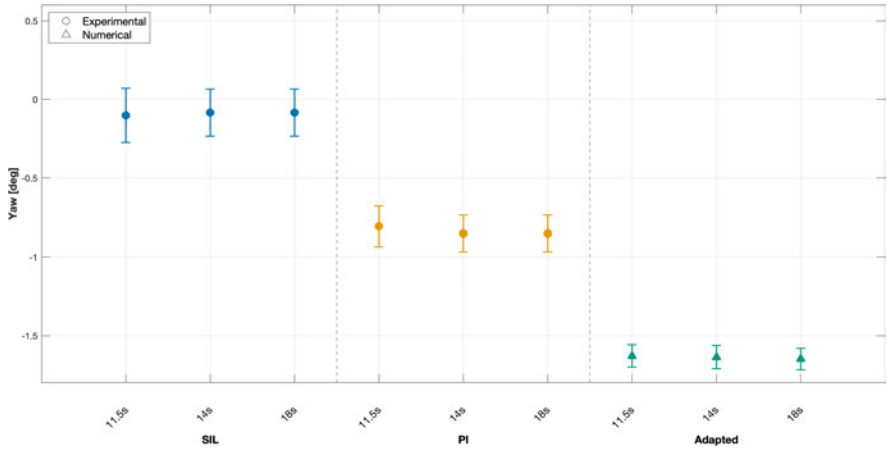

(b) 11 m/s wind speed

Figure 4.40: Grouped mean and standard deviation for yaw motion across all wind speeds.

Wind–wave misalignment: Results for mooring tensions

The mooring line tensions under $\Delta = -30^\circ$ misalignment are shown in Figures 4.41, 4.42, and 4.43. For the fore line, both *SIL* and *PI* produce similar mean tensions across the three wave periods, with *PI* typically about 5–10% higher than *SIL*. The adapted numerical model, shows the biggest fore mooring tension by approximately 21–34% at $U = 8\ \mathrm{m\,s^{-1}}$ and by 3–12% at $U = 11\ \mathrm{m\,s^{-1}}$. Standard deviations for *SIL* exceed those of the numerical model by up to 83%, whereas the difference in spread between *SIL* and *PI* remains below 11%.

For the port line, *SIL* again yields the highest mean tensions, followed by *PI*, with the numerical model sitting highest overall. At $U = 8\ \mathrm{m\,s^{-1}}$, *SIL* under-predicts the numerical mean by about 100%, and at $U = 11\ \mathrm{m\,s^{-1}}$ by about 85%. The port line standard deviations differ from the numerical model by over 58%, and the two experimental methods differ from each other by roughly 50% in both mean and spread.

By contrast, the starboard line carries almost no load in the tank: both *SIL* and *PI* mean tensions remain close to zero with very small variability, whereas the adapted model maintains a large mean tension of ~ 2.1–2.2×10^6 N regardless of wave period or wind speed.

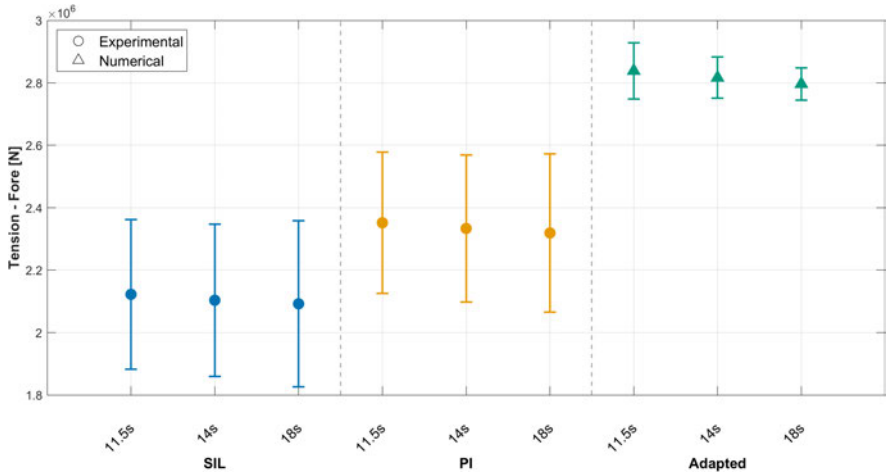

(a) 8 m/s wind speed

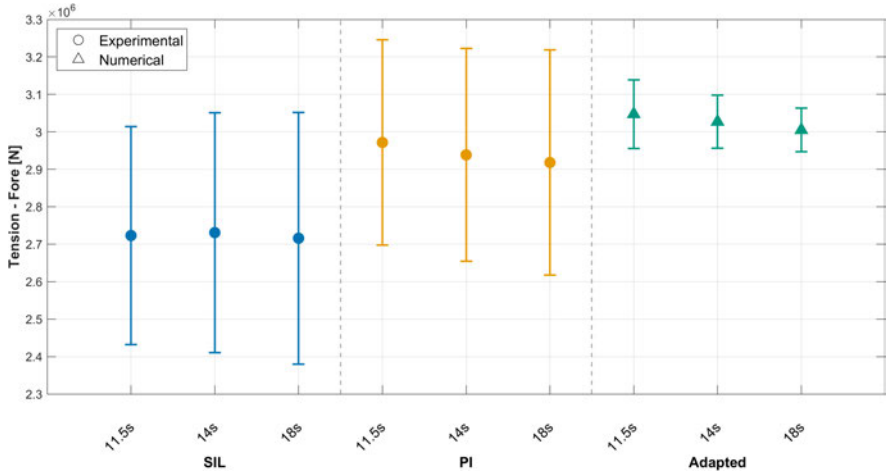

(b) 11 m/s wind speed

Figure 4.41: Grouped mean and standard deviation for fore mooring line tension across all wind speeds.

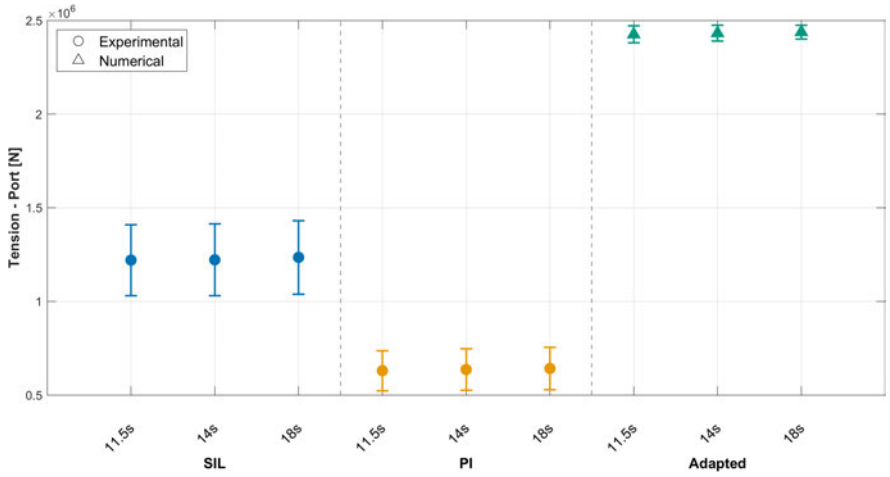

(a) 8 m/s wind speed

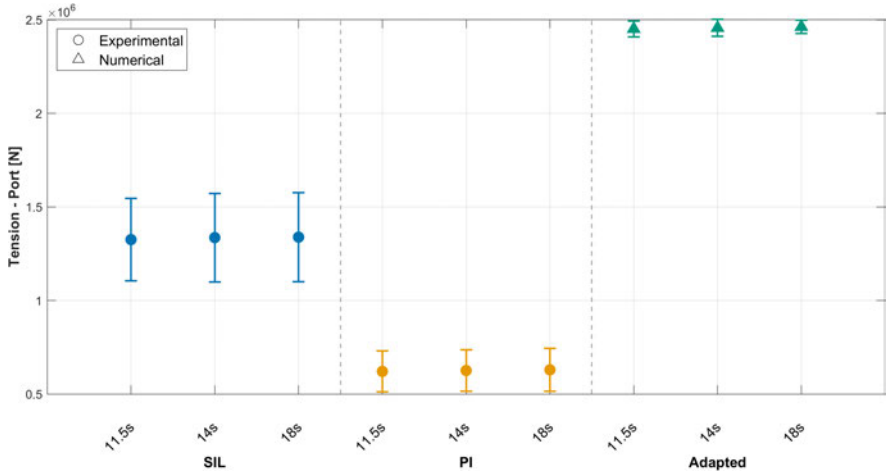

(b) 11 m/s wind speed

Figure 4.42: Grouped mean and standard deviation for port mooring line tension across all wind speeds.

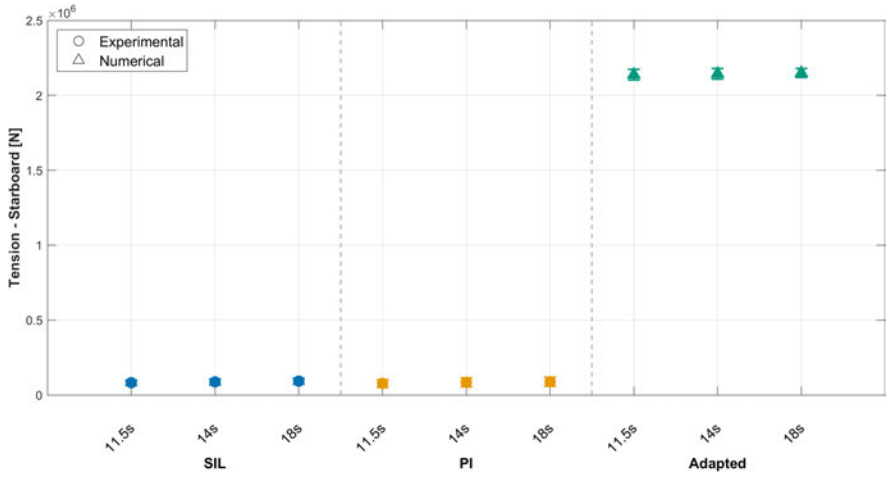

(a) 8 m/s wind speed

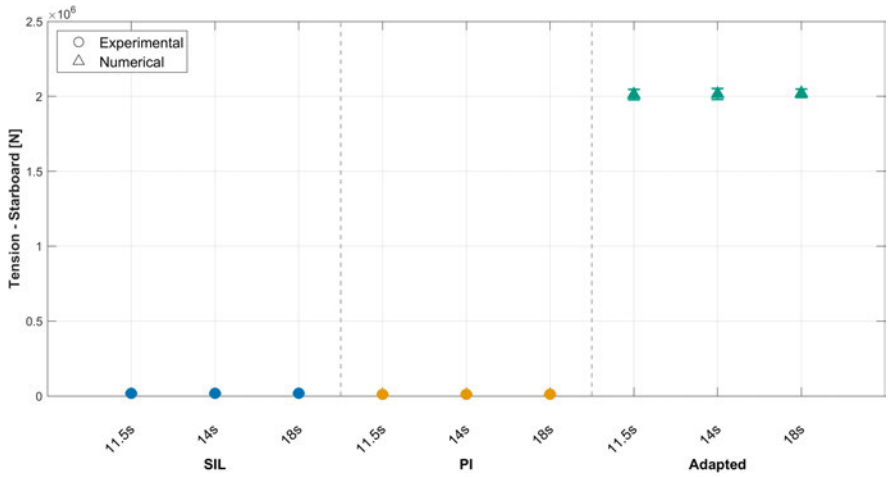

(b) 11 m/s wind speed

Figure 4.43: Grouped mean and standard deviation for starboard mooring line tension across all wind speeds.

The difference in results can be explained by not only the directionality of the load vector in the experimental setup, but also by the difference in pre-tensions. Table 4.9 summarises the static pretensions applied to each mooring line in the experimental tests and in the adapted numerical model. These pretensions form the baseline about which the drift-induced loads add, and they explain the observed mean tensions under $\Delta = -30^\circ$ misalignment.

Table 4.9: Baseline mooring pretensions for SIL, PI, and Adapted numerical model.

Line	SIL (N)	PI (N)	Adapted (N)
Fore	9.82×10^5	9.38×10^5	1.1625×10^6
Port	1.1220×10^6	9.03125×10^5	1.1625×10^6
Starboard	9.5355×10^5	7.70825×10^5	1.1625×10^6

The adapted model applies an identical pretension $T_0 = 1.1625 \times 10^6\,\mathrm{N}$ to all three lines, its mean tensions remain high and symmetric under misalignment. In contrast, the experimental configurations use unequal pretensions, especially *SIL*:

$$T_{0,\mathrm{port}} > T_{0,\mathrm{fore}} > T_{0,\mathrm{starboard}}.$$

When the platform is driven off-axis ($\Delta = -30^\circ$), the quasi-static drift loads superimpose on these baselines. Thus:

$$\overline{T}_{\mathrm{port}} > \overline{T}_{\mathrm{fore}} > \overline{T}_{\mathrm{starboard}},$$

exactly matching the experimental tension ordering seen in Figures 4.41–4.43. This indicates that the initial pretension distribution contributes to the observed asymmetry in mean tensions under misaligned loading. However, the asymmetry itself primarily arises from the off-axis wind loading, while the pretension differences influence how the resulting loads are distributed among the lines.

Despite this, the experimental results show higher mean fore-line tensions than port or starboard tensions, indicating that the thrust vector intended to be applied at -30° is not being consistently maintained in the tank tests.

Chapter Summary

This chapter presented a comprehensive evaluation of wind actuation methods for floating offshore wind turbine model testing through a structured comparison between numerical simulations and experimental results. The work progressed from numerical sensitivity analyses using OpenFAST to physical wave basin testing, addressing both aerodynamic loading representations and the performance of a custom-designed spring-rope mooring system.

By examining platform motions and mooring line tensions under regular and irregular wave conditions, including wind–wave misalignment cases, the chapter highlighted the relative performance of the tested actuation strategies, *Static Weight*, *PI*, and *SIL*, and compared their responses with those predicted numerically. The findings establish a basis for assessing the fidelity and practicality of each method within the context of floating offshore wind turbine model testing.

A more in-depth interpretation of these results, focusing on their implications for experimental design and connection to its TRL level, is provided in the following chapter.

Chapter 5

Discussion: Balancing Test Objectives and Actuation Complexity

This chapter discusses the wider implications for floating offshore wind turbine model testing based upon the results and observations from the analyses presented up to this point. It addresses the central question of whether increased complexity in wind actuation methods leads to appreciably better physical fidelity for experimental testing of floating offshore wind structures. By comparing the application of Static Weight, Proportional–Integral (PI) and Software-in-the-Loop (SIL) approaches (i.e. results of Sections 4.4.1–4.4.2) under both regular and irregular wave conditions, this chapter assesses the differences in the responses produced by each method, the extent to which these responses are consistent with the trends observed in the numerical model, and the consequences for future test campaigns.

Throughout this chapter, the numerical model is treated as a useful comparative reference rather than as a ground truth. Accordingly, consistency with the numerical prediction is interpreted only as agreement with that particular modelling framework, and not as proof that a given experimental response is inherently more physically correct.

Beyond purely technical performance, the trade-offs between physical fidelity and practicality are also considered. Although higher-complexity methods such as SIL can better represent motion-dependent aerodynamic loading, the additional time and effort required for calibration and implementation are substantial and cannot be ignored. The findings indicate that the benefit of complexity varies across wave types, degrees of freedom, and test objectives, calling for a more nuanced approach to method selection.

In order to inform decision-making and support Technology Readiness Level (TRL) progression, a staged development strategy is proposed based on the results presented. This framework aligns test complexity with the design maturity of the FOWT, balancing resource constraints against the need for high-quality data. Furthermore, the chapter discusses the frequency-response characteristics and control limitations of each system, identifying the conditions under which PI and SIL perform adequately and where control lag may lead to under- or over-damping effects.

Ultimately, this chapter not only consolidates the experimental observations, but also offers practical recommendations for choosing wind actuation strategies according to specific objectives and project stage. It highlights the importance of context-driven experimental design in advancing novel floating wind platforms through validation pipelines.

5.1 Limitations and Simplifications

Despite the comprehensive approach adopted in this study, several limitations and simplifications were necessary due to modelling constraints, experimental feasibility, and project scope. These factors do not undermine the core findings, but it is essential that these are not overlooked to accurately interpret the results and contextualise the observed discrepancies between numerical predictions and experimental measurements. Moreover, since numerical model tuning (i.e., calibrating hydrodynamic coefficients, damping, mooring properties, or controller gains to fit the tank tests) was not within the scope of this study, it is important to acknowledge the inherent differences between numerically modelling the system and testing it at scale in a physical environment. Including the numerical results alongside the experimental data provides a clearer benchmark for comparison, even in the absence of model calibration.

The limitations of the present study fall into three broad categories:

- Hydrodynamic numerical modelling assumptions: the numerical solver relies on linear, inviscid potential-flow theory which diverges from the viscous and scale-sensitive reality of wave basin experiments;
- Mooring system simplifications: the reference catenary system was approximated using a spring-rope setup in the wave tank, introducing differences in restoring, damping, and inertial characteristics;
- Control system latency and fidelity: particularly relevant for the SIL actuation, the control system affects the system's ability to track time-varying loads with high accuracy.

Each of these areas is discussed in detail in the following subsections, with emphasis on their physical origin, manifestation in the data, and implications for future modelling and testing campaigns.

5.1.1 Inherent Differences Between Numerical and Experimental Hydrodynamic Models

The linear, inviscid radiation–diffraction model implemented in OpenFAST reproduces the basin measurements well in terms of natural periods (see Section 4.3.6) and most response-amplitude operators (RAOs) (see Section 4.3.5 within the primary energy band of the site (≈ 0.05–$0.20\,\mathrm{Hz}$). Systematic discrepancies nevertheless persist. They stem from modelling assumptions, scale effects and facility artefacts rather than experimental error. The main limitations and the practical trends they induce, are summarised below.

a. Potential-flow hydrodynamics *versus* viscous reality

The numerical solver is inviscid and linear, so damping enters only through amplitude-independent radiation and user-defined damping terms, whereas the $1{:}50$ model operates at Reynolds numbers much lower than at full scale, causing form drag and vortex shedding to contribute additional viscous dissipation in every degree of freedom, most strongly in roll, yaw, and heave. The consequence is that low-frequency pitch RAOs are under-predicted, since the decay tests showed substantially higher damping ratios in the experiments than in the numerical model. Although heave periods align well, the numerical heave peak RAO still falls by approximately 10%, indicating a residual mismatch in excitation or added mass rather than in stiffness.

b. Low-frequency excitation and effective inertia

Low-frequency surge and the coupled pitch that accompanies it, are consistently larger in the basin than in the simulation, even though surge natural periods match ($\Delta T \approx 0.4\%$). The most plausible explanation is that the potential-flow database under-represents second-order (slow-drift) excitation and slightly overestimates added mass and radiation damping below $0.05\,\mathrm{Hz}$. The ratio of experimental to numerical surge RAO exceeds unity by 30–70% in this band. It is also worth noting that the experimental model exhibits lower pitch stiffness than the numerical model, possibly due to differences in inertia, mass distribution, or overall system stiffness. The concurrent indication of lower pitch stiffness in the experiment increases surge–pitch coupling, elevating low-frequency pitch excursions and fore–aft tower-base moments, while shifting mean offset and pretension requirements. Under-prediction of this band by the numerical model is therefore non-conservative for watch-circle estimates, line utilisation and fatigue assessment, and can mislead parameter tuning (e.g., added mass, radiation/viscous damping) during model calibration.

c. Spectral and processing artefacts

A few numerical RAO spikes at resonance stem from finite record length and the discrete FFT grid ($\Delta f = 0.005\,\mathrm{Hz}$, 24 steady-state cycles), not from hydrodynamic theory. Conversely, measured RAOs remain non-zero at high frequency most probably due to sensor noise and minor viscous effects while the numerical RAOs decay smoothly to zero. This mismatch artificially inflates experimental-to-numerical ratios above $\sim 0.18\,\mathrm{Hz}$.

d. Facility effects and asymmetries

Small port–starboard ballast offsets, gauge-alignment tolerances and generic tank artefacts (e.g. reflections) inevitably add scatter to the measurements, though their magnitude was not quantified in this campaign. The FloWave characterisation reports centre-tank reflections typically $< 10\%$ for 0.3–0.6 Hz (irregular) and $< 20\%$ at 0.75 Hz, stabilising after 64–128 s, with higher values only near the boundary (Draycott, 2017). Consequently, any residual bias in the RAOs may partly reflect such facility effects rather than hydrodynamic modelling errors alone.

5.1.2 Mooring-system simplification and its implications

A true catenary mooring layout could not be replicated in the wave basin, as explained in Section 3.3.9. Instead, a spring-rope, semi-taut system was designed to replicate the quasi-static restoring behaviour of the catenary configuration at relevant offsets. While this simplification was necessary, it introduces key, but manageable, differences.

a. Restoring mechanism

A weight-dominated catenary system carries high pretension and therefore higher *mean* line tensions, whereas the EA-dominated semi-taut (spring–rope) system achieves the required restoring with markedly lower pretension. As a result, the experimental setup and the adapted semi-taut model show lower mean tensions, while the original catenary model predicts uniformly higher means ($\approx 2\times$). The impact is twofold. First, ultimate loads and utilisation are directly affected, since design peaks scale approximately as $T_{\mathrm{peak}} \approx \bar{T} + k\,\sigma_T$ for a given dynamic range σ_T. Reducing $\bar{T}$ lowers anchor reactions, end-fitting loads, and required line size. Second, the trade-off is greater low-frequency compliance: with lower pretension the horizontal restoring is weaker, leading to larger offsets and slow-drift tension ranges that govern watch-circle and clearance checks. In summary, the catenary assumption is conservative for line sizing and anchor capacity but can be non-conservative for offset predictions and low-frequency dynamics; the semi-taut representation better reflects the measured behaviour and should be used for station-keeping assessments.

b. Natural periods

By matching quasi-static stiffness, the adapted model brings surge and yaw natural periods within $\pm 0.5\%$ of experimental values, and heave within approximately 7%. However, natural frequencies in pitch and roll remain shorter in the numerical model (approximately $29\,\mathrm{s}$) than in the basin (approximately 33–$34\,\mathrm{s}$). This discrepancy suggests lateral and rotational compliance in the physical spring-rope system that is not captured by MoorDyn. Additionally, the vertical component of pretension in the spring ropes stiffens heave in the physical setup, resulting in a shorter heave period compared to the catenary prediction.

c. Damping with moorings attached

Attaching the moorings in the experiment introduces additional effective damping due to rope hysteresis, fairlead friction, and other mechanical dissipation mechanisms that are not fully represented in the numerical model. Since MoorDyn does not currently capture internal hysteresis directly, this additional energy dissipation is difficult to reproduce in a physically explicit way. This limitation contributes to under-damped pitch responses and larger mean pitch offsets in the adapted model simulations, as seen in the extreme-wave no-wind results (see Figure 4.22a). Collectively, over-predicted pitch statistics can misrepresent tower-base bending, nacelle accelerations, and mooring fatigue, leading to over-conservative mass/pretension choices.

d. Choice of reference model

The adapted semi-taut model reproduces natural periods, RAOs, extreme-sea motions, and mean mooring tensions within reasonable accuracy (approximately 10–15%). In contrast, the original catenary configuration is overly pre-tensioned for the basin conditions, leading to overestimated line tensions (by about a factor of two). For these reasons, the adapted mooring model is adopted as the numerical reference.

5.1.3 Actuation System Constraints and Control Fidelity

The wind loads were imposed using either a proportional–integral (PI) control loop with fixed set-point or a software-in-the-loop (SIL) configuration where time-varying loads were derived from a simplified numerical solver. While each method allowed for controlled application of thrust in the basin, they both introduced non-negligible latency and force-tracking limitations, especially under short-period (high-frequency) excitation. These effects must be considered when interpreting floater responses and comparing with idealised numerical models.

a. Performance Evaluation of PI Method

Figure 5.1 reveals a clear, repeatable sequence of phase lags between the physical wave and each control or response signal. To suppress high-frequency PI jitter, the set-point, measured force, and motor-current signals were low-pass filtered at $f_c = 0.5\,\mathrm{Hz}$ (zero-phase); the wave-elevation and pitch traces were left unfiltered. All traces were then downsampled by a factor of 4 for plotting efficiency and finally normalised to $[0, 1]$ (per-signal).

The wave crest (black) provides a convenient reference signal against which the relative timing of the control and response signals can be compared. The commanded set-point (blue) remains nearly constant near the top of its own normalised range (~ 0.9). The low-pass-filtered force (red) peaks roughly 0.5–$0.7\,\mathrm{s}$ after the wave crest, corresponding to the combined PI-loop computation and actuator response required to impose the target load. The motor current (magenta) follows with a similar delay of approximately 0.4–$0.6\,\mathrm{s}$, reflecting the drive electronics and motor dynamics. Finally, the platform pitch (green) reaches its maximum around 0.6–$0.8\,\mathrm{s}$ after the wave crest, capturing the floater's hydrodynamic and structural response time. These delays remain consistent from cycle to cycle, indicating an end-to-end latency of the PI-controlled system under regular-wave excitation on the order of half a second (tank time).

The observed end-to-end delay is $\tau \simeq 0.4$–$0.6\,\mathrm{s}$ in *tank* time, which at 1:50 Froude scale corresponds to $\tau \simeq 2.8$–$4.2\,\mathrm{s}$ full scale. For the regular wave used here ($T = 11.5\,\mathrm{s}$ full scale, $T \approx 11.5/\sqrt{50} = 1.63\,\mathrm{s}$ tank), the associated phase lag is

$$\phi = \omega\tau = \frac{2\pi\,\tau}{T} \approx 89^\circ\text{–}133^\circ.$$

This places the PI actuation and pitch response close to quadrature with the wave crest. It should be noted, however, that being in phase with the wave elevation is not itself the performance target of the controller. Rather, the comparison with wave elevation is used here only to illustrate the relative timing of the control and response signals under regular-wave forcing. Since the PI set-point is quasi-steady, the main implication of the observed lag is not a simple loss of "in-phase" loading, but a reduced ability of the actuation system to respond promptly to wave-driven variations in platform motion and cable tension. The latency should nevertheless be represented as a transport delay in high-fidelity models and considered in controller tuning; for shorter wave periods the same τ yields a larger phase lag and therefore a greater loss of responsiveness.

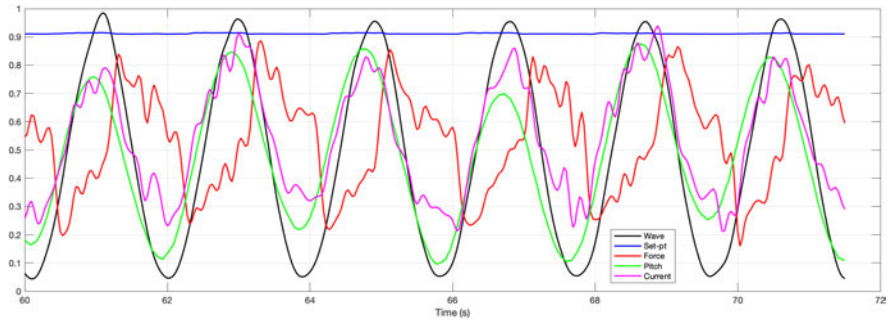

Figure 5.1: Normalised and low-pass-filtered control signals over 11.5 seconds period waves. The black trace is the physical wave elevation, the blue trace the commanded set-point, the red trace the low-pass filtered load-cell force, the magenta trace the low-pass filtered motor current, and the green trace the platform pitch.

To further quantify the tracking performance of the proportional–integral (PI) controller under irregular wave excitation (see Section 4.4.2), the following signals were logged synchronously at the tank-scale sampling rate (≥ 128 Hz):

- $F_{\mathrm{sp}}(t)$: commanded force set-point from the PI loop [N],
- $F_{\mathrm{m}}(t)$: measured force from the wind-load cell [N],
- $I(t)$: motor output current [A].

From these time series, five scalar metrics were computed over each test duration T:

$$e(t) = F_{\mathrm{sp}}(t) - F_{\mathrm{m}}(t), \tag{5.1}$$

$$\mathrm{RMSE} = \sqrt{\frac{1}{T}\int_0^T e(t)^2\,\mathrm{d}t}, \tag{5.2}$$

$$\mathrm{MAE} = \frac{1}{T}\int_0^T \left|e(t)\right|\mathrm{d}t, \tag{5.3}$$

$$e_{\max} = \max_{0\leq t\leq T}\left|e(t)\right|, \tag{5.4}$$

$$I_{\mathrm{rms}} = \sqrt{\frac{1}{T}\int_0^T \left[I(t)\right]^2\mathrm{d}t}. \tag{5.5}$$

Here, $e(t)$ denotes the instantaneous tracking error, RMSE and MAE respectively quantify its root-mean-square and mean-absolute deviations, $e_{\max}$ captures the worst-case deviation, and I_{rms} reflects the control effort in terms of effective current draw.

Results are first reported in absolute terms, i.e. directly in Newtons and Amperes, as shown in Table 5.1. Each row corresponds to one test case, identified by its commanded constant force $F_{\mathrm{cmd}} \in \{9, 14, 20\}$ N and the wave peak period T_p.

To facilitate comparison across different set-point levels, the error metrics are also expressed as percentages of the commanded force:

$$\mathrm{Error}_{\%} = \frac{\mathrm{Error}_{\mathrm{N}}}{F_{\mathrm{cmd}}} \times 100\%. \tag{5.6}$$

These normalised metrics appear in Table 5.2 and emphasise the controller's relative accuracy. Finally, Figure 5.2 plots the normalised RMSE against T_p for each load level. All presented results are reported at the model (tank) scale of $1:50$, while the wave peak periods T_p and wind speeds U_∞ have been converted to their corresponding full-scale values. This choice ensures the metrics in Tables 5.1 and 5.2, and the curve in Figure 5.2 can be directly related to the full-scale wave conditions discussed in Section 4.4.2.

Table 5.1 shows that the absolute errors depend on both commanded load and test condition. Across the three force levels, RMSE, MAE, and I_{rms} increase with increasing F_{cmd}, reflecting the greater actuation effort required at higher thrust demand. Within each force level, however, the absolute errors decrease as T_p increases from 11.5 s to 18 s, indicating that the controller tracks more effectively when the wave-induced load variations occur over longer time scales. The peak error $e_{\max}$ remains of the same order as the set-point, but also decreases as T_p increases for each F_{cmd}, showing that the most severe instantaneous tracking losses occur in the shortest-period cases.

When normalised by the commanded force (Table 5.2), the relative errors decrease with both increasing T_p and increasing F_{cmd}. Over the tested range, the RMSE% falls from approximately 22.6% to 14.3%, while the normalised MAE and peak error show similar reductions. This indicates that the controller becomes relatively more accurate both when the commanded load is larger and when the wave-induced variations occur more slowly, which is consistent with improved signal-to-noise ratio and reduced bandwidth demand.

During each trough–to–crest transition the winch line momentarily loses tension, causing the measured force $F_{\mathrm{m}}(t)$ to fall below the commanded set-point $F_{\mathrm{sp}}(t)$ until the PI controller increases the motor current $I(t)$ to re-tension the line. This dynamic "catch-up" appears in the error signal

$$e(t) = F_{\mathrm{sp}}(t) - F_{\mathrm{m}}(t)$$

whose peak values $e_{\max}$ approach the magnitude of the set-point (for example, $e_{\max} = 9.15\,\mathrm{N}$ at $F_{\mathrm{cmd}} = 9\,\mathrm{N}$, Table 5.1), and correspond to normalised peak errors of approximately 100% (Table 5.2). Such transient lag is an inherent consequence of finite actuation bandwidth and line dynamics under rapidly changing wave loads.

Overall, the PI controller remains robustly stable with no oscillatory behaviour. It exhibits a transient lag, manifested as large, momentary misses at each trough-to-crest jump and shows performance that deteriorates under faster wave forcing but improves in relative accuracy at higher commanded loads.

Table 5.1: Absolute performance metrics for each test condition.

F_{cmd} [N]	U_∞ [m/s]	T_p [s]	RMSE [N]	MAE [N]	$e_{\max}$ [N]	I_{rms} [A]
9	22	11.5	2.03	1.63	9.15	2.04
9	22	14.0	1.92	1.54	8.95	2.08
9	22	18.0	1.76	1.39	8.76	2.11
14	8	11.5	2.81	2.24	12.87	3.17
14	8	14.0	2.61	2.08	12.02	3.17
14	8	18.0	2.32	1.83	10.52	3.25
20	11	11.5	3.40	2.74	10.54	4.31
20	11	14.0	3.19	2.56	10.05	4.36
20	11	18.0	2.87	2.27	9.52	4.39

Table 5.2: Normalised error metrics (percent of F_{cmd}).

F_{cmd} [N]	U_∞ [m/s]	T_p [s]	RMSE [%]	MAE [%]	$e_{\max}$ [%]
9	22	11.5	22.57	18.08	101.72
9	22	14.0	21.34	17.11	99.44
9	22	18.0	19.54	15.44	97.31
14	8	11.5	20.06	15.98	91.93
14	8	14.0	18.67	14.87	85.87
14	8	18.0	16.57	13.07	75.11
20	11	11.5	16.99	13.71	52.72
20	11	14.0	15.97	12.80	50.23
20	11	18.0	14.33	11.37	47.61

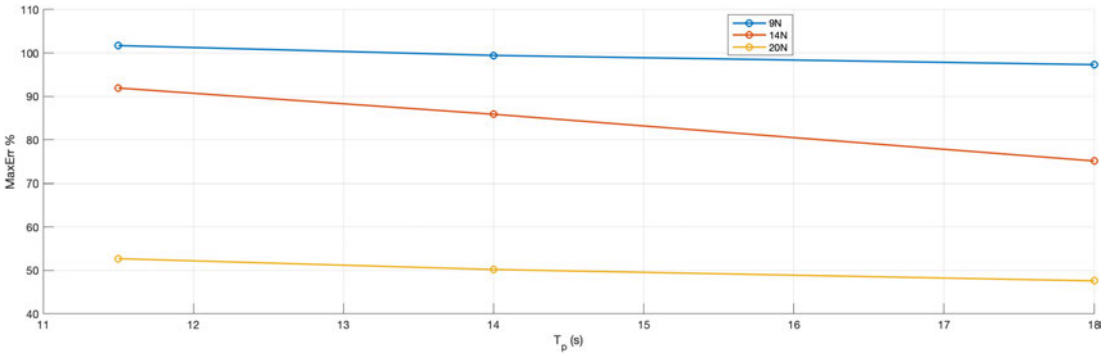

Figure 5.2: Normalised RMSE (% of F_{cmd}) as a function of wave peak period for the three load levels.

b. Performance Evaluation of SIL Method

Prior to examining the *SIL* performance, it is important to recall that the SIL method makes use of the same PI motor controller described in Section 3.3.8, but instead of holding a constant force set-point, the commanded force $F_{\mathrm{sp}}(t)$ is recalculated every $\Delta t = 0.010\,\mathrm{s}$ (tank scale) by the BEM solver. At each time step the BEM code ingests the instantaneous floater motions, the velocities and accelerations are calculated and outputs the required force to maintain optimal loading, which is then passed to the PI controller as its time-varying set-point.

To validate this in the wave tank, a regular wave test was used with wave height $H = 6\,\mathrm{m}$ and period $T = 13.5\,\mathrm{s}$. Figure 5.3 overlays three normalised time series: the wave elevation (green), the BEM-computed force set-point delivered by the SIL loop (blue), and the resulting platform pitch response (red).

Several key observations emerge from Figure 5.3. First, the BEM-computed set-point (blue curve) peaks consistently $\Delta t_{\mathrm{SIL}} \approx 0.2$–$0.3\,\mathrm{s}$ after the wave crest (green). This phase lag directly quantifies the combined computational and communication latency in the SIL implementation of the BEM solver.

Second, the measured pitch response (red curve) reaches normalised amplitudes near unity, yet it peaks even later than the set-point, introducing an additional mechanical delay $\Delta_{\mathrm{mech}} \approx 0.2$–$0.3\,\mathrm{s}$. Consequently, the total lag between the physical wave crest and the realized platform rotation is

$$\Delta t_{\mathrm{total}} = \Delta t_{\mathrm{SIL}} + \Delta t_{\mathrm{mech}} \approx 0.5\ \mathrm{s}.$$

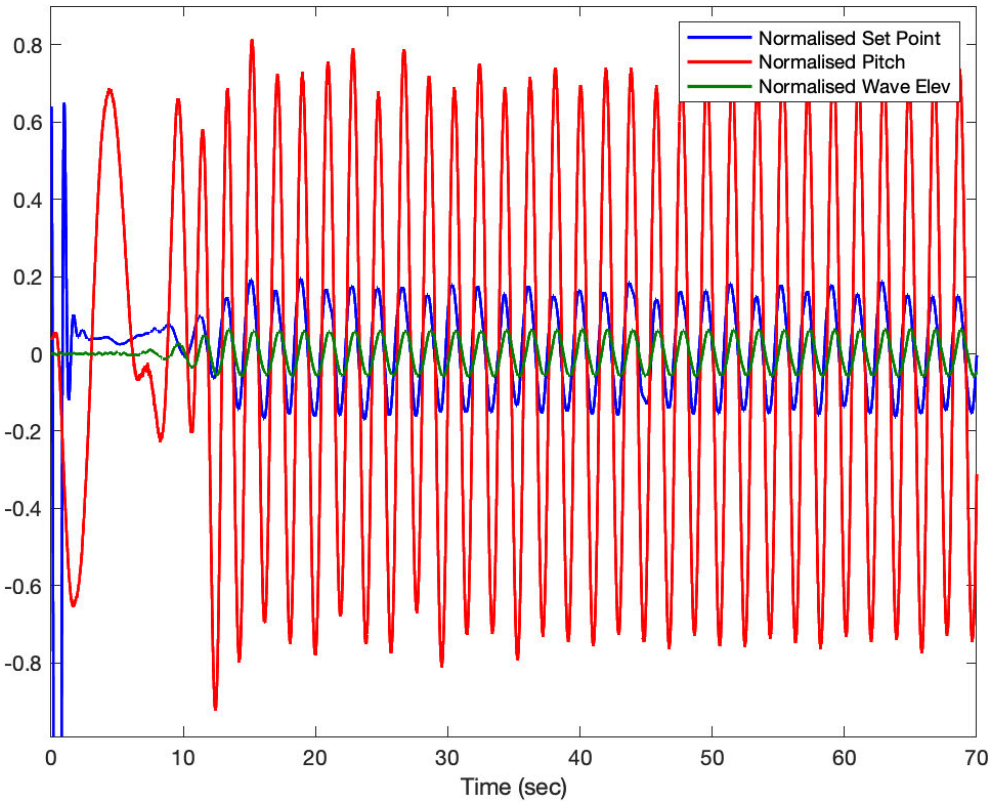

Figure 5.3: Overlay of normalised wave elevation, SIL set-point, and measured pitch for a regular wave of $H = 6\,\text{m}$ and $T = 13.5\,\text{s}$.

Finally, the pitch waveform shows slight asymmetry and higher-frequency ripples, indicating that the platform's natural dynamics and actuator bandwidth further distort the ideal sinusoidal response. Any high-fidelity simulation or controller design must therefore account for both the measured latency Δt_{total} and the non-ideal frequency content of the response in order to achieve precise phase tracking of the wave load in SIL mode.

Under irregular waves

In order to assess the fidelity of the SIL winch controller for the irregular waves results previously presented, two complementary sets of results are shown. First, Table 5.3 summarises the root-mean-square error (RMSE), mean absolute error (MAE), maximum absolute error (MaxErr), and root-mean-square current demand I_{rms} as functions of the free-stream wind speed U_∞ and the peak wave period T_p. Second, Figure 5.4 displays the time series of the measured wind load-cell signal and the commanded force set-point for each U_∞, with three subplots corresponding to $T_p = 1.63$, 1.98, and $2.55\,\text{s}$. These results are shown in tank scale except for the wind speed and T_p values on the table and the wind speeds in the timeseries. Together, these results illustrate both the quantitative error metrics and the dynamic tracking behaviour of the controller.

The results in Table 5.3 indicate that, for each fixed wind speed U_∞, both the root-mean-square error and the mean absolute error decrease slightly as T_p increases. The peak absolute error MaxErr shows the same tendency, with the largest values occurring for the $U_\infty = 11\,\mathrm{m/s}$ cases and the smallest values for $U_\infty = 22\,\mathrm{m/s}$. The current demand I_{rms} follows the same broad pattern: it is highest for the $11\,\mathrm{m/s}$ cases, lower for $8\,\mathrm{m/s}$, and lowest for $22\,\mathrm{m/s}$, while varying only weakly with T_p within each wind-speed set. Overall, the SIL metrics are fairly consistent across the tested conditions, but they do not show the strong intermediate-period peak that had been inferred from the earlier version of the dataset.

The SIL metrics do not support a sharp resonance-like peak at the intermediate wave period. Instead, the tracking errors vary more smoothly across the tested wave periods, while the differences between wind-speed cases are more pronounced than previously inferred. This suggests that the observed SIL performance is controlled by the combined effects of actuation bandwidth, controller dynamics, and the magnitude of the commanded aerodynamic load, rather than by a single dominant resonance at $T_p = 14.0\,\mathrm{s}$.

Comparison of the time-series traces of the wind load-cell signal and the set-point reveals persistent high-frequency fluctuations in the measured load, superimposed on a slowly varying commanded force. The measured load occasionally undershoots the set-point by several newtons, suggesting that the motor and winch assembly may be limited in bandwidth or torque such that they cannot instantaneously track the desired force profile under the combined wind-wave loading.

Finally, it should be noted that the underlying blade-element-momentum (BEM) model employed in this SIL study remains highly simplified: it omits tip-loss and unsteady aerodynamic corrections, tower interference, and only incorporates floater pitch via Qualisys motion-capture data. Under these simplifying assumptions, the observed tracking errors should be interpreted as arising from both the model limitations and the physical constraints of the actuation system.

Table 5.3: Summary of SIL absolute performance metrics for each free-stream wind speed U_∞ and peak wave period T_p after correction of the load-cell calibration.

$U_\infty\,(\mathrm{m/s})$	$T_p\,(\mathrm{s})$	$\mathrm{RMSE}\,(\mathrm{N})$	$\mathrm{MAE}\,(\mathrm{N})$	$\mathrm{MaxErr}\,(\mathrm{N})$	$I_{\mathrm{rms}}\,(\mathrm{A})$
8	11.5	1.1549	0.9187	4.7186	3.3270
8	14.0	1.1417	0.9095	4.3128	3.3436
8	18.0	1.0867	0.8631	4.2346	3.3595
11	11.5	1.3756	1.0931	9.2448	4.6343
11	14.0	1.3438	1.0607	9.8725	4.6551
11	18.0	1.3102	1.0315	9.6508	4.6680
22	11.5	1.0475	0.8502	3.6470	2.2752
22	14.0	1.0269	0.8390	3.6740	2.2773
22	18.0	1.0206	0.8345	3.7225	2.2795

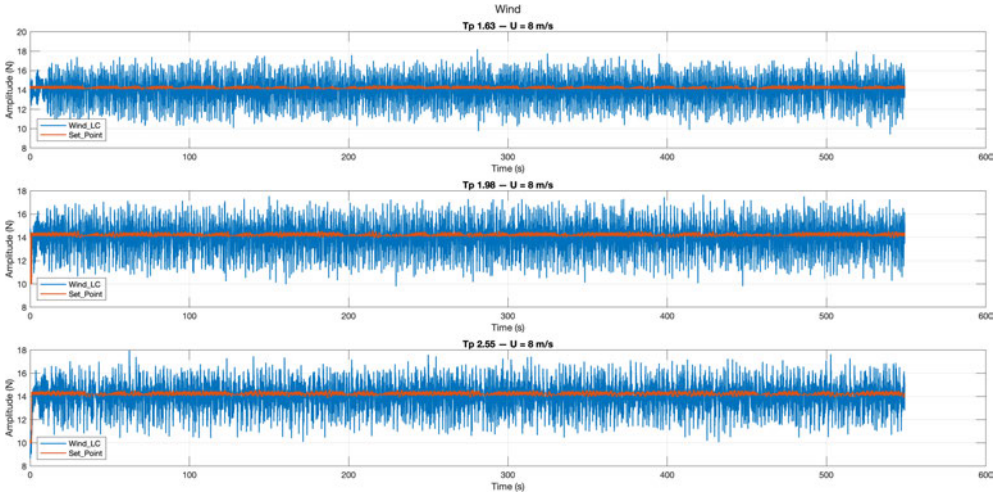

(a) $U_\infty = 8\,\text{m/s}$

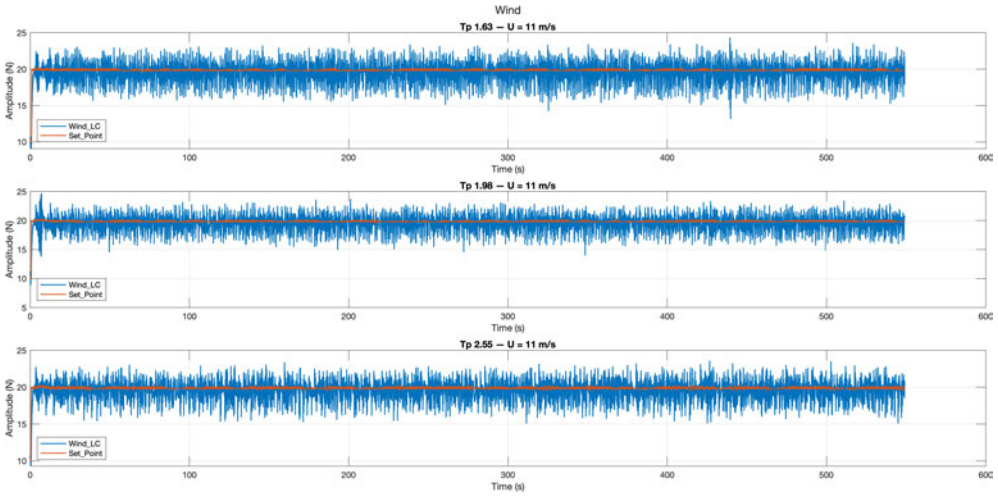

(b) $U_\infty = 11\,\text{m/s}$

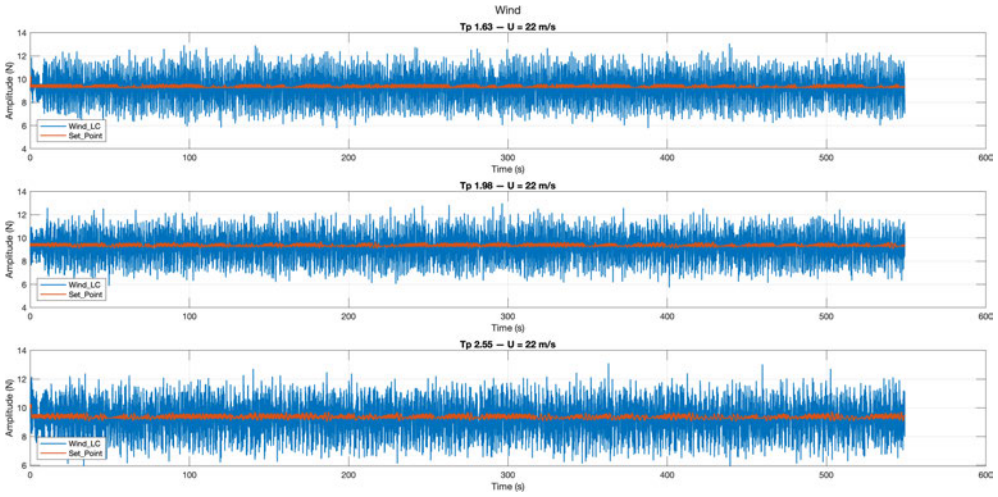

(c) $U_\infty = 22\,\text{m/s}$

Figure 5.4: Time series of the measured wind load-cell signal (blue) versus the commanded force set-point (orange) for each free-stream wind speed. Within each subplot, the three traces correspond to wave periods $T_p = 1.63, 1.98, 2.55\,\text{s}$ from top to bottom.

5.1.4 Synthesis of PI and SIL Control Performance

The comparative results in Sections 5.1.3–5.1.3 reveal two principal differences between the control strategies. First, the proportional–integral (PI) loop sustains a larger mean winch force than the software-in-the-loop (SIL) implementation, i.e.

$$F_{\mathrm{LC}}^{\mathrm{PI}} > F_{\mathrm{LC}}^{\mathrm{SIL}} \quad \forall\, T_p, U_\infty,$$

where F_{LC} denotes the wind load-cell reading. The higher holding force stiffens the floater, yielding smaller surge displacements and pitch angles (lower means and variances) than those recorded during SIL runs. Conversely, the SIL controller permits larger platform excursions, trading reduced average load for increased low-frequency motions.

Second, both systems exhibit an end-to-end latency of approximately 0.5 s *in tank scale*. Applying Froude scaling for the 1 : 50 model ($\sqrt{\lambda} = \sqrt{50} \approx 7.07$) gives a full-scale delay of

$$\Delta t_{\mathrm{full}} = 0.5\ \mathrm{s} \times 7.07 \approx 3.5\ \mathrm{s}.$$

Relative to the full-scale regular-wave periods used here ($T_{\mathrm{full}} \approx 13.5$–$18$ s), this corresponds to a phase shift of roughly 70°–93°, i.e. almost a quarter cycle. For irregular seas with energetic components at $T_{\mathrm{full}} \lesssim 5$ s, the same delay yields a phase lag in excess of 250°. The impact is two-fold: (i) diminished ability to track rapidly varying aerodynamic loads and (ii) amplification of low-frequency surge and pitch.

Implications and Pathways for Improvement

The present SIL architecture therefore proves adequate only for very long-period, low-bandwidth loading and falls short once the wave–wind spectrum contains energy at periods below ≈ 11.5 s. Two remedial actions are recommended:

1. **Reduce computational latency.** Executing the blade-element–momentum solver on a real-time processor or GPU, or coarsening the blade discretisation, could shorten each update from 10 ms to 1 ms and lower the total delay.
2. **Introduce predictive control.** A model-based predictor (e.g. Smith predictor or disturbance observer) could phase-advance the commanded force, compensating the remaining delay and restoring synchrony with the wave field.

This campaign was conceived as a *proof-of-concept* rather than an attempt at a fully optimised SIL system. Developing a low-latency, high-bandwidth SIL architecture demands substantial effort in control design, hardware integration, and real-time implementation, and was beyond the intended scope of the present work. The results nonetheless provide an initial operational benchmark at FloWave and delineate the technical priorities for subsequent development.

5.1.5 Wind–wave misalignment and directional fidelity

The misalignment tests (Section 4.4.3) revealed an additional class of discrepancies between numerical predictions and basin measurements that cannot be explained solely by hydrodynamic or mooring simplifications. Instead, they highlight the critical role of directional fidelity in wind-load application.

In the numerical model, the thrust vector was held at a fixed azimuth of $\beta_v = -30^\circ$, yielding the expected resolution of forces: reduced surge by $\cos 30^\circ$, increased sway and yaw by $\sin 30^\circ$, and corresponding redistribution of mooring tensions. The tank tests, however, did not maintain this fixed vector. As the platform drifted and oscillated in waves, the winch cable reoriented towards the bow and altered its vertical angle. Consequently, a large forward (surge-aligned) component of thrust persisted in both PI and SIL cases. This explains why experimental surge means remained high (comparable to head-sea conditions) rather than decreasing as predicted.

The same vector deviation also generated unintended cross-coupling into roll and pitch. In SIL mode, where the commanded thrust continuously tracked instantaneous kinematics, these deviations were transmitted more faithfully, producing the largest mean offsets. PI control, with its more constant thrust, partially filtered such excursions and gave closer agreement with the adapted numerical model. The consistent ordering observed across surge, sway, pitch, and roll:

$$\textit{SIL} > \textit{PI} > \text{Adapted}$$

illustrates that increased actuation complexity does not necessarily yield increased accuracy when directional control is imperfect.

Mooring pretensions compounded these effects. The adapted numerical model assumed equal pretension in all three lines, whereas the tank setup imposed unequal values (Table 4.9), with port $>$ fore $>$ starboard. Under misaligned loading, this asymmetry dictated the ordering of mean tensions. The starboard line carried negligible load in the basin while remaining heavily loaded in the model. Thus, even before dynamic effects are considered, baseline pretension distributions strongly influence how misaligned thrust is resisted.

Taken together, these results underline two broader points for FOWT model testing:

1. **Directional fidelity is as important as amplitude fidelity.** A thrust system that reproduces the correct mean force but deviates in azimuth can give systematically biased offsets and mooring loads, particularly in coupled DOFs such as sway, roll, and yaw.
2. **Initial pretension matters.** Differences of only 10–20% in line pretensions are sufficient to change which line dominates load-sharing under off-axis thrust. Unless pretensions are carefully matched, comparisons with numerical models risk misinterpretation.

These observations connect back to the broader question of actuation complexity. While SIL is theoretically superior for capturing unsteady aero–hydro coupling, its advantage is contingent upon accurate force orientation and realistic baseline mooring states. Without these, the added complexity may amplify rather than reduce discrepancies. In practical terms, ensuring correct directional application of thrust, through hardware design (e.g. gimballed fairleads, multiple winches) or software compensation is a prerequisite before SIL can deliver its intended fidelity in misaligned wind–wave conditions.

5.2 Does Complexity Improve Accuracy?

This section explores whether increasing the complexity of wind actuation methods, moving from Static Weight to PI control and finally to Software-in-the-Loop, actually results in improved physical fidelity. This is a central question of the present work, especially considering the trade-offs involved in test campaign planning.

In practical applications, when the primary objective is to reproduce fully coupled aero–hydro spectral responses and to capture dynamics pertinent to fatigue, the Software-in-the-Loop (SIL) methodology is the most physically representative of the three tested approaches, provided that its control loop and filtering operate on a sufficiently short timescale to inject thrust at the requisite frequencies. By contrast, both the PI-controlled thrust approach and the static-weight method should be regarded as simplified loading strategies. The PI approach can reduce some mean offsets relative to the static-weight case, but in the present experiments this was often accompanied by clear control artefacts, including excessive low-frequency damping and transient tracking errors. The static-weight method, although simple, provides a transparent and robust approximation of mean thrust loading. Accordingly, neither PI nor static weight can be regarded as a generally superior intermediate solution; rather, their usefulness depends on whether the test objective is mean loading, motion envelopes, or dynamic fidelity.

In the comparison of response-amplitude operators, all three tank-test methods reduce low-frequency motions in heave and pitch relative to the no-wind case. At rated wind speed, the SIL actuation gives the lowest experimental surge RAOs and follows the numerical trend more closely than the other experimental methods. By contrast, the static-weight and PI methods reproduce primarily the mean thrust input and do not capture the same degree of motion-dependent aerodynamic damping and restoring. Above approximately $0.05\,\mathrm{Hz}$, however, the SIL method exhibits less suppression than both the PI and static-weight approaches, because its thrust output varies with platform pitch and is subject to a finite control delay. This same delay also affects higher-amplitude waves.

Under below-rated wind conditions, the PI scheme often produces the smallest RAOs at the very lowest frequencies, occasionally falling below the numerical reference. This apparent improvement should not be interpreted as greater physical realism. Rather, it is a control artefact: integral action combined with load-cell feedback generates a phase-favourable counterforce, leading to excessive low-frequency damping. SIL remains marginally higher but more physically representative, since its thrust follows realistic kinematics and bandwidth limitations. In the mid-frequency band (≈ 0.05–$0.15\,\mathrm{Hz}$), all methods converge closely. A slight uplift in pitch RAOs under wind, absent in the numerical model, appears linked to control delay and actuation dynamics. At higher frequencies, all methods again show similar behaviour.

Irregular-sea experiments offer a conditional verdict. Added actuation complexity improves physical fidelity only when the control system is sufficiently mature to capture coupled aero–hydro dynamics and spectral content. Otherwise, even SIL may not deliver its theoretical advantage, while PI may appear to reduce some response measures through control-induced damping rather than through a more realistic representation of aerodynamic loading. The present results therefore suggest that apparent reductions in motion under PI control should be interpreted cautiously, since they may arise from actuator and controller behaviour rather than from improved physical realism.

For mean quantities, the static-weight approach delivers fore-line tensions of similar magnitude to SIL for wind speeds of 8–$11\,\mathrm{m/s}$, while PI is systematically higher and more variable. Surge and pitch mean offsets are also larger under Static Weight than under PI or SIL, and all three methods converge by $22\,\mathrm{m/s}$ as thrust declines. Thus, if the goal is a rapid estimate of mean line loads or conservative motion envelopes, static weight may be sufficient. More sophisticated metrics, such as motion spectra, fatigue-relevant spreads, controller interaction, or wind–wave misalignment, justify the additional complexity of SIL, but the present data do not support a general recommendation of PI as a superior intermediate solution.

Finally, comparisons with the numerical model reveal persistent differences in response level and damping behaviour, which are traceable not only to the presence or absence of the complete aerodynamic load vector, but also to the inherent differences between numerical hydrodynamic modelling and physical testing discussed earlier in this chapter.

In summary:

- **SIL** is the most appropriate method when spectral fidelity and motion-dependent aerodynamic coupling are required, provided its control system is sufficiently developed to meet bandwidth and delay requirements.
- **PI** can be useful as a regulated mean-thrust approach, but in the present experiments it introduced clear control artefacts and therefore cannot be recommended as a generally superior intermediate method.

- **Static weight** is adequate when the objective is limited to approximate mean loading or conservative motion envelopes, and when low implementation complexity is a priority.

5.3 Is Complexity Justified?

When the three actuation methods are arranged by increasing control complexity, Static Weight (simplest, no active control) $\rightarrow$ PI loop $\rightarrow$ SIL (most complex), a clear increase in implementation cost, latency, and potential for artefacts is observed. The improvement in physical fidelity, however, is not monotonic in practice, because the benefits of added complexity depend on how well the actuation system is implemented.

Static Weight (Low Complexity)

- **Captures:** Primarily the mean thrust level.
- **Misses:** Motion-dependent aerodynamic forces, unsteady aerodynamic damping, and force-phase effects.
- **Observed behaviour:**
  - Produces larger mean surge and pitch offsets than the other experimental methods.
  - Provides a transparent and robust approximation of mean loading, but not of dynamic aerodynamic coupling.
  - Introduces no active-control artefacts, although the suspended-mass system is not perfectly force-invariant because cable kinematics and mass inertia can still influence the transmitted load.
- **Use case:** Early conceptual design; approximate mean loading and conservative motion envelopes.

PI Control (Moderate Complexity)

- **Captures:** A regulated mean-thrust set-point via closed-loop feedback.
- **Characteristics:**
  - Regulates around a prescribed mean-thrust target under dynamic loading.
  - Introduces additional low-frequency damping through control action.
- **Limitations:**
  - *Control artefacts*: Deep RAO dips and transient overshoots around resonance.
  - *Latency*: ~ 0.5 s (tank) / ~ 3.5 s (full scale), corresponding to a substantial phase lag.
  - *Tracking error*: RMS force errors remain significant, and peak errors can approach the order of the set-point.
- **Observed behaviour:**

  - Can reduce some mean offsets relative to Static Weight.
  - Distorts the frequency response through control artefacts, especially at the lowest frequencies.
- **Use case:** Situations where a regulated mean-thrust input is desired, but where the resulting control artefacts can be tolerated and explicitly accounted for.

SIL (High Complexity)

- **Captures:** Real-time, motion-dependent aerodynamic loads via a simplified BEM solver.
- **Gains:**
  - Better representation of unsteady aerodynamic loading than the simpler experimental actuation methods.
  - More physically representative coupling between aerodynamic input and floater response.
- **Limitations:**
  - *Compute & actuator latency*: ~ 0.2–0.3 s (solver) + ~ 0.2–0.3 s (mechanical response), for a total of roughly ~ 0.5 s tank scale.
  - *System complexity*: Requires robust real-time BEM, hardware integration, and high-bandwidth actuation.
  - *Model simplifications*: The present implementation still omits some aerodynamic effects and only partially captures floater kinematics.
- **Observed behaviour:**
  - Provides the most physically representative loading framework of the three methods tested.
  - Remaining discrepancies are strongly influenced by phase lag, controller bandwidth, and implementation limitations.
- **Use case:** Final validation, fatigue analysis, and controller co-design where motion-dependent aerodynamic coupling is essential.

Increased actuation complexity can improve physical fidelity where motion-dependent aero–hydro coupling is important, particularly at rated wind and in pitch and surge, but only if the control architecture is sufficiently mature. Simpler methods can still serve targeted purposes, although they introduce systematic biases: PI through control-induced low-frequency damping and tracking artefacts, and Static Weight through the omission of motion-dependent aerodynamic loading.

5.3.1 Cost and Effort vs. Performance

Setup effort was compared against the observed gains in physical fidelity, revealing that SIL offers the most representative dynamic loading on selected degrees of freedom but incurs substantially greater experimental complexity. The study yielded these implementation conclusions:

- **Static Weight:** Minimal development effort and no active tuning are required. Fidelity is limited mainly to mean-thrust loading, making it suitable for preliminary validation and conservative motion-envelope estimation.
- **PI Control:** Moderate development effort is needed. The method provides a regulated mean-thrust input, but the present results also show clear control artefacts. Development from scratch may take several months for users without prior experience. Control delays, common to both PI and SIL, remain to be addressed.
- **SIL:** The highest potential fidelity is obtained, capturing motion-dependent aerodynamic loading and stronger aero–hydro coupling, however the cost of development, calibration, and integration time is extensive. Primary challenges included:
  - Achieving low-latency motor response while maintaining rope tension;
  - Selecting a motor that does not introduce unwanted vibrations and is capable of applying the necessary load range;
  - Interconnecting all necessary inputs and outputs in the control loop.

Cost–benefit guidance

Each actuation method incurs distinct implementation costs and operational efforts in addition to its accuracy characteristics. Table 5.4 summarises these trade-offs on a qualitative scale: “Low” denotes minimal additional hardware or software requirements and setup time, while “High” denotes substantial investment in equipment, computation, or tuning. These qualitative ratings reflect only the incremental resources needed beyond those already available at the test facility.

Hardware and software cost ratings exclude foundational assets (e.g. computers, LabVIEW licenses) that are assumed to be in place. Instead, they account only for any additional purchases required to deploy each method. For example, “Static Weight” is rated “Low” because calibration weights were already present, obtaining new weights would, by contrast, raise the cost.

Regarding setup and tuning effort, “Static Weight” is straightforward and imposes negligible extra effort during a tank-testing campaign. By comparison, both PI control and SIL require control-system configuration and validation, in particular, SIL setup is highly complex and non-trivial to deploy.

Ultimately, the optimal choice must balance budget, timeline, and fidelity requirements. Fidelity is directly linked to the test objectives, and in the next (and final) section of this chapter these factors are discussed in relation to the Technology Readiness Level of the design being tested.

Table 5.4: Qualitative comparison of implementation effort and expected fidelity for the three wind actuation methods investigated in this study.

Method	Hardware & SW Cost	Setup & Tuning Effort	Fidelity Gain
Static Weight	Low	Very Low	Limited to approximate mean thrust loading and conservative motion envelopes
PI Control	Medium	Medium	Regulated mean-thrust loading, but susceptible to control artefacts and low-frequency damping bias
SIL	High	Very High	Highest potential fidelity for motion-dependent aerodynamic loading and coupled response, but still sensitive to latency and implementation limitations

5.4 Staged Development Approach: Recommended Application Strategy

This section synthesises the experimental results, cost–benefit analysis and the staged development framework originally devised for wave-energy converters in order to formulate practical guidance for floating offshore wind turbine (FOWT) tank testing. The approach intentionally aligns the fidelity of the wind-actuation system with the Technology Readiness Level (TRL) of the concept under investigation, thereby ensuring that each successive stage deploys only the minimum additional resources required to satisfy its objectives.

Stage 1: Concept Model (TRL 1–3)

a) *Wind loading*. A constant-thrust winch or static-weight system is recommended, acting in a single degree of freedom (surge/pitch axis as appropriate). The target thrust should reproduce the rated mean rotor load at model scale.

b) *Control*. No closed-loop wind controller is required; the imposed load remains fixed throughout each run.

c) *Environmental conditions*. Regular waves and long-crested irregular seas with or without uniform wind are sufficient. Complex misalignment or turbulence is unnecessary.

d) *Primary objectives*.

- Establish hydrostatic stability and obtain natural periods.

- Measure maximum offsets, trim angles, and mooring tensions under combined wind–wave extremes.
- Generate a first validation data set for linear numerical models.

e) *Exit criteria (Stage Gate 1)*. Agreement within ± 10–15% between measured and numerically predicted natural periods and mean offsets, no structural or mooring red-flags.

Stage 2: Design Model (TRL 4)

a) *Wind loading*. Either (i) a regulated mean-thrust system using PI control or (ii) a real-time Software-in-the-Loop (SIL) implementation using a simplified blade-element–momentum (BEM) solver. At least one DOF (pitch) should be represented. In light of the present results, PI should be treated as a simplified regulated-thrust option rather than as a substitute for physically representative dynamic loading.

b) *Control*. Closed-loop testing of prototype rotor-speed and blade-pitch algorithms is encouraged; PI or model-predictive controllers may be exercised provided total closed-loop latency in the order of milliseconds in tank scale.

c) *Environmental conditions*. Regular waves, lomg-crested irregular waves, wave–wind misalignment cases, and unsteady and turbulent wind time-series should be introduced progressively.

d) *Primary objectives*.

- Quantify coupled aero–hydro–servo dynamics and validate non-linear time-domain simulations.
- Examine the sensitivity of platform response to limited-bandwidth wind actuation and control delay.
- Identify frequency bands most affected by aerodynamic damping or amplification.

e) *Exit criteria (Stage Gate 2)*.

- RAO amplitudes and phases within $\pm 10\%$ of fully coupled numerical predictions.
- Successful closed-loop operation without loss-of-tension events or actuator saturation.
- Demonstrated repeatability across at least three irregular-sea realisations.

Guidelines for Selecting the Actuation Method

- If the test matrix is limited to approximate mean offsets, line loads, or ultimate limit states, the added fidelity of dynamic thrust may not be justified. A simple static-weight system or a regulated mean-thrust PI system may be sufficient, provided their limitations are recognised.
- Where spectral response, fatigue damage, controller interaction, or realistic motion-dependent aerodynamic loading is of interest, a motion-dependent load (*SIL*) becomes essential.
- *SIL* delivers the highest potential fidelity but only if its computational and actuation latency is held sufficiently low relative to the shortest target wave period, otherwise its theoretical advantage is reduced by implementation limitations.

Wind Actuation Implementation Road-Map

1. *Baseline definition*: Replicate Stage-1 tests numerically and experimentally to establish a reference data set against which future complexity can be judged.
2. *Incremental upgrades*: Add DOFs and closed-loop control one at a time, first pitch, then surge/roll, verifying stability and bandwidth at each step.
3. *Latency mitigation*: For SIL, prioritise real-time hardware or predictive control to constrain end-to-end delay, ensure that the winch servo bandwidth exceeds five times the dominant wave frequency.
4. *Documentation*: Record all actuator calibration curves, control gains, and communication latencies so that the numerical model can replicate them in “digital twin” studies.

Outlook to Stage 3 and Beyond (TRL 5+) The results of this study validate the SIL approach up to TRL 4. Extrapolating these findings to higher TRLs is necessarily more speculative, but suggests the following pathway: Once a design progresses to sub-system or prototype sea trials (Stages 3–5), wave-basin results should mainly serve to de-risk offshore operations. A logical next step for research is the implementation and validation of fully coupled SIL with gyroscopic loading, atmospheric turbulence, and grid-coupled generator models, which would become the preferred wind-actuation route for these advanced stages. The incremental strategy outlined above provides a structured pathway to develop this capability with demonstrable confidence at each gate.

In summary, a *staged development approach* rooted in TRL thinking enables tank-testing campaigns to deploy only as much complexity as is warranted by the maturity of the FOWT design and the objectives of the test. Concept models benefit from simplicity and speed, whereas design-stage models require higher-fidelity aerodynamics to investigate coupled dynamics and control performance. Applying the recommended strategy therefore maximises knowledge gained per tank-hour while minimising unnecessary cost and schedule risk.

Chapter 6

Conclusions and Recommendations

Floating offshore wind (FOW) is expanding opportunities for renewable energy by unlocking access to deeper waters and stronger, more persistent wind resources. Its development, however, requires careful navigation of a fundamental challenge: the coupled aero–hydro–servo–elastic physics that govern floating offshore wind turbine (FOWT) behaviour are complex, yet early-stage design decisions must be made with confidence and at manageable cost. Across Technology Readiness Levels (TRL) 1–5, physical model testing and numerical simulation remain the primary tools for validating concepts, informing design, and de-risking investment. Within this context, a central practical question persists: how complex must wind-load actuation in wave basins be in order to achieve decision-relevant accuracy?

6.1 Summary of Findings

This thesis examined how the complexity of wind-load actuation influences the interpretation of floating offshore wind turbine model tests. Three actuation strategies were investigated: Static Weight, Proportional–Integral (PI) control, and Software-in-the-Loop (SIL). Experiments were performed in regular and irregular wave conditions and compared with numerical simulations in order to understand how each method influences the observed system response.

The results demonstrate that increased actuation complexity does not automatically lead to improved physical accuracy. Instead, the suitability of each method depends strongly on the objective of the test and the ability of the actuation system to reproduce the intended loading conditions.

- **SIL** provides the most physically representative framework for applying motion-dependent aerodynamic loading and therefore offers the greatest potential fidelity when investigating coupled aero–hydro dynamics. However, the experiments also showed that control latency (equivalent to approximately $\sim$3.5 s full scale) and actuation bandwidth limit the achievable accuracy. If these delays are not sufficiently reduced, the benefits of SIL may be partially offset by phase lag and tracking limitations.

- **PI control** enables regulation of a constant mean thrust through closed-loop feedback. In the present experiments this approach reduced some mean offsets compared with static-weight loading, but it also introduced clear control artefacts, including low-frequency damping effects and transient tracking errors. Consequently, PI control cannot be considered a universally superior intermediate solution; its usefulness depends on whether a regulated mean thrust is required and whether its control effects can be tolerated in the analysis. It should also be noted that the latency observed in the PI-controlled system did not influence the results in the same way as in the SIL implementation. In the PI case the applied thrust was largely constant, so the delay mainly affected the timing of tension adjustments rather than the magnitude of the aerodynamic loading itself. In contrast, the SIL method continuously recalculated the thrust based on floater motion, meaning that any delay directly altered the phase relationship between the aerodynamic forcing and the platform response. Consequently, latency has a more significant influence on SIL performance than on PI control, even when the absolute delay in the actuation chain is similar.
- **Static Weight** provides the simplest and most robust loading strategy. Although it cannot reproduce motion-dependent aerodynamic effects, it captures mean thrust sufficiently well to estimate average mooring tensions and conservative motion envelopes. This makes it particularly suitable for early-stage concept testing where simplicity and repeatability are priorities.

Overall, the findings indicate that wind-actuation complexity should be introduced selectively and only when it directly supports the objectives of the experiment.

Stage 1: Concept models (TRL 1–3). At this stage, the primary objectives are to establish hydrostatic stability, identify natural periods, and evaluate maximum offsets and mean mooring loads. Simplicity and efficiency are paramount, making static-weight or constant-thrust approaches sufficient. These methods capture mean loading adequately and enable rapid early de-risking of new concepts.

Stage 2: Design models (TRL 3–4). As the design matures, validation of coupled aero–hydro–servo dynamics becomes essential. Dynamic thrust representation may therefore be required, for example through PI and SIL implementations where latency and bandwidth constraints can be sufficiently controlled. Theses methods allows spectral fidelity, fatigue analysis, and the latter can even include emerging controller strategies to be examined, supporting robust numerical validation and design optimisation.

Stage 3 and beyond (TRL 5+). For prototype and pre-commercial demonstrations, SIL becomes the preferred actuation strategy, provided that real-time performance is achieved. At this level, inclusion of unsteady aerodynamics, turbulence, and generator dynamics will be necessary to capture fully coupled system behaviour and inform offshore deployment.

An important additional insight emerged from the misalignment studies. These revealed that *directional fidelity* of the applied thrust vector is as critical as bandwidth or latency. In the basin, cable reorientation caused thrust to remain largely surge-aligned even at $\beta_v = -30^\circ$, suppressing the expected cosine reduction in surge and inflating sway and roll. SIL, while theoretically higher fidelity, transmitted these deviations more accurately than PI, leading to larger differences relative to the numerical predictions. This demonstrates that increasing actuation complexity does not necessarily guarantee improved experimental fidelity.: unless directional control is ensured, advanced actuation may amplify errors. The results also confirmed that initial mooring pretension strongly influences load sharing under off-axis thrust, with small asymmetries dictating line tension hierarchies.

6.2 Limitations

The analysis also highlighted the physical and numerical simplifications inherent in the study:

- The hydrodynamic numerical model relied on linear, inviscid potential-flow assumptions, which diverge from the viscous, scale-sensitive reality of wave basin experiments and contributed to discrepancies in damping and low-frequency response.
- The mooring system was represented experimentally by a semi-taut spring–rope configuration rather than a true catenary, altering restoring, damping, and inertial properties.
- Both PI and SIL actuation systems exhibited latency and bandwidth limits, which proved critical in shaping dynamic responses, particularly near resonance and under misalignment.
- Replication of irregular seas with multiple random realisations was not feasible within the project timeframe, limiting statistical robustness.
- Only steady wind forcing was considered. This simplification reduced complexity and enabled clearer method development, but it excluded the dynamic effects of gusts, turbulence, and directionality that are present in realistic offshore conditions.

These simplifications were necessary to constrain scope and feasibility but must be borne in mind when interpreting the results.

6.3 Recommendations for Future Work

Future research should build on these findings in several directions:

- **Actuation fidelity.** Reduce SIL latency through real-time computation, predictive control, or high-bandwidth hardware to enable accurate spectral tracking across the full energy band.
- **Directional control.** Develop hardware solutions (e.g. gimballed fairleads, multi-winch systems) or software corrections to ensure accurate thrust vector orientation under misalignment.
- **Statistical robustness.** Perform irregular sea tests with multiple seeds to improve confidence in spectral metrics and fatigue-related quantities.
- **Aerodynamic realism.** Extend testing beyond steady wind conditions to include time-varying wind speeds, gusts and turbulence for more representative offshore environments.
- **Cross-study harmonisation.** Establish benchmark datasets and coordinated protocols across facilities to enable consistent comparison of actuation methods and accelerate best-practice development.

6.4 Closing Statement

In conclusion, the thesis has shown that the complexity of wind-load actuation in FOWT model testing must be carefully matched to design maturity and test objectives. Simpler methods remain valuable for early-stage de-risking, while advanced SIL approaches offer the greatest potential for high-fidelity representation of coupled aerodynamic loading of fully coupled dynamics, provided that latency and directional fidelity are controlled. By framing actuation choice within a staged, TRL-aligned strategy, this work offers the floating wind community a structured pathway to balance cost, fidelity, and practicality in experimental campaigns, supporting more informed experimental design and more efficient progression of FOWT technologies toward commercial deployment.

Appendix A

Model Build

This appendix provides a collection of photographs documenting the construction of the scaled model used in the experiments described in this study. Figure A.1 illustrates the completed 50th scaled VolturnUS-S model in the FloWave tank with highlighted critical components.

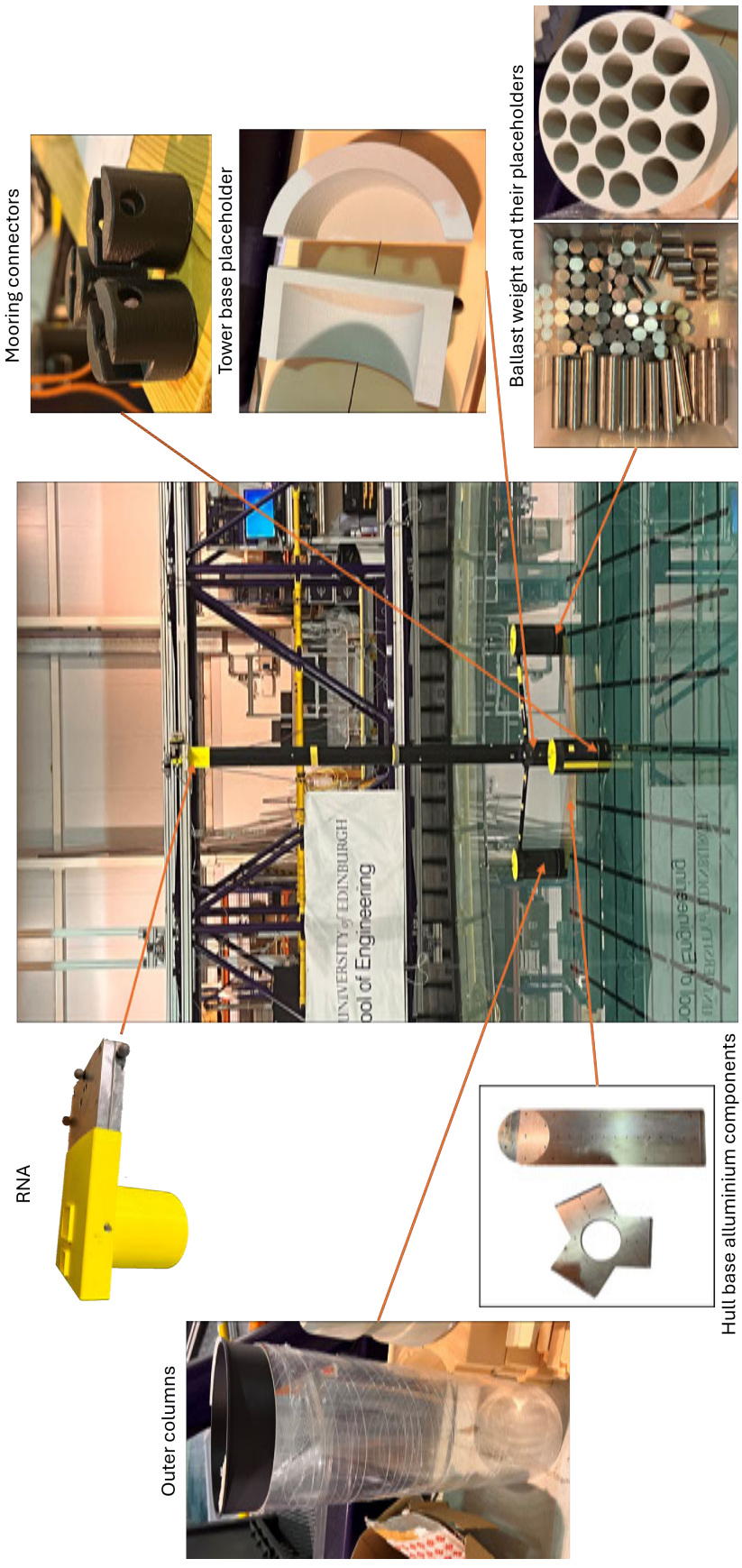

Figure A.1: Constituent parts of the 50th scaled VolturnUS-S model built at FloWave.

Appendix B

Winch System Set-up

This appendix provides additional information on the implementation of the winch system used to simulate wind thrust on the floating wind turbine during the tank test campaigns.

B.1 Overview

The winch setup was designed to apply a constant or a dynamic wind thrust force by using a motor and winch system. The control and feedback loop mechanisms, already detailed in the main document, ensured a precise application of the simulated forces. This section complements the description by summarising the key specifications of the hardware and software components involved in the wind load application.

B.2 Component Specifications

The table below provides the specifications of the primary components used in the system, including the motor, winch, and data acquisition system (DAQ):

Motor	Maxon, EC 90 flat Ø90 mm, brushless, 160 W, with Hall sensors
Motor controller	Maxon Escon 50/5
Encoder	SICK, Incremental encoder, DBS60E-TJFK02000
Load cell	FUTEK LSB210, 10 lb
NI DAQ	cRIO 9082/cDAQ 9171
NI Modules	NI Module 9403/NI Module 9237/NI module 9411/NI module 9263
Transformer	TRACO POWER, TSP 360-124

Table B.1: List of components of the winch system.

B.3 General scheme of the DAQ and actuator connection

Figure B.1 illustrates the interconnection of key components in the SIL setup. The system integrates a motor, winch, data acquisition and motion capture system, load cell and control software. For the constant thrust case, the same configuration is applied, except there is no input from the motion capture system and the BEM (Blade Element Momentum theory) code is not applied, as the thrust remains constant.

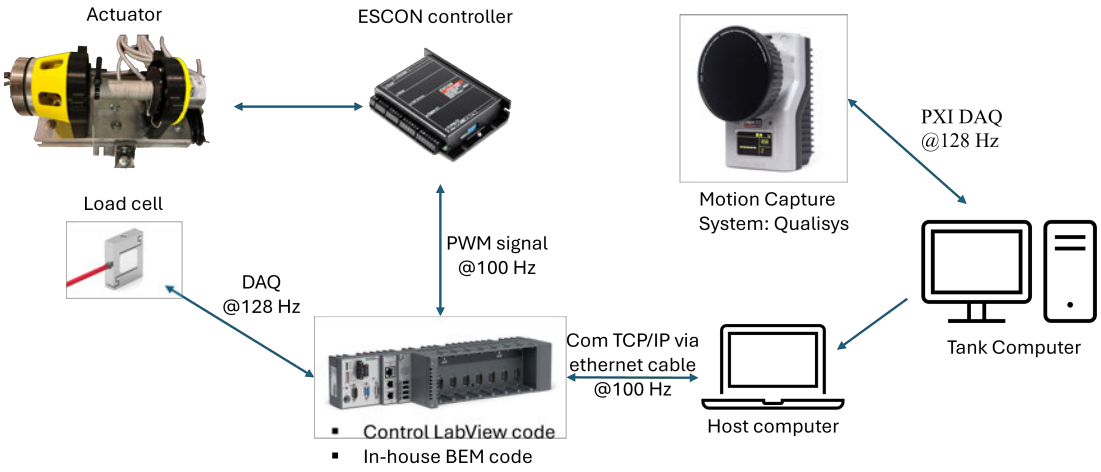

Figure B.1: Overview of the DAQ and actuator system for the SIL application.

Appendix C

Submitted manuscript: Implementation of wave basin spring–rope mooring system for floating offshore wind turbines

This appendix reproduces the manuscript titled *Implementation of wave basin spring–rope mooring system for floating offshore wind turbines*, which has been submitted to the *Journal of Ocean Engineering and Marine Energy* and is currently under peer review. The paper documents the mooring design and its experimental validation that support the results presented in this thesis. The version included here is the submitted manuscript.

Implementation of wave basin spring-rope mooring system for floating offshore wind turbines

Anita Leite[1,2*], Katherine Smith[1,2], Ajit C. Pillai[3], Callum Guy[2], Thomas Davey[2], Saishuai Dai[4], Tom Bruce[5]

[1*]EPSRC and NERC Centre for Doctoral Training in Offshore Renewable Energy (IDCORE), University of Edinburgh, Exeter and Strathclyde, Grant Institute, King's Buildings, W Mains Rd, Edinburgh, EH9 3JW, UK.
[2]School of Engineering, FloWave Ocean Energy Research Facility, University of Edinburgh, Edinburgh, EH9 3BF, UK.
[3]Renewable Energy Group, Department of Engineering, Faculty of Environment, Science, and Economy, University of Exeter, Penryn, TR10 9FE, UK.
[4]Kelvin Hydrodynamics Laboratory, University of Strathclyde, 80 Acre Road, Glasgow, G20 0TL, UK.
[5]School of Engineering, The University of Edinburgh, Edinburgh, EH9 3BF, UK.

*Corresponding author(s). E-mail(s): ;

Abstract

Scaled hydrodynamic testing in wave basins is an important tool for developing designs for floating offshore wind turbine platforms. When designing such scale tests, accurate representation of the mooring system behaviour is crucial. However, designers must overcome challenges including: the availability of materials that replicate mooring static and dynamic stiffness and truncation of the mooring footprint to match the wave basin's dimensions and its scaled depth.

This study proposes a method to represent a scaled catenary mooring using a tensioned spring-rope configuration in a wave basin. This mooring system is designed by analytically calculating the mooring line elasticity acquired from the linear mooring stiffness matrix. This catenary-equivalent mooring system is then experimentally tested in the wave basin at the FloWave Ocean Energy Research Facility using a 1:50 scale VolturnUS-S semi-submersible platform fitted with the 15 MW IEA reference wind turbine.

This method shows that the mooring system captures surge variability and pitch dynamics well, with pitch errors under regular waves ranging from 0.14% to 14.69%. However, mooring tensions exhibited large deviations in mean values, despite standard deviation ratios generally remaining close to 1. These results underscore the limitations of spring-rope systems in replicating catenary restoring forces and highlight the importance of accurately modelling mooring properties when simulating semi-taut configurations.

Keywords: Mooring system, Tank testing, Floating Wind Turbines

1 Introduction

Offshore wind, which has evolved from decades of technological development onshore, benefits from stronger wind resource, expansive geographic area, and minimal visual impact. A pioneering technology emerging within this sector is floating offshore wind (FOW), which involves moored platforms mounted with wind turbines. This technology allows for greater installation flexibility, enabling deployment in deeper water sites. Currently, the UK has 77.5 MW of prototype-scale FOW demonstration projects (Edwards et al. 2023; Principle Power 2024; Equinor 2024). These projects contribute towards the ambition to deploy 5 GW of commercial FOW by 2030 (Department for Business & Trade 2024; HM Government 2021). Moreover, 19.2 GW of FOW projects were awarded by the Crown Estates Scotland's first seabed leasing round, ScotWind (Crown Estate Scotland 2024), which further evidences the national investment and significant generation potential of this technology. However, the marked contrast between installed capacity and projects in the pipeline highlights that substantial technological challenges must still be overcome to achieve these deployment targets.

Scaled experimental modelling, such as tank testing in wave basins, is an essential stage for FOW technology development, not only for certification (alongside other relevant standards) (International Electrotechnical Commission 2019, 2011), but also for understanding the complex coupling effects between aero- and hydrodynamic forces. Tank testing serves to validate developer's numerical models, thereby optimising power performance and mitigating deployment and project risk. Additionally, tank testing offers a cost-effective route to support sea-trial prototype deployments in a controlled and repeatable environment, reducing uncertainty and risk.

The mooring and anchoring system performance and properties are clearly crucial to any FOW turbine (FOWT). Given their high degree of technological novelty, these systems have become a focus for design optimisation and innovation, requiring both robust modelling and testing. Medium-scale tank testing offers an opportunity to investigate how the mooring and anchoring system interacts with other subsystems and the device as a full integrated system. However, accurately representing these mooring systems in the tank can be challenging due to the constraints on mooring geometry imposed by the tank dimensions, and difficulties in matching scaled line material properties (Ma et al. 2019b).

2 Background

2.1 Mooring systems used in floating offshore wind

The mooring and anchoring system of a FOWT generally encompasses any set of lines, anchors and ancillary components that connect the platform to its surroundings. The primary function of a mooring system is station-keeping, meaning to maintain the FOWT's position and orientation relative to some fixed location. Depending on the platform design, the mooring may also contribute towards the system's stability.

Mooring systems come in many forms (Ma et al. 2019a; Jump, Ellen 2021), and those typically used in FOW are illustrated in Figure 1. This diagram includes:

- **Catenary moorings** consist of very long, freely hanging lines, typically heavy chain. The restoring force of the mooring stiffness is dependent on the weight of the lines and causes only horizontal loading on the anchors.
- **Semi-taut moorings** are a hybrid between taut and catenary moorings. Semi-taut lines generally consist of a rope segment followed by free-hanging heavy anchor chain, creating a distorted catenary shape. The restoring force of this mooring combines contributions from the elastic stiffness of the rope and the weight of the anchor chain.
- **Tensioned moorings**, either spread or vertical as in a tension leg platform (TLP), utilise lightweight, elastic lines or stiff tendons, respectively. Lines are shorter than catenary lines, however, anchoring must sustain both horizontal and vertical loading. Tensioned mooring systems restore motion in every degree of freedom (DOF).

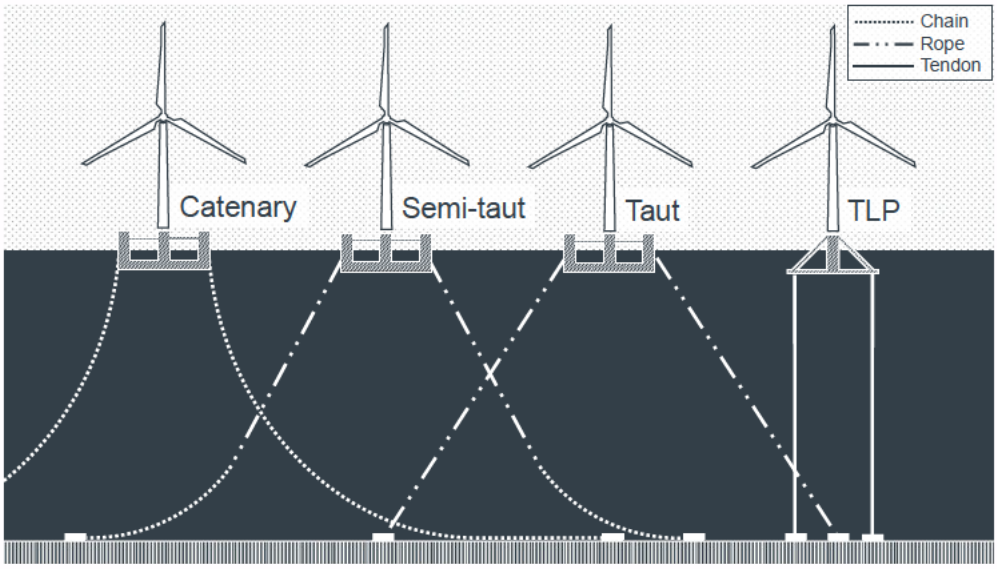

Fig. 1: Mooring layouts typically used in floating offshore wind. From left: catenary, semi-taut, spread taut, tension leg platform (TLP).

2.1.1 Catenary mooring systems

Despite the variety of moorings proposed in FOW, catenary mooring systems are the predominant layout for installations to date (Bhattacharya et al. 2018; Principle Power 2024). Catenary systems have been extensively utilised by the oil and gas industry and as such their dynamics, installation methods and failure mechanisms are well understood (Ma et al. 2021). Additionally, the supply chain has a large depth of resource and experience. Therefore, use of catenary moorings is seen as decreasing the uncertainty of deploying early-stage floating wind turbines.

The restoring stiffness of a catenary mooring system, assuming the chain is inextensible, is a function of two time-varying parameters; the mooring line submerged weight, and the fairlead horizontal tension (Faltinsen 1993). Both these parameters are directly dependant on the instantaneous length of line that is suspended in the water column. As the platform moves away from its equilibrium position due to environmental loading, a portion of the line either lifts off or lays down on the seabed, so that the suspended length of each line either increases or decreases. This has the direct effect of changing the horizontal tension of each line at the fairleads. This dynamic relationship therefore describes how the restoring stiffness of a catenary mooring system is non-linear in time.

2.2 Hydrodynamic tank testing in wave basins

2.2.1 Typical test programme and measured outputs

While the objectives of each tank test program are different, the key objectives and test cases considered here are as provided by Det Norske Veritas (2021). A brief description of those applicable to this study is given:

- **Free decay tests**: Used to determine the natural frequencies and damping characteristics of a structure. The model is displaced along a single degree of freedom from its equilibrium position in the absence of waves and then released, allowing it to oscillate freely. The displacement is measured and subsequently used to extract the natural frequencies and damping ratios;
- **Response Amplitude Operators (RAOs)**: Mathematical representations used in hydrodynamics and structural analysis to describe the dynamic response of a marine or offshore structure to external forces, i.e. waves or other environmental loads. RAOs are expressed as complex functions and are used to quantify the amplitude and phase relationship between the applied forces and the resulting motion of the structure. RAOs can be obtained by subjecting the model to a series of regular waves with varying frequencies and measuring the resulting motions;
- **Mooring stiffness tests**: Evaluation of the stiffness characteristics of the mooring lines in each DOF. These are used to understand the restoring forces and moments imposed by the mooring system when the structure is displaced from its equilibrium position;
- **Regular waves**: It is important to study the steady-state response of the structure and to identify behaviors as a function of wave frequency and amplitude. Regular wave analysis can also aid in validating numerical models;

- **Irregular waves**: These tests simulate the random nature of real sea states by using wave spectra representative of ocean conditions at the final deployment locations. Allows for the assessment of the structure's performance under realistic and non-linear environments;
- **Extreme conditions**: Subjects the model to the worst-case scenarios with respect to environmental conditions usually representative of a 50-year or 100-year event. These test the structural integrity and safety of offshore structures under extreme events. These conditions are particularly challenging to simulate in numerical models due to coupled system interactions, large deformations, and the unpredictability of extreme waves, all of which are essential to validate accurately for model reliability.

2.2.2 Representation of scaled mooring systems

Given that mooring systems are a key focus for design innovation and optimisation of FOW turbines, it has become increasingly important to accurately include them in scaled model testing. For design validation, international standards, specifications and industry guidance recommend using accurately scaled moorings, achieving geometric and structural similitude (British Standards Institution 2013; American Petroleum Institute 2018; Det Norske Veritas 2013). Figure 2 presents a selection of different tank mooring systems used for scaled testing of FOW systems in wave basins. This selection illustrates the diversity of approaches to design tank-scale mooring systems as well as the different configurations and materials that are commonly used.

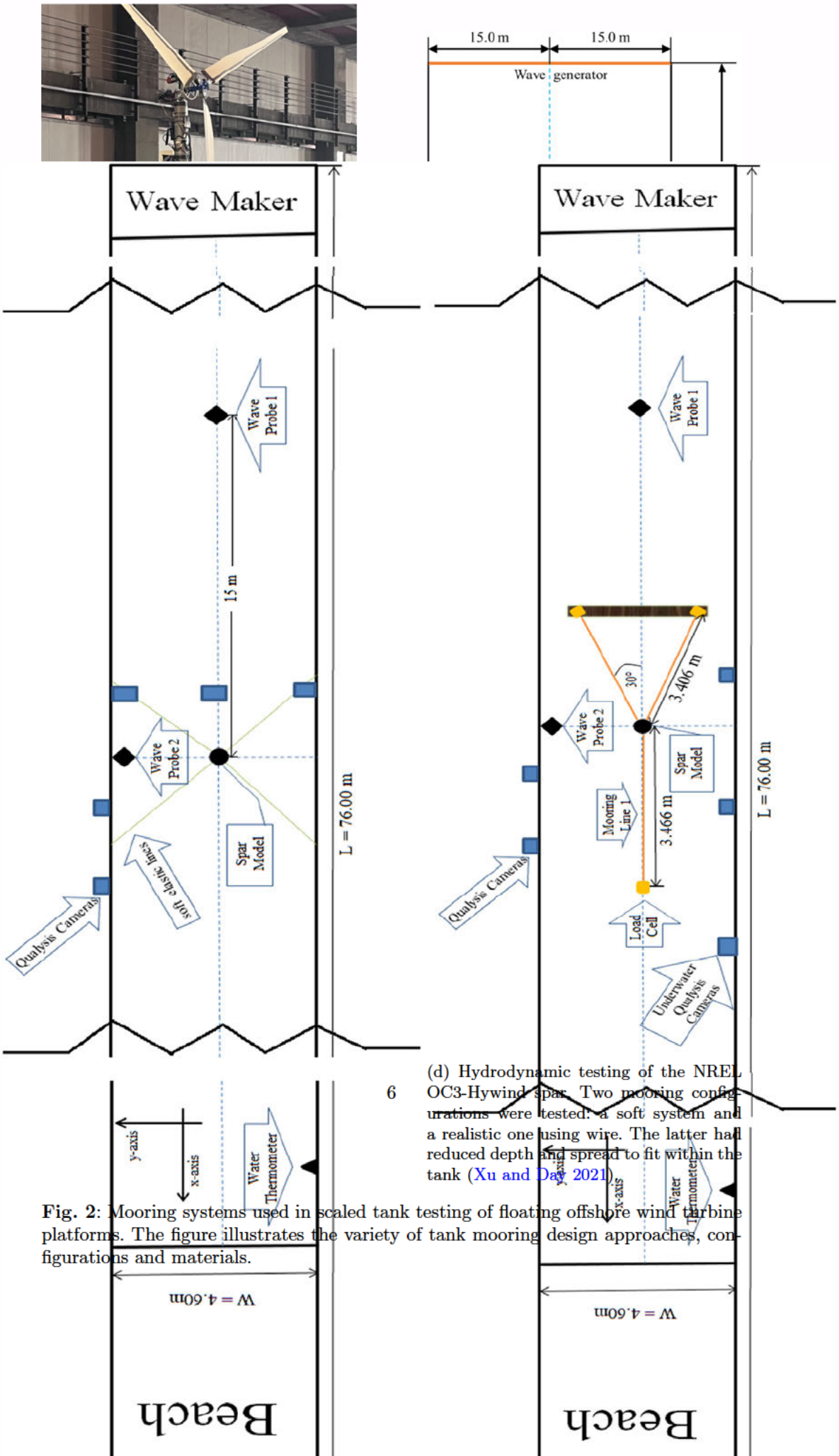

(d) Hydrodynamic testing of the NREL OC3-Hywind spar. Two mooring configurations were tested: a soft system and a realistic one using wire. The latter had reduced depth and spread to fit within the tank (Xu and Day 2021).

Fig. 2: Mooring systems used in scaled tank testing of floating offshore wind turbine platforms. The figure illustrates the variety of tank mooring design approaches, configurations and materials.

For the purposes of this work, there are two key scaling challenges in designing mooring systems for tank testing (Ma et al. 2019b). Hydrodynamic testing in wave basins typically scale using the Froude Number which describes the relationship between inertial and gravitational forces (Zwart 2009).The two challenges can be summarised as:

1. **Fitting mooring geometry in the tank dimensions at the chosen scale:** Each wave tank has a unique shape, size, and depth which impacts the scaling of both mooring geometry and expected platform excursions. This limitation is especially problematic for FOW catenary moorings, which are characterised by a much larger footprint and line length than their tensioned counter-parts, requiring methods such as truncation to adjust the geometry to physically fit in the tank (Molins et al. 2015; Qiao and Ou 2014).
2. **Selecting materials to achieve the scaled line properties:** A mooring line configuration used in wave basins that has emerged is the combined use of ropes and springs to achieve the desired levels of axial compliance. This configuration can be treated analytically as a tensioned system, and as such the restoring of the mooring line is via the stretch of the springs. Additionally, materials like lead wire and iron chain have been used to increase the weight of line sections for catenary tank scale moorings (Yang et al. 2024). The difficulty herein is maintaining consistent scaling across all material properties, and so certain properties are often prioritised depending on the objectives of the mooring system or testing (Berthelsen et al. 2016).

As such, there is always a compromise on the scaled model's ability to capture every aspect of the full-scale response accurately.

2.3 Mooring stiffness matrix

The mooring stiffness matrix provides the coefficients that define the reactionary loads of the mooring system in each degree of freedom resulting from applied displacements and rotations. It provides information on the slow drift response of a floating body under second-order waves and it also contributes to the numerical calculation of a body's RAOs (Pessoa et al. (2012)).

The mooring stiffness matrix itself is a linearised numerical representation of the physical mooring system, often taken when the floating body is in static equilibrium. It therefore has its limitations, especially when dealing with dynamic and non-linear behaviours. In reality as previously mentioned, the behaviour of mooring systems can exhibit non-linearities, especially under large deformations or extreme loading conditions. Despite these limitations, the mooring stiffness matrix remains a valuable tool for representing the mooring system's influence on a body's hydrodynamic response.

Numerous studies have been published on analytic methods for deriving the mooring stiffness matrix, as summarised in Table 2 of Amaral (2020). These methods vary in the calculation of restoring forces and the DOF for which the stiffness coefficients are defined. The primary advantage of using an analytical method is that it provides developers with a quick and easy way to incorporate mooring dynamics into the design of floating systems.

2.3.1 Analytic formulation

One such analytical method to derive the mooring stiffness matrix that is referred to throughout this article is the work presented by Amaral (2020). This approach develops a 6-DOF closed-form analytical formulation to acquire the mooring system restoring forces. One of the contributions of Amaral (2020) is the development of a general analytical formulation that can be applied not just for the system's equilibrium position but also to a wide range of scenarios with any arbitrary mooring line configuration.

This methodology includes four main steps; first the generalised coordinates for the problem are assessed, the system is geometrically defined and the geometric relations of the mooring lines are set. The problem is then focused on the assessment of the restoring force for one mooring line and its decomposition in the vertical and horizontal planes. The formulation considers a conservative system where the friction forces were neglected. This way, the mooring line restoring forces are described as functions of the positions only. Also, the effect of any currents on the mooring line were neglected.

The system is then linearised around a generic position in order to acquire the complete mooring system stiffness matrix. Lastly, individual segments of the mooring line are considered and the tension is calculated for each one of the segments as function of horizontal and vertical distances between anchor and fairlead. It is only at this step, that the specific configuration of the mooring system becomes significant. The procedure for evaluating the mooring stiffness coefficients as laid out by Amaral (2020) is illustrated in Figure 3. This particular formulation offers the advantage that only the translational stiffness coefficients require definition, as all the others are functions of these and the system geometry. Further simplifications are introduced when considering a symmetrical mooring.

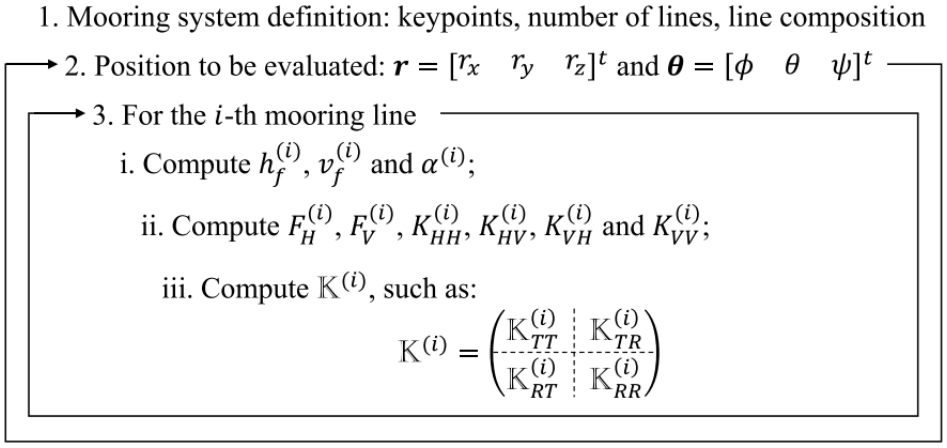

Fig. 3: Step-by-step procedure for the mooring system stiffness matrix calculation. (Reproduced from Amaral et al. (2022) with permission from Elsevier).

Amaral (2020) demonstrated this approach using a case study of the OC4-DeepCwind mooring configuration, which features an equidistant three-spread mooring system. Each mooring line in this system is represented as a single-segment mooring chain with a catenary shape. The formulations for non-null stiffness coefficients are presented in Equations 1 to 8, where l is the radius from the platform vertical central line to the fairleads, $k_{HH} = \left[\frac{\partial F_H}{\partial h_f}\right]_{q_0}$, $k_{VV} = \left[\frac{\partial F_V}{\partial v_f}\right]_{q_0}$ and $k_{HV} = \left[\frac{\partial F_H}{\partial v_f}\right]_{q_0}$ are the horizontal, vertical and coupled local stiffness and $\bar{k}_{HH} = \frac{F_H(h_f^0, v_f^0)}{h_f^0}$ is the so called horizontal "string stiffness", see Amaral et al. (2022).

$$K_{11} = \frac{3}{2}(k_{HH} + \bar{k}_{HH}) \tag{1}$$

$$K_{15} = K_{51} = \frac{3}{2}(k_{VH}R_f + k_{HHp\zeta} + \bar{k}_{HHp\zeta}) \tag{2}$$

$$K_{22} = \frac{3}{2}(k_{HH} + \bar{k}_{HH}) \tag{3}$$

$$K_{24} = K_{42} = -\frac{3}{2}(k_{VH}R_f + k_{HHp\zeta} + \bar{k}_{HHp\zeta}) \tag{4}$$

$$K_{33} = Nk_{VV} \tag{5}$$

$$K_{44} = \frac{3}{2}(p_\zeta^2 k_{HH} + p_\zeta^2 \bar{k}_{HHp\zeta} + 2p_\zeta R_f k_{HV} + R_f^2 k_{VV} + R_f F_H - 2p_\zeta F_V) \tag{6}$$

$$K_{55} = \frac{3}{2}(p_\zeta^2 k_{HH} + p_\zeta^2 \bar{k}_{HHp\zeta} + 2p_\zeta R_f k_{HV} + R_f^2 k_{VV} + R_f F_H - 2p_\zeta F_V) \tag{7}$$

$$K_{66} = N\bar{k}_{HH}R_f^2(1 + \frac{h}{R_f}) \tag{8}$$

In the present document "local stiffness" refers to the resistance of a specific part or segment of a structure to deformation, and it is particularly relevant when acquiring the linear stiffness coefficients in each DOF. "Axial stiffness", on the other hand, is a measure of a material's resistance to deformation along its length when subjected to axial forces, such as tension or compression. In the context of mooring system analysis using software packages, e.g. mooring dynamics modules that are part of the NREL's coupled aero-hydro-servo-elastic simulation tool OpenFAST (National Renewable Energy Laboratory 2022) such as MoorDyn or MAP++, axial stiffness is a critical property of the mooring material, influencing the overall dynamics of the mooring lines under operational and extreme conditions.

Thus, while local stiffness focuses on the behaviour of specific segments in multiple directions, axial stiffness pertains to the longitudinal performance of mooring materials under axial loads. These definitions are crucial for understanding the subsequent application of the analytical formulations in the present work.

2.4 Statement of aims

This work aims to quantify the dynamic impacts of scaling a catenary mooring system and representing it in the tank using a linearised spring-rope configuration. The motivation of this study is to address the challenge of representing catenary moorings of FOW turbines within the confines of the tank dimensions by instead using

a common spring-rope tank mooring. The approach involves comparing the dynamic results of a simulated catenary mooring system with the scaled-up experimental results of the tested linearised spring-rope mooring. The variables of the spring-rope tank mooring will be obtained from the mooring stiffness matrix of the catenary system which is calculated using the approach presented by Amaral (2020) and described in Section 2.3.1.

The approach is applied to the IEA 15 MW reference wind turbine and VolturnUS-S semi-submersible platform case-study (Allen et al. 2020). The outcomes of this work aim to assist wave basin test facilities to design tank mooring systems that produce accurate hydrodynamic results.

3 Methodology

This section outlines the approach to design a tank-scale spring-rope mooring to represent a full-scale catenary mooring. Firstly, the mooring stiffness matrix of the full-scale catenary mooring is found by using a numerical model and the coefficients within this matrix are Froude scaled for application in the wave basin. The coefficients of the scaled mooring stiffness matrix are then interpreted to inform the tank-scale mooring parameters such as the footprint and choice of spring stiffness.

The benefit of this approach is that all geometric contributions to the mooring stiffness are captured within the full-scale mooring stiffness matrix, including water depth. This ensures that the dimensions of the tank do not compromise the tank-scale mooring design. The one limitation of this approach is that any non-linear behaviour of the moorings will not be captured.

The overall four main steps to apply this method are shown in Figure 4 and explained in detail below.

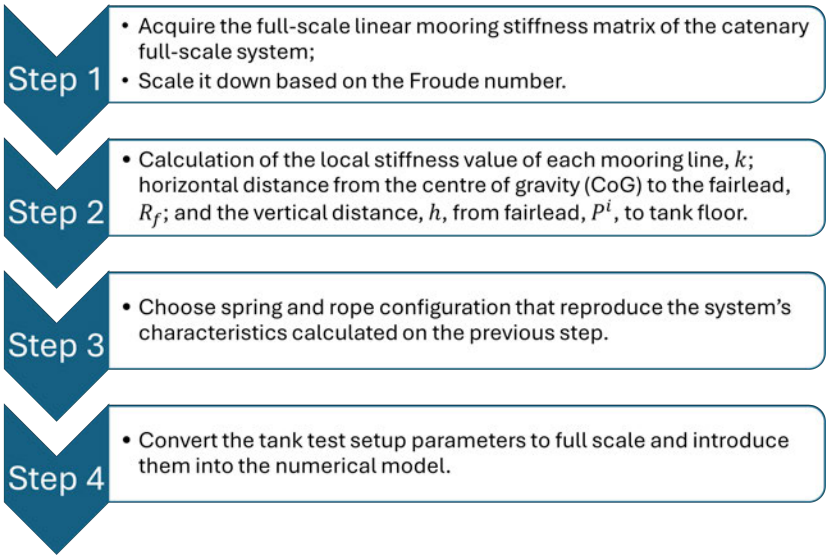

Fig. 4: Methodology applied to convert a catenary mooring system into a spring-rope configuration for the testing of ORE devices in wave basins.

3.1 Step 1

Acquire the full-scale linear mooring stiffness matrix, $\mathbf{M}$, using the analytical formulation described in Section 2.3.1 and presented in Figure 3. Then apply Froude scaling to M $\mathbf{M}$ for wave tank deployment, designated as matrix $\mathbf{m}$. The values located on the diagonal of the scaled linear mooring stiffness matrix, $\mathbf{K}$, are the stiffness coefficients required for the next step.

3.2 Step 2

Step 2 consists of calculating the required spring-rope setup values: the local stiffness value of each mooring line, k; the horizontal distance from the centre of gravity (CoG) to the fairlead, R_f; and the vertical distance, h, from fairlead, $P^{(i)}$, to tank floor which consequently define the line declination angle, α. These parameters are conditioned on the available working area and depth of the wave basin. An iterative approach may be needed to accomplish an acceptable result.

In accordance with the formulation presented by Amaral (2020), a perfect polar symmetric mooring system can be calculated analytically by the set of equations presented in Section 2.3.1. Of these equations, emphasis will be directed exclusively towards the determination of the mooring stiffness coefficients in surge, K_{11}, heave, K_{33}, and yaw, K_{66}, as these are the DOFs which at a minimum are required for the calculation of the local stiffness value of a singular mooring line.

Following Amaral (2020), the linear mooring stiffness value in heave, K_{33} is given by Equation (5). The K_{33} value in the equation is replaced by the value from the

scaled mooring stiffness matrix, $\mathbf{M}$. N represents the number of mooring lines. The resultant value for K_{vv} represents the "vertical-vertical local stiffness".

To find the "horizontal-horizontal local stiffness value", k_{HH}, the "horizontal–horizontal string stiffness" value, $\bar{k}_{HH}$ needs to calculated. For that purpose, Equation (8) will be used.

To determine the value of $\bar{k}_{HH}$, the horizontal distance from the centre of gravity (CoG) to the fairlead, R_f, and the vertical distance, h, from fairlead, $P^{(i)}$, to tank floor, as shown in Figure 5, must be known.

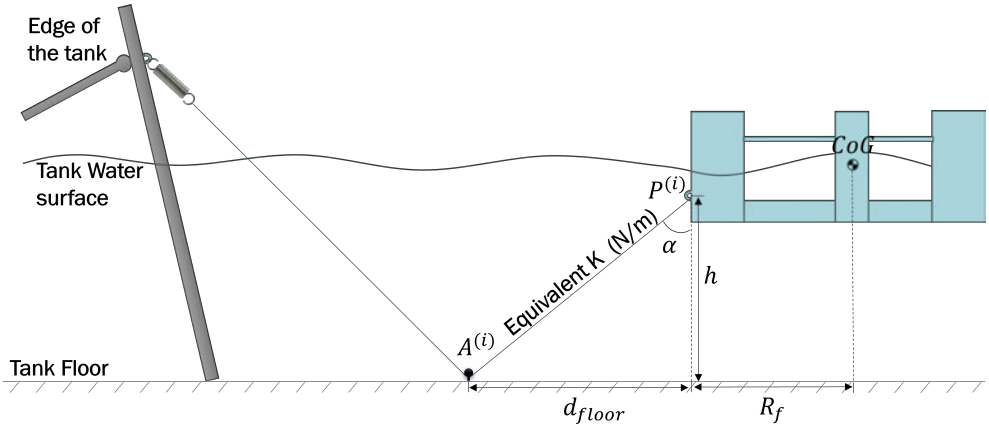

Fig. 5: Illustration of the essential parameters required for the calculation of mooring line local stiffness. Where: $P^{(i)}$ and $A^{(i)}$ are the fairlead and anchor positions, k is the line local stiffness, and α is the line declination angle.

The choice of the R_f value is dependant on the available space on the tank floor to set up the mooring line. The full-scale equivalent coordinates are applied in the numerical mooring in order to check if the resultant linear stiffness matrix is maintained or is at least relatively close to the original, $\mathbf{M}$.

This procedure involves an iterative approach represented in Figure 6, alternating between adjusting the declination angle at the fairlead α and assessing the resulting mooring linear stiffness matrix in order to ensure that it matches the stiffness matrix of the original catenary configuration, $\mathbf{M}$. This analysis is performed using the specific configuration established in the tank setup, i.e. the values for anchor locations in the numerical model are the full-scale representation of the distances present in the wave basin.

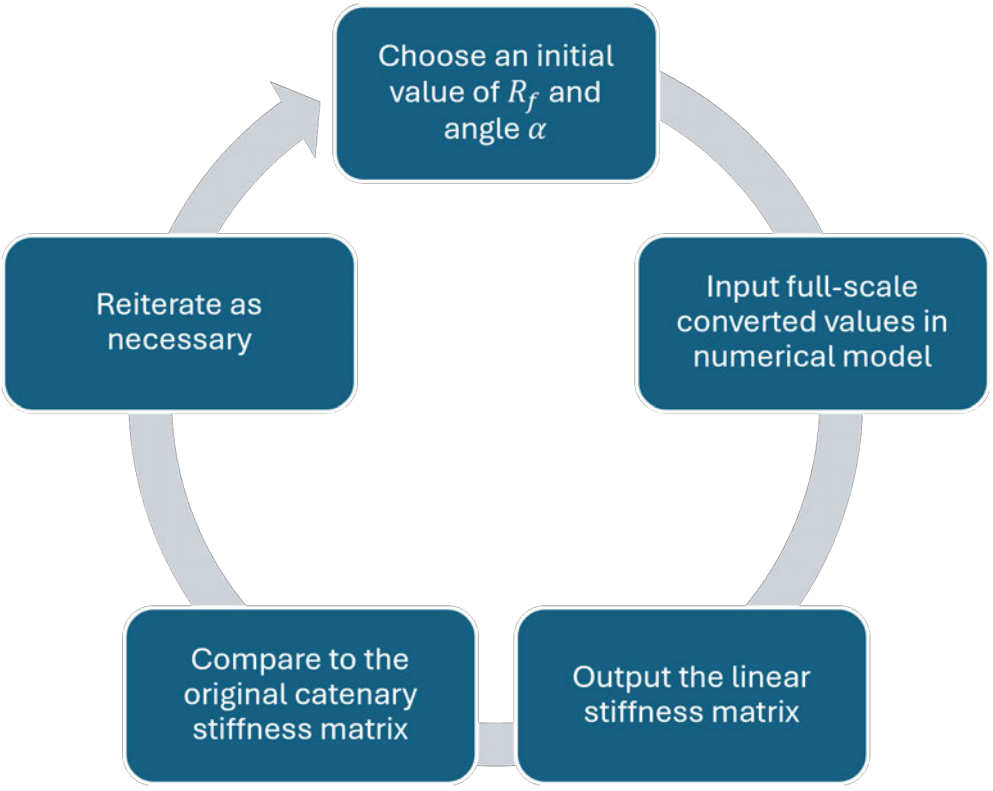

Fig. 6: General iterative process used for the choice of the R_f.

The vertical distance from $P^{(i)}$ to the tank floor is determined by the depth of the tank and the fairlead location. With these two constants known, R_f and h, the $\bar{k}_{HH}$ is calculated using Equation (8).

Using Equation (1), the value of k_{HH} can then be calculated.

$$K_{11} = \frac{N}{2}(k_{HH} + \bar{k}_{HH}) \tag{9}$$

Finally, by applying the Pythagorean theorem with the "horizontal-horizontal local stiffness" value, k_{HH} and the "vertical-vertical local stiffness" value, k_{VV}, the value of the local stiffness, k of each mooring line can be calculated.

3.3 Step 3

At this stage, with the local stiffness value of each mooring line known, the spring and rope configuration can be chosen in order to obtain that value in the physical experiment.

3.4 Step 4

Convert the tank test setup parameters to full scale. These parameters will then be used to tune the numerical model according to the experiment. Lastly, compare the natural frequencies between the tuned numerical model (referred to as the "adapted system") and the original values with the catenary mooring configuration (referred to as "catenary") to assess their similarity.

4 Case Study: Tank testing experiment with semi-submersible platform

The tank test experiment was performed at the FloWave Ocean Energy Research Facility (The University of Edinburgh 2023) located at the University of Edinburgh, United Kingdom, as part of a tank testing campaign aimed at comparing various methods for applying aerodynamic loads and correlating them with the technology readiness level of the FOW turbine design under examination in accordance with the study by Leite et al. (2022).

The FloWave facility features a circular wave basin and provides hydrodynamic testing services for small- to medium-scale ORE projects (Ingram et al. 2014). Figure 7 shows a diagram of the tank with key dimensions and features. The tank is specifically designed to test ORE models within the range of 1:20 to 1:50 scale.

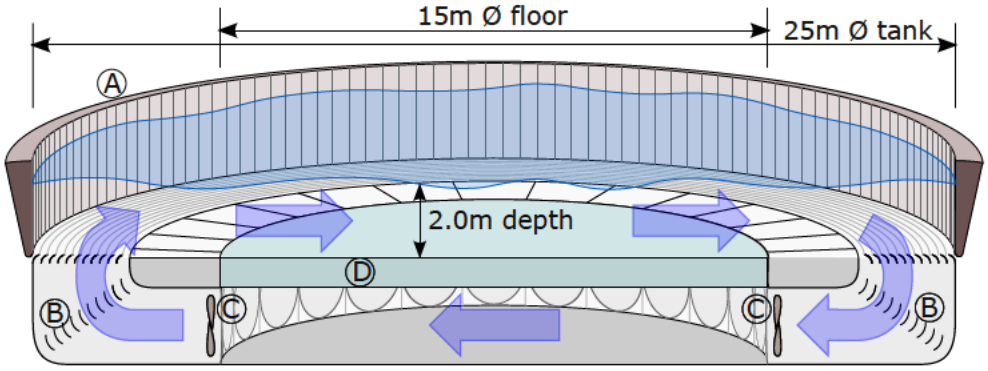

Fig. 7: Section diagram of FloWave circular tank with dimensions. A) Wavemaker paddles around circumference; B) Turning vanes and flow conditioning filters; C) Current drive impeller units; D) Buoyant raisable floor below test area; E) Idealised streamlines of flow across tank floor (Noble et al. 2015).

The constraints that must be considered for designing a mooring to be installed in the FloWave wave basin are:

1. The tank depth is limited to 2 m, which reflects 50-100 m depth at full-scale (i.e. between 1:25 and 1:50 scale). Some deep-water moorings are beyond this, especially as FOW devices are deployed further offshore.

2. It is challenging to access the tank floor beyond the buoyant raisable floor (label D in Figure 7), resulting in increased complexity on the mooring install if the anchor location falls outwith this radius.
3. The maximum tank diameter is 25 m, reflecting 500-1250 m mooring spread at full-scale depending on the scale. Some catenary mooring footprints are beyond this.

The common spring-rope system comprises tensioned lines of Dyneema rope and extension springs designed to match the local mooring stiffness. These lines are installed in the tank as depicted in Figure 5, with fairlead and anchor positions indicated by $P^{(i)}$ and $A^{(i)}$, respectively. The anchor point is situated on the tank's buoyant raisable floor where a pulley is attached.

The mooring design relies on three key parameters:

1. The local stiffness for each line, k;
2. Line declination angle, α;
3. The spread angle in between each mooring line.

These parameters were determined as described in Section 3.

4.1 Model description

A 1:50 scale model of the VolturnUS-S reference platform with the 15 MW IEA reference wind turbine was built by FloWave and it is shown in Figure 8.

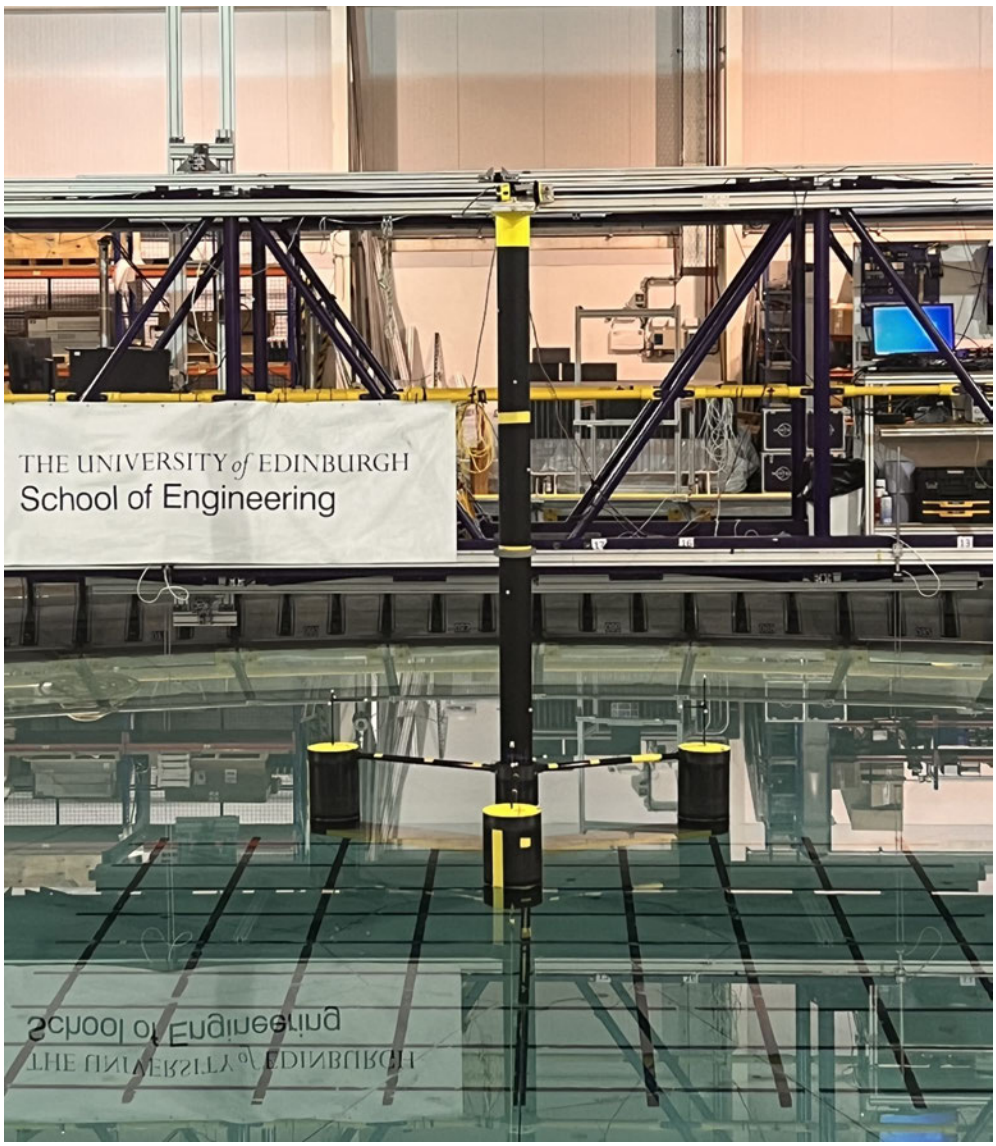

Fig. 8: 50^{th} scale model of the VolturnUS-S reference platform developed for the IEA 15-MW offshore reference wind turbine.

The model's properties were calculated from the reference document Allen et al. (2020) and converted to a 1:50 Froude scale. A correction was also made to account for the difference in density between the fresh water used in the tank rather than seawater used at full-scale, which results in a reduction of 2.44% to both the mass and force values.

The full-scale and model scale properties of the physical model are given in Table 1. To ensure alignment, the moments of inertia were adjusted to match those of the full-scale floating wind turbine, a process carried out using a detailed digital model built with the CAD software SolidWorks. This adjustment necessitated a reduction in the tower height by 3 *cm* and the rotor was modelled as a lumped mass. The column labelled as *Ideal* contains the theoretical values used as a basis for constructing the physical model.

Table 1: Model properties

	Full-scale	**Physical model**	
		Ideal	**Actual**
RNA mass (kg)	991×10^3	7.73	7.90
Tower mass (kg)	1263×10^3	9.86	10.48
Platform mass (kg)	$17\,839 \times 10^3$	139.23	136.92
Total mass (kg)	$20\,711 \times 10^3$	165.69	155.30
Mooring pre-tension (N)	6065×10^3	47.34	27.90
Centre Column ϕ (m)	10.00	0.20	0.20
Edge Columns ϕ (m)	12.50	0.25	0.25
Column Height (m)	35.00	0.70	0.70
Tower ϕ (m)	8.25	0.17	0.17
Tower Height (m)	129.50	2.59	2.55
Pontoon Height (m)	7.00	0.14	0.14
Pontoon Length (m)	51.75	1.04	1.04
Pontoon Width (m)	12.50	0.25	0.25
Mooring fairlead (m)	14.00	0.28	0.28
Draft (m)	20.00	0.39	0.38

4.2 Application of the proposed methodology

In the first step, as outlined in Section 3.1, the linear mooring stiffness matrix is acquired from OpenFAST (National Renewable Energy Laboratory 2022) using the pyMAP++ tool (Garrett 2018) using the VolturnUS-S input files as distributed on the relevant IEA GitHub repository (International Energy Agency 2023).

The resultant full-scale linear stiffness matrix, $\mathbf{M}$, is presented in Table 2.

Matrix $\mathbf{M}$ is Froude scaled at 1:50 scale (eq. (10)), referenced as matrix $\mathbf{m}$ and is shown in Table 3. From these stiffness values, the parameters needed to implement the spring-rope set-up in the wave basin are calculated.

$$\begin{bmatrix} \frac{F}{L} & \frac{F}{\text{rad}} \\ \frac{FL}{L} & \frac{FL}{\text{rad}} \end{bmatrix} \begin{bmatrix} \frac{\lambda^3}{\lambda^1} & \frac{\lambda^3}{1} \\ \frac{\lambda^3\lambda^1}{\lambda^1} & \frac{\lambda^3\lambda^1}{1} \end{bmatrix} = \begin{bmatrix} (\frac{F}{L})_s & (\frac{F}{\text{rad}})_s \\ (\frac{FL}{L})_s & (\frac{FL}{\text{rad}})_s \end{bmatrix} \tag{10}$$

Table 2: Full-scale mooring stiffness matrix, **M**, for the VolturnUS-S semi-submersible platform on a 200 m depth site. All values are scaled by a factor of 10^4. Units: (N/m, N/rad, N, Nm/rad).

	Surge	Sway	Heave	Roll	Pitch	Yaw
Surge	7.31	0	0	0	115	0
Sway	0	7.31	0	-115	-0	-0
Heave	0	0	6.11	0	0	0
Roll	0	-115	0.10	26100	0	0
Pitch	115	-0.01	0	-0.02	26100	0
Yaw	0	-0	0	0	0	25600

where: F = force units
L = length units
rad = angle units
λ = Froude's scaling factor
s = scaled matrix coefficient

Table 3: Scaled mooring linear stiffness matrix, **m** (N/m, N/rad, N, and Nm/rad).

	Surge	Sway	Heave	Roll	Pitch	Yaw
Surge	29.26	0	0	0	9.23	0
Sway	0	29.26	0	-9.23	0	0
Heave	0	0	24.44	0	0	0
Roll	0	-9.22	0.01	41.7	0	0
Pitch	9.22	-0.01	0	0	41.7	0
Yaw	0	0	0	0	0	40.88

4.3 Spring-rope set-up

As presented in Section 3, specific parameters must be derived from the mooring stiffness values to identify the suitable and deployable components for the tank-scale spring-rope mooring system. The calculation of these parameters is shown below following the methodology presented in Section 3.2.

The VolturnUS-S platform was defined with a three-line chain catenary mooring system (Allen et al. 2020) as a reference mooring. This catenary system spans radially to anchors spaced equally at 120° intervals in the surge-sway plane. In the reference design, this model is deployed in 200 m deep water. It is not possible to scale this depth for a 50^{th} scale model at FloWave given the basin's maximum depth of 2 m. Consequently, the numerical simulations executed in OpenFAST, employing MoorDyn for the simulation of the adapted tank mooring system, will be conducted with a depth of 100 m since this is the achievable depth at this scale. Additionally, the anchors on the original design are located at 779.6 m from each fairlead, corresponding to 15.60 m

at tank scale. This value surpasses the FloWave tank radius of 12.5 m requiring further adjustment of the mooring system.

4.3.1 Acquiring the local stiffness value of each mooring line

Following the process outlined in Section 3.2, the stiffness coefficient in heave, K_{33} is taken from the matrix **m** presented in Table 3.

From Equation (5), replacing the value of K_{33} for the value $m_{3,3}$ which from Table 3 is 24.44 N/m, and as N is 3, the K_{vv} value is found to be 8.15 N/m.

The next parameters to be determined are the horizontal distance from the centre of gravity (CoG) to the fairlead, R_f, and the vertical distance, h, from fairlead, $P^{(i)}$, to tank floor. The R_f value for FloWave takes into account the diameter of the buoyant raisable floor, 15 m. In practice, when the model is positioned at the centre of the tank the distance available from fairlead, $P^{(i)}$, to the edge of the buoyant raisable floor is 6.34 m. As explained in Section 3.2, in order to acquire the correct R_f value and consequently the α angle, the mooring linear stiffness matrix from the numerical model is used which in this case computed using the PyMAP tool. The iterative approach for this case study is presented in Figure 6.

Table 4: Resultant mooring linear stiffness matrix for $\alpha = 65°$ (N/m, N/rad, N, and Nm/rad).

	Surge	Sway	Heave	Roll	Pitch	Yaw
Surge	29.95	0	0	0	9.23	0
Sway	0	29.95	0	-9.23	0	0
Heave	0	0	16.74	0	0	0
Roll	0	-9.22	0.01	24.30	0	0
Pitch	9.22	-0.01	0	0	24.29	0
Yaw	0	0	0	0	0	37.20

Given the constraints of the available space in the tank floor and value of the α angle published in the reference document (Allen et al. 2020), 56.4°, a range of angles starting from 50° were tested. With an angle of 50°, the resultant stiffness matrix presented very low stiffness values, thereby identifying that a greater angle was required. The second angle applied was 70°, for which the stiffness values where higher than the original stiffness matrix. Following an iterative process, the angle of 65° was chosen since the coefficients of the stiffness matrix were the closest to the reference values for surge, sway and yaw DOF as shown in Table 4. The restoring forces and moment for these DOF are directly dependent on the moorings.

The vertical height from $P^{(i)}$ to tank floor is 1.72 m. With these two constants known, R_f and h, the $\bar{k}_{HH}$ calculated using Equation (8) is equal to 2.25 N/m.

From Equation (9), the value of k_{HH} is found to be 17.26 N/m. Taking into account that the scaled mooring line length is 4.07 m, the total "string" stiffness per mooring line is approximately 9.14 N. As highlighted by Pesce et al. (2018), the "string" stiffness value is a crucial term that contributes to yaw rigidity. Furthermore,

for an arbitrary equilibrium position for a symmetric mooring line configuration, the yaw stiffness coefficient is only function of the "string" stiffness.

Finally, by applying Pythagorean theorem with the "horizontal-horizontal local stiffness" value, k_{HH} and the "vertical-vertical local stiffness" value, k_{vv}, the value of local stiffness, k of each mooring line is computed to be 0.02 N/mm.

4.3.2 Determining spring and rope configuration

For step 3 in the design approach as outlined in Section 3.3, to effectively represent the simplified mooring, a 3 mm diameter "*D-Racer Low Stretch Dyneema Dinghy Rope*" was selected for its very low elasticity, high strength-to-weight ratio and abrasion resistance. The selected rope has an average breaking load of approximately 3.63 kN and a mass of 6 g/m. This selection ensured that the spring response characteristics of the mooring system as a whole were confined to the mechanical spring configuration implemented. A photograph of the isolated spring system is shown in Figure 9, and a further photograph of the spring system within the mooring setup can be seen in Figure 10.

To supply the required spring rate as calculated above, it was necessary to use a combination of springs, connected both in parallel and series. This was due to spring availability with respect to maximum extension, force range and spring rate. This led to a spring system composed of six 0.03 N/mm springs (Sodemann Industrial Springs 2024). The springs were arranged into two "*branches*" each composed of three springs each. In this configuration, the spring system per mooring line featured two parallel branches of three springs in series, resulting in an overall spring rate of 0.02 N/mm. The maximum available extension of each mooring line was thus 1.22 m, with a breakout load of 2.96 N and a maximum available load of 32.6 N.

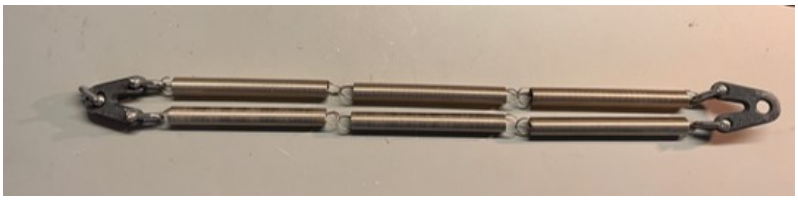

Fig. 9: Mooring spring configuration.

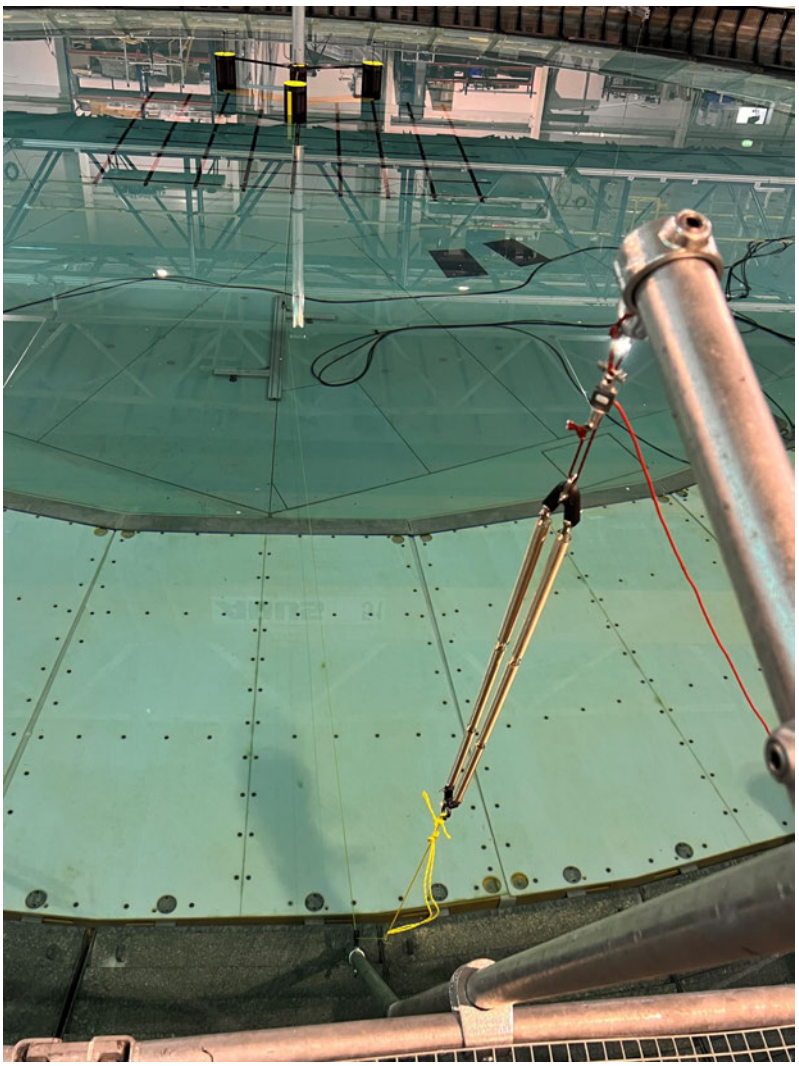

Fig. 10: Mooring in the tank.

4.3.3 Mooring System Verification in MAP++

The fourth and final step as presented in Section 3.4 firstly verifies the analytical values calculated in Table 4 by changing the MAP++ input file to represent the spring-rope configuration used in the tank. PyMap is then used to output the corresponding linear stiffness matrix.

The input parameters changed in the MAP++ input file included line diameter, *Diam (m)*, line density in air, *MassDenInAir (kg/m)* and axial stiffness, *EA (N)*. Only one line type was used since the input values are calculated taking into account the

combined properties of Dyneema rope and springs. The properties of the Dyneema and springs were converted to full-scale and are shown in Table 5.

Table 5: Spring–Dyneema rope properties used to calculate the inputs for the MAP++ input file.

	50th scale	**Full-scale**
Dyneema		
Diameter (mm)	3.00	150.00
Density (kg/m)	0.006	14.55
Length (m)	3.92	196.00
Spring		
Diameter (mm)	2.00	100.00
Density (kg/m)	0.67	1663.33
Length (m)	0.15	7.50
Line Equivalent		
Diameter (mm)	2.96	148.16
Density (kg/m)	0.03	75.31
Length (m)	4.07	203.50

The EA value is calculated using Equation (11).

$$EA = k \times L \tag{11}$$

E is the Young's Modulus, A is the cross-sectional area, L is the unstretched length of the mooring line, and k corresponds to the local stiffness value calculated in Section 4.3.1. Given that the standard Dyneema rope exhibits notable rigidity, characterised by an equivalent stiffness of 2.34×10^5 N/m calculated from the corresponding Young's modulus, E (Vlasblom and Van Dingenen 2009) and the cross-sectional area of the rope, the stiffness of the rope can be effectively represented by the spring stiffness.

Another important input into MAP++ includes the line length. While the theoretical geometric length, distance between fairlead and anchor point, is 4.07 m, the line length introduced in MAP++ must be lower in order to achieve the desired pre-tension and to avoid slacking. A study was performed to understand what line length should be introduced in MAP++ to maintain a close match with the stiffness coefficients of the linear stiffness matrix (Table 4).

Figure 11 shows the stiffness coefficients for varying line lengths between 3.40 and 4 m. As can be seen, the stiffness coefficients are dependent on the line length. 3.65 m is selected to be introduced in MAP++ as it most closely matches the surge stiffness coefficient value given in Table 4. However, by maintaining this length, the stiffness coefficient values will be lower for the rest of the DOF.

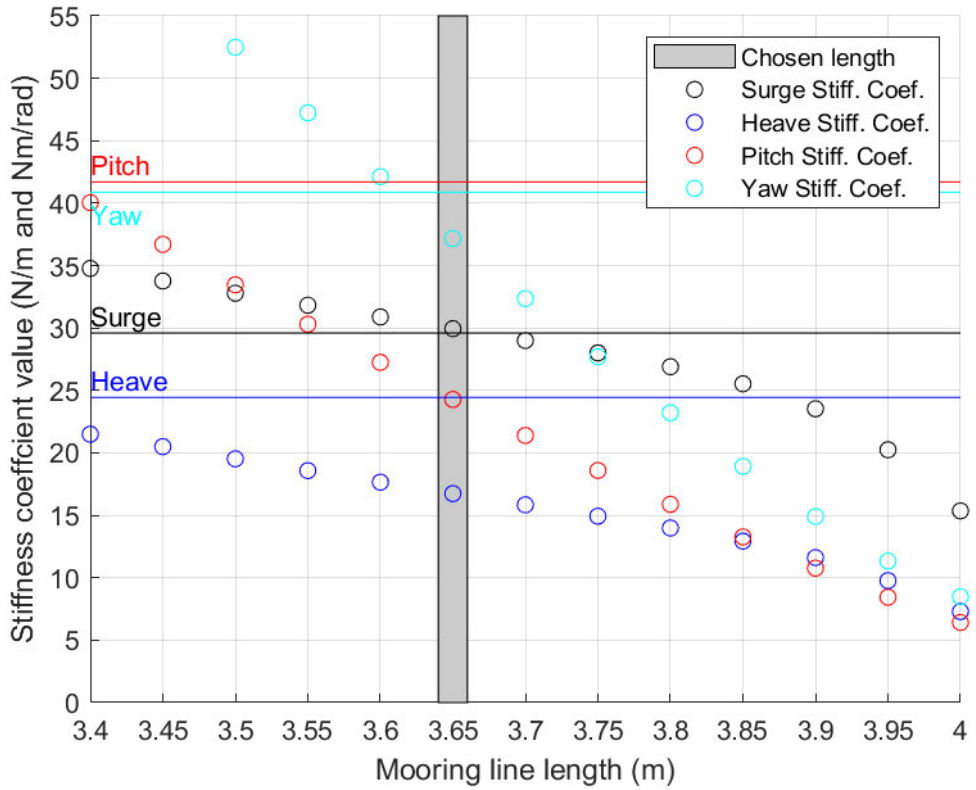

Fig. 11: Stiffness coefficient values in surge, heave, pitch and yaw, obtained when changing the line length input value in MAP++ input file. Grey area represents the values for the chosen line length. The horizontal lines labelled with the respective DOF represent to the target value from the linear stiffness matrix (Table 4).

4.4 Test Instrumentation

The sensors used in the experiment included three load cells, each attached to a mooring line, to measure the mooring loads, Qualisys motion capture system to obtain the translations and rotations of the model, two wave gauges to collect water elevation positioned 4 metres distance from the model and two accelerometers positioned on the nacelle. All data was collected at a frequency of 128 Hz.

4.5 Test plan and layout

The selected sea states for the campaign were based on data for the North Sea, off the coast of Norway relevant to offshore renewable energy developments. Based on this location, data was collected from the open-source ESOX database (LAUTEC/E-SOX 2024). ESOX uses ERA5 reanalysis data produced by the European Center for Medium-Range Weather Forecasts (ECMWF) for the Copernicus Climate Change

Service (C3S). The ESOX map covers areas up to 200+ km offshore, with data from 70°N to 60°S, totalling over 150,000 data points. Each point includes 30 years of data (1990–2019) provided by mean values every hour, for four metocean parameters: mean wind speed at 10 and 100 meters, significant wave height, and peak wave period. The datapoint used near the coast of Haugesund corresponds to a latitude of 59.5° and a longitude of 5°.

The conditions that were particularly relevant for the current study are presented in Table 6. The same load cases were run at full scale using OpenFAST, with the MoorDyn inputs adapted to the equivalent depth of 100 m to better represent the mooring set-up used in the tank. This is referred to as the "OpenFast adapted" mooring system. Simulations were also ran with the original catenary mooring configuration, named "OpenFast catenary" mooring system.

Table 6: Test parameters selected.

Test Parameter	**Description**
Free decay tests in all DOF	Acquiring the model's natural frequencies.
Response Amplitude Operators (RAOs)	Subjecting the model to a frequency sweep of regular waves with a 1 m wave height, covering frequencies from 0.035 Hz to 0.21 Hz.
Mooring stiffness (sway and surge)	Recording the force from a load cell attached to a line connected to the model's COG and pulling it in sway and surge, while measuring displacement.
Mooring static stiffness (pitch)	Inclination test in the tank using calibration weights (0.5 to 2 kg) to displace the model in pitch and minimise other DOF displacement. The tilt angle was recorded.
Comparison of motions and mooring tensions (regular waves)	Three regular waves of equal amplitude but different period: $H = 5\ m$, $T = 11.5\ s$ $H = 5\ m$, $T = 14.0\ s$ $H = 5\ m$, $T = 18.0\ s$
Comparison of motions and mooring tensions (irregular waves)	Three irregular waves with JONSWAP spectrum of equal significant wave height but different peak periods: $H_s = 5\ m$, $T_p = 11.5\ s$, $\gamma = 1.0$ $H_s = 5\ m$, $T_p = 14.0\ s$, $\gamma = 1.0$ $H_s = 5\ m$, $T_p = 18.0\ s$, $\gamma = 1.0$
Comparison of motions and mooring tensions (extreme waves)	Extreme wave conditions: Wave I: $H_s = 13\ m$, $T_p = 16.0\ s$, $\gamma = 1.10$ Wave II: $H_s = 14\ m$, $T_p = 18.0\ s$, $\gamma = 1.24$ Wave III: $H_s = 7\ m$, $T_p = 13.0\ s$, $\gamma = 1.91$

The layout of the FloWave tank is shown in Figure 12. The points labelled A_i where $i \in \{1, 2, 3\}$ mark the anchor positions, in this case, they are the attachment

points to pulleys positioned on the tank floor. The points labelled P_i correspond to the fairlead positions when the system is at equilibrium.

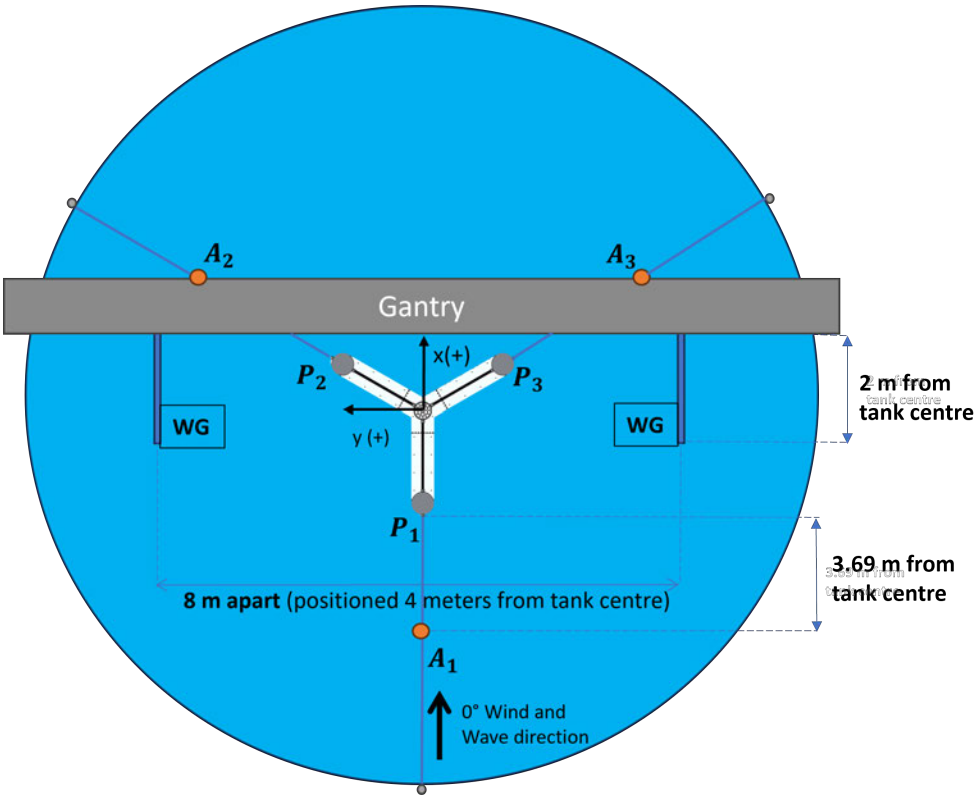

Fig. 12: Schematic of the tank test set-up at FloWave.

The body's centre of gravity is aligned with the origin of the reference system O_{xy}. In regard to z coordinate, $z = 0$ at the water level which corresponds to, approximately, 0.38 m from the bottom of the floating structure as shown in Figure 13. The signal convention used follows the right-hand rule, where x is positive towards the downwind direction, consequently y is positive to the left and z is positive upwards. WG corresponds to the positions of the two wave gauges used.

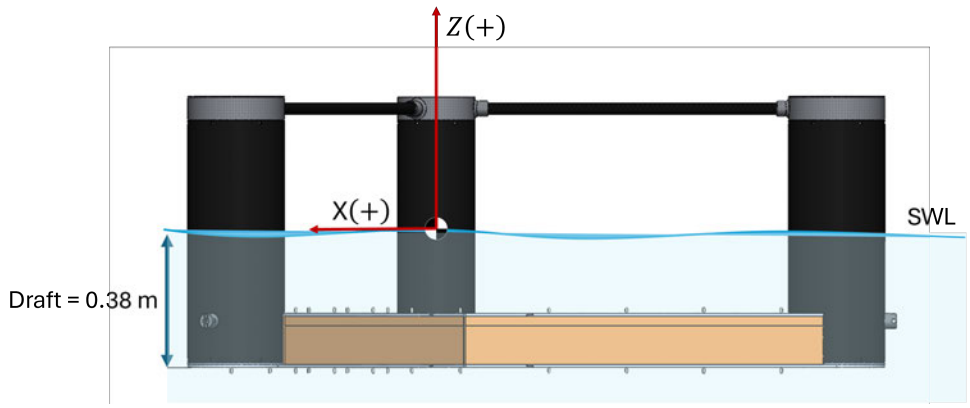

Fig. 13: Visualisation of the location of the centre of gravity of the scaled model.

4.6 Data Processing

Three types of results will be compared, "Experimental", "OpenFast adapted" and "OpenFast catenary". The "Experimental" results correspond to the full-scaled experimental results obtained in the wave tank by the use of spring-rope mooring configuration; the "OpenFast adapted" corresponds to the numerical simulation results where the mooring configuration in MoorDyn is a full-scale representation of the experimental spring-rope system with a depth of 100 m and finally, the "OpenFast catenary" corresponds to the numerical results using the original catenary configuration with a depth of 200 m. This is to try and understand in which way the experimental results compare with the original catenary system but also to how well compare to the tuned numerical model.

The decay tests for the 6 DOF were executed in OpenFAST. As described in Section 4.3.3, the MoorDyn input file is modified to ensure consistency with the tank testing. The natural frequencies for both experimental and numerical results, were acquired by fitting the analytical solution of a linear spring-mass-damper system to the experimental time history, in the form:

$$x(t) = \bar{x} + \hat{x}e^{-\zeta\omega t}\cos\left((1-\zeta)\omega t - \phi\right) \tag{12}$$

where $x(t)$ is the time history of the displacement, $\hat{x}$ is the mean value, $\hat{x}$ is the initial amplitude, ζ is the critical damping ratio, ω is the undamped natural frequency, and ϕ is the phase angle. The values of these variables were calculated by minimising the mean squared error over the time history, using a Generalised Reduced Gradient (GRG) optimisation approach.

4.7 Mooring pre-tensions

The mooring pre-tension from the "OpenFast adapted" system in static water is equal to 9.3 N at tank scale. This value corresponds to a pre-tension of 1162.8 kN at full-scale. This value served as the target pre-tension for the physical test, where the final measured mooring pre-tensions are provided in Table 7.

Table 7: Mooring line pre-tensions as measured in the physical experiment, compared to full-scale values. Refer to Figure 12 for line labels.

Scale	**Fore** (P_1A_1)	**Starboard** (P_2A_2)	**Port** (P_3A_3)
Tank	9.67 N	9.08 N	9.97 N
Full	1.21×10^6 N	1.14×10^6 N	1.25×10^6 N

These were established as the final values, taking into consideration the constraint of time and the understanding that further adjustments might lead to marginal variations. Therefore, the presented pre-tension values represent a practical application for an operational tank test programme.

5 Results and Discussion

This section provides a comprehensive presentation of the experimental and numerical results obtained from modelling the case-study floating offshore wind turbine, conducted in accordance with the testing plan outlined in section 4.5. Several aspects are taken into account with the main objective of comparing how well a linear mooring system in the tank can represent a full-scale catenary mooring system.

A subset of that is the how well the experimental mooring system provides the correct structure's dynamics. As the whole system dynamics are highly coupled, it is not possible to isolate the mooring performance, therefore the results as a whole are used to build up an assessment of the tank mooring design, and by extension, the tank mooring design method.

The results will always be compared between the 'Experimental' data and both numerical models: 'OpenFAST adapted' and 'OpenFAST catenary'. The primary focus of the comparison is between the experimental results and the numerical simulations using the original catenary system. The adapted system represents a tuned numerical model of the tank test setup, designed to numerically assess the effects of simulating a catenary mooring system based on its stiffness properties, geometrically resembling a semi-taut mooring system.

5.1 Model Natural Frequencies

The initial set of results focuses on the verification of natural frequencies within the proposed mooring configuration during the tank test. This involves comparing the observed natural frequencies with those documented in the platform definition document (Allen et al. 2020) with the OpenFAST results for the adapted mooring system.

Table 8 presents a comparison between the natural frequencies presented on the reference model document (Allen et al. 2020), with those obtained using the configured system referred to as the "Adapted mooring system" in OpenFAST simulations and the natural frequencies acquired experimentally in the physical testing.

Nevertheless, differences emerge when comparing the natural frequencies derived from physical testing to the OpenFAST results, particularly in sway and yaw, where up to 20% disparity is identified. This can impact on how well the dynamic behaviour of the original wind turbine system is represented and consequently add error on the overall dynamics of the body as well as mooring tensions. However, the comparison of the natural frequencies for the DOF of interest in this study, pitch and surge, the error is less than 10 %, which is considered a good margin in experimental testing.

Table 8: Full-scale rigid-body natural frequencies comparison between the reference document (Allen et al. 2020), OpenFAST simulations with the adapted mooring system and the decay tests in the physical test. The percentage difference between the OpenFAST (Adapted mooring system) and physical testing natural frequencies are given in the final column.

DOF	**Reference Document (Hz)**	**Adapted mooring system (Hz)**	**Physical Testing (Hz)**	**Difference (%)**
Surge	0.007	0.008	0.008	0%
Sway	0.007	0.008	0.006	20%
Heave	0.049	0.049	0.048	2%
Roll	0.036	0.034	0.031	9%
Pitch	0.036	0.034	0.031	9%
Yaw	0.011	0.011	0.009	15.5%

5.2 Response Amplitude Operators

The comparison for the rigid-body wave-induced motion Response Amplitude Operators (RAOs) in pitch, surge and heave of the floating offshore wind turbine exposed to a regular wave of 1 m amplitude is shown in Figures 14-16.

The RAO profiles in surge and heave consistently exhibit alignment between the results derived from both the experimental data and OpenFAST simulations. The ratio between the experimental and numerical results falls within the range between 1 and 2, with the exception of the highest frequency at 0.2 Hz, where the numerical value approaches zero, so small errors lead to large ratios.

The numerical results between the two mooring systems, adapted and catenary, show good agreement indicating that the system adapted to 100 m depth is functionally similar to the reference design at 200 m depth by including the properties of its linear mooring stiffness matrix which should capture the effects of depth. The ratios with the experimental data are also similar.

In heave, it is observed that near the heave natural frequency (0.048 Hz), there is a slight difference between the structure's response for the three sets of results, with the experimental results showing a lower response. This may be explained by the difference on the mooring heave stiffness coefficient for the three systems.

The adapted mooring system according to Figure 11, had a smaller heave stiffness coefficient compared to the catenary system, potentially explaining why the response in heave, as a greater response is observed near its natural frequency. For the experimental set-up, despite this value not being acquired directly, it can be acquired from the calculation of the vertical mooring stiffness, where the value for the heave stiffness coefficient used was the value from the catenary mooring linear stiffness matrix in surge as explained in Subsection 4.3.1. Despite these values between catenary and experimental configurations being theoretically similar, there's always slight changes in the model construction. Other factors that could be considered, other than the mooring restoring force, which contribute to the structure's response in heave, include the hydrostatic stiffness. Despite this, the ratios between the experimental and numerical results stayed around 1.

In pitch, an increase in amplitude response in the experimental results is evident around the natural frequency (0.03 Hz), as illustrated in Figure 14a. The two ratios depicted in Figure 14b, are higher around pitch natural frequency. The mooring stiffness in pitch might not be the major contributor for the restoring moment in this DOF since the pitch mooring stiffness coefficients for the adapted and the catenary systems are not the same, however, the model geometry and mass distribution is the same.

Other factors might be at play, as for example the waterplane area and metacentric height as well as numerical simulation errors in calculating the added mass and damping coefficients for rectangular pontoon shapes. Throughout the remaining profile, the outcomes are consistent between OpenFAST simulations and the experimental data, except for the highest frequency of 0.2 Hz where the OpenFAST values are close to zero.

It's important to emphasise that none of the OpenFAST numerical models were tuned using experimental results for damping. The damping parameters, including both linear and quadratic components, were kept as originally defined by the model settings without adjustment based on the experimental data. This means that the drag coefficients and added mass coefficients were not calibrated to match the basin test results. As a result, the numerical models relied solely on the inherent hydrodynamic formulations present in OpenFAST, without any modifications to better align with observed damping behaviour from physical testing.

Overall, the RAO in pitch, surge and heave tends to follow similar shapes between the numerical and experimental results. The range of frequencies below the wave frequency range (< 0.05 Hz) shows the biggest differences and the cause might due to not fully matching hydrodynamic and mooring coefficients. Within the wave excitation frequency ($0.05 - 0.2$ Hz), the results are visibly similar.

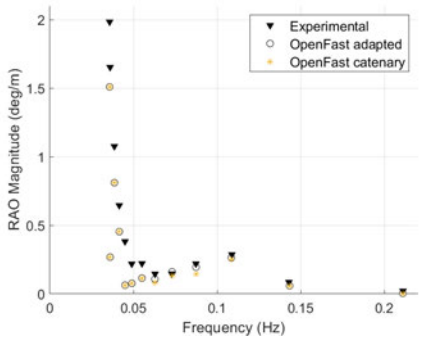

(a) RAO amplitude response in Pitch for 1 m wave amplitude.

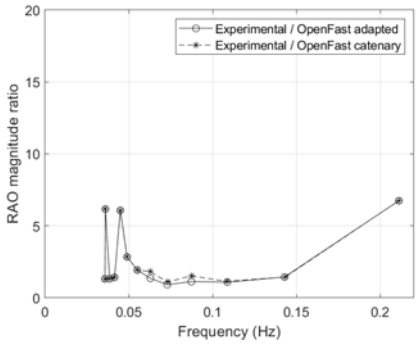

(b) Ratio of RAO amplitude response in Pitch (Experimental vs OpenFAST).

Fig. 14: RAO results in Pitch.

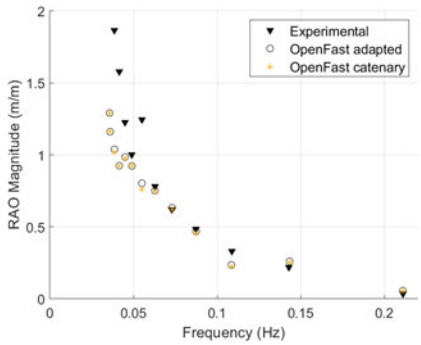

(a) RAO amplitude response in Surge for 1 m wave amplitude.

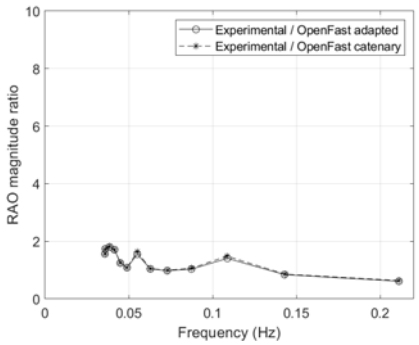

(b) Ratio of RAO amplitude response in Surge (Experimental vs OpenFAST).

Fig. 15: RAO results in Surge.

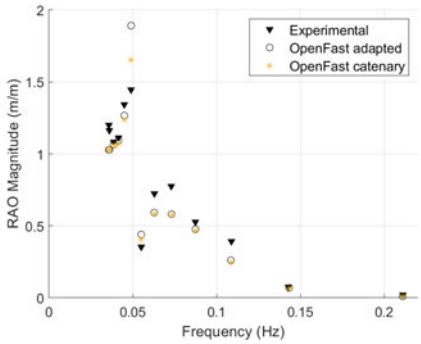

(a) RAO amplitude response in Heave for 1 m wave amplitude.

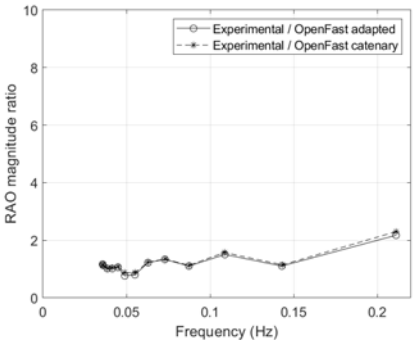

(b) Ratio of RAO amplitude response in Heave (Experimental vs OpenFAST).

Fig. 16: RAO results in Heave.

The mooring restoring force responses in surge and sway are illustrated in Figures 17 and 18, respectively. A first order polynomial is fitted to the data and the gradient of the line corresponds to the mooring stiffness coefficient for the correspondent DOF. The gradient is found to be 28 N/m (7.0×10^4 N/m in full-scale) in surge and 24.7 N/m (6.2×10^4 N/m in full-scale) in sway. The stiffness coefficient in surge is close to the target mooring stiffness matrix value for surge given in Table 4 with a difference of 6.5%. However, this difference increases to 17.5% when comparing the values in sway. These differences remain similar when compared to the catenary mooring linear stiffness matrix Table 3. In theory, the mooring stiffness for these DOF, surge and sway should be equal. In practical terms, there's always errors associated with model asymmetries, sensors and the springs themselves. This might introduce differences in mooring tensions and motions in sway.

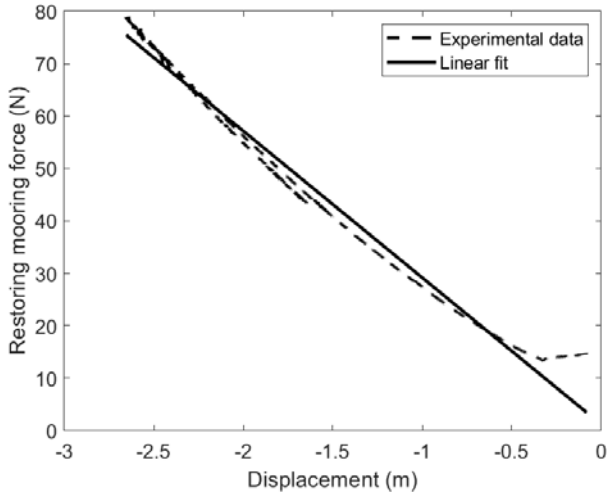

Fig. 17: Experimental mooring restoring force vs displacement in surge.

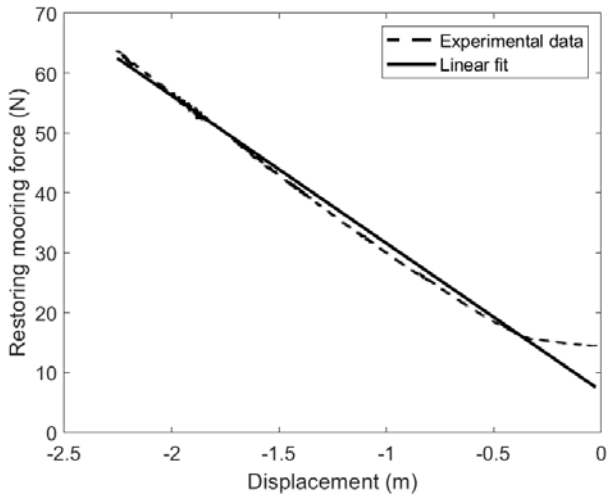

Fig. 18: Experimental mooring restoring force vs displacement in sway.

The mooring stiffness in pitch was acquired from an inclination test. This was performed for the model both with and without moorings attached. This way the mooring contribution could be isolated and assessed. Following the same procedure used for the other 2 DOFs (surge and sway), the gradient of the line of best fit was used. In this case, the difference between the gradient for the inclination test

with mooring lines attached and for no mooring lines attached gives a measure of the mooring stiffness in pitch. The difference between the two was found to be to 42.54 Nm/rad (2.7×10^8 Nm/rad in full-scale). This represents a difference of 43% when compared to the adapted mooring system shown in Table 4 and to a difference of 2% when compared to the catenary system's value shown in Table 3.

The discrepancy between the adapted and catenary systems can likely be attributed to differences in the line length values used in MAP++, theoretical value and those measured in the tank test. The theoretical line length is 4.07 m, while in the tank test, a geometric length of 3.83 m was measured. In the tank test, pre-tension was achieved through the elongation of springs. However, in MAP++, pre-tension was instead accomplished by stretching the line itself, resulting in a reduced effective length of 3.65 m. As shown in Figure 11, the line length significantly influences the stiffness coefficients.

5.3 Regular Waves

Figure 19 shows the mean mooring loads and standard deviations for each wave period, categorised by three different setups: OpenFAST Adapted (tuned numerical model simulating tank test configuration), Experimental (spring-rope system in tank tests), and OpenFAST Catenary (original catenary simulation). While an earlier version of the analysis involved subtracting the mooring pre-tension from all three datasets to allow for easier visual comparison, this approach was ultimately reconsidered. Removing the pre-tension required significant manipulation of the data and tended to obscure meaningful differences in behaviour between the semi-taut systems (Experimental and Adapted) and the Catenary configuration. As a result, the current presentation retains the original mean values — including pre-tension — to more accurately reflect the actual load levels and the influence of each mooring setup.

The significant difference in mean mooring tensions between the catenary and the other two configurations can be primarily attributed to the disparity in initial pre-tension levels. In the original catenary mooring system, the pre-tension was set to 2.02×10^6 N, whereas the experimental tank setup exhibited a lower pre-tension of 1.16×10^6 N — a deviation of approximately 42.5%. Although attempts were made to increase the pre-tension in the OpenFAST adapted model, these led to unstable system displacements, particularly in heave. Moreover, the physical spring elements used in the tank had a load capacity of only 4.08×10^6 N, which would have been exceeded once dynamic wave loading was introduced. These constraints help explain the lower mean mooring tensions in both the experimental and adapted cases compared to the catenary results.

The OpenFAST results exhibit more symmetrical line tensions compared to the physical testing results. In the experimental results, the tensions in Line 2 and Line 3 show a discrepancy of 9% from each other, while those same values in the OpenFAST results are nearly identical. If the asymmetry in Line 2 is disregarded, the difference in the mean values is kept under 10%. This asymmetry is inherent to the challenges of experimental testing, where exactly matching the mooring line pre-tensions can be difficult, and some margin for error is expected.

At the shortest wave period of 11.5 s (Figure 19a), the fore mooring line exhibits slightly higher mean tension values compared to the port and starboard lines across all configurations. This may be attributed to first-order wave excitation effects, as shorter-period waves provide less time for the structure to return to equilibrium between wave cycles, leading to stronger surge-induced loading on the fore line. This can result in sustained displacement (e.g., in surge, as shown in Figure 20), increasing the mean surge over time. As the wave period increases (Figures 19b and 19c), the mean tensions tend to align across all three mooring lines in the numerical models (OpenFAST Adapted and Catenary), indicating a more balanced load distribution. This trend is consistent across all the results. However, this convergence is not observed in the experimental results, where asymmetries in the spring-rope system may have influenced the load sharing between lines.

A key observation is the differing behaviour of the three systems as the wave period increases (or the frequency decreases). It can be seen that the standard deviations for the adapted and experimental systems increase with increasing wave periods. This aligns with the longer waves exciting more platform motions, leading to more significant tension changes. Conversely, the standard deviations for the catenary system decrease with increasing wave period (Figure 19c), reflecting the more gradual and smoother motions typical of longer-period waves, with fewer tension spikes.

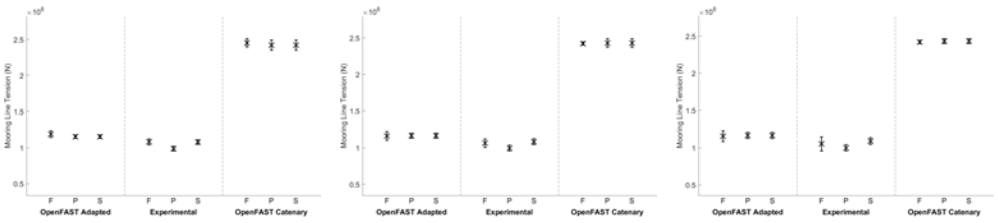

(a) Comparison of the mooring loads experienced under regular wave of 5 m wave height and wave period of 11.5 s.

(b) Comparison of the mooring loads experienced under regular wave of 5 m wave height and wave period of 14 s.

(c) Comparison of the mooring loads experienced under regular wave of 5 m wave height and wave period of 18 s.

Fig. 19: Comparison of the mooring tensions (N) between the OpenFAST adapted mooring, OpenFAST catenary mooring and experimental results with no wind load being applied and exposed to regular waves of equal height, 5 m and three different wave periods, T = 11.5 s, 14.0 s and 18.0 s. 'F' corresponds to the fore mooring line, 'P' to the port mooring line and 'S' to the starboard mooring line. The mean value is represented by the black cross sign and the vertical lines represent the standard deviations.

The simplified spring-rope system resembles a semi-taut system and may introduce more abrupt tension variations because it lacks the inherent damping and gradual restoring forces of a catenary line. Also, spring-rope systems are more sensitive to platform motions because they rely more on tension than on line sag. Even small

platform movements can cause significant tension changes, leading to larger standard deviations. In contrast, catenary systems "buffer" these movements by allowing more line extension, which stabilises the tension variations (i.e. lower standard deviations).

The model's motions in pitch and surge is presented in Figure 20 across the three distinct wave periods. The mean values for pitch and surge displacement compare reasonably well. One observed distinction is the standard deviation values on the pitch displacement box plots in Figure 20a, where the experimental results show a lower dispersion of the data around the mean value in comparison to the adapted numerical simulation results.

On the comparison between the adapted system and experimental results one main difference between the two is the mooring stiffness value in pitch which is 43% higher in the tank test set-up compared to the adapted mooring system. Consequently, the mooring restoring force in pitch is higher in the tank experiments. To verify if increasing the pitch stiffness coefficient reduces the motion of the model in pitch, the pitch stiffness coefficient value in HydroDyn was manually varied between 1×10^8 and 1×10^9 Nm/rad, and the pitch displacement was recorded when exposed to a wave height of 5 meters and a wave period of 14 seconds. The results are presented in Figure 21.

With an increase in the pitch stiffness coefficient in the numerical model, the mean pitch displacement slightly increases, as does the standard deviation from 1×10^8 to 2×10^8 Nm/rad. From pitch stiffness coefficient values higher than 2×10^8 Nm/rad the standard deviation range is generally maintained. However, the pitch motions observed in the tank testing results show lower standard deviations compared to the adapted mooring results.

Therefore, it is inconclusive if the increased mooring stiffness in pitch explains why the pitch motions in the tank test have lower standard deviation values compared to the numerical simulations. In principle, a stiffer mooring system in pitch would decrease the standard deviation values around the mean value. However, that is not verified by the adapted system numerical simulations. In fact, the opposite is observed, almost making the system more elastic. This effect is not noticeable in the experimental results.

Other factors that could contribute to the more damped pitch response seen in the experimental results other than higher mooring pitch stiffness coefficient, include the model's damping coefficients. According to the decay tests, the damping coefficient for the physical model with the moorings attached is 0.042, whereas for the adapted and catenary systems, it is 0.0105 and 0.019, respectively. However, these values were acquired only for the resonant frequency. The damping term may vary with different wave frequencies and is not linear.

Additional factors that might influence the more damped pitch response in the experimental results include the added mass coefficients and moments of inertia, which could not be compared due to the lack of necessary tests to acquire those values. It is difficult to identify the primary cause of the differences, as multiple factors could contribute, including the potential accumulation of various errors. Nevertheless, the overall pitch results are not significantly different, and no clear explanation is evident.

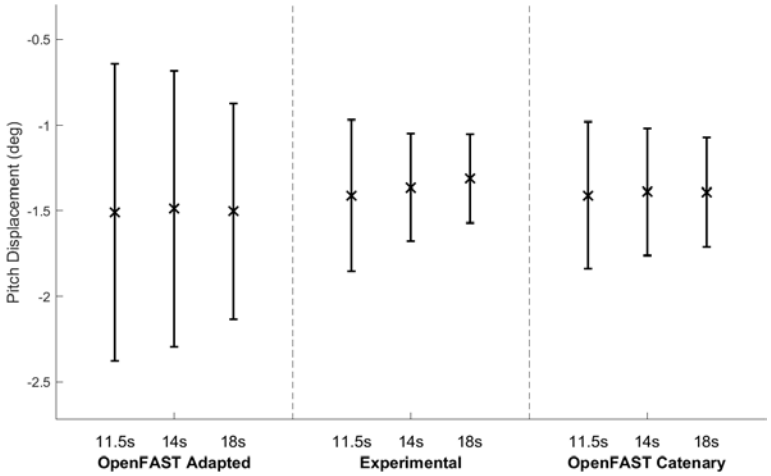

(a) In pitch.

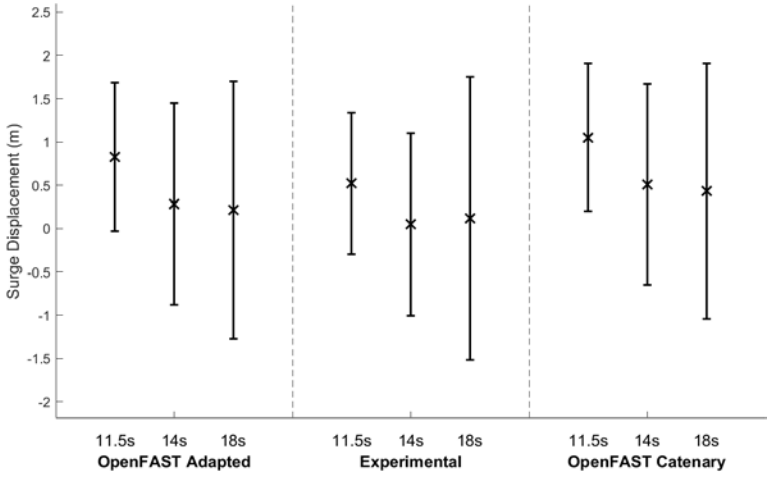

(b) In surge.

Fig. 20: Comparison of pitch and surge motions between tank experiment and numerical simulations exposed to the regular waves of varying periods. The mean value is represented by the black cross sign and the vertical lines represent the standard deviations.

In the case of surge displacements, the density distribution of both sets of results is similar, with standard deviations closely aligned, as shown in Figure 20b. As previously explained for the mooring tensions, the mean surge displacement is higher for higher frequency waves ($T = 11.5\ s$), as the mooring restoring force does not act quick enough to return the model to its original mean position. This behaviour is well captured across all configurations.

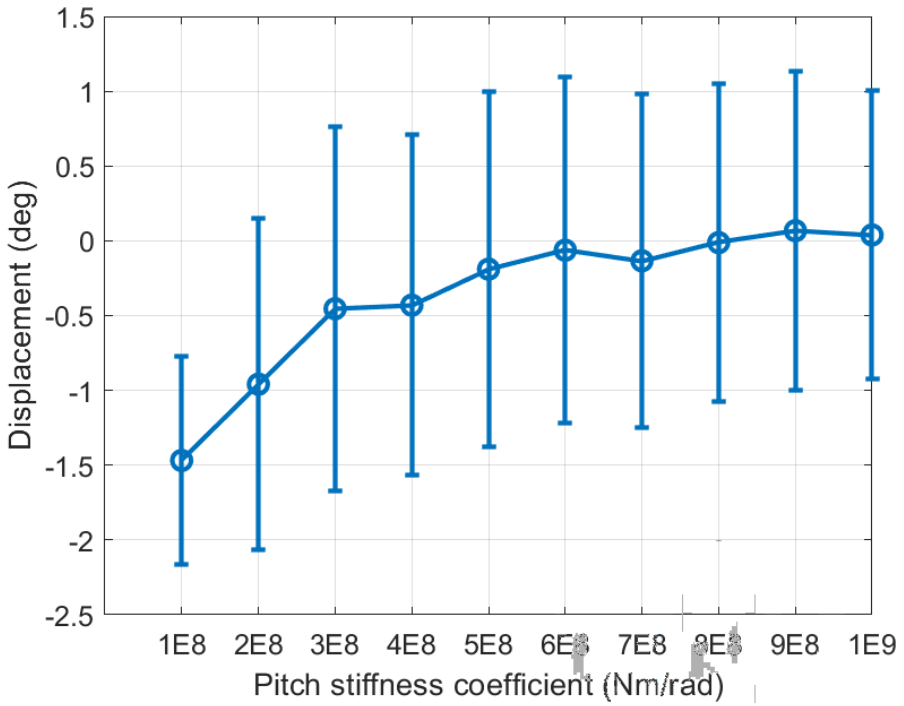

Fig. 21: Pitch displacement for different values of pitch stiffness coefficient exposed to regular waves of 5 m height and 14 s wave period. Results of OpenFAST numerical simulation using HydroDyn additional linear stiffness matrix.

5.4 Irregular Waves

The analysis of the mooring line tensions and pitch and surge displacements under irregular wave conditions, is shown in Figures 22 and 23. When looking at the surge displacement it is visible that the mean values are away from zero which could be explained by the presence of first order wave loads as seen in the regular waves results but also some second-order effects including drift. Drift loads, which accumulate over time due to nonlinear interactions between the waves and the structure, cause a gradual shift in the platform's position. This is apparent for all three configurations, however the catenary mooring configuration demonstrates a slightly higher mean displacement.

With regards to the mooring tensions, it is evident that the fore mooring line in all configurations exhibits the highest standard deviations, which aligns with expectations given its exposure to one direction incoming waves. Both the experimental setup and the adapted system show lower standard deviations for higher frequency waves, reflecting the behaviour typical of semi-taut mooring systems. These systems are more sensitive to surge and heave displacements, leading to greater variability in mooring

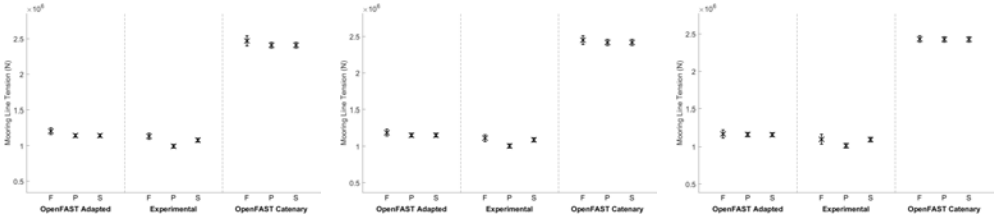

(a) Comparison of the mooring loads experienced under irregular waves of 5 m significant wave height and wave period of 11.5 s.

(b) Comparison of the mooring loads experienced under irregular waves of 5 m significant wave height and peak wave period of 14 s.

(c) Comparison of the mooring loads experienced under irregular waves of 5 m significant wave height and peak wave period of 18 s.

Fig. 22: Comparison of the mooring tensions (N) between the OpenFAST adapted mooring, OpenFAST catenary mooring and experimental results with no wind load being applied and exposed to irregular waves of equal significant wave height, 5 m and three different peak wave periods, $T_p = 11.5$ s, 14.0 s and 18.0 s. 'F' corresponds to the fore mooring line, 'P' to the port mooring line and 'S' to the starboard mooring line. The mean value is represented by the black cross sign and the vertical lines represent the standard deviations.

tensions under such conditions as it was concluded by the regular waves results. Conversely, the catenary mooring system is more effective at accommodating larger surge and heave displacements, particularly in lower frequency waves, due to its inherent flexibility and ability to absorb and distribute forces more smoothly.

In regards to the pitch displacement, when looking at the the mean values and standard deviations, experimental results show no significant difference between the three types of sea states. This is seen as well for the mean value the catenary mooring configuration. The standard deviations change slightly. However, these are differences of less than 0.5 deg. The behaviour of the adapted system is not closer to the experimental results, showing bigger displacements in pitch for all the sea states. In this case, when comparing both numerical model's results, it is visible that the mooring configuration excites the structure's displacement in pitch.

5.5 Extremes

In Figure 24, the results for selected extreme wave conditions are presented. Wave 1 corresponds to a 1-year return period sea state. Waves 2 and 3 correspond to 50-year return period sea states presented first in extreme conditions under section 4.5.

The results show similar statistical parameters across the different sets of results. Overall, under more extreme conditions, with waves aligned at 0°, corresponding to the downwind direction, the fore mooring line experiences the highest tensions while the two backward moorings experience lower loads. For the catenary mooring case, it represents that the two back moorings will have more weight on the floor and for the spring-rope systems, it means the tension in the lines is less without being slack. During the experimental testing, this condition was checked. The mean values for the

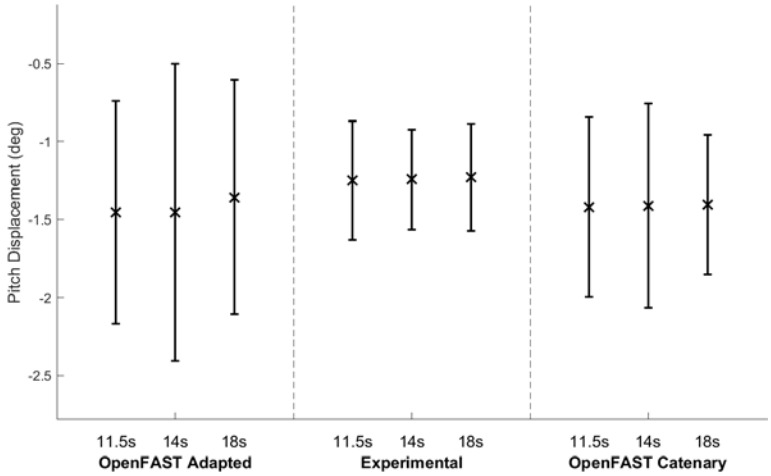

(a) In pitch.

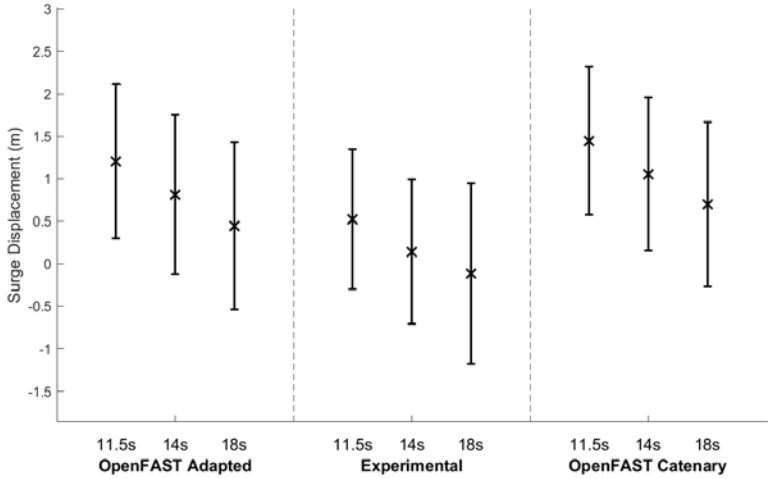

(b) In surge.

Fig. 23: Comparison of pitch and surge motions between tank experiment and numerical simulations exposed to irregular waves of varying peak periods. The mean value is represented by the black cross sign and the vertical lines represent the standard deviations.

mooring tensions and surge displacements are positioned away from its pre-tension value, which might indicate the presence of first and second order effects including drift, more accentuated then when compared to the irregular waves results. These effects are captured by all the three configurations.

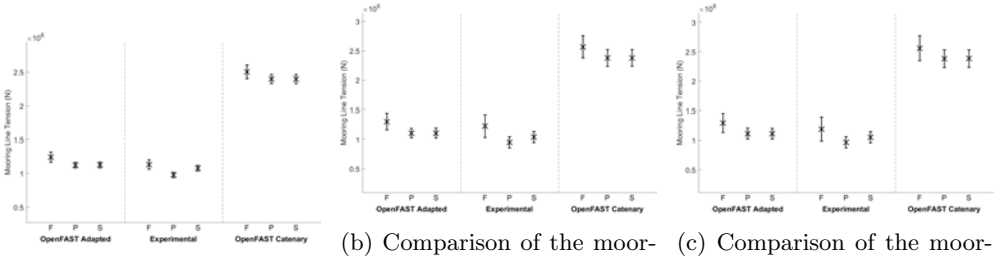

(a) Comparison of the mooring loads experienced under wave 1 parameters, $H_s = 7m$, $T_p = 13.0s$ and $\gamma = 1.10$.

(b) Comparison of the mooring loads experienced under wave 2 parameters, $H_s = 13m$, $T_p = 16.0s$ and $\gamma = 1.24$.

(c) Comparison of the mooring loads experienced under wave 3 parameters, $H_s = 14m$, $T_p = 18.0s$ and $\gamma = 1.91$.

Fig. 24: Comparison of the mooring tensions (N) between the OpenFAST adapted mooring, OpenFAST catenary mooring and experimental results with no wind load being applied and exposed to extreme waves. 'F' corresponds to the fore mooring line, 'P' to the port mooring line and 'S' to the starboard mooring line. The mean value is represented by the black cross sign and the vertical lines represent the standard deviations.

These waves compared to the irregular wave cases, present much harsher conditions with larger wave heights. It can be seen that the mooring tensions' standard deviations for the catenary mooring configuration present the same trend as the other two configurations. As seen in Figure 25b, the standard deviations of surge displacement increase with wave severity, consistent with the trend observed in the mooring tension variability (Figure 24). However, the OpenFAST Catenary configuration shows slightly smaller surge standard deviations compared to the Experimental and Adapted cases. This can likely be attributed to the nature of the catenary mooring system, where the restoring force—derived from the weight of the chain as it lifts from the seabed—provides a more gradual and stabilising response to large displacements in surge.

In terms of the pitch displacement results shown in Figure 25, the adapted system shows, once again, significant differences compared to the other two configurations. Second-order forces might significantly excite the adapted system. On the other hand, the experimental results show that the displacement in pitch is quite damped compared to the results for the catenary system.

5.5.1 Overall comparison

Tables 9 and 10 present overall comparisons of the relative error of the mean value and the standard deviation ratio under different wave conditions (regular, irregular, and extreme waves). Table 9 compares the OpenFAST catenary simulation results with the experimental data, while 10 provides a dedicated comparison between the experimental results and the adapted numerical model, capturing the performance of the tank-test-representative configuration.

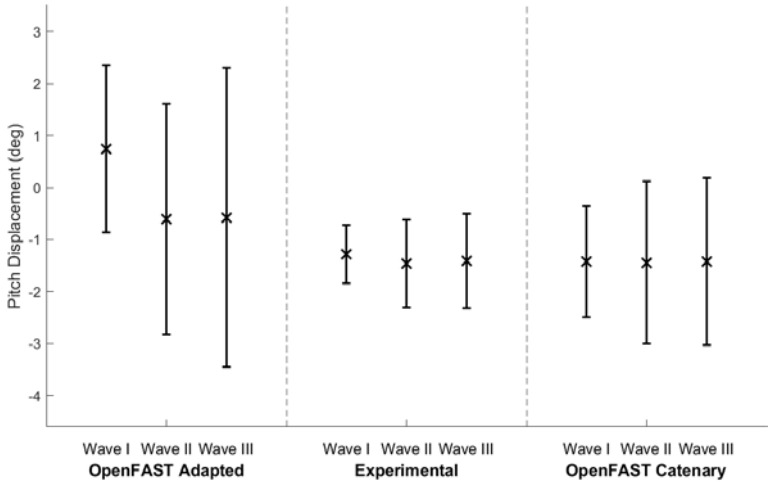

(a) In pitch.

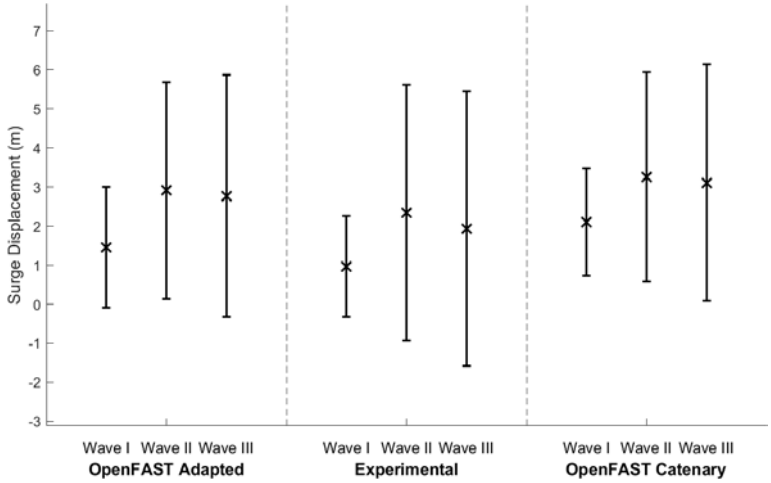

(b) In surge.

Fig. 25: Comparison of pitch and surge motions between tank experiment and numerical simulations exposed to the extreme waves of 1 and 50-year return periods. The mean value is represented by the black cross sign and the vertical lines represent the standard deviations.

The relative error quantifies how closely the mean values from the simulation match the experimental measurements. It is calculated as the absolute difference between the simulated and experimental means, divided by the experimental mean and expressed as a percentage. The standard deviation ratio assesses how well the variability in the simulation corresponds to that in the experimental data. It is computed as the ratio

of the simulation's standard deviation to that of the experimental result with a value of 1 indicating a perfect match in variability.

For the results presented, different wave periods are separated by slashes ("/") and listed in ascending order of wave period. For example, in the case of the relative error for pitch under regular waves in Table 9, the first value of 0.14% corresponds to a wave period of 11.5 seconds. For extreme wave conditions, the results are provided in the order of wave I, wave II, and wave III.

Under regular wave conditions, the results in Table 9 show that the OpenFAST catenary model reproduces pitch motions with high accuracy, both in terms of mean values and variability, indicated by very low relative errors and standard deviation ratios close to 1. However, it significantly overpredicts the mean mooring tensions and shows inconsistent variability, particularly for the port and starboard lines. Surge displacement is also not well captured, with large relative errors. It is important to note that a known discrepancy exists in mooring pre-tension levels between the catenary model and the experimental setup, with the catenary system exhibiting a pre-tension approximately 42.5% higher than the experimental value. This difference contributes to the consistently high relative errors observed in the mooring tension comparisons.

In contrast, Table 10 demonstrates that the Adapted model provides a substantially better match for mooring line tensions in terms of mean values, especially for the fore and side lines. Standard deviation ratios are also closer to 1, indicating improved representation of the dynamic response. While pitch predictions are slightly less accurate than in the catenary case, they remain within acceptable bounds. Surge displacement remains a challenge for both models, though the Adapted model does not show improvement in mean surge accuracy. Nevertheless, in both cases, the standard deviation ratios for surge remain reasonably close to 1, suggesting that the models are able to capture the variability of the surge motion with acceptable accuracy, even if the mean values are less well predicted.

Under irregular and extreme wave conditions, the trends observed in Tables 9 and 10 further highlight the respective strengths and limitations of the spring-rope system. In pitch, both models show acceptable agreement in mean values under irregular conditions, but tend to overestimate variability, as reflected in standard deviation ratios significantly above 1. Under extreme waves, the experimental results maintain good agreement with the catenary model in pitch mean values, while the adapted model shows inconsistent accuracy in this regard.

For surge, both models continue to show large relative errors in mean values across irregular and extreme conditions. However, in both cases, the standard deviation ratios remain close to 1, indicating that surge variability is consistently well captured, even when the absolute position of the structure is not.

The most notable differences appear in the mooring tension results. The OpenFAST catenary model consistently shows higher mean mooring line loads, with relative errors above 100%, though the variability is moderately well predicted. In contrast, the adapted model offers a much better match, with relative errors typically below 20% and standard deviation ratios close to 1 across all lines. This strong agreement under both irregular and extreme conditions highlights the effectiveness of the adapted model in replicating the mooring system behaviour observed in the tank tests.

An important trend to note is the increase in mooring tension relative errors under irregular and extreme conditions, particularly for the catenary model. This reflects the growing difficulty of capturing the non-linear and coupled dynamics of a catenary mooring system, especially as wave conditions become more energetic and complex. These non-linearities — such as segment lifting, seabed interactions, and geometric stiffness changes — are inherently hard to replicate with a simplified spring-rope system, which may explain the divergence between the numerical catenary predictions and the experimental results.

Table 9: Comparison of relative error and standard deviation ratio between OpenFAST Catenary simulation results and Experimental results.

Wave Condition	Variable	Relative Error (%)	Standard Deviation Ratio
Regular	Pitch	0.14 / 1.88 / 5.92	0.97 / 1.18 / 1.23
	Surge	50.54 / 89.65 / 72.96	1.04 / 1.10 / 0.90
	Fore Mooring Tension	55.90 / 56.10 / 56.50	1.42 / 0.42 / 0.24
	Port Mooring Tension	59.20 / 59.00 / 58.90	2.12 / 1.44 / 0.73
	Starboard Mooring Tension	55.50 / 55.40 / 55.1	2.19 / 1.44 / 0.72
Irregular	Pitch	12.00 / 12.00 / 12.50	1.50 / 2.05 / 1.31
	Surge	63.80 / 86.60 / 116.50	1.06 / 1.07 / 0.92
	Fore Mooring Tension	117.90 / 120.20 / 121.40	1.63 / 1.25 / 0.65
	Port Mooring Tension	142.40 / 140.90 / 139.80	1.56 / 1.50 / 1.13
	Starboard Mooring Tension	123.20 / 122.30 / 121.70	1.51 / 1.45 / 1.10
Extreme	Pitch	10.40 / 1.10 / 0.80	1.91 / 1.85 / 1.78
	Surge	53.90 / 28.00 / 37.6	1.07 / 0.82 / 0.86
	Fore Mooring Tension	120.80 / 109.20 / 114.70	1.44 / 0.98 / 1.04
	Port Mooring Tension	144.70 / 150.70 / 147.00	1.68 / 1.51 / 1.59
	Starboard Mooring Tension	122.20 / 128.50 / 126.40	1.67 / 1.50 / 1.55

Table 10: Comparison of relative error and standard deviation ratio between OpenFAST Adapted simulation results and Experimental results.

Wave Condition	Variable	Relative Error (%)	Standard Deviation Ratio
Regular	Pitch	6.87 / 9.15 / 14.69	1.95 / 2.56 / 2.43
	Surge	57.98 / 440.57 / 72.96	1.05 / 1.11 / 0.90
	Fore Mooring Tension	10.10 / 9.20 / 9.90	1.15 / 1.03 / 0.76
	Port Mooring Tension	17.00 / 17.10 / 16.70	0.69 / 0.86 / 0.96
	Starboard Mooring Tension	7.10 / 7.60 / 7.00	0.71 / 0.86 / 0.95
Irregular	Pitch	16.30 / 16.90 / 10.5	1.86 / 2.98 / 2.19
	Surge	130.30 / 474.80 / 491.3	1.10 / 1.11 / 0.93
	Fore Mooring Tension	6.50 / 6.70 / 6.50	1.04 / 1.00 / 0.82
	Port Mooring Tension	15.10 / 14.90 / 14.70	0.88 / 0.93 / 0.89
	Starboard Mooring Tension	5.90 / 6.00 / 6.00	0.85 / 0.90 / 0.84
Extreme	Pitch	158.10 / 58.50 / 59.40	2.86 / 2.63 / 3.17
	Surge	50.50 / 24.00 / 42.80	1.20 / 0.85 / 0.88
	Fore Mooring Tension	9.80 / 6.10 / 8.70	1.08 / 0.73 / 0.78
	Port Mooring Tension	14.90 / 16.70 / 15.50	1.03 / 0.85 / 0.96
	Starboard Mooring Tension	4.70 / 6.30 / 5.70	1.06 / 0.88 / 0.95

6 Limitations

All studies that compare numerical models with experimental testing will have inherent limitations. In this study, which focused on understanding how well a spring-rope system could represent a catenary mooring configuration in experimental testing, there were limitations mainly associated with four areas: (1) the restoring characteristics of both systems, catenary and spring-rope; (2) physical constraints of the springs and wave basin; (3) limitations associated with simplifications used in numerical models; and (4) errors associated with model build and experimental testing, e.g., mooring pre-tensions not matching perfectly, which is easily avoided in numerical settings. It is important to note that no tuning of the numerical model was performed in this study, ensuring that the results reflect the direct application of the modeling assumptions.

Although the dynamics of the model in pitch are sufficiently similar across all configurations, the same is not observed for surge. While the standard deviations of surge displacement are reasonably well captured, the mean surge values show significant discrepancies between the numerical models and the experimental results. It is important to note that these discrepancies in relative error are partly due to the use of a ratio-based metric, which becomes highly sensitive when the reference (experimental) mean value is close to zero — as it is the case for surge in some conditions. As such, relative errors exceeding 400% should be interpreted with caution, as they may overstate the mismatch in absolute terms. The standard deviation ratios offer a more reliable indication of dynamic agreement in these instances.

Furthermore, the mooring tensions in the catenary mooring configuration are more than double those measured in the experimental testing and in the adapted configuration. As mentioned previously, the restoring force in a catenary mooring system is primarily due to its weight, whereas in a spring-rope system, this force arises from the mooring's stiffness properties. Consequently, the spring-rope systems behave as a semi-taut system, highly sensitive to surge displacements. In contrast, the catenary system's more flexible and gradual energy absorption characteristics help to mitigate these variations, resulting in lower standard deviations.

Introducing a set of weights on the mooring lines in the tank could potentially replicate the gradual restoring force of a catenary system; however, the maximum load capacity of the springs would limit this approach. These limitations become even more pronounced under wind loads, which would increase the tension on the fore mooring line. Typically developers do not rely on a single mooring line per fairlead, instead using at least two lines to ensure redundancy. This practice is advantageous as it distributes the tension applied to the fore mooring line between the two mooring lines, an aspect not accounted for in this experimental setup.

Additionally, introducing non-linear external loads, as in the irregular and extreme wave cases, results in non-linear responses, raising questions about whether a spring-rope system can accurately replicate second-order effects such as structural drift. In the numerical model, this drift component is captured using Quadratic Transfer Functions (QTFs) calculated by hydrodynamic solvers such as WAMIT (Newman and Lee 1999). However, linear wave theory is predominantly used to simulate the wave field, which introduces limitations, as most wave conditions in this study would be better represented by a 2^{nd} order wave theory.

Lastly, when comparing numerical and physical models, it is important to account for cumulative errors from model build to hydrostatic and hydrodynamic properties. In this work, some properties were compared, while others (e.g., added mass and damping coefficients for different wave frequencies) were not acquired. These limitations highlight the challenges in comparing results and the complexity of tank testing. Another consideration is the presence of physical asymmetries in the tank test experiments, which are potentially closer to real-world behaviour than the symmetry assumed in numerical models. For example, each mooring line in the tank had slightly different pretensions, which became apparent, particularly in the mooring tension plots. Achieving perfect symmetry in the tank was a significant challenge, requiring compromises that further influenced the results.

7 Conclusion

The present study explored how well a catenary mooring system can be represented using a spring-rope system in a wave basin using a floating wind turbine reference model. Tank testing facilities face many challenges to meet the requirements of each device, particularly in accurately representing mooring lines and simulating the coupled effects of mooring lines along with external loads such as waves and wind.

The primary objective for developers when testing scaled models in a wave basin is to create a representative model that allows for the assessment of six degrees of freedom (DOF) motions and mooring line tensions. This is crucial for validating the numerical model and enabling the testing of additional load cases. Hence, accurately representing the mooring system in the tank is of utmost importance.

Tank test results for natural frequencies showed good alignment with the full-scale design documents and OpenFAST simulations for most DOFs, with the notable exception of sway and yaw, where discrepancies of up to 20% were observed. This suggests that while the spring-rope mooring system using linear springs can approximate the natural frequencies of a full-scale catenary mooring system in some DOFs, there are significant deviations in others.

Response amplitude operators (RAOs) in surge and heave demonstrated reasonable agreement between tank tests and OpenFAST simulations, with RAO amplitude ratios close to one, indicating that the linear spring mooring system can sufficiently replicate the dynamic response of the catenary system in these DOFs. However, in pitch, for lower frequencies ($< 0.05Hz$), slight discrepancies were found. An increase in amplitude response around the natural frequency was observed in the tank tests, suggesting the linear spring system may overestimate the pitch response compared to the catenary system, likely due to differences in stiffness and damping characteristics. While in heave, the experimental results showed a more damped response for the experimental setting compared to the other two sets of results.

Other reasons for this mismatch could come from the added mass and damping characteristics between the experimental and numerical models. The numerical model, was not calibrated using physical test data. Despite these differences, the profiles of both datasets followed a similar shape, with the ratio of observed to experimental data points ranging from one to two.

Experimentally derived mooring stiffness values in surge, sway and pitch were within 6.5%, 17.5% and 2% of analytical values from the catenary mooring stiffness matrix, respectively, indicating that the linear spring mooring system deployed in the tank fulfilled its design intention. However,compared to the adapted system, in pitch, the mooring stiffness was found to be 43% higher in tank tests. This might affect the overall dynamics as could be seen from the results of pitch displacement for the adapted system exposed to the different sea states. On the other hand, for the adapted system it was proved that by increasing mooring pitch stiffness does not necessarily reduce pitch motion standard deviation values.

Tank test results under regular, irregular, and extreme wave conditions showed reasonable agreement between the three configurations, particularly for pitch under regular waves, where relative errors remained low—for example, between 0.2% and 5.92% in the catenary model and between 6.87% and 14.69% in the adapted model (Tables 9 and 10). Standard deviation ratios for pitch in regular waves were also close to 1 for the catenary case, with values ranging from 0.97 to 1.23. On the other hand, these values ranged between 1.95 to 2.43 for the adapted model.

For surge, both models struggled to capture the mean values accurately, with relative errors reaching up to 89.65% in the catenary and over 440% in the adapted model for the regular wave cases. However, the standard deviation ratios remained close to 1 in both cases (between 0.90 and 1.11), indicating that the variability of the surge motion was still reasonably well reproduced.

The most significant differences appeared in the mooring tensions. The catenary model, which represents the full-scale reference configuration, showed substantially higher mooring tensions compared to the experimental and adapted systems, with relative errors between them up to 150% for the port and starboard lines under both irregular and extreme waves. For instance, in the catenary model under regular waves, fore mooring tensions were around 56% higher than those observed experimentally, with standard deviation ratios up to 1.42, while the adapted model showed markedly improved agreement, with relative errors below 10% and standard deviation ratios close to 1.00 under the same conditions.

This contrast is particularly evident in the irregular and extreme wave cases, where the adapted model maintained mooring tension errors below 18% across all lines and standard deviation ratios between 0.69 and 1.08, whereas the catenary model continued to show large deviations. These results reinforce the suitability of the adapted system configuration to replicate the experimental spring-rope system in terms of mooring tension response.

Physically representing the catenary pre-tension in the mooring lines is a challenge, as pre-tension values overcome the breaking load limit of the springs. Consequently, the experimental results revealed substantial differences in pre-tension compared to the catenary numerical model. Conversely, the mooring pre-tensions in the experimental tests showed good agreement with the adapted numerical model results. Discrepancies were more pronounced for specific lines, such as the starboard mooring line, where relative errors ranged from 55.1% to 128.5% in the catenary model and from 4.7% to 7.6% in the adapted model across wave conditions, highlighting the issue with the symmetry and uniformity of mooring forces in the tank setup.

Overall, representing a catenary system using a spring-rope configuration in experimental testing can be an effective approach for capturing global motions, particularly pitch, which showed consistently low relative errors, and surge variability, which was reasonably reproduced. However, accuracy in surge mean values remains more challenging, and mooring tensions require special attention, as the two systems exhibit fundamentally different restoring behaviours. In a catenary system, a significant portion of the restoring force derives from the weight of the mooring line, enabling gradual tension recovery as the chain lifts off the seabed. This aspect is not replicated in a spring-rope system, which relies purely on stiffness and exhibits greater sensitivity to low-frequency excitation. Developing a method to physically approximate the weight-based restoring behaviour—for example through distributed or concentrated weights—could improve the realism and performance of experimental spring-rope setups.

Moreover, it is important to note that even when a semi-taut mooring system is the intended design, discrepancies between numerical and experimental results may still arise. In this study, the adapted system configuration in the numerical model led to notable differences in pitch and surge responses compared to the tank test results, despite strong agreement in mooring line tensions. This suggests that semi-taut mooring systems may behave differently in numerical simulations than in physical environments, and such differences should be carefully accounted for during validation and design.

Acknowledgements. The authors declare the following financial interests/personal relationships which may be considered as potential competing interests: This research is Funded by the EPSRC and NERC for the Industrial CDT in Offshore Renewable Energy (EP/S023933/1) and sponsored by the FloWave Ocean Energy Research Facility.

Declarations

- Conflict of interest/Competing interests (Not applicable)

References

Amaral, G.A.: Analytical assessment of the mooring system stiffness. Mestrado em engenharia de estruturas, Universidade de São Paulo, São Paulo (2020). https://doi.org/10.11606/D.3.2020.tde-05112020-114447 . Accessed: 2023-09-27. https://www.teses.usp.br/teses/disponiveis/3/3144/tde-05112020-114447/

American Petroleum Institute: Design and Analysis of Stationkeeping Systems for Floating Offshore Structures - Draft (2018)

Amaral, G.A., Pesce, C.P., Franzini, G.R.: Mooring system stiffness: A six-degree-of-freedom closed-form analytical formulation. Marine Structures **84** (2022) https://doi.org/10.1016/j.marstruc.2022.103189

Allen, C., Viselli, A., Dagher Andrew Goupee, H., Gaertner, E., Abbas, N., Hall, M., Barter, G.: Definition of the UMaine VolturnUS-S Reference Platform Developed for the IEA Wind 15-Megawatt Offshore Reference Wind Turbine Technical Report, Golden, CO (2020)

Berthelsen, P.A., Bachynski, E.E., Karimirad, M., Thys, M.: Real-time hybrid model tests of a braceless semi-submersible wind turbine. Part III: Calibration of a numerical model. In: Proceedings of the ASME 2016 35th International Conference on Ocean, Offshore and Arctic Engineering, Busan, South Korea (2016)

Bhattacharya, S., Nikitas, G., Jalbi, S.: On the use of scaled model tests for analysis and design of offshore wind turbines. In: Geotechnics for Natural and Engineered Sustainable Technologies, Developments in Geotechnical Engineering. Springer, Singapore (2018). https://doi.org/10.1007/978-981-10-7721-0_6

British Standards Institution: Petroleum and natural gas industries - Specific requirements for offshore structures Part 7: Stationkeeping systems for floating offshore structures and mobile offshore units. BS EN ISO 19901-7:2013 (2013)

Crown Estate Scotland: ScotWind leasing round (2024). www.crownestatescotland.com/scotlands-property/offshore-wind/scotwind-leasing-round

Department for Business & Trade: Offshore wind (2024). https://www.great.gov.uk/international/content/investment/sectors/offshore-wind/

Det Norske Veritas: Design of Floating Wind Turbine Structures. DNV-OS-J103 (2013)

Det Norske Veritas: Coupled analysis of floating wind turbines. DNV-RP-0286 (2021)

Edwards, E.C., Holcombe, A., Brown, S., Ransley, E., Hann, M., Greaves, D.: Evolution of floating offshore wind platforms: A review of at-sea devices. Renewable and Sustainable Energy Reviews **183** (2023) https://doi.org/10.1016/j.rser.2023.113416

Equinor: Hywind Scotland (2024). www.equinor.com/energy/hywind-scotland

Faltinsen, O.: Sea Loads on Ships and Offshore Structures. Cambridge Ocean Technology Series. Cambridge University Press, UK (1993)

Fenu, B., Bonfanti, M., Bardazzi, A., Pilloton, C., Lucarelli, A., Mattiazzo, G.: Experimental investigation of a Multi-OWC wind turbine floating platform. Ocean Engineering **281** (2023) https://doi.org/10.1016/J.OCEANENG.2023.114619

Garrett, B.: pyMAP for Python Module of MAP. https://github.com/WISDEM/pyMAP/blob/dev/NOTICE.txt

HM Government: Net Zero Strategy: Build Back Greener (2021)

International Electrotechnical Commission: Wind turbines, Part 22: Conformity testing and certification. IEC 61400-22 (2011)

International Electrotechnical Commission: Wind energy generation systems, Part 3-2: Design requirements for floating offshore wind turbines. IEC TS 61400-3-2 (2019)

International Energy Agency: IEA-15-240-RWT. https://github.com/IEAWindTask37/IEA-15-240-RWT Accessed 01.05.2023

Ingram, D., Wallace, R., Robinson, A., Bryden, I.: The design and commissioning of the first, circular, combined current and wave test basin. In: Proceedings of the Oceans 2014 MTS/IEEE, Taipei, Taiwan, Province of China (2014). https://doi.org/10.1109/OCEANS-TAIPEI.2014.6964577

Jump, Ellen: Mooring and Anchoring Systems - Market Projections (2021)

LAUTEC/ESOX: ESOX - Map: Download and Analyze Metocean Data. https://esox.lautec.com/map/. Accessed: 2024-08-06 (2024)

Leite, A., Davey, T., Dai, D., Pillai, A.C., Bruce, T.: Cross-sectorial learning of model testing methodologies aligned to technology TRL. In: Proceedings of the ASME 2022 4th International Offshore Wind Technical Conference, Boston, Massachusetts, USA (2022). https://doi.org/10.1115/iowtc2022-93886

Ma, K.-T., Luo, Y., Kwan, T., Wu, Y.: Chapter 15 - Mooring for floating wind turbines. In: Mooring System Engineering for Offshore Structures, pp. 299–315. Gulf Professional Publishing, Houston, TX (2019). Chap. 15. https://doi.org/10.1016/B978-0-12-818551-3.00015-6

Ma, K.-T., Luo, Y., Kwan, T., Wu, Y.: Chapter 7 - model tests. In: Mooring System Engineering for Offshore Structures, pp. 139–153. Gulf Professional Publishing, Houston, TX (2019). Chap. 15. https://doi.org/10.1016/B978-0-12-818551-3.00007-7

Molins, C., Trubat, P., Gironella, X., Campos, A.: Design optimization for a truncated catenary mooring system for scale model test. Journal of Marine Science and Engineering **3**(4), 1362–1381 (2015) https://doi.org/10.3390/JMSE3041362

Ma, K.-T., Wu, Y., Stolen, S., Bello, L., Horst, M., Luo, Y.: Mooring designs for floating offshore wind turbines leveraging experience from the oil & gas industry. In: Proceedings of the ASME 2021 40th International Conference on Ocean, Offshore and Arctic Engineering (2021). https://doi.org/10.1115/OMAE2021-60739

National Renewable Energy Laboratory: OpenFAST v3.1.0. https://github.com/openfast/openfast/. Accessed: 2023-09-27 (2022)

Noble, D., Davey, T., Smith, H., Kaklis, P., Robinson, A., Bruce, T.: Spatial variation

in currents generated in the FloWave Ocean Energy Research Facility. In: Proceedings of the 11th European Wave and Tidal Energy Conference, Nantes, France (2015)

Newman, J., Lee, C.: WAMIT: A Radiation-Diffraction Panel Method for Wave-Body Interactions, Chestnut Hill, MA (1999). www.wamit.com

Pesce, C.P., Amaral, G.A., Franzini, G.R.: Mooring System Stiffness: A General Analytical Formulation With an Application to Floating Offshore Wind Turbines. International Conference on Offshore Mechanics and Arctic Engineering, vol. ASME 2018 1st International Offshore Wind Technical Conference (2018). https://doi.org/10.1115/IOWTC2018-1040

Pessoa, J., Fonseca, N., Guedes Soares, C.: Analysis of the first order and slowly varying motions of an axisymmetric floating body in bichromatic waves. Journal of Offshore Mechanics and Arctic Engineering **135** (2012) https://doi.org/10.1115/1.4007045

Principle Power: The Windfloat® advantage: Installation - Principle Power (2024). www.principlepower.com/windfloat/advantage/installation

Qiao, D.S., Ou, J.P.: Truncated model tests for mooring lines of a semi-submersible platform and its equivalent compensated method. Journal of Marine Science and Technology **22**(2), 125–136 (2014) https://doi.org/10.6119/JMST-013-0108-1

Ren, Y., Shi, W., Venugopal, V., Zhang, L., Li, X.: Experimental study of tendon failure analysis for a TLP floating offshore wind turbine. Applied Energy **358** (2024) https://doi.org/10.1016/J.APENERGY.2024.122633

Sodemann Industrial Springs: Compression Spring E05000375000S. Accessed: 2024-11-10 (2024). www.industrial-springs.com/e05000375000s

The University of Edinburgh: FloWave Ocean Energy Research Facility. www.flowavett.co.uk/ (2023)

Vlasblom, M.P., Van Dingenen, J.L.J.: Chapter 13 - The manufacture, properties and applications of high strength, high modulus polyethylene fibers. In: Handbook of Tensile Properties of Textile and Technical Fibres, pp. 437–485. Woodhead Publishing, Cambridge, UK (2009). https://doi.org/10.1533/9781845696801.2.437

Xu, X., Day, S.: Experimental investigation on dynamic responses of a spar-type offshore floating wind turbine and its mooring system behaviour. Ocean Engineering **236**, 109488 (2021) https://doi.org/10.1016/J.OCEANENG.2021.109488

Yang, C., Xiao, L., Deng, S., Chen, P., Liu, L., Cheng, Z.: An experimental study on the aerodynamic-induced effects of a semi-submersible floating wind turbine. Renewable Energy **222**, 119930 (2024) https://doi.org/10.1016/J.RENENE.2023.119930

Zwart, S.D.: Scale modelling in engineering: Froude's case. In: Philosophy of Technology and Engineering Sciences, pp. 759–798. North-Holland, Amsterdam (2009). https://doi.org/10.1016/B978-0-444-51667-1.50032-X

Bibliography

Pd iec ts 62600-103:2024: Marine energy. wave, tidal and other water current converters: Guidelines for the early stage development of wave energy converters. best practices and recommended procedures for the testing of pre-prototype devices, 2018.

Christopher Allen, Anthony Viscelli, Habib Dagher, Andrew Goupee, Evan Gaertner, Nikhar Abbas, Matthew Hall, and Garrett Barter. Definition of the UMaine VolturnUS-s reference platform developed for the IEA wind 15-megawatt offshore reference wind turbine. Technical Report NREL/TP-5000-76773, 1660012, MainId:9434, NREL, 2020.

Giovanni A. Amaral, Celso P. Pesce, and Guilherme R. Franzini. Mooring system stiffness: A six-degree-of-freedom closed-form analytical formulation. *Marine Structures*, 84:103189, 2022. ISSN 09518339. doi: 10.1016/j.marstruc.2022.103189.

Giovanni Aiosa do Amaral. Analytical assessment of the mooring system stiffness. https://www.teses.usp.br/teses/disponiveis/3/3144/tde-05112020-114447/, 2020.

Raffaello Antonutti, Jean-Charles Poirier, and Sébastien Gueydon. Coupled testing of floating wind turbines in waves and wind using winches and software-in-the-loop. In *Day 2 Tue, May 05, 2020*, page D021S019R001. OTC, 2020. doi: 10.4043/30555-MS.

José A. Armesto, Javier Sarmiento, Víctor Ayllón, Arantza Iturrioz, Alfonso Jurado, Raúl Guanche, and Iñigo J. Losada. Numerical and experimental study of a multi-use platform. In *Volume 6: Ocean Space Utilization; Ocean Renewable Energy*, page V006T09A018. American Society of Mechanical Engineers, 2016. ISBN 978-0-7918-4997-2. doi: 10.1115/OMAE2016-54427.

Vincent Arnal. *Experimental modelling of a floating wind turbine using a " software-in-the-loop " approach*. PhD thesis, École centrale de Nantes, 2020. URL `https://theses.hal.science/tel-03237441`.

José Azcona, Faisal Bouchotrouch, Marta González, Joseba Garciandía, Xabier Munduate, Felix Kelberlau, and Tor A Nygaard. Aerodynamic thrust modelling in wave tank tests of offshore floating wind turbines using a ducted fan. *Journal of Physics: Conference Series*, 524:012089, 2014. ISSN 1742-6596. doi: 10.1088/1742-6596/524/1/012089.

José Azcona, Faisal Bouchotrouch, and Felipe Vittori. Low-frequency dynamics of a floating wind turbine in wave tank–scaled experiments with sil hybrid method. *Wind Energy*, 22(10): 1402–1413, 2019. ISSN 1095-4244, 1099-1824. doi: 10.1002/we.2377.

Erin E. Bachynski, Valentin Chabaud, and Thomas Sauder. Real-time hybrid model testing of floating wind turbines: Sensitivity to limited actuation. *Energy Procedia*, 80:2–12, 2015. ISSN 1876-6102. doi: https://doi.org/10.1016/j.egypro.2015.11.400.

Erin E. Bachynski, Maxime Thys, Thomas Sauder, Valentin Chabaud, and Lars Ove Sæther. Real-time hybrid model testing of a braceless semi-submersible wind turbine: Part II — experimental results. In *Volume 6: Ocean Space Utilization; Ocean Renewable Energy*, page V006T09A040. American Society of Mechanical Engineers, 2016. ISBN 978-0-7918-4997-2. doi: 10.1115/OMAE2016-54437.

I. Bayati, A. Facchinetti, A. Fontanella, H. Giberti, and M. Belloli. A wind tunnel/HIL setup for integrated tests of floating offshore wind turbines. *Journal of Physics: Conference Series*, 1037:052025, 2018. ISSN 1742-6588, 1742-6596. doi: 10.1088/1742-6596/1037/5/052025.

Petter Andreas Berthelsen, Erin E Bachynski, Madjid Karimirad, and Maxime Thys. Real-time hybrid model tests of a braceless semi-submersible wind turbine. Part III: Calibration of a numerical model. In *Proceedings of the ASME 2016 35th International Conference on Ocean, Offshore and Arctic Engineering*, Busan, South Korea, 2016.

Pietro Bortolotti, Jennifer Rinker, Latha Sethuraman, Frederik Zahle, Benjamin Anderson, Garrett Barter, Nikhar Abbas, Fanzhong Meng, Pietro Bortolotti, Witold Skrzypinski, George Scott, Roland Feil, Henrik Bredmose, Katherine Dykes, Matt Shields, Christopher Allen, and Anthony Viselli. Definition of the iea wind 15-megawatt offshore reference wind turbine. Technical report, International Energy Agency, https://www.nrel.gov/docs/fy20osti/75698.pdf, 2020.

Paul Breeze. *Chapter 9 - Offshore Wind*. Academic Press, 2016. ISBN 978-0-12-804038-6. doi: https://doi.org/10.1016/B978-0-12-804038-6.00009-8. URL `https://www.sciencedirect.com/science/article/pii/B9780128040386000098`.

BSI. Marine energy - wave, tidal and other water current converters, part 103: Guidelines for the early stage development of wave energy converters - best practices and recommended procedures for the testing of pre-prototype devices, 2024. PD IEC TS 62600-103:2024.

Tony Burton, Nick Jenkins, David Sharpe, and Ervin Bossanyi. *Wind Energy Handbook*, chapter 3. Wiley, Chichester, UK, 2 edition, 2011. ISBN 9780470699751. doi: 10.1002/9781119992714.

Lucas Carmo, Pedro C. de Mello, Renato M. Monaro, Jordi Mas-Soler, Alexandre N. Simos, and Daniel Fonseca de Carvalho e Silva. Numerical modeling of wave basin experiments of a floating wind turbine with active thrust emulation: A discussion of important aspects. *Ocean Engineering*, 309:118379, 2024. ISSN 0029-8018. doi: https://doi.org/10.1016/j.oceaneng.2024.118379. URL `https://www.sciencedirect.com/science/article/pii/S0029801824017177`.

ORE Catapult. An innovator's guide to technology commercialisation in offshore wind. Technical report, ORE Catapult, 2020. URL https://ore.catapult.org.uk/wp-content/uploads/2020/10/OREC01_7489-SME-Wind-Technology-Commercialisation-SP.pdf.

Christian Cermelli, Dominique Roddier, and Alexia Aubault. WindFloat: A floating foundation for offshore wind turbines—part II: Hydrodynamics analysis. In *Volume 4: Ocean Engineering; Ocean Renewable Energy; Ocean Space Utilization, Parts A and B*, pages 135–143. ASMEDC, 2009. ISBN 978-0-7918-4344-4. doi: 10.1115/OMAE2009-79231.

Christian A. Cermelli and Dominique G. Roddier. Experimental and numerical investigation of the stabilizing effects of a water-entrapment plate on a deepwater minimal floating platform. In *International Conference on Offshore Mechanics and Arctic Engineering*, volume 24th International Conference on Offshore Mechanics and Arctic Engineering: Volume 2, pages 517–525, 06 2005. doi: 10.1115/OMAE2005-67077.

Subrata Chakrabarti. Physical model testing of floating offshore structures. In *DYNAMIC POSITIONING CONFERENCE*, 1998.

Subrata Chakrabarti. *Handbook of Offshore Engineering (2-volume set)*. Elsevier Science, San Diego, 1 edition, 2005.

Subrata Kumar Chakrabarti. *Offshore Structure Modeling*. World Scientific Publishing Co. Pte. Ltd. Singapore, 1994.

Toshiki Chujo, Shigesuke Ishida, Minami. Yoshimasa, Tadashi Nimura, and Shunji Inoue. Model experiments on the motion of a spar type floating wind turbine in wind and waves. In *ASME 2011 30th International Conference on Ocean, Offshore and Arctic Engineering*, volume 5, pages 655–662, Rotterdam, The Netherlands, January 2011. doi: 10.1115/OMAE2011-49793.

European Commission. Communication from the commission to the european parliament, the council, the european economic and social committee and the committee of the regions - the european green deal. Technical report, European Commission, 2019. URL https://eur-lex.europa.eu/resource.html?uri=cellar:b828d165-1c22-11ea-8c1f-01aa75ed71a1.0002.02/DOC_1&format=PDF.

Erik-Jan de Ridder, William Otto, Gert-Jan Zondervan, Fons Huijs, and Guilherme Vaz. Development of a scaled-down floating wind turbine for offshore basin testing. In *Volume 9A: Ocean Renewable Energy*, page V09AT09A027. American Society of Mechanical Engineers, 2014. ISBN 978-0-7918-4553-0. doi: 10.1115/OMAE2014-23441.

Antonio De Rose, Nicolo Olivieri, Carlo Strazza, Daniel Tawil-Jamault, Marina Buna, Leen Peeters, and Tine Stevens. Technology readiness levels (trl): Guidance for the research and innovation community. Technical report, Directorate-General for Research and Innovation (European Commission), 2017. URL https://op.europa.eu/en/publication-detail/-/publication/27d5e4e3-4a1b-11e8-be1d-01aa75ed71a1.

João Gorenstein Dedecca, Rudi A. Hakvoort, and J. Roland Ortt. Market strategies for offshore wind in europe: A development and diffusion perspective. *Renewable and Sustainable Energy Reviews*, 66:286–296, 2016. ISSN 1364-0321. doi: https://doi.org/10.1016/j.rser.2016.08.007. URL https://www.sciencedirect.com/science/article/pii/S1364032116304233.

Flavie Didier, Salah Laghrouche, and Daniel Depernet. Trust region policy optimization-based pitch control for floating offshore wind turbines in above-rated wind conditions. *Renewable Energy*, 256:123893, 2026. ISSN 0960-1481. doi: https://doi.org/10.1016/j.renene.2025.123893. URL https://www.sciencedirect.com/science/article/pii/S0960148125015575.

DNV. Dnv-st-0119: Floating wind turbine structures, 2018. URL https://www.dnv.com/energy/standards-guidelines/dnv-st-0119-floating-wind-turbine-structures/.

DNV. Dnv-rp-0286: Coupled analysis of floating wind turbines, 2021. URL https://www.dnv.com/energy/standards-guidelines/dnv-rp-0286-coupled-analysis-of-floating-wind-turbines/.

DNV. *Bladed 4.16 Documentation*, 2024. URL https://dnvgldocs.azureedge.net/BladedManual/4_16/index.html. Version 4.16.

G. Doisenbant, M. Le Boulluec, Y. M. Scolan, and M. Guyot. Numerical and experimental modeling of offshore wind energy capture: Application to reduced scale model testing. *Wind Engineering*, 42:108–1143, 2018. doi: 10.1177/0309524X18756967.

Samuel Thomas Draycott. *On the re-creation of site-specific directional wave conditions*. PhD thesis, The University of Edinburgh, Edinburgh, UK, July 2017. URL http://hdl.handle.net/1842/31472. PhD thesis.

Emma C. Edwards, Anna Holcombe, Scott Brown, Edward Ransley, Martyn Hann, and Deborah Greaves. Evolution of floating offshore wind platforms: A review of at-sea devices. *Renewable and Sustainable Energy Reviews*, 183:113416, 2023. ISSN 13640321. doi: 10.1016/j.rser.2023.113416. URL https://linkinghub.elsevier.com/retrieve/pii/S1364032123002733.

European Commission. Communication from the commission to the european parliament, the council, the european economic and social committee and the committee of the regions - a new era for research and innovation. https://eur-lex.europa.eu/legal-content/EN/TXT/PDF/?uri=CELEX:52020DC0741, 2020.

European Commission. Repowereu plan: Communication from the commission to the european parliament, the european council, the council, the european economic and social committee and the committee of the regions. COM(2022) 230 final, May 2022. URL https://eur-lex.europa.eu/legal-content/EN/TXT/?uri=COM%3A2022%3A230%3AFIN&qid=1653033742483. SWD(2022) 230 final.

EuropeWave. Tender document td02 annex a: Phase 1 testing, 2024. URL https://www.europewave.eu/deliverables. Accessed: 2024-08-08.

Emilio Faraggiana, Giuseppe Giorgi, Massimo Sirigu, Alberto Ghigo, Giovanni Bracco, and G. Mattiazzo. A review of numerical modelling and optimisation of the floating support structure for offshore wind turbines. *Journal of Ocean Engineering and Marine Energy*, 8, 2022. doi: 10.1007/s40722-022-00241-2.

A. Fontanella, Y. Liu, J. Azcona, O. Pires, I. Bayati, S. Gueydon, E. J. de Ridder, J. W. van Wingerden, and M. Belloli. A hardware-in-the-loop wave-basin scale-model experiment for the validation of control strategies for floating offshore wind turbines. *Journal of Physics: Conference Series*, 1618:032038, 2020. ISSN 1742-6588, 1742-6596. doi: 10.1088/1742-6596/1618/3/032038.

Matthew J. Fowler, Richard W. Kimball, Dale A. Thomas, and Andrew J. Goupee. Design and testing of scale model wind turbines for use in wind/wave basin model tests of floating offshore wind turbines. In *Volume 8: Ocean Renewable Energy*, page V008T09A004. American Society of Mechanical Engineers, 2013. ISBN 978-0-7918-5542-3. doi: 10.1115/OMAE2013-10122.

Andrew J. Goupee, Bonjun J. Koo, Richard W. Kimball, Kostas F. Lambrakos, and Habib J. Dagher. Experimental comparison of three floating wind turbine concepts. *Journal of Offshore Mechanics and Arctic Engineering*, 136(2), 2014. ISSN 0892-7219. doi: 10.1115/1.4025804.

S. Gueydon, I. Bayati, and E.J. de Ridder. Discussion of solutions for basin model tests of fowts in combined waves and wind. *Ocean Engineering*, 209:107288, 2020. ISSN 00298018. doi: 10.1016/j.oceaneng.2020.107288.

Sebastien Gueydon, Frances M. Judge, Michael O'Shea, Eoin Lyden, Marc Le Boulluec, Julien Caverne, Jérémy Ohana, Shinwoong Kim, Benjamin Bouscasse, Florent Thiebaut, Sandy Day, Saishuai Dai, and Jimmy Murphy. Round robin laboratory testing of a scaled 10 MW floating horizontal axis wind turbine. *Journal of Marine Science and Engineering*, 9 (9):988, 2021. ISSN 2077-1312. doi: 10.3390/jmse9090988.

A. F. Haselsteiner, J. Lemkuhl, T. Pape, K.-L. Windmeier, and K.-D. Thoben. Virocon: A software to compute multivariate extremes using the environmental contour method. *SoftwareX*, 2020. Accepted.

Valentin Heller. *Development of Wave Devices from Initial Conception to Commercial Demonstration*, chapter 8, pages 79–110. Elsevier, 2012. ISBN 9780080878737. doi: 10.1016/B978-0-08-087872-0.00804-0.

Fons Huijs, Erik-Jan de Ridder, and Feike Savenije. Comparison of model tests and coupled simulations for a semi-submersible floating wind turbine. In *Volume 9A: Ocean Renewable Energy*, page V09AT09A012. American Society of Mechanical Engineers, 2014. ISBN 978-0-7918-4553-0. doi: 10.1115/OMAE2014-23217.

Christian Elkjær Høeg and Zili Zhang. The influence of gyroscopic effects on dynamic responses of floating offshore wind turbines in idling and operational conditions. *Ocean Engineering*, 227:108712, 2021. ISSN 00298018. doi: 10.1016/j.oceaneng.2021.108712.

IEC. Wind energy generation systems, Part 3-1: Design requirements for fixed offshore wind turbines (IEC 61400-3-1:2019), 2019. URL `https://webstore.iec.ch/en/publication/29360`.

IEC. Bs en iec 61400-3-2:2025: Wind energy generation systems: Design requirements for floating offshore wind turbines, 2025. URL `https://bsol-bsigroup-com.eux.idm.oclc.org/Bibliographic/BibliographicInfoData/000000000030428830`.

Leaders in Global Business. Energy axis: Energy projects' tension leg buoy technology to harness potential of floating offshore wind, 2024. URL `https://www.leadersgb.co.uk/news/energy-axis-energy-projects-tension-leg-buoy-technology-to-harness-potential-of-floating-offshore-wind`. Accessed: 2024-08-05.

ITTC. Recommended procedures and guidelines, 7.5-02 07-03.2: Analysis procedure for model tests regular waves, 2017a. URL `https://www.ittc.info/media/8117/75-02-07-032.pdf`.

ITTC. Recommended procedures and guidelines, 7.5-02 07-03.8: Guideline for model tests for offshore wind turbines, 2017b. URL `https://www.ittc.info/media/8127/75-02-07-038.pdf`.

ITTC. Recommended procedures and guidelines, 7.5-02 07-03.16: Guideline for model construction of offshore systems, 2021. URL `https://www.ittc.info/media/9733/75-02-07-0316.pdf`.

J Jonkman and W Musial. Offshore code comparison collaboration (OC3) for IEA task 23 offshore wind technology and deployment. *Renewable Energy*, 2010.

J.M. Jonkman and M.L. Buhl Jr. *FAST User's Guide*, 2006.

Richard Kimball, Andrew J. Goupee, Matthew J. Fowler, Erik-Jan de Ridder, and Joop Helder. Wind/wave basin verification of a performance-matched scale-model wind turbine on a floating offshore wind turbine platform. In *Volume 9B: Ocean Renewable Energy*, page V09BT09A025. American Society of Mechanical Engineers, 2014. ISBN 978-0-7918-4554-7. doi: 10.1115/OMAE2014-24166.

Bonjun J. Koo, Andrew J. Goupee, Richard W. Kimball, and Kostas F. Lambrakos. Model tests for a floating wind turbine on three different floaters. *Journal of Offshore Mechanics and Arctic Engineering*, 136(2):020907, 2014. ISSN 0892-7219, 1528-896X. doi: 10.1115/1.4024711. URL https://asmedigitalcollection.asme.org/offshoremechanics/article/doi/10.1115/1.4024711/375234/Model-Tests-for-a-Floating-Wind-Turbine-on-Three.

LAUTEC/ESOX. Esox - map: Download and analyze metocean data. https://esox.lautec.com/map/, 2024. Accessed: 2024-08-06.

Marc Le Boulluec, Jérémy Ohana, Alexis Martin, and Anne Houmard. Tank testing of a new concept of floating offshore wind turbine. In *Volume 8: Ocean Renewable Energy*, page V008T09A100. American Society of Mechanical Engineers, 2013. ISBN 978-0-7918-5542-3. doi: 10.1115/OMAE2013-11577.

Liang Li, Yan Gao, Zhiqiang Hu, Zhiming Yuan, Sandy Day, and Haoran Li. Model test research of a semisubmersible floating wind turbine with an improved deficient thrust force correction approach. *Renewable Energy*, 119:95–105, 2018. ISSN 09601481. doi: 10.1016/j.renene.2017.12.019.

Chenyu Luan, Zhen Gao, and Torgeir Moan. Comparative analysis of numerically simulated and experimentally measured motions and sectional forces and moments in a floating wind turbine hull structure subjected to combined wind and wave loads. *Engineering Structures*, 177:210–233, 2018. ISSN 01410296. doi: 10.1016/j.engstruct.2018.08.021.

Tianqi ma and Chao Sun. Large eddy simulation of combined wind-wave loading on offshore wind turbines, 10 2023.

Ed Mackay, Guillaume de Hauteclocque, Erik Vanem, and Philip Jonathan. The effect of serial correlation in environmental conditions on estimates of extreme events. *Ocean Engineering*, 242, 2021. doi: https://doi.org/10.1016/j.oceaneng.2021.110092. URL https://www.sciencedirect.com/science/article/pii/S0029801821014189.

Heather R Martin, Richard W Kimball, Anthony M Viselli, and Andrew J Goupee. Methodology for wind/wave basin testing of floating offshore wind turbines. *Journal of Offshore Mechanics and Arctic Engineering*, (136):10, 2012.

Heather R. Martin, Richard W. Kimball, Anthony M. Viselli, and Andrew J. Goupee. Methodology for wind/wave basin testing of floating offshore wind turbines. *Journal of Offshore Mechanics and Arctic Engineering*, 136(2):020905, 2014. ISSN 0892-7219, 1528-896X. doi: 10.1115/1.4025030. URL https://asmedigitalcollection.asme.org/offshoremechanics/article/doi/10.1115/1.4025030/375201/Methodology-for-WindWave-Basin-Testing-of-Floating.

Sarah McElman, Arjen Koop, Erik-Jan de Ridder, and Andrew Goupee. Simulation and development of a wind-wave facility for scale testing of offshore floating wind turbines. In *Volume 6: Ocean Space Utilization; Ocean Renewable Energy*, page V006T09A035. American Society of Mechanical Engineers, 2016. ISBN 978-0-7918-4997-2. doi: 10.1115/OMAE2016-54281.

Huiwen Meng, Yongqian Liu, De Tian, Kai Long, and Zhang Han. Analysis of platform motion effects on fatigue loads and aerodynamic unsteadiness in 15 mw novel floating offshore wind turbines with transient impact. *Ocean Engineering*, 340:122359, 2025. ISSN 0029-8018. doi: https://doi.org/10.1016/j.oceaneng.2025.122359. URL https://www.sciencedirect.com/science/article/pii/S0029801825020438.

Climent Molins, Pau Trubat, Xavi Gironella, and Alexis Campos. Design optimization for a truncated catenary mooring system for scale model test. *Journal of Marine Science and Engineering*, 3(4):1362–1381, 2015. ISSN 2077-1312. doi: 10.3390/JMSE3041362.

NASA. *Technology Readiness Level (TRL) as the foundation of Human Readiness Level (HRL)*, September 2020.

Finn Gunnar Nielsen, Tor David Hanson, and Bjorn Skaare. Integrated dynamic analysis of floating offshore wind turbines. In *Volume 1: Offshore Technology; Offshore Wind Energy; Ocean Research Technology; LNG Specialty Symposium*, pages 671–679. ASMEDC, 2006. ISBN 978-0-7918-4746-6 978-0-7918-3777-1. doi: 10.1115/OMAE2006-92291.

Yasunori Nihei and Hiroyuki Fujioka. Motion characteristics of TLP type offshore wind turbine in waves and wind. In *29th International Conference on Ocean, Offshore and Arctic Engineering: Volume 3*, pages 283–292. ASMEDC, 2010. ISBN 978-0-7918-4911-8. doi: 10.1115/OMAE2010-21126.

NREL. Openfast v3.1.0. https://github.com/openfast/openfast/, 2022.

NREL. Openfast documentation. Technical report, National Renewable Energy Laboratory, 2024. URL https://openfast.readthedocs.io/en/main/.

M. K. Ochi and J. E. Wahlen. Prediction of severest significant wave height. *Coastal Engineering*, 36:587–599, 1980.

OffshoreWindInnovationHub. *EC scale of technology readiness as adapted by Offshore Wind innovation Hub*. Offshore Wind Innovation Hub, 2024.

Elif Oguz, Alexander H Day, David Clelland, Atilla Incecik, Saishuai Dai, Juan Amate Lopez, Gonzalo González, and Gustavo D Sánchez. Experimental study of a tlp offshore floating wind turbine. Technical report, Innovate UK, 2016. URL `https://strathprints.strath.ac.uk/58351/1/Oguz_etal_ICMT2016_Experimental_study_of_a_TLP_offshore_floating_wind_turbine.pdf`.

Elif Oguz, David Clelland, Alexander H. Day, Atilla Incecik, Juan Amate López, Gustavo Sánchez, and Gonzalo González Almeria. Experimental and numerical analysis of a tlp floating offshore wind turbine. *Ocean Engineering*, 147:591–605, 2018. ISSN 0029-8018. doi: https://doi.org/10.1016/j.oceaneng.2017.10.052.

Orcina. *OrcaFlex help*, 2024. URL `https://www.orcina.com/webhelp/OrcaFlex/`. Version 11.4c.

Joao Pessoa, Nuno Fonseca, and Carlos Guedes Soares. Analysis of the first order and slowly varying motions of an axisymmetric floating body in bichromatic waves. *Journal of Offshore Mechanics and Arctic Engineering*, 135, 05 2012. doi: 10.1115/1.4007045.

Maxime Philippe, Adrien Courbois, Aurélien Babarit, Félicien Bonnefoy, Jean-Marc Rousset, and Pierre Ferrant. Comparison of simulation and tank test results of a semi-submersible floating wind turbine under wind and wave loads. In *Volume 8: Ocean Renewable Energy*, page V008T09A081. American Society of Mechanical Engineers, 2013. ISBN 978-0-7918-5542-3. doi: 10.1115/OMAE2013-11271.

Principia. *DeepLines Documentation*, 2024. URL `https://www.principia-support.com/Software/Deeplines/Theory/Hydrodynamics/`. Version 5.8.

Dong Sheng Qiao and Jin Ping Ou. Truncated model tests for mooring lines of a semi-submersible platform and its equivalent compensated method. *Journal of Marine Science and Technology*, 22(2):125–136, 2014. ISSN 2709-6998. doi: 10.6119/JMST-013-0108-1.

Edward J. Ransley, Scott A. Brown, Emma C. Edwards, Tom Tosdevin, Kieran Monk, Alastair M. Reynolds, Deborah Greaves, and Martyn R. Hann. Real-time hybrid testing of a floating offshore wind turbine using a surrogate-based aerodynamic emulator. *ASME Open Journal of Engineering*, 2:021017, 2023. ISSN 2770-3495. doi: 10.1115/1.4056963. URL `https://asmedigitalcollection.asme.org/openengineering/article/doi/10.1115/1.4056963/1160164/Real-Time-Hybrid-Testing-of-a-Floating-Offshore`.

Amy N. Robertson, Jason M. Jonkman, Andrew J. Goupee, Alexander J. Coulling, Ian Prowell, James Browning, Marco D. Masciola, and Paul Molta. Summary of conclusions and recommendations drawn from the deepcwind scaled floating offshore wind system test campaign. In *Volume 8: Ocean Renewable Energy*, page V008T09A053. American Society of Mechanical Engineers, 2013. ISBN 978-0-7918-5542-3. doi: 10.1115/OMAE2013-10817.

Dominique Roddier, Christian Cermelli, and Alla Weinstein. WindFloat: A floating foundation for offshore wind turbines—part i: Design basis and qualification process. In *Volume 4: Ocean Engineering; Ocean Renewable Energy; Ocean Space Utilization, Parts A and B*, pages 845–853. ASMEDC, 2009. ISBN 978-0-7918-4344-4. doi: 10.1115/OMAE2009-79229.

Dominique Roddier, Christian Cermelli, Alexia Aubault, and Alla Weinstein. WindFloat: A floating foundation for offshore wind turbines. *Journal of Renewable and Sustainable Energy*, 2(3):033104, 2010. ISSN 1941-7012. doi: 10.1063/1.3435339.

Thomas Sauder, Valentin Chabaud, Maxime Thys, Erin E. Bachynski, and Lars Ove Sæther. Real-time hybrid model testing of a braceless semi-submersible wind turbine: Part i — the hybrid approach. In *Volume 6: Ocean Space Utilization; Ocean Renewable Energy*, page V006T09A039. American Society of Mechanical Engineers, 2016. ISBN 978-0-7918-4997-2. doi: 10.1115/OMAE2016-54435.

Hyunkyoung Shin, Sangrai Cho, and Kwangjin Jung. Model test of an inverted conical cylinder floating offshore wind turbine moored by a spring-tensioned-leg. *International Journal of Naval Architecture and Ocean Engineering*, 6(1):1–13, 2014. ISSN 20926782. doi: 10.2478/IJNAOE-2013-0159.

SINTEF. *SIMA Documentation*, 2024. URL `https://www.sima.sintef.no/doc/4.6.0/sima/index.html`.

Gordon Stewart, Amy Robertson, Jason Jonkman, and Matthew Lackner. The creation of a comprehensive metocean data set for offshore wind turbine simulations. *Wind Energy*, 19, 07 2015. doi: 10.1002/we.1881.

Duncan R.J. Sutherland, Donald R. Noble, Jeffrey Steynor, Thomas Davey, and Tom Bruce. Characterisation of current and turbulence in the flowave ocean energy research facility. *Ocean Engineering*, 139:103–115, 2017. doi: https://doi.org/10.1016/j.oceaneng.2017.02.028. URL `https://www.sciencedirect.com/science/article/pii/S0029801817300951`.

Holger Söker. 2 - loads on wind turbine blades. In Povl Brøndsted, Rogier Nijssen, and Stergios Goutianos, editors, *Advances in Wind Turbine Blade Design and Materials (Second Edition)*, Woodhead Publishing Series in Energy, pages 55–78. Woodhead Publishing, second edition edition, 2013. ISBN 978-0-08-103007-3. doi: https://doi.org/10.1016/B978-0-08-103007-3.00002-1. URL https://www.sciencedirect.com/science/article/pii/B9780081030073000021.

Albert M. Urbán and Raúl Guanche. Wind turbine aerodynamics scale-modeling for floating offshore wind platform testing. *Journal of Wind Engineering and Industrial Aerodynamics*, 186:49–57, 2019. ISSN 01676105. doi: 10.1016/j.jweia.2018.12.021.

Det Norske Veritas. Dnv-rp-c205: Environmental conditions and environmental loads, 2025. URL https://standards.dnv.com/explorer/document/01C72BD89E90416C89C4CA942694391E/6.

Anthony M. Viselli, Andrew J. Goupee, and Habib J. Dagher. Model Test of a 1:8-Scale Floating Wind Turbine Offshore in the Gulf of Maine1. *Journal of Offshore Mechanics and Arctic Engineering*, 137(4), 05 2015. ISSN 0892-7219. doi: 10.1115/1.4030381.

Felipe Vittori, José Azcona, Irene Eguinoa, Oscar Pires, Alberto Rodríguez, Alex Morató, Carlos Garrido, and Cian Desmond. Model tests of a 10 MW semi-submersible floating wind turbine under waves and wind using hybrid method to integrate the rotor thrust and moments. *Wind Energy Science*, 7(5):2149–2161, 2022. ISSN 2366-7451. doi: 10.5194/wes-7-2149-2022. URL https://wes.copernicus.org/articles/7/2149/2022/.

Fabian Vorpahl, Michael Strobel, Jason M. Jonkman, Torben J. Larsen, Patrik Passon, and James Nichols. Verification of aero-elastic offshore wind turbine design codes under iea wind task xxiii. *Wind Energy*, 17(4):519–547, 2014. doi: https://doi.org/10.1002/we.1588. URL https://onlinelibrary.wiley.com/doi/abs/10.1002/we.1588.

Simon Watson, Alberto Moro, Vera Reis, Charalampos Baniotopoulos, Stephan Barth, Gianni Bartoli, Florian Bauer, Elisa Boelman, Dennis Bosse, Antonello Cherubini, Alessandro Croce, Lorenzo Fagiano, Marco Fontana, Adrian Gambier, Konstantinos Gkoumas, Christopher Golightly, Mikel Iribas Latour, Peter Jamieson, John Kaldellis, Andrew Macdonald, Jimmy Murphy, Michael Muskulus, Francesco Petrini, Luca Pigolotti, Flemming Rasmussen, Philippe Schild, Roland Schmehl, Nafsika Stavridou, John Tande, Nigel Taylor, Thomas Telsnig, and Ryan Wiser. Future emerging technologies in the wind power sector: A european perspective. *Renewable and Sustainable Energy Reviews*, 113:109270, 2019. ISSN 1364-0321. doi: https://doi.org/10.1016/j.rser.2019.109270. URL https://www.sciencedirect.com/science/article/pii/S1364032119304782.

Binrong Wen, Xinliang Tian, Xingjian Dong, Zhanwei Li, Zhike Peng, Wenming Zhang, and Kexiang Wei. Design approaches of performance-scaled rotor for wave basin model tests of floating wind turbines. *Renewable Energy*, 148:573–584, 2020. ISSN 09601481. doi: 10.1016/j.renene.2019.10.147.

WindEurope. *Horizon 2020 Work Programme 2016–2017*. European Comission, April 2017. URL `https://ec.europa.eu/research/participants/data/ref/h2020/other/wp/2016-2017/annexes/h2020-wp1617-annex-ga_en.pdf`.

WindEurope. European offshore wind farms map public. https://windeurope.org/intelligence-platform/product/european-offshore-wind-farms-map-public/, April 2024. WindEurope.

X-Engineer. How to get the state-space model of a dynamic system. Technical report, X-Engineer, 2024. URL `https://x-engineer.org/state-space-model-dynamic-system/`.

Can Yang, Longfei Xiao, Shi Deng, Peng Chen, Lei Liu, and Zhengshun Cheng. An experimental study on the aerodynamic-induced effects of a semi-submersible floating wind turbine. *Renewable Energy*, 222:119930, 2 2024. ISSN 0960-1481. doi: 10.1016/J.RENENE.2023.119930.